



**HAL**  
open science

## Structural and dynamical studies on confined water

Eleonora Stefanutti

► **To cite this version:**

Eleonora Stefanutti. Structural and dynamical studies on confined water. Physics [physics]. Université Pierre et Marie Curie - Paris VI; Università degli studi Roma Tre, 2017. English. NNT: 2017PA066730 . tel-02406335

**HAL Id: tel-02406335**

**<https://theses.hal.science/tel-02406335>**

Submitted on 12 Dec 2019

**HAL** is a multi-disciplinary open access archive for the deposit and dissemination of scientific research documents, whether they are published or not. The documents may come from teaching and research institutions in France or abroad, or from public or private research centers.

L'archive ouverte pluridisciplinaire **HAL**, est destinée au dépôt et à la diffusion de documents scientifiques de niveau recherche, publiés ou non, émanant des établissements d'enseignement et de recherche français ou étrangers, des laboratoires publics ou privés.

UNIVERSITÀ DEGLI STUDI ROMA TRE  
UNIVERSITÉ PIERRE ET MARIE CURIE



DOCTORAL THESIS

---

# Structural and dynamical studies on confined water

---

*Author:*  
Eleonora STEFANUTTI

*Ph.D. Coordinator:*  
Prof. Fabio BRUNI

*Supervisors:*  
Prof. Fabio BRUNI  
Prof. Livia BOVE

*A thesis submitted in fulfillment of the requirements  
for the degree of Doctor of Philosophy*

*in the*

Science of Matter, Nanotechnology and Complex Systems (cycle XXIX)  
Department of Science

October 12, 2017



## Declaration of Authorship

I, Eleonora STEFANUTTI, declare that this thesis titled, “Structural and dynamical studies on confined water” and the work presented in it are my own. I confirm that:

- This work was done wholly or mainly while in candidature for a research degree at this University.
- Where any part of this thesis has previously been submitted for a degree or any other qualification at this University or any other institution, this has been clearly stated.
- Where I have consulted the published work of others, this is always clearly attributed.
- Where I have quoted from the work of others, the source is always given. With the exception of such quotations, this thesis is entirely my own work.
- I have acknowledged all main sources of help.
- Where the thesis is based on work done by myself jointly with others, I have made clear exactly what was done by others and what I have contributed myself.

Signed:  \_\_\_\_\_

Date: \_\_\_\_\_



*To Andrea*

*Sine causa et principio, impossibile est aliquid esse, vel fieri.*

---

*Aristotle (Rhetorica, 2)*

# Contents

<b>List of Figures</b>	<b>xi</b>
<b>List of Tables</b>	<b>xv</b>
<b>List of Abbreviations</b>	<b>xvii</b>
<b>Physical Constants</b>	<b>xix</b>
<b>Introduction</b>	<b>1</b>
<b>1 Generalities on water</b>	<b>5</b>
1.1 Water molecule . . . . .	6
1.1.1 Molecular structure . . . . .	6
1.1.2 Hydrogen bond . . . . .	6
1.2 Thermodynamic properties and water anomalies . . . . .	9
Thermal compressibility $\kappa_T$ . . . . .	9
Specific heat $C_P, C_V$ . . . . .	10
Thermal expansivity, $\alpha_P$ . . . . .	11
Statistical fluctuations . . . . .	12
Diffusion coefficient . . . . .	13
1.3 Phase diagram of bulk water . . . . .	16
1.3.1 The <i>stable</i> phase diagram . . . . .	16
1.3.2 The <i>metastable</i> phase diagram . . . . .	18
1.3.3 Homogeneous and heterogeneous nucleation . . . . .	22
Classical Nucleation Theory . . . . .	22
1.4 Interpretations of water anomalies . . . . .	24
1.4.1 The retracing spinodal . . . . .	25
1.4.2 The singularity-free scenario . . . . .	25
1.4.3 The second critical point hypothesis . . . . .	27
1.4.4 Relation between nucleation rate and water anomalies . . . . .	31
<b>2 Confined water</b>	<b>35</b>
2.1 Introduction . . . . .	35
2.2 Capillary condensation in mesopores . . . . .	36
2.3 Adsorption . . . . .	40
2.4 Effect of confinement on water . . . . .	42

2.4.1	Freezing and melting under confinement . . . . .	42
	Hexagonal or cubic ice? . . . . .	44
2.4.2	Structure and dynamics under confinement . . . . .	46
	Structural modifications . . . . .	47
	Dynamic behaviour . . . . .	48
2.4.3	From confined to bulk water: does it make sense? . . . . .	50
2.5	MCM-41 . . . . .	51
2.5.1	Synthesis of MCM-41 . . . . .	52
<b>3</b>	<b>Experimental techniques: Neutron scattering</b>	<b>55</b>
3.1	Theoretical background . . . . .	56
3.1.1	Basic principles of neutron scattering . . . . .	56
3.1.2	The scattering cross section . . . . .	57
3.1.3	The Fermi pseudopotential . . . . .	61
3.1.4	Coherent and incoherent cross sections . . . . .	62
3.1.5	Correlation functions . . . . .	62
3.1.6	Molecular fluids and multicomponent systems . . . . .	64
3.1.7	The isotopic substitution and EPSR simulations . . . . .	65
3.1.8	Small Angle Neutron Scattering (SANS) . . . . .	66
	SANS data analysis . . . . .	67
3.2	From an ideal to a real scattering experiment . . . . .	68
3.3	The experimental apparatus . . . . .	69
3.3.1	The neutron source . . . . .	69
3.3.2	The <i>NIMROD</i> diffractometer at ISIS . . . . .	70
<b>4</b>	<b>Experimental techniques: Infrared spectroscopy</b>	<b>73</b>
4.1	Theoretical background . . . . .	74
4.1.1	Vibrational transitions . . . . .	74
4.1.2	Rotational transitions . . . . .	75
4.1.3	Vibrational modes of water molecule . . . . .	76
4.2	The experimental apparatus . . . . .	78
4.2.1	The synchrotron radiation . . . . .	78
4.2.2	The <i>AILES</i> beamline at synchrotron SOLEIL . . . . .	80
	The high-pressure/low-temperature (HPLT) set-up . . . . .	82
<b>5</b>	<b>Experimental results: Neutron Scattering</b>	<b>85</b>
5.1	Overview and motivations . . . . .	85
5.2	Sample preparation . . . . .	86
5.3	Neutron diffraction experiments . . . . .	88
5.3.1	Experimental details . . . . .	88
5.3.2	Raw data reduction . . . . .	88
5.3.3	Substrate characterization and determination of the sample density . . . . .	91
5.4	Experimental results . . . . .	94
5.4.1	Dry substrates . . . . .	94
5.4.2	Hydrated samples . . . . .	96
5.4.3	Short-range correlations: $D_2O$ peak . . . . .	98
5.4.4	Medium-range correlations: silica peak . . . . .	105
	Background subtraction . . . . .	107
	Data analysis . . . . .	108

5.4.5	Long-range correlations: Porod region . . . . .	113
5.4.6	Discussion and conclusions . . . . .	115
<b>6</b>	<b>Experimental results: Infrared spectroscopy</b>	<b>121</b>
6.1	Overview and motivations . . . . .	121
6.2	Sample preparation . . . . .	123
6.3	Infrared spectroscopy experiments . . . . .	124
6.3.1	Experimental details . . . . .	124
6.3.2	Data treatment . . . . .	127
	Wavelet denoising . . . . .	129
	Detrending . . . . .	132
	Background subtraction . . . . .	133
6.4	Experimental results . . . . .	134
6.4.1	Mid-infrared data (MIR) . . . . .	134
6.4.2	Far-infrared data (FIR) . . . . .	141
6.5	Discussion and conclusions . . . . .	145
<b>7</b>	<b>Conclusions</b>	<b>155</b>
	<b>Bibliography</b>	<b>161</b>



# List of Figures

1.1	Water molecule and HBs. . . . .	7
1.2	Water isothermal compressibility as a function of temperature at atmospheric pressure. . . . .	10
1.3	Constant-pressure specific heat of water as a function of temperature at ambient pressure. . . . .	11
1.4	(a) Liquid water density as a function of temperature at ambient pressure. (b) Temperature dependence of the thermal expansion coefficient for stable and supercooled water. . . . .	12
1.5	Schematic comparison between the temperature dependence of the main thermodynamic response functions for simple liquids and water. . . . .	13
1.6	Angell's strong-fragile behaviour of viscosity for different liquids. . . . .	15
1.7	Water phase diagram. . . . .	16
1.8	Structure of hexagonal and cubic ice. . . . .	18
1.9	Metastable phase diagram of water. . . . .	19
1.10	Irreversible transformations between non-crystalline forms of water. . . . .	20
1.11	(a) Experimental realization of LDA and HDA. (b) Comparison of the short-range structures of HDA, LDA, ice $I_h$ and liquid water using the spatial density function representation obtained from neutron scattering data. . . . .	21
1.12	Free energy of formation of nucleation clusters during a homogeneous nucleation process. . . . .	23
1.13	Water phase diagram showing the continuous retracing spinodal curve $T_{sr}$ as postulated by Speedy's stability limit conjecture. . . . .	26
1.14	Example of response function for different pressures derived from the mean-field solution of the lattice-model by Sastry <i>et al</i> [10]. This is known as the singularity-free scenario. . . . .	27
1.15	(a) Metastable phase diagram tracked following the second-critical-point interpretation. (b) Phase diagram of ST2 water. (c) The main result from the work of Palmer <i>et al.</i> [126]: free-energy isosurfaces show two minima corresponding to two distinct forms of liquid water differing in density, separated by a first-order phase transition. . . . .	29
1.16	Time-temperature-transformation (TTT) diagram of mW water by Moore and Molinero [122]. . . . .	33

2.1	(a) Schematic diagram of contact angle of a liquid droplet adsorbed onto a solid surface. (b) Water condensation on pore wall with the formation of a meniscus at the vapour-liquid interface. . . . .	38
2.2	IUPAC classification of gas adsorption isotherms. . . . .	41
2.3	Molecular simulation of water (red particles) confined within a nanopore of length $L$ , radius $R + \lambda$ and a disordered hydrophilic surface that mimic silica in the matrix named MCM-41. . . . .	45
2.4	(a) Snapshot of ice crystal structure at 220 K as observed in Monte Carlo molecular simulations. (b) Sequences of cubic (red) and hexagonal (green) ice with a regular (fault-free) structure. . . . .	46
2.5	Density profile, $\rho(r)$ , of water confined in cylindrical pores, projected along the radial direction with respect to pore axis. . . . .	48
2.6	$(P, T)$ phase diagram of water with the fragile-to-strong crossover temperature, the temperature of maximum density line and the Widom line. . . . .	50
2.7	TEM image of MCM-41 produced by ACS Material. . . . .	52
2.8	Sketch of the synthesis pathway of MCM-41 via the liquid-crystal templating (LCT) mechanism. . . . .	53
3.1	Schematic representation of a neutron scattering experiment. . . . .	56
3.2	Geometry of a typical scattering experiment. . . . .	58
3.3	Radial distribution function for a typical Lennard-Jones liquid of diameter $\sigma$ . . . . .	64
3.4	Cutaway diagram of NIMROD with an overview of its key components. . . . .	71
4.1	Vibrational modes of water molecule. . . . .	78
4.2	FIR and MIR spectra of liquid water at 298 K. . . . .	79
4.3	Schematic representation of a Michelson interferometer unit (FTIR). . . . .	82
4.4	External view of the HPLT set-up at the AILES beamline. . . . .	83
4.5	(a) Schematic view of a DAC. (b) Layout of the HPLT setup and the spectrometer. . . . .	84
5.1	Constant time-of-light trajectories in $(Q, \epsilon)$ space sampled in a time-of-flight diffractometer (SANDALS at ISIS) at a scattering angle of $30.71^\circ$ ( $Q$ and $\epsilon$ are the momentum and the energy transfer respectively). . . . .	91
5.2	Left: Example of "steps" in the DCS of C10 sample filled with $D_2O$ at 284 K, due to an unfitting merge of the scattered intensity revealed by different detector groups. Right: Some of the 25 NIMROD detector groups individually represented. . . . .	92
5.3	Differential scattering cross section for dry C10 (a) and C18 (b) MCM-41 at ambient and low temperature (285 K and 209 K, respectively). (c) Two dimensional hexagonal structure of MCM-41 material. . . . .	95
5.4	Example of neutron differential cross section of C10 hydrated with $D_2O$ at 284 K, measured at the NIMROD diffractometer. In the graph four $Q$ -ranges are evidenced with different colours, corresponding to the different size scales accessible. . . . .	96
5.5	DCS of C10 sample (pore size 2.8 nm), hydrated with the HD mixture. . . . .	97
5.6	DCS of C18 sample (pore size 4.5 nm), hydrated with the HD mixture. . . . .	98
5.7	Differential cross sections of C10 sample (pore size 2.8 nm), hydrated with $D_2O$ at different temperatures. . . . .	100

5.8	Comparison between DCS of C10 and C18 samples, hydrated with D <sub>2</sub> O at different temperatures. . . . .	101
5.9	Results obtained from light and heavy water confined in MCM-41 matrix by [174]. The plot shows the temperature difference between melting/freezing transition in bulk and confined water ( $\Delta T_p$ ) as a function of the inverse pore radius ( $R' = R - \lambda$ ), also accounting for the non-freezable interfacial water layer ( $\lambda$ ). . . . .	102
5.10	Differential cross-sections of wet <sub>D<sub>2</sub>O</sub> C10 at different temperatures: solid lines represent scattering patterns obtained along the cooling path (from 284 K to 220 K), dashed lines indicate scattering patterns measured along the warming path (from 220 K to 284 K); each colour corresponds to a different temperature. . . . .	103
5.11	EPSR simulations of cubic and hexagonal ice, performed employing the SPC/E water model (courtesy of Alan Soper), compared to the experimental differential cross-section of D <sub>2</sub> O (dashed line) confined in C10 matrix (pore size 2.8 nm). . . . .	104
5.12	$Q$ -region corresponding to the silica peak (i.e. the porous substrate) in wet <sub>HD</sub> (a) and wet <sub>D<sub>2</sub>O</sub> (b) MCM-41/C10 samples (pore size 2.8 nm). . . . .	106
5.13	Figure from [70] showing the average D <sub>2</sub> O density inside MCM-41-S-15 measured by SANS technique as a function of temperature. . . . .	106
5.14	Background at low $Q$ , $I(Q) = A \cdot Q^p$ , with $p < 0$ , modelled as a power law decay for each DCS obtained from wet <sub>D<sub>2</sub>O</sub> C10. . . . .	107
5.15	(A) Silica Bragg peak at different temperatures after background subtraction. (B) The same plot taken from [70]. . . . .	108
5.16	Analysis of the Bragg peak intensity distribution by using the model given by eq.5.9. . . . .	111
5.17	Temperature evolution of D <sub>2</sub> O density upon cooling, calculated as a fit parameter obtained by eq.5.9. . . . .	112
5.18	Comparison between data calculated in the present work (red symbols) and those reported in [70] (blue symbols).(a) Temperature evolution of D <sub>2</sub> O density upon cooling.(b) Thermal expansion coefficient, $-\alpha_P = \rho_m^{-1}(\partial\rho/\partial T)$ as a function of temperature. . . . .	114
5.19	Porod region of DCS obtained from wet <sub>D<sub>2</sub>O</sub> C10 sample at different temperatures. . . . .	114
5.20	Scattered intensity as a function of temperature for selected $Q$ values in the Porod region. Straight lines represent linear fits of the experimental data. . . . .	115
6.1	$P - T$ phase diagram of water confined in mesoporous silica matrix MCM-41-S (with 14 Å nominal pore diameter). . . . .	123
6.2	The FT-IR transmission spectrum of Nujol and Fluorolube <sup>®</sup> . . . . .	125
6.3	Comparison between FIR spectra acquired along cooling and warming paths for some selected temperatures at 0.11 GPa. . . . .	126
6.4	Example of raw data in the MIR frequency domain. The absorbance intensity obtained from the interferogram recorded at the AILES beamline presents some evident oscillations superimposed to the signal containing information we were interested in. . . . .	127
6.5	Example of MIR absorbance (red line), recorded at 297 K and 0.07 GPa, fitted by using eq.6.3 with $n = 3$ (blue line) in order to remove the "big" oscillations, which represent the undesired component in the experimental signal. . . . .	129

6.6	Signal obtained as the subtraction of the sinusoid term $S(\omega)$ of the fit function reported in fig.6.5 (blue line) from the raw data (red line). . . . .	129
6.7	Fit of the left (a) and right (b) tail of the signal (red line) obtained as the subtraction of the sinusoidal term in eq.6.3 from the experimental raw data (fig.6.6). . . . .	130
6.8	Denoised signal as a result of the application of the Stationary Wavelet Decomposition technique described in the text (purple), and the residuals calculated as the difference between original and denoised signal (yellow). . . . .	133
6.9	Example of the application of the Stationary Wavelet Decomposition (SWD) technique to filter the MIR spectra collected at the AILES beamline. . . . .	134
6.10	Example of detrending procedure applied to MIR signals after wavelet denoising. . . . .	135
6.11	Example of background subtraction procedure applied on the MIR signals after wavelet denoising and detrending. . . . .	136
6.12	Temperature evolution of the OH-stretching band of H <sub>2</sub> O trapped in MCM-41/C10 at different pressures (0.07, 0.15, 0.20, 0.25 GPa). . . . .	137
6.13	Position of the maximum of the OH-stretching band of confined water as a function of temperature, for different pressures. . . . .	138
6.14	Example of the spectral deconvolution of the OH-stretching band of confined water in the MIR frequency range, collected at 223 K and 0.07 GPa. For all temperatures, the OH-stretching band has been decomposed in four distinct intramolecular sub-bands modelled as Gaussian curves, centred around $\sim 3080 \text{ cm}^{-1}$ (green band, number 1), $\sim 3200 \text{ cm}^{-1}$ (blue band, number 2), $\sim 3450 \text{ cm}^{-1}$ (yellow band, number 3), $\sim 3630 \text{ cm}^{-1}$ (magenta band, number 4). . . . .	139
6.15	Position of the centre of the peaks relative to the four sub-bands coming from the decomposition of the OH-stretching band of confined water as a function of temperature. . . . .	140
6.16	Temperature evolution of the relative integrated areas (fractional areas) of the spectral components contributing to the OH-stretching band of confined water. . . . .	141
6.17	Overview of the FIR raw data (spectra as acquired, with no pre-processing) collected by varying temperature and pressure. . . . .	142
6.18	Temperature evolution of the connectivity band of H <sub>2</sub> O confined in MCM-41/C10 at different pressures (0.11, 0.16, 0.21, 0.30 GPa) after denoising and linear background subtraction. . . . .	144
6.19	Temperature evolution of the integrated area under the connectivity band (empty symbols) for each pressure. Solid lines are linear fits, while dotted curves are guides for the eyes. . . . .	145
6.20	Comparison between the temperature evolution of the relative populations (fractional area) of the main spectral contributions to the OH-stretching band found by us at the lowest pressure (a) and that reported by Mallamace and his co-workers at ambient pressure (b) [69]. . . . .	149
6.21	Comparison between FIR spectra of water confined in a porous silica substrate obtained from our experiment (a) and the signal of hexagonal or amorphous ice and liquid water over the same spectral region available in [306] (b). . . . .	150
6.22	Analysis of FIR spectra of 2D water performed by [306]. . . . .	151

# List of Tables

1.1	Typical bond energies. . . . .	7
1.2	Possible transformations between non-crystalline forms of water. . . . .	20
3.1	Basic properties of the neutron. . . . .	56
3.2	Comparison between the coherent and incoherent scattering lengths ( $b_{coh}$ and $b_{inc}$ , respectively) and the total, coherent and inchoerent cross-sections ( $\sigma_{tot}$ , $\sigma_{coh}$ and $\sigma_{inc}$ , respectively) of two largely used isotopes: hydrogen (H) and deuterium (D). . . . .	60
3.3	Main nominal characteristics of the diffractometer NIMROD. . . . .	72
4.1	Spectral acquisition ranges available at the beamline AILES. . . . .	81
5.1	Main properties of the two MCM-41 preparations used for our samples. . . . .	87
5.2	Hydration level $h$ (defined as in eq.5.1) obtained for the two MCM-41 matrices when loaded with pure D <sub>2</sub> O and the HD mixture made of 92% H <sub>2</sub> O and 8% D <sub>2</sub> O. . . . .	87
5.3	Principal fitted model parameters (Bragg peak position, Lorentzian width and D <sub>2</sub> O mass density) as a function of temperature. . . . .	112



# List of Abbreviations

<b>ASW</b>	<b>Amorphous Solid Water</b>
<b>CF</b>	<b>Correlation Function</b>
<b>CP</b>	<b>Critical Point</b>
<b>DAC</b>	<b>Diamond Anvil Cell</b>
<b>DSC</b>	<b>Differential Scanning Calorimetry</b>
<b>FFT</b>	<b>Fast Fourier Transform</b>
<b>FIR</b>	<b>Far-Infrared</b>
<b>FS</b>	<b>Fragile-to-Strong</b>
<b>FSC</b>	<b>Fragile-to-Strong Crossover</b>
<b>FTIR</b>	<b>Fourier Transform Infrared</b>
<b>FWHM</b>	<b>Full Width at Half Maximum</b>
<b>HB</b>	<b>Hydrogen Bond</b>
<b>HDA</b>	<b>High Density Amorphous</b>
<b>HDL</b>	<b>High Density Liquid</b>
<b>IR</b>	<b>Infrared</b>
<b>ISF</b>	<b>Intermediate Scattering Function</b>
<b>IWT</b>	<b>Inverse Wavelet Transform</b>
<b>LDA</b>	<b>Low Density Amorphous</b>
<b>LDL</b>	<b>Low Density Liquid</b>
<b>LLPT</b>	<b>Liquid-Liquid Phase Transition</b>
<b>MCT</b>	<b>Mode Coupling Theory</b>
<b>MD</b>	<b>Molecular Dynamics</b>
<b>MIR</b>	<b>Mid-Infrared</b>
<b>NIR</b>	<b>Near-Infrared</b>
<b>NMR</b>	<b>Nuclear Magnetic Resonance</b>
<b>PDF</b>	<b>Pair Distribution Function</b>
<b>PSF</b>	<b>Partial Structure Factor</b>
<b>QENS</b>	<b>Quasi-Elastic Neutron Scattering</b>
<b>RCM</b>	<b>Relaxing Cage Model</b>
<b>RDF</b>	<b>Radial Distribution Function</b>
<b>RS</b>	<b>Retracing Spinodal</b>
<b>RTN</b>	<b>Random Tetrahedral Network</b>
<b>SANS</b>	<b>Small Angle Neutron Scattering</b>
<b>SAXS</b>	<b>Small Angle X-ray Scattering</b>
<b>SF</b>	<b>Singularity Free</b>

<b>SSF</b>	<b>Static Structure Factor</b>
<b>TEM</b>	<b>Transmission Electron Microscopy</b>
<b>TP</b>	<b>Triple Point</b>
<b>WAXS</b>	<b>Wide Angle X-ray Scattering</b>
<b>WT</b>	<b>Wavelet Transform</b>
<b>UV</b>	<b>Ultraviolet</b>
<b>1D</b>	<b>One Dimension</b>
<b>2D</b>	<b>Two Dimensions</b>
<b>3D</b>	<b>Three Dimensions</b>

# Physical Constants

Avogadro's number	$N_A = 6.022 \times 10^{23} \text{ mol}^{-1}$
Boltzmann constant	$k_B = 1.381 \times 10^{-23} \text{ J/K}$
Elementary charge	$e = 1.602 \times 10^{-19} \text{ C}$
Nuclear magneton	$\mu_N = 5.051 \times 10^{-27} \text{ J/T}$
Universal gas constant	$\mathcal{R} = 8.314\,459\,8 \text{ JK}^{-1}\text{mol}^{-1}$



# Introduction



Understanding the essential role played by water on our Planet and in all aspects of life phenomena has attracted the human curiosity since the dawn of philosophical thought. We have to come back to ancient Greece, in Mileto during VI sec. B.C., to track down the first attempts of fathoming the role of water on Earth, when Talete identified water as the “principle” of everything. Several other ancient philosophers followed this way, regarding water as a fundamental constituent of Nature and life. Through centuries, the attention devoted to water did not cease, but rather rose up, keeping its role as a source of inspiration for naturalists, scientists, poets and artists, and attesting its central place in human collective imagination [1]. Importantly for our purposes, still today it represents one of the most challenging and fascinating research problems in science and technology [2-4].

If we carefully think about it, this should sound quite surprising. In fact, we all learned from school about water and its simple structure, so that we may believe nothing more is really needed to be understood and no truly intriguing aspects are still waiting to be disclosed. However nothing could be further from the truth. The reason is that, with respect to other liquids, a deceptive simple molecular structure does not result in a simple and fully understandable behaviour. For example, everyone has experienced in his daily life that ice floats in liquid water, meaning that water solid phase is less dense than the liquid one. This is the consequence of the fact that water exhibits a density maximum at a temperature higher than its melting point. Thus, what appears so natural to our common sense is actually one of the most evident traces of the strange behaviour of water. But this is just a little piece of the whole story: many other response functions and dynamic properties, such as isothermal compressibility, isobaric heat capacity and diffusion coefficient, reveal

unexpected and counter-intuitive trends upon cooling. The problem is that a comprehensive molecular model of water is currently unavailable and over the years many plausible (but not exhaustive) explanations of this unusual behaviour have been proposed. Despite the various and different interpretations, one aspect seems to make everybody agree: the extended three-dimensional hydrogen-bond network established between water molecules and related cooperative phenomena are accountable for all water anomalies [5].

Interestingly, anomalies become drastically enhanced in the region of the phase diagram where water is said to be *supercooled*: under carefully controlled experimental conditions, water can remain as a liquid even if temperature is lowered under the melting point, being in a state that is metastable with respect to ice. Studies of supercooling phenomenology occurring in water are far to be a new effort, as the first review concerning this topic has been published in 1775 [6]. Despite this long time, an intense curiosity and fervid research activity have been notably renewed in the last three decades [7].

Amid the many theoretical approaches developed for describing water in its supercooled state [5, 8–14], the liquid-liquid phase transition (LLPT) hypothesis is of particularly active interest, being the subject of an intense and controversial debate among the scientific community. On the basis of LLPT model, supercooled water is a mixture of two liquid phases differing in density: the low-density liquid (LDL), with a local "ice-like" structure, and the high-density liquid (HDL), with a highly disordered structure, being the local tetrahedral hydrogen bond (HB) network not fully developed. These two phases are regarded to be separated by a coexistence line ending in a critical point located at  $T_C \sim 220$  K and  $P_C \sim 1$  kbar, and should be the thermodynamic continuations of the amorphous solid phases observed at lower temperature (below the glass transition) [15, 16].

Experimental proofs of the existence of the second critical point have been provided so far, but none of them seems to unambiguously confirm theoretical previsions [9, 17]. The reason lies in the difficulties to explore the metastable phase diagram of water preventing its spontaneous nucleation. In fact, an experimental limit of stability exists for bulk liquid water: the *homogeneous* nucleation temperature ( $T_H$ ), that is around 232 K at ambient pressure. Usually water crystallizes between 273 K ( $T_m$ ) and 232 K ( $T_H$ ) because of impurities, that boost the liquid-ice phase transition. In this case, the crystallization process is not regarded as spontaneous and is known as *heterogeneous* nucleation.

Crystallization can be avoided by rapid cooling water under  $T_H$ , leading water to freeze into a glassy amorphous solid. But if we heat again amorphous ice attempting to penetrate the supercooled region of the phase diagram from below, we encounter another limiting temperature: the temperature of spontaneous crystallization,  $T_X \sim 150$  K, above which water inexorably crystallizes [17]. This implies that probing bulk liquid water in the temperature range between  $T_X$  and  $T_H$  is impossible: this is what is commonly known as *No man's land* [18]. The hypothetical second critical point is located below the homogeneous nucleation line into this deeply supercooled region [9, 17, 19], and this explains why the number of theoretical works clearly supporting the LLPT hypothesis markedly overwhelms the number of reliable experimental tests currently available.

As a consequence, several strategies have been developed over the years to circumvent such a hindrance. Hyperquenching [20, 21], aqueous solutions [22–25] and confinement into restricted geometric environments represent some of the most employed tricks to avoid crystallization of supercooled water and investigate its oddities.

Among these possibilities, in the present thesis we opted for nanoconfinement. By confining water in nanometric space we can cause a downshift of the nucleation temperature to an extent that depends on the size of the confining volume, hopefully allowing us to enter the *No man's land*; if the confining volume is small enough, the formation of nucleation centres can

be avoided at all. In particular, we used MCM-41 as confining matrix. MCM-41 has been an attractive and intensively studied material since the early 1990s when it was discovered independently for the first time in Japan by Kuroda's group [26] and in the USA by Kresge and his coworkers employed at the "Mobil Research and Development Corporation" [27]. The widespread interest about MCM-41 is due to its very regular structure and easy synthesis. Essentially it is a molecular sieve belonging to the family of mesoporous silicates with a hexagonal array of uniform-sized parallel cylindrical pores whose diameter can be varied between 1.5 and 10 nm, depending on the preparation method [28–31].

We studied water inside MCM-41 pores by taking advantage of the opportunity to perform scattering experiments at synchrotron and neutron facilities, rapidly grown up in recent years. More specifically, we employed a suite of experimental techniques: neutron diffraction, small angle neutron scattering, and infrared spectroscopy. These allowed us to obtain a complete picture about *structure* of supercooled water as a function of temperature at ambient pressure. Moreover, infrared spectroscopy over a wide frequency range (mid- and far-infrared) made it possible to gather important hints about water *dynamics*, focusing our attention on hydrogen bonds (HBs) vibrations by varying both temperature and pressure. Nevertheless, the interest on a deep understanding of water properties is not limited to physics, and many implications can indeed be found in other fields of knowledge. For example, supercooled and solid water is found in clouds and celestial bodies, respectively, and water is naturally confined inside rocks, so that aspects related to our research might be of importance also for atmospheric physics, geology and astronomy. Moreover, water in biological systems is seldom found as a bulk; more commonly it appears as a solvent, in confined environments or layered on surfaces. Plants, living cells, membranes, ions, proteins, enzymes, DNA and RNA filaments and other macromolecules represent just some of the huge amount of examples we could think about. In addition, also implications in our daily life related to this topic are not lacking. For instance, studies on strategies for water supercooling take on an important role in the food industry and storage [32, 33]. In case someone was still doubtful, we hope to have convinced him that studying water and its anomalies is not merely a curiosity of physicists and chemists, but it is worth all the efforts it implicates and has demanded so far.

In the light of the foregoing, irrespective of specific interests moving the endeavours aimed at comprehension of water and its strange behaviour, we can thus conclude that, despite intense inspection over the years, scientific community is still far from reaching a coherent, complete and fulfilling understanding of all water puzzling properties. It is within such a framework that this thesis should be seen: the goal is to contribute to shed light on the complex behaviour of this apparently simple system, assessing nanoconfinement as a suitable strategy to seep through the *No man's land* and find experimental insights proving or ruling out the existence of a second critical point in the metastable phase diagram of supercooled water. As it will be shown further, our experiments show results similar to those obtained during the last two decades by other authors. However comparison between structural and dynamic information led us to conclude that, although supercooled water exhibits at least two populations, nothing justifies us to identify them as LDL and HDL phases, as asserted by supporters of the LLPT hypothesis.

This thesis comes from the fruitful collaboration between the Liquids Group (*Department of Science*) at *University of Roma Tre* (Rome) and the *Institut de Minéralogie, de Physique des Matériaux et de Cosmochimie* (IMPMC) at *Université Pierre et Marie Curie* (Paris). From one

side, the cooperation, sustained by a joint program signed by the Italian and French aforementioned universities, has taken great advantage of the Italian group's long-time experience in neutron diffraction experiments, especially devoted to the study of water structure; on the other side, the research activity has benefited from the French group's expertise in inelastic neutron and X-rays scattering on liquid and solid systems, from its deep knowledge of high-pressure techniques, and from the strong know-how of the chemistry lab, that has provided the samples used in our experiments.

This thesis is organized as follows:

- In Chapter 1 some important properties and anomalies of bulk water are reviewed, in order to establish the context throughout this thesis will be developed.
- Chapter 2 is devoted to water under confinement, with particular emphasis on the peculiar properties that will reveal to be relevant in the context of the discussion of our experimental results. A brief description of the characteristics of MCM-41 substrates as confining medium is given.
- In Chapter 3 basic principles of neutron diffraction and small angle neutron scattering are illustrated. The last part of this chapter is dedicated to the instrumental apparatus used for our neutron experiments (at ISIS), paying particular attention to the *NIMROD* diffractometer.
- In Chapter 4 infrared spectroscopy is described: after a short theoretical background, the description of the experimental apparatus available at the synchrotron SOLEIL is given, with particular attention to the *AILES* beamline.
- Chapter 5 is dedicated to the presentation and discussion of the experimental results obtained from the analysis of neutron diffraction and small angle neutron scattering data.
- In Chapter 6 experimental results obtained from IR experiments are presented and discussed.
- In Chapter 7 general conclusions will be drawn, along with some ideas for future experiments to perform with the aim to further improve and detail our knowledge about the challenging problem tackled in the present thesis.

# Chapter 1

## Generalities on water

*Although liquid water has been the focus of intensive research for over 100 years, a coherent physical picture that unifies all of the known anomalies of this liquid is still lacking.*

*O.Mishima & H.E.Stanley [19]*

Water is ubiquitous: on Earth's surface (oceans occupy  $10^9$  km<sup>3</sup>) [34], dissolved in the Earth's mantle [35, 36], in the Solar System (in the form of ice) [37, 38], inside living organisms acting as solvent, temperature buffer, metabolite, and living environment [39–42]. Water is a truly special liquid: its properties are extraordinary and appear to be similar to those found in liquids made of large molecules or that are either ionic or metallic. For example, it has an exceptionally high viscosity and cohesion, that manifests itself through high melting and boiling temperature and large specific heat. Just to give an idea, energy needed to heat up water is three times that required for the same mass of pentane, and ten times more for the same mass of iron. Moreover, at odds with most liquids, specific heat of liquid water is twice that of the corresponding solid phase (ice). Such difficulties in changing water temperature are at the basis of the role of oceans as thermal regulators, with important climatic implications. In addition, water presents markedly high dielectric constants and a series of dynamic and thermodynamic anomalies, discussed further in much detail.

In order to better understand the origin of all these peculiar features, we cannot restrict our attention to water as a single molecule but we must also consider how water molecules arrange themselves in space and what kind of intermolecular interactions they establish.

In this chapter a brief description of the main properties of water molecule will be given, together with an overview of the most relevant thermodynamic and dynamic anomalies of water behaviour. Space will be devoted to the stable and metastable water phase diagrams, with the last section focusing on the most accredited theories that try to explain water anomalies and to better define the regions of the water phase diagram remaining still uncertain.

## 1.1 Water molecule

### 1.1.1 Molecular structure

Water molecule ( $\text{H}_2\text{O}$ ) is much smaller than almost all other molecules, with a molecular diameter of about  $2.75 \text{ \AA}$ . As demonstrated starting from the 1780s by experiments of Cavendish and Lavoisier and then by Gay-Lussac, Humboldt and Dumas, it is made up of two hydrogen (H) atoms covalently bonded to one oxygen (O). Water molecule is V-shaped, being symmetric with respect to rotations around two axis (point group  $C_2$ ) and reflections through any of the two mirror planes, perpendicular to each other, containing the rotation axis of symmetry.

The only electron of each of the hydrogen atoms occupies an orbital  $1s$ . By contrast, oxygen atom holds eight electrons, distributed in four lobe-shaped hybrid orbitals  $sp^3$ . According to the VSEPR (Valence-Shell Electron-Pair Repulsion) theory [43, 44],  $sp^3$  orbitals arrange themselves around the nucleus in a tetrahedral configuration, due to the electric repulsion between electrons. In particular, two of these  $sp^3$  orbitals share their electrons with  $1s$  orbitals of hydrogen atoms forming covalent bonds, while the other two hybrid  $sp^3$  orbitals remain as lone pairs. Due to the repulsion between the two lone pairs (that are more repulsive than the bond electrons), water molecule undergoes a slight structural deformation and the angle between the O-H bonds is around  $104.5^\circ$ , instead of  $109^\circ$  (typical for a perfect tetrahedral configuration) (fig.1.1).

Although water molecule is electrically neutral, oxygen atom is much more electronegative than hydrogens, so that a partial negative charge shifts closer to the O atom, while two partially positive charges lie near the H atoms. Such a charge distribution lends a non-zero dipole moment, that has a magnitude of 1.85 D for the isolated water molecule [45]. Polarity plays a key role in the unusual water properties, being the responsible of the formation of hydrogen bond between water molecules.

### 1.1.2 Hydrogen bond

Water molecules interact forming hydrogen bonds, which are mainly responsible for the crucial role of water in chemistry and biology and in its unique properties summarized at the beginning of this chapter.

For instance, if water molecules were not hydrogen-bonded, water would be a gas at room temperature, exactly as methane, whose single molecule is similar in mass and structure to water but does not present the same kind of intermolecular interactions.

Hydrogen bonds (HB) are formed when the hydrogen atoms of a water molecule point towards the lone electron pairs of another water molecule, resulting in a tetrahedral arrangement of molecular neighbours around each water molecule [46]. Positive charge left around H atom of a single water molecule after the formation of the covalent bond with the more electronegative O atom acts as a hydrogen bond *donor*. In turn, the positive charge density attracts the lone pair of an electronegative atom on another molecule, being it therefore an *acceptor*. Roughly speaking, a HB is formed when two oxygen atoms belonging to two different water molecules interact via a hydrogen atom (fig.1.1).

The hydrogen bond strength depends on the electronegativity of the atoms involved in the

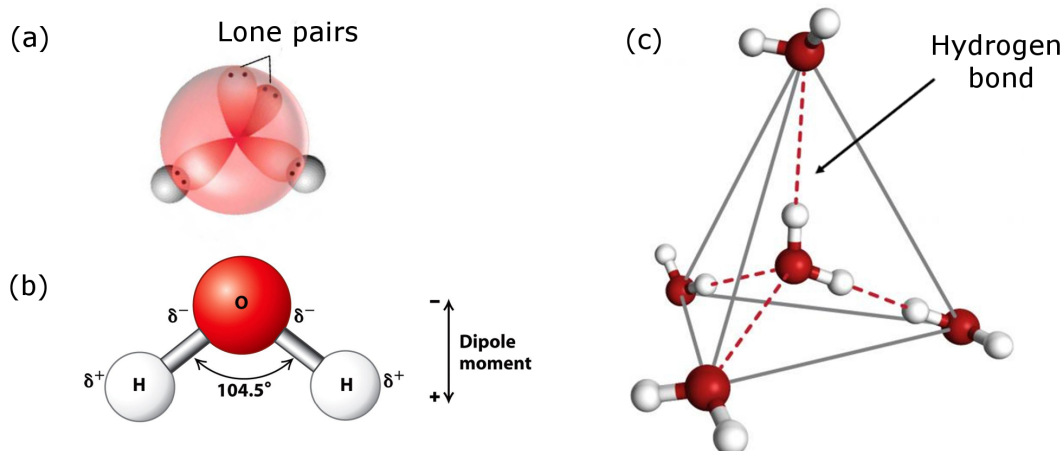


Figure 1.1: (a) Electronic distribution in water molecule: the tetrahedral structure of the molecular orbitals is shown, with the electrons involved in the covalent bonds and the lone pairs, according to the VSEPR theory [43, 44]. (b) Structure of single water molecule (hydrogen atoms are white, oxygen atom is red) [by Greg Stewart, graphic designer at SLAC National Accelerator Laboratory, USA], represented according to the ball-and-stick model. (c) Tetrahedral arrangement of hydrogen-bonded water molecules [Molecular Cell Biology, Sixth Edition ©2008, W.H. Freeman and Company].

bond; however, in the case of water at room temperature, HB average energy is  $\sim 23$  kJ/mol [34]. This means that HB is approximately an order of magnitude weaker than a typical covalent bond but stronger than Van der Waals interactions (tab.1.1). This aspect is quite notable. The heat of fusion of ice  $I_h$  (the ordinary form of ice at ambient pressure) is  $6.01$  kJ mol $^{-1}$  and the heat of sublimation at the triple point is  $51.09$  kJ mol $^{-1}$ . This means that local tetrahedral symmetry persists in water close to the triple point and even more in supercooled water, although the order is transient and short-ranged [17]. Hydrogen bond in liquid water is characterized by a  $\text{OH}\cdots\text{O}$  distance of  $\sim 2.7$  Å and a  $\text{O}\cdots\text{H}$  distance of  $\sim 1.7$  Å, as measured by several experiments [47].

Bond	Bond energy [kJ/mol]
Ionic bond $\triangle$	700-4000
Covalent triple bond $\triangle$	800-1000
Covalent double bond $\triangle$	500-700
Covalent single bond $\triangle$	200-500
Ion-dipole interaction $\star$	40-600
Hydrogen bond $\star$	10-40
Van der Waals interactions $\star$	5-25

Table 1.1: Typical values for intra- and inter-molecular bonding energies. The types of bonds are reported in descending order with respect to bonding energy. The symbols  $\triangle$  and  $\star$  denote intra- and inter-molecular interactions, respectively.

H-bonding exhibits a strongly cooperative behaviour. This effect derives from the fact that

the angle between the two lone pairs orbitals on a given oxygen decreases as the number of HB involving that oxygen increases. Moreover, calculations performed using the Effective Fragment Potential (EFP) method [48] suggest that the reduction of the angle between the lone pair dipole vectors is the primary responsible for the enhancement of the dipole moment of water molecule. As a consequence, when a HB has been established, it fosters the formation of further HB because water molecule acting as HB donor increases the negative charge density on the oxygen atom; vice versa, water molecule behaving as acceptor sees a reduction in electron density encouraging the hydrogen atom to be a donor. The hydrogen bond is highly directional and this limits to four the maximum number of bonded neighbours per water molecule. The presence of the HB makes intramolecular covalent bond between oxygen and hydrogen weaker and reduces the repulsion between electron orbitals. As a consequence, O-H length and  $\text{O}\hat{\text{H}}\text{O}$  angle become bigger as the number of established HB increases. This means that bond lengths and angles are not to be regarded as constant, but affected by the local environment of water molecules and their state of aggregation. In fact, as water undergoes a phase transition, the number of established HB changes (from zero for monomers in gaseous form up to four in the crystalline ice structure). Notwithstanding typical values and trends can be inferred from experiments [47, 49–51] and numerical simulations, with a variability due to the different calculation methods adopted [52, 53]. In particular, the average number of HB established in the solid state (ice) is esteemed to be close to 4 per water molecule, as firstly predicted by Stanley and Teixeira [54] and subsequently confirmed by molecular dynamics simulations and X-ray and neutron scattering experiments. Moving to liquid state, the average number of HB is found between 3.3 and 3.5: this slight decrease compared to ice is due to the thermal energy inducing vibrations that break hydrogen bonds [34, 55–57]. This picture is to be regarded from a statistical point of view: HB lifetime is extremely short (order of picosecond [58]) and strongly depending on temperature. Thus HB are created and broken continuously and at any given time all water molecules do not have the same number of neighbours: we expect to find a water network with some molecules slightly connected (zero or 1 HB), another fraction of molecules strongly connected (3 or 4 HB) and the remainder with a number of HB intermediate between these two extremes.

On the basis of what has been said so far, considering the high polarizability of water molecules and the properties of HB mentioned above, it is reasonable to argue that water is not a simple liquid made of individual molecules: its complex nature is held in water molecules ability to form hydrogen-bonded chains and small clusters, depending on the experimental conditions (e.g. temperature and pressure). In the last decades, the structure types of water molecules have been widely studied and discussed, both by theoretical and experimental investigations [59–61].

The fundamental role of HB and tetrahedrality in determining the complex physics of water can be readily figured out by thinking that models with potentials forming only two hydrogen bonds are not able to reproduce most of the water-like properties. This result clarifies quite well that the structural and thermodynamic peculiar properties of water are determined by the molecules' connectivity, rather than the specific nature of their mutual interactions [62].

## 1.2 Thermodynamic properties and water anomalies

The peculiar molecular structure of water is closely related to its manifold anomalies<sup>1</sup>, some of which quite recently discovered [63]. As discussed below by taking under consideration only the main thermodynamic response functions, all of the puzzling properties of water appear even more striking upon supercooling under the normal melting temperature  $T_m$  [54], showing a power low divergence toward a singular temperature  $T_s \sim 228$  K (at ambient pressure) [64]. In fact, lowering the temperature, the strength of the hydrogen bond network, together with cooperative effects between molecules (and probably quantum effects [65]), become more relevant. This clearly explains why a deeper comprehension of water metastable states represents a strictly necessary request.

### Thermal compressibility $\kappa_T$

Thermal compressibility is a thermodynamic response function defined as  $\kappa_T = \bar{\rho}^{-1}(\partial\bar{\rho}/\partial P)_T$ , where  $\bar{\rho}$  is the mean mass density,  $P$  the pressure,  $T$  the temperature. In normal liquids  $\kappa_T$  decreases with decreasing temperature. Water, instead, exhibits the same behaviour only at high temperature: for  $T \lesssim 46^\circ$  C,  $\kappa_T$  actually shows a pronounced rise upon cooling, that is indeed a distinguishing feature of supercooled water (fig.1.2). For pressures greater than atmospheric, the  $\kappa_T$  anomalous low-temperature behaviour becomes progressively weaker.

With regards to  $\kappa_T$ , attention deserves to be paid to the *Temperature of Maximum Density* (TMD), that is the locus of temperatures at which density has a maximum at a fixed pressure. At positive pressure, TMD has a negative slope in the  $(P, T)$  plane, implying that compressibility must necessarily increase upon cooling, as follows from the thermodynamic identity:

$$\left(\frac{\partial\kappa_T}{\partial T}\right)_{P, \text{at TMD}} = \frac{v^{-1} \left(\frac{\partial^2 v}{\partial T^2}\right)_{P, \text{at TMD}}}{\left(\frac{\partial P}{\partial T}\right)_{\text{TMD}}} \quad (1.1)$$

where  $v$  is the molar volume and the subscript 'TDM' means that the partial derivative is evaluated along the TMD locus. By observing the thermodynamic relation between  $\kappa_T$  and the thermal expansion coefficient  $\alpha_p$  (see below for  $\alpha_p$  definition):

$$\left(\frac{\partial\kappa_T}{\partial T}\right)_P = - \left(\frac{\partial\alpha_P}{\partial P}\right)_T \quad (1.2)$$

we can infer that, since TMD separates states with  $\alpha_P > 0$  and  $\alpha_P < 0$  and  $\alpha_P$  is a negative quantity for temperatures lower than  $4^\circ$  C at ambient pressure, water's thermodynamic anomalies are suppressed upon compression and heating.

<sup>1</sup>Water anomalies are at least 74, as reported by M.Chaplin ([http://www1.lsbu.ac.uk/water/water\\_anomalies.html](http://www1.lsbu.ac.uk/water/water_anomalies.html)).

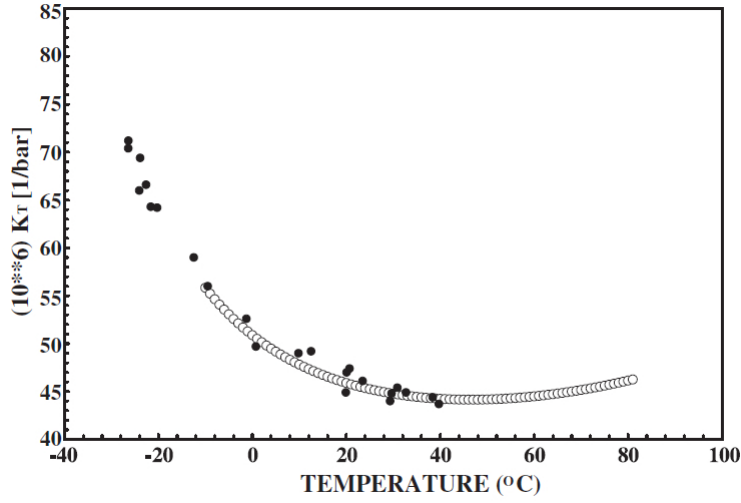


Figure 1.2: Water isothermal compressibility  $\kappa_T$  as a function of temperature at atmospheric pressure. A minimum appears at  $\sim 46^\circ\text{C}$ : for lower temperatures  $\kappa_T$  increases following the opposite dependence expected for a simple liquid. Filled points represent data from Speedy and Angell [66], while empty circles indicate a multiparametric fit of the data for stable and moderately supercooled water [17].

### Specific heat $C_P, C_V$

The (molar) specific heat is defined as the amount of energy required to raise the temperature of one mole of a substance by one degree by keeping constant either volume ( $V$ ) or pressure ( $P$ ). Hence it is defined as  $C_P = T(\partial\bar{S}/\partial T)_P$  or  $C_V = (\partial\bar{U}/\partial T)_V$ , respectively, where  $\bar{S}$  is the mean molar entropy and  $\bar{U}$  the mean internal energy. As an example, for liquid water at  $25^\circ\text{C}$ , we have  $C_V = 1\text{ cal g}^{-1}\text{K}^{-1}$ , that is much larger than that of other non-hydrogen-bonded liquids. In fact, as water is heated, molecules start to increase movement, causing hydrogen bonds to bend and possibly break. This process partly absorbs heat provided to the system, so that not the whole amount of energy is available to increase the kinetic energy of water molecules.

Fig.1.3 shows the temperature dependence of water isobaric specific heat at atmospheric pressure: at temperature higher than  $\sim 35^\circ\text{C}$  nothing strange can be pointed out, since, as expected,  $C_P$  monotonically increases when temperature rises. By contrast, for  $T \lesssim 35^\circ\text{C}$  water reveals its anomalous behaviour as  $C_P$  rapidly increases while temperature decreases reaching the supercooled region. The temperature dependence of  $C_P$  for supercooled water become less sharp under pressures greater than atmospheric [67].

The constant-volume specific heat may be obtained starting from  $C_P$ , using the thermodynamic identity:  $C_V = C_P - TV\alpha_P^2/\kappa_T$ , where  $\kappa_T$  is the thermal compressibility and

$$\alpha_P = -\frac{1}{\bar{\rho}} \left( \frac{\partial \bar{\rho}}{\partial T} \right)_P \quad (1.3)$$

is the thermal expansivity, with  $\bar{\rho}$  the mean water density. As a consequence, the thermodynamic identity does hold:

$$\left(\frac{\partial C_P}{\partial P}\right)_T = -T \left(\frac{\partial^2 v}{\partial T^2}\right)_P \quad (1.4)$$

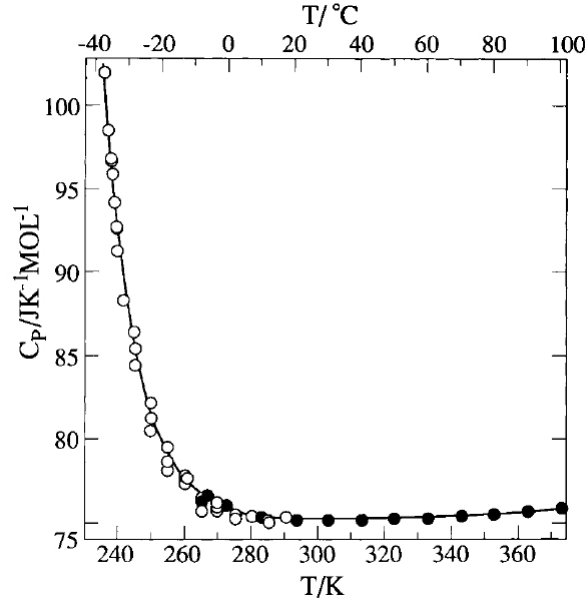


Figure 1.3: Constant-pressure specific heat of water as a function of temperature at ambient pressure. At high temperature ( $T \gtrsim 35^\circ\text{C}$ ) water behaves as a normal fluid:  $C_P$  monotonically increases as temperature grows up. Conversely, for  $T \lesssim 35^\circ\text{C}$ ,  $C_P$  exhibits the opposite trend: it sharply increases upon cooling. Open and filled symbols indicate data from two different experiments [17].

The dramatic increase of specific heat upon cooling, at temperatures far from the glass transition  $T_g$  (see section 1.3.2), has been interpreted in literature as an evidence for a phase transition impending just below the homogeneous nucleation temperature ( $\sim 232\text{K}$  at ambient pressure).

### Thermal expansivity, $\alpha_P$

For most liquids thermal expansivity is expected to be weakly variable with decreasing temperature, implying that the mean density  $\bar{\rho}$  increases roughly linearly in  $T$  upon cooling (eq.1.3). However water behaviour is in sharp contrast:  $\bar{\rho}(T)$  increasing is highly non-linear, so that  $\alpha_P$  is not a constant even at high temperatures. We can model this unusual trend assuming that an anomalous contribution, negative and whose absolute value increases with decreasing temperature, has to be added to the normal temperature-independent one. These two contributions to  $\alpha_P$  cancel at the temperature of *maximum* density, that is  $4^\circ\text{C}$  at atmospheric pressure (fig.1.4). The temperature-dependence of  $\alpha_P$  turns to resemble that of a normal fluid for pressures greater than atmospheric.

In addition to the well-known density maximum, discovered more than 300 years ago, also a density *minimum* is believed to exist below the homogeneous nucleation temperature. The supercooled water density minimum has been inferred on the basis of considerations

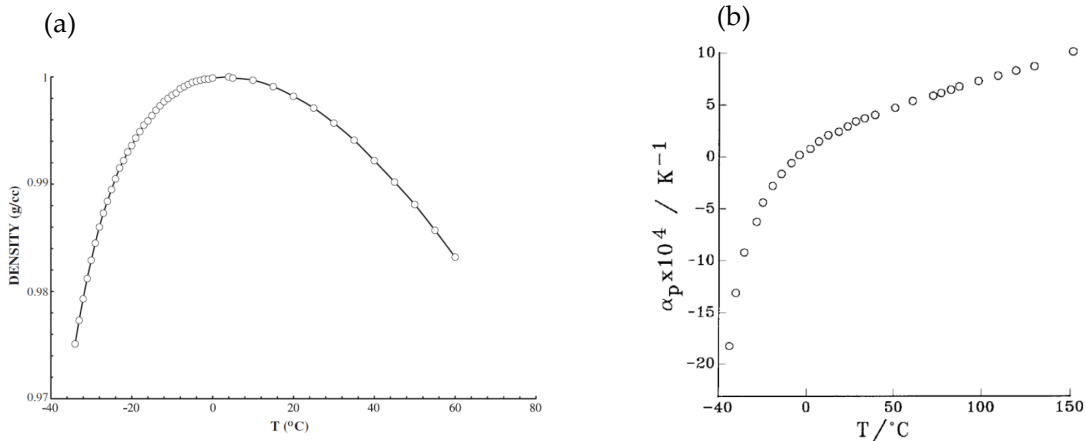


Figure 1.4: (a) Liquid water density as a function of temperature at atmospheric pressure (data reported in [17]). (b) Temperature dependence of the thermal expansion coefficient  $\alpha_P$  for stable and supercooled water (data from [68]).

concerning the thermodynamic continuity: the experimental expansivity is positive at high temperature and becomes negative at low temperature; if the volumetric behaviour of the system connects smoothly with thermal expansivity, it can be speculated that water density reaches a maximum at 4° C, then progressively decreases until it approaches the density of ice close to the homogeneous nucleation temperature  $T_H$  and then it turns to increase for temperatures  $T < T_H$  if the system is kept in the supercooled liquid phase, causing  $\alpha_P$  to run towards positive values. This implies that the thermal expansivity must vanish and, consequently, the density must pass through a minimum value. Nevertheless, the existence of such a minimum has not been unambiguously proved yet, even if some authors claim to have recently achieved experimental evidence of it by supercooling water in hydrophilic silica mesopores (MCM) [69–71].

The water density minimum, albeit less famous with respect to the density maximum, assumes an outstanding role in the present debate involving the scientific community in finding an incontestable proof concerning the origin of water anomalies. Moreover, if a density minimum follows the density maximum at lower temperatures, it can be argued that many of the water anomalies ultimately disappear under sufficient deep supercooling, indicating the possibility to return to a “normal” behaviour. The reasons lying behind these last statements will be clarified in the experimental part of this thesis (chapter 5).

### Statistical fluctuations

On the basis of statistical mechanics, each of the aforementioned response functions is associated with a corresponding fluctuation. More specifically, the compressibility  $\kappa_T$  is proportional to volume fluctuations ( $\delta V = V - \bar{V}$ ), and its divergence can be accounted for a manifestation of anomalous density fluctuations. Then the isobaric heat capacity is a measure of entropy fluctuations ( $\delta S = S - \bar{S}$ ) experienced at fixed pressure, while the thermal expansion coefficient  $\alpha_P$  reflects the correlation between entropy and volume fluctuations, as summarized in the following relations:

$$\langle (\delta V)^2 \rangle = V k_B T \kappa_T, \quad \langle (\delta \rho)^2 \rangle = (V^{-1} k_B T \bar{\rho}^2) \kappa_T \quad (1.5)$$

$$\langle (\delta S)^2 \rangle = N k_B C_P \quad (1.6)$$

$$\langle (\delta S \delta V) \rangle = V k_B T \alpha_P \quad (1.7)$$

where  $k_B$  is the Boltzmann constant. Usually, volume and entropy fluctuations in liquid systems become smaller with decreasing temperature and are positively correlated: the system reacts to a volume increase with increasing entropy. However, on the basis of what has been discussed before, this does not find any confirmation in the case of water: rather, fluctuations in volume and entropy and their cross-fluctuations significantly increase on lowering temperature. Furthermore, below the temperature of maximum density ( $4^\circ\text{C}$ ), volume and entropy fluctuations are anti-correlated. Such a surprising behaviour is the consequence of the formation of an open HB network, that entails a decrease in orientational entropy coupled to an increase in volume. Despite HB network in liquid water has a transient nature and is short-ranged, it seems to represent the molecular origin of all water anomalies (fig.1.5).

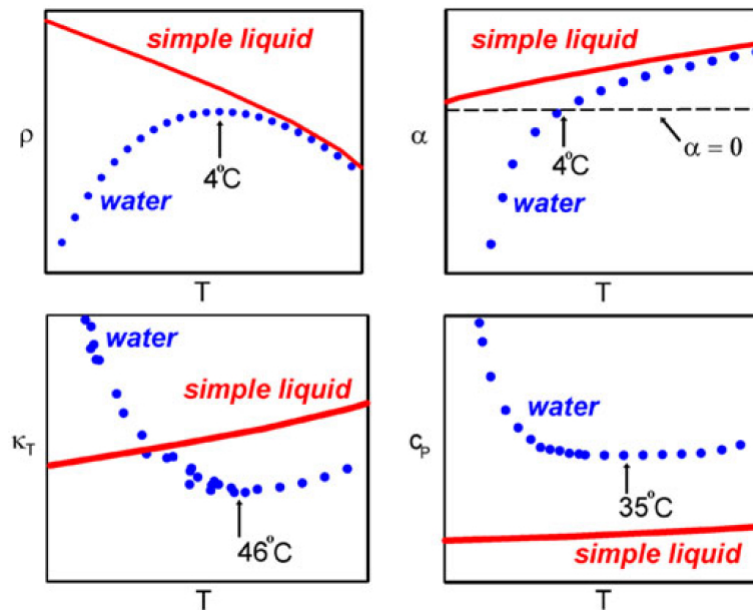


Figure 1.5: Schematic comparison between the temperature dependence of the main thermodynamic response functions for simple liquids and water. As clearly visible, density  $\rho$ , thermal expansion coefficient  $\alpha$ , isothermal compressibility  $\kappa_T$  and isobaric heat capacity  $C_P$  vary monotonically with temperature for simple liquids, while water ever shows a maximum or a minimum, with an increasing slope (absolute value) moving towards lower temperatures in the supercooled state [17].

### Diffusion coefficient

Also dynamical parameters may attest the outstanding character of water, the diffusion coefficient  $D$  among all. Diffusion coefficient is directly related to the structural relaxation

time  $\tau$  ( $D \propto \tau^{-1}$ ), or viscosity  $\eta = G_\infty \tau$  (where  $G_\infty$  is the instantaneous shear modulus). As shown by Chen [72] and Teixeira [73] by means of their pioneering quasi-elastic neutron scattering experiments on diffusion motion of supercooled water, two relaxation times can be identified: a short time  $\tau_1$  associated with rotational motion ( $\tau_1 \sim 2$  ps) and a second time  $\tau_2$  accounting for translational diffusion ( $\tau_2 \sim 23$  ps).

It is well known that at high temperature (i.e. above the melting temperature  $T_m$ ) the structural relaxation time of a liquid follows an Arrhenius law:

$$\tau = \tau_0 \cdot \exp\left(\frac{E_a}{k_B T}\right) \quad (1.8)$$

where  $\tau_0$  is a material-dependent exponential factor and  $E_a$  is the temperature-independent activation energy of the relaxation process, related to the configurational entropy via the Adam–Gibbs equation [74]<sup>2</sup>. For simple liquids, eq.1.8 holds upon cooling as well, until crystallization occurs. However, in the case of glass-forming liquids like water, the structural relaxation time dramatically increases by orders of magnitude<sup>3</sup> and is observed to change to a non-Arrhenius behaviour, with  $\tau$  rising significantly faster than expected from eq.1.8. This behaviour is associated to a non-physical value of the pre-exponent of Arrhenius equation, often interpreted as the manifestation of the cooperative nature of the relaxation process in supercooled liquids [75].

In 1920s H. Vogel, G. Tammann and W. Hess, and G.S. Fulcher [76] introduced, independently, a three-parameter empirical equation for oxide glass melts:

$$\tau = A \cdot \exp\left(\frac{BT_0}{T - T_0}\right) \quad (1.9)$$

where  $A$ ,  $B$  and  $T_0$  are material-dependent constants, being  $A$  and  $B$  independent of temperature. Eq.1.9 is known as "VFT equation" and, because of its simplicity, it has been widely used and successfully applied also to other materials, including water. Nonetheless, eq.1.9 is a phenomenological relation and a clear physical interpretation of its parameters is missing. In particular,  $T_0$  is regarded to be related to the temperature of the structural arrest of the *Mode Coupling Theory* [77] and represents the ideal glass transition temperature. In this case an effective activation energy can be defined, being it dependent on temperature; in particular, it increases upon cooling leading to the structural and dynamic arrest towards  $T_g$ , that is a signature of glass transition.

The distinction between Arrhenius-like and VFT-like dynamic behaviour introduces the definition of "fragility" (fig.1.6): this term is commonly used to quantify the deviation of the

<sup>2</sup>The Adam-Gibbs equation provides a connection between kinetics and thermodynamics and is expressed as  $\tau = A \cdot \exp(B/Ts_c)$ , where  $\tau$  is a relaxation time (or, equivalently, the viscosity),  $A$  and  $B$  are two constants and  $s_c$  is the configurational entropy. The latter parameter is related to the number of minima in the multi-dimensional potential energy surface. This means that, according to Adam-Gibbs interpretation, the dynamic slow-down approaching  $T_g$  is due to a decrease in the number of configurations sampled by the system.

<sup>3</sup>Macroscopic dynamic parameters, like viscosity  $\eta$  and diffusion coefficient  $D$ , show a sharp slow-down as well. The viscosity of molecular liquids, for instance, can vary by 3 orders of magnitude in a temperature interval of 10 K close to  $T_g$ .

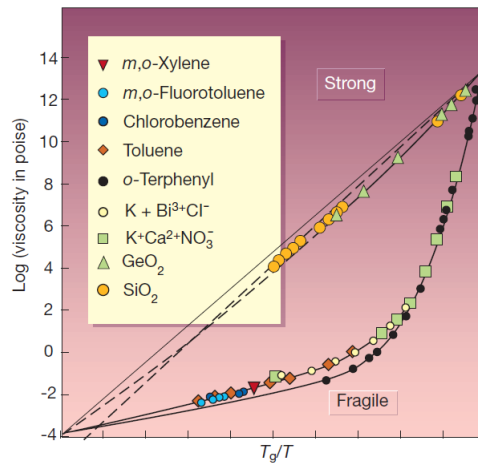


Figure 1.6: Angell's strong-fragile behaviour of viscosity for different liquids (temperature  $T$  is scaled by the glass transition temperature  $T_g$ ). Strong liquids exhibit a linear trend (Arrhenius behaviour on logarithmic scale), indicative of a temperature-independent activation energy. Fragile liquids, instead, exhibit a super-Arrhenius behaviour (described by VFT equation), with an effective activation energy increasing as temperature decreases (figure from [78]).

relaxation time–temperature dependence from a simple Arrhenius behaviour. In particular, Arrhenius law (eq.1.8) describes a “strong” liquid, while VFT equation (eq.1.9) is the signature of a “fragile” liquid [75]. The transition from fragile to strong liquid is usually addressed as *dynamic crossover*. The crossover temperature identifies the violation of the well known Stokes-Einstein (SE) relation:  $D = k_B T / 6\pi\eta R$ , that expresses a linear dependence between the transport parameters  $D$  and  $\eta$ , with  $R$  the radius or a characteristic dimension of the moving particle. The SE relation breakdown can be described using a scaling concept, therefore SE can be replaced by the so-called “fractional SE”:  $D \sim (\eta/T)^{-\xi}$ , being  $\xi$  the result of the ratio between the temperature–dependent scaling exponents of  $D$  and  $\tau$  [64]. As far as the transition occurs,  $D$  and  $\eta$  become uncoupled, inducing strong density fluctuations and abrupt increase in the corresponding correlation lengths. This phenomenon is often explained as the manifestation of dynamic heterogeneities inside the liquid, leading to a spatial correlation between atomic motion and uncoupled vibrational and rotational modes. As a consequence, distinct areas arise whose structural relaxation times may differ by several orders of magnitude with respect to the average value of the bulk system, leading the different dynamics to fluctuations dominating the transport properties near the glass transition [78].

In distinct contrast with other network-forming liquids, bulk water behaves as a fragile liquid over the whole temperature window experimentally accessible [68]. Thus, since analogies with other network-forming liquids do exist and considering the properties of water amorphous phases, it can be argued that a dynamical crossover of liquid water from fragile to strong must occur in the deeply supercooled region under  $T_H$ . The framework commonly accepted for water (and other glass-formers) is then a continuous<sup>4</sup> transition from a VFT-like behaviour at high temperature to an Arrhenius-like trend at low temperatures, but an experimental verification of such a dynamic crossover is rather demanding for bulk water, as it would require entering the *No man's land* (section 1.3.2).

<sup>4</sup>Some authors in recent works have also argued the possibility that this transition is not continuous [79].

## 1.3 Phase diagram of bulk water

### 1.3.1 The *stable* phase diagram

As a mirror of its intricate set of mysterious properties, water has a rather complex phase diagram. If we observe how water structure changes by varying temperature and pressure, we can identify three *stable* (or equilibrium) phases: liquid, solid (crystalline ice) and gas (vapour).

The phase diagram shown in fig.1.7, described in terms of the Clapeyron equation<sup>5</sup>, shows that evaporation and sublimation lead to a simultaneous increase of volume and entropy, as the slope of the coexistence line is positive. Conversely, the transition from ice to liquid water is characterized by a negative slope of the coexistence line, thus entropy increases while volume decreases, as discussed in section 1.2. In fig.1.7 we can also note two special points: the triple point (TP) and the vapour-liquid critical point (CP). At TP the three phases of liquid, ice and vapour appear simultaneously, while approaching CP, moving along the liquid-vapour boundary line, the liquid and vapour phases become more and more similar. Exactly at CP ( $T_{CP} = 374.15^\circ\text{C}$ ,  $P_{CP} = 218\text{ atm}$ ) the two phases have the same density, so that we just observe a single phase. Beyond the CP (i.e. increasing pressure or temperature), the two phases are not distinguishable and the single phase we recognise may be referred to as either a highly compressed gas or as an expanded liquid [46].

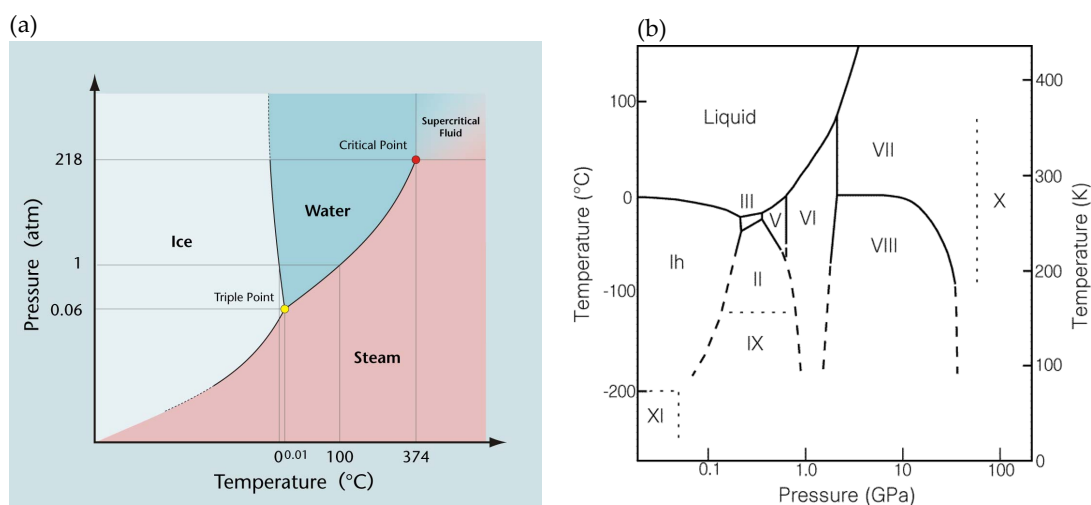


Figure 1.7: Water phase diagram. (a) P-T phase diagram of water with stable states: solid (ice), liquid and vapour (steam). (b) Water crystalline ice phases in the T-P plane (figure from [80]).

Ice poses a compelling problem to deal with, as there exist more than fourteen different crystalline phases. Generally speaking, crystalline ice structures are characterized by oxygen atoms arranged in a regular lattice, while proton positions may be more or less disordered (due to the disordered hydrogen bonding), and are responsible for the residual entropy of

<sup>5</sup> $dP/dT = (S_b - S_a)/(V_b - V_a)$ , where  $P$  is the pressure,  $T$  the temperature,  $S$  the molar entropy,  $V$  the molar volume and  $a$ ,  $b$  denote the two thermodynamic states connected by the phase transition.

ice. Protons tend to occupy a regular configuration, reducing the residual entropy, at very low temperatures.

At ambient pressure and temperature below the melting point ( $T_m = 273$  K), water crystallizes forming a hexagonal and thermodynamically stable structure, commonly called "ordinary ice" or "hexagonal ice" ( $I_h$ ) [81]. The principal feature of  $I_h$  is that oxygen atoms form a hexagonal lattice and protons (hydrogen atoms) arrange in an orientationally disordered tetrahedral geometry [82]: each oxygen atom is surrounded by four other oxygen atoms disposed at the vertices of a regular tetrahedron, 0.276 nm far from the central oxygen atom (all the water molecules have a coordination number close to four). This network creates an open lattice, made of a series of hexagonal rings of water molecules, characterized by a high intermolecular cohesion (fig.1.8(a), (c)).

Ordinary ice is just one of the numerous polymorphic forms of ice. For instance, ice II to VII are crystalline modifications forming at high pressure, while ice VIII is a low-temperature modification of ice VII. The structure of these high-pressure polymorphs is still tetrahedral, but much less regular than ice I because of hydrogen bonds, being them shorter and distorted. These structures let non-nearest neighbours be closer approaching, also resulting in a greater compactness. Ice VI, VII and VIII (being the last two forms the most abundant ice for pressures above 2 GPa) are formed by interpenetrating structures: a fully hydrogen-bonded framework creates cavities where molecules of a second but identical framework can reside. For example, ice VIII has a body-centred cubic structure, with each oxygen atom having eight nearest neighbours; such a structure can be regarded as two interpenetrating but not interconnecting ice  $I_h$  lattices [83]. Ice IX has the same structure as ice III apart from the proton ordering; it is slightly denser than ice III and is at equilibrium at low temperature ( $\sim 160 - 165$  K) and high pressure ( $\sim 280$  MPa). Ice X is obtained from continuous transition of cubic ice VII: the oxygen atoms are organized in a body-centred cubic arrangement (eight neighbours) and the hydrogen atoms in a body-centred truncated cubic arrangement (12 neighbours), being them less mobile than in ice VII. Ice XI is the proton-ordered form of  $I_h$  and creates orthorhombic crystals where an ordered array of protons and all hydrogen bonds are aligned along the same direction. This peculiar structure confers ice XI ferroelectric properties [84].

For the sake of brevity, we will not describe in more depth the characteristics of the different ice polymorphs, since this aspect is out of the scope of the present thesis. However huge literature has been produced about the structure of these forms of ice, the experimental conditions able to obtain them and the thermodynamic transformations which allow for going from one to another [85–88].

In addition to stable crystalline ice, also metastable ice forms can be observed. For reasons that will be clearer further, special attention is to be devoted to cubic ice ( $I_c$ ) [81, 89, 90]: since it spontaneously transforms into hexagonal ice ( $I_h$ ) for temperatures above  $\sim 240$  K, it is regarded as a metastable ice form. Both ice  $I_c$  and  $I_h$  are made of hexagonal rings, but ice  $I_c$  differs from ice  $I_h$  in the stacking of the layers constituting them (fig.1.8(b), (d)): in ice  $I_h$  there is an overall hexagonal symmetry, being each layer the mirror image of the previous one; in ice  $I_c$  each layer is shifted with respect to the previous one of a distance equal to half diameter of a ring, so that oxygen atoms arrange in the same manner as carbons in the cubic lattice of diamond [91]. Formation of ice  $I_c$  is observed over a wide temperature range, from about 120 K up to the melting point. It may be found in the Earth's atmosphere (e.g. cirrus and noctilucent clouds) and in some extraterrestrial environments [92–95], and plays a central role in several cryopreservation techniques. The main established routes able to form ice  $I_c$  are: condensation of vapour; freezing of gels, emulsified supercooled water,

aqueous solutions, hyperquenched micrometer-size water droplets, confined water; warming of high-pressure ice recovered at ambient pressure; warming of amorphous ices [94].

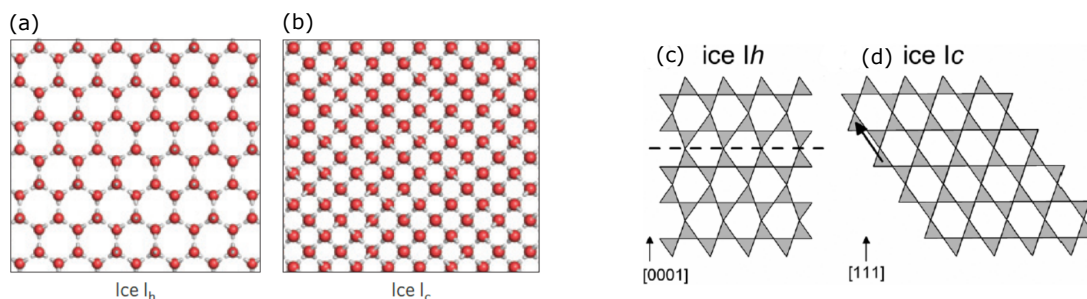


Figure 1.8: Left panel: different structure of ice  $I_h$  (a) and  $I_c$  (b) (figure from [96]). These two forms of ice are the most relevant for the nucleation process in supercooled water and will be considered in the experimental investigation presented in chapter 4. Right panel: comparison between stacking of layers in ice  $I_h$  (c) and ice  $I_c$  (d). The dashed line in (c) indicates the mirror plane between two adjacent layers, whereas the arrow in (d) marks the displacement vector from a layer to the next (figure from [86]).

### 1.3.2 The metastable phase diagram

Water, like any other substance, can also exist in metastable states, which represent the most interesting area of investigation for the aim of the present thesis.

Before to go ahead, it may be useful to distinguish between a state of *stable* equilibrium and a *metastable* state. The equilibrium is stable if the system stays there irrespective of external conditions: once perturbed and brought out of equilibrium state, the system spontaneously comes back to it as the perturbation has ceased. The equilibrium is metastable if the system remains in that state for long time, but, as soon as it experiences a sufficiently strong perturbation, it leaves the metastable state to reach the corresponding state of stable equilibrium. Moreover, we can consider as metastable all states whose relaxation time is much longer than time needed for an experimental measurement ( $\tau_{state} \gg \tau_{exp}$ ).

The metastable phase diagram of water is partly well known and currently represents object of active interest, but, at the same time, many aspects have to be clarified and some regions have not been certainly traced yet (fig.1.9).

The stable liquid range for water has its bottom limit in the equilibrium melting point (273 K at atmospheric pressure) and the upper limit in its boiling points. Nonetheless, water can be superheated up to about 553 K (280° C) and supercooled down to about  $\sim 232$  K ( $-41^\circ$  C), extending more than three times the temperature range over which water is liquid. In other words, we can have liquid water even if we are well above the boiling or under the melting point.

Supercooling is not a recent discovery: it has been already unveiled by Fahrenheit in 1724, rising a renewed interest as active research topic starting from the beginning of the 1900s. However, still today the supercooling phenomenology is not completely clear and stokes

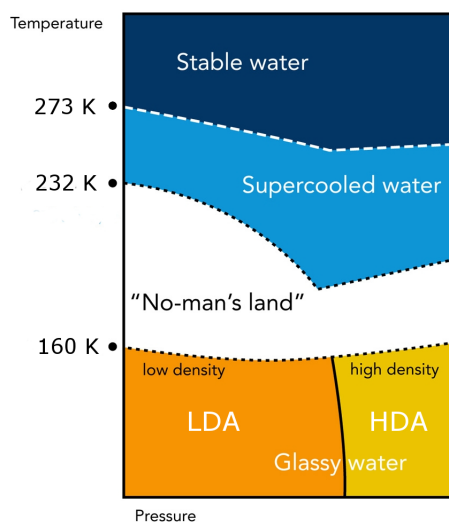


Figure 1.9: Metastable phase diagram of water. Proper experimental conditions allow for keeping water in liquid phase even under the melting temperature  $T_m = 273$  K (supercooled water). By rapid cooling down, crystallization of liquid water can be avoided and (at least) two glassy forms of water can be obtained, differing in density (LDA and HDA). The spontaneous crystallization of water (homogeneous nucleation) prevents direct experimental access to the region approximately extending between 150 K and 232 K. This is what is commonly addressed as *No man's land*.

animated debates amid the scientific community. As reported in literature for the first successful attempts [97, 98], the simplest way to obtain supercooled water is to reduce the concentration of impurities which induce the heterogeneous nucleation process. This requires water sample is purified and subdivided into small droplets ( $1 - 10 \mu\text{m}$  in diameter). Such droplets can be easily supercooled down to the homogeneous nucleation temperature, where the rate of crystallization becomes abruptly so large that the lifetime of the droplet becomes vanishingly small [17]. Similar conditions (micrometer water droplets below the freezing temperature) naturally occur in cirrus clouds, where indeed it is possible to observe supercooled water.

If very rapidly cooled, faster than the crystallization rate, water molecules have not enough time to establish and arrange HB to form a full crystalline ordered network. In this way, homogeneous nucleation can be suppressed and water forced to become an amorphous solid (ASW), i.e. a glass, where order is maintained just at short range. This result is true for all liquids, but water is again special because can form more than one glassy form [15]. Among these, two have been extensively studied: the low-density and the high-density amorphous ice (LDA and HDA, respectively). Just to give an idea about the interest residing in studying these amorphous forms of water, LDA is believed to be the most abundant form of water in the universe, deriving from water condensed in dense molecular clouds on interstellar dust particles and agglomerated into comets [16, 37, 99].

In addition, very-high-density amorphous ice (VHDA) has been proposed as a third distinct form of glassy water [100]. Indeed Loerting and co-workers [101] have found that, by heating HDA (from 77 K to 170 K) under pressure ( $\sim 10 - 20$  kbar), volume decreases continuously leading to a distinct form of ASW, even denser than HDA.

Although the assignment of the glass transition temperature ( $T_g$ ) of bulk water is rather controversial [16, 75, 102], a value commonly accepted for  $T_g$  is 136 K. Vitrification has usually a clear thermodynamic signature, such as a sudden drop in specific heat due to the "freezing"

of all translational and rotational degrees of freedom by which the liquid molecules absorb energy. Instead, in the case of water, the glass transition signature is exceptionally weak, as the jump in specific heat is only 2% and this is the reason of the controversy [16].

There are different thermodynamic paths allowing for transformation of water to an amorphous solid (summarized in fig.1.10) [16, 17]: by depositing water vapour onto a sufficiently cold substrate, as done by Burton and Olivier [103] reporting the first experimental evidence of ASW, by compressing the ordinary ice ( $I_h$ ) or by starting directly from liquid water. The latter technique is known as *hyperquenching* and consists in quickly cooling small aerosolized water droplets (size of the order of some micrometers in diameter), requiring a very high cooling rate (up to  $\sim 10^7$  K/s); the resulting material is called hyperquenched glassy water (HWG).

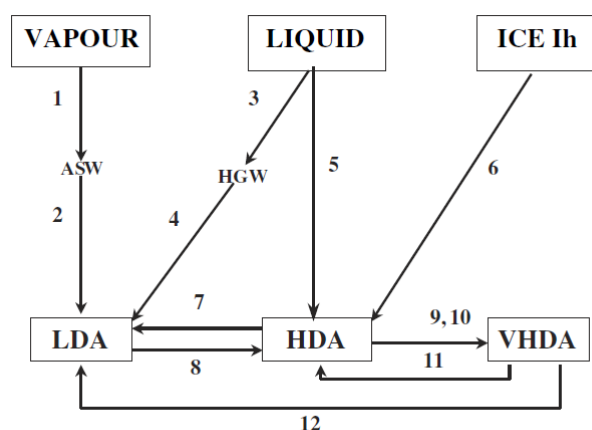


Figure 1.10: Irreversible transformations between non-crystalline forms of water. Details on thermodynamic paths are given in tab.1.2.

Step	Experimental conditions	Reference (e.g.)
1	Vapour deposition on cold substrate	[103]
2	Annealing in vacuum at 113 K	[104]
3	Hyperquenching of $\mu\text{m}$ -sized droplets on cryoplate	[105]
4	Annealing at 130 K	[105]
5	Quenching of emulsified water ( $T < 130$ K, $P \simeq 5$ kbar) at $10^4$ K/s	[106]
6	Compression of ice $I_h$ at 77 K at $\sim 10$ kbar	[107]
7	Decompression of HDA at 77 K+heating to $\sim 120$ K at 1 bar	[107]
8	Compression of LDA at 77 K to $\sim 5$ kbar	[108]
9	Isobaric heating of HDA to 165 K at 11 kbar	[100]
10	Isobaric heating of HDA to 177 K at 19 kbar	[100]
11	Isochoric heating of VHDA from 77 to $\sim 140$ K, starting at 200 bar	[100]
12	Isobaric heating of VHDA from 77 to $\sim 127$ K at 1.1 kbar	[100]

Table 1.2: Possible transformations between non-crystalline forms of water (see fig. 1.10).

From a structural point of view, LDA is similar to ice  $I_h$ , showing a higher local order with respect to HDA, whose structure more resembles liquid water. In particular, similarities between HDA and liquid water extend to the second and third coordination shells (fig.1.11)

[15, 17].

The transition between LDA and HDA under compression has been experimentally verified for the first time by Mishima and co-workers [108] in 1985 and further confirmed using Raman spectroscopy [109] and neutron diffraction [110, 111]. The sharpness and reversibility of transformation are consistent with a first-order transition causing a decrease in volume of about 22% [112], even if there is not full agreement about this point [113].

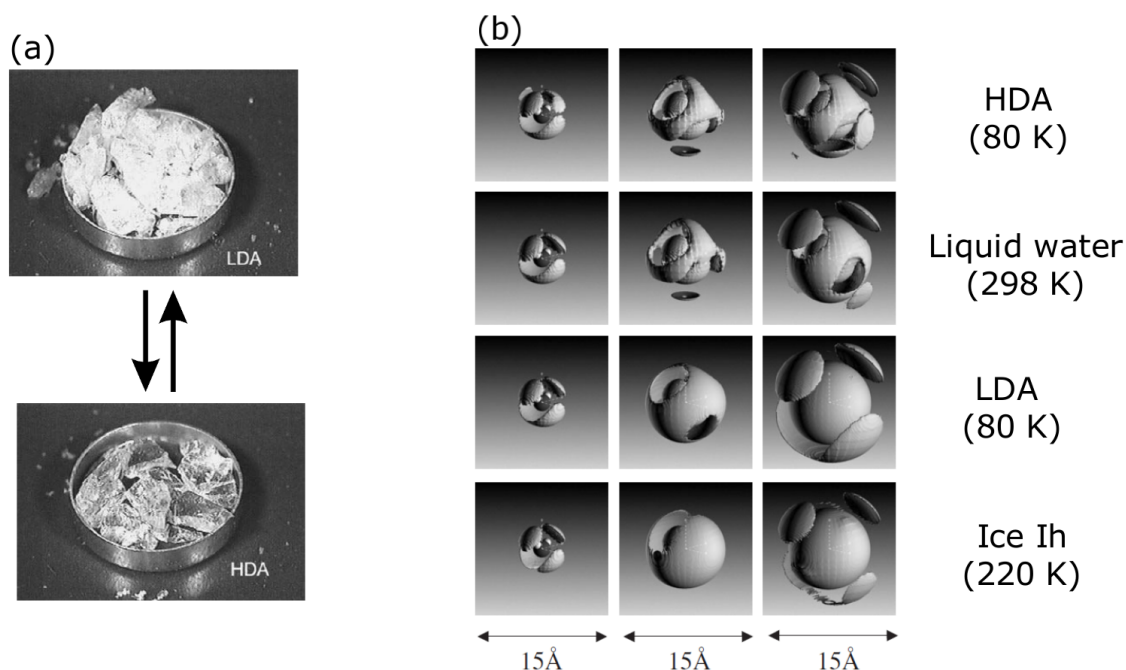


Figure 1.11: (a) Experimental realization of the two forms of glassy water, firstly proposed by Mishima and co-workers in 1985 [108]. LDA is formed by rapidly cooling water at atmospheric pressure; HDA is formed by compressing either LDA or ordinary ice at low temperature (figure from [114]). (b) Comparison of the short-range structures of HDA, LDA, ice  $I_h$  and liquid water using the spatial density function representation obtained from neutron scattering data (image from [115]). Contour plots represent areas with a constant density of water molecules around a central  $H_2O$  molecule. Each shell, starting from the central molecule, represents the first-, second- and third-neighbour water molecules, respectively. The contour density plots have been produced on the basis of Monte Carlo simulations generating an ensemble of water molecules whose structure is consistent with experimental data (see section 3.1.7).

When glassy water is heated, it spontaneously crystallizes to cubic ice ( $I_c$ ) at  $\sim 150$  K. The region of the phase diagram included between the homogeneous nucleation temperature,  $T_H$ , and the temperature of spontaneous crystallization to ice  $I_c$ ,  $T_X$ , is often regarded as *No man's land*, because a direct observation of liquid water is not feasible therein (fig.1.9). Thus the challenge is to make measurements upon supercooling in the very short time during which water is still liquid or discover smart strategies to avoid crystallization, as discussed in the next chapter (chapter 2).

### 1.3.3 Homogeneous and heterogeneous nucleation

In general, nucleation refers to any initial process (vapour condensation, melting, boiling, crystal nucleation, etc.) implying the localized emergence of a distinct thermodynamic phase which grows in size at a macroscopic scale as the result of the aggregation, at atomistic level, of growth units to the starting one. Involved length and time scales are of the order of  $10^{-10}$  m and  $10^{-13}$  s, respectively, equivalent to the atomic vibrational frequencies. This explains why nucleation appears as a challenging topic for both experimental and computational techniques. Hence, even though a notable amount of literature has been produced so far about fundamental aspects of nucleation, a complete knowledge of related phenomena is demanding and still far from complete.

In particular, with reference to water, we are interested in the nucleation process inducing the liquid-solid transition. In the introductory chapter a hint was given about the distinction between *homogeneous* and *heterogeneous* nucleation. The former is a spontaneous crystallization, unavoidable for bulk water below  $T_H \simeq 232$  K. Conversely, if crystallization takes place at temperatures higher than  $T_H$  (but lower than the melting point  $T_m$ ) and is prompted by the presence of impurities, dust particles, vessel walls, then nucleation is called heterogeneous.

#### Classical Nucleation Theory

Various theories describing homogeneous nucleation are available, based on phenomenological, kinetic and microscopic approaches. The first theoretical model for describing the homogeneous nucleation process is the *Classical Nucleation Theory* (CNT), coming from the work of Volmer and Weber, Becker and Doring, and Frenkel (a good review can be found, for instance, in [116]). CNT is an approximate theory, but it provides a reasonable prediction of nucleation rates and well captures the underlying physics and the essential features of the nucleation phenomenon.

Homogeneous nucleation can be described as the transition process whereby a system, in an initial state of stable thermal equilibrium, becomes metastable as a result of thermal fluctuations. Thus a new thermodynamic state with a low-free energy organized structure arises from an old phase with a higher free energy. The CNT theory was originally formulated for the description of vapour condensation to liquid, but it can be extended to crystallization from liquid phase, that is the case of our interest.

When the system is in a metastable state, it needs to exceed a potential barrier in order to nucleate in its stable phase. Thus the transition requires an energetic cost in terms of free energy, whose change during homogeneous nucleation of a microscopic nucleus or cluster of radius  $r$  is given by the sum of a bulk and a surface term:

$$\Delta G = \frac{4}{3}\pi r^3 \Delta g + 4\pi r^2 \sigma \quad (1.10)$$

where  $\Delta g < 0$  is the difference in free energy per unit volume of supersaturated air (or supercooled water, metastable) and that of liquid water (or ice, stable) at the same pressure, while  $\sigma$  is the specific surface energy of interface between the growing phase and the old one. Whilst the bulk term is referred to the stable phase under formation, the surface term concerns the development of the interface between metastable and stable phase. For big  $r$

values, the bulk term dominates and  $\Delta G$  decreases. When  $r$  is small, the second term becomes dominant, indicating the creation of a new surface which increases  $\Delta G$ . By inspection of  $r$  dependence in eq.1.10, we see that the free energy of formation  $\Delta G$  reaches a maximum at  $r_c$ , being  $r_c$  the radius of critical nucleus, corresponding to a minimum in the probability of nucleus formation (fig.1.12).

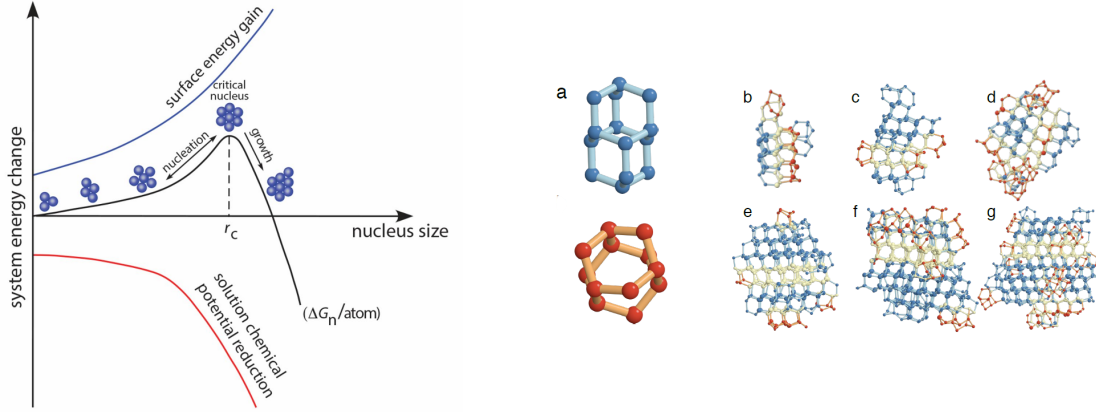


Figure 1.12: (Left) Free energy of formation of nucleation clusters during a homogeneous nucleation process. When the nucleus reaches the critical size  $r_c$ , the change in free energy is maximum: this signs the end of the nucleation stage. Then the probability to add new molecules for growing larger nuclei become exponentially bigger and the growth stage takes place. (Right) (a) Double-Diamond (blue) and hexagonal (red) cages, addressed as DDC and HC, respectively. The former is the building block of  $I_c$ , the latter is that of  $I_h$  in computer simulations by [117]. (b-g) Several configurations obtained by [117] during the nucleation process: (b-c) are pre-critical steps, (f) is critical, (g) is post-critical. Molecules that are part of a DDC are blue, those comprised in a HC are red, and those shared between DDC and HC are yellow.

Differentiating eq.1.10 with respect to  $r$  for finding  $r_c$ , we obtain  $r_c = -2\sigma/\Delta g$ , corresponding to an energy barrier  $\Delta G^* = \Delta G(r_c) = 16\pi\sigma^3/(3\Delta g^2)$ . As a result, as far as the forming nuclei are small, they are unstable and tend to rapidly disappear melting again to the metastable liquid phase (small nuclei are created and remelted continuously). But occasionally a spontaneous fluctuation can occur, leading to the formation of a critical nucleus ( $r = r_c$ ) which is sufficiently stable to grow up rather than melt. Hence, adding new molecules to nuclei larger than  $r_c$  causes a free energy reduction, making the nucleation process more probable.

The probability  $\mathcal{P}$  to have such a spontaneous fluctuation able to overcome the energy barrier  $\Delta G^*$  and let the nucleus to grow up is proportional to the Boltzmann factor:

$$\mathcal{P} \propto \exp\left(-\frac{\Delta G}{k_B T}\right) \quad (1.11)$$

Thus  $\mathcal{P}(\Delta G^*)$  is the probability of forming a critical nucleus, that sets a limit to the rate at which nucleation occurs. Additionally, eq.1.11 shows that homogeneous nucleation, being it a spontaneous process, needs supercooling to be allowed and promoted.

CNT is based on some simplifying assumption: *i*) the microscopic nucleus is described with the same macroscopic properties as the final stable phase (density, composition, structure);

*ii*) the nucleus is spherical and the interface between the metastable and stable phase is a sharp boundary; *iii*) the vapour-liquid (or liquid-solid) interface is approximated as planar, disregarding the critical cluster size. This is known as capillary approximation and it is reasonable only if the surface is not too curved, i.e. for not too small clusters. For many years CNT has been the most widely used theoretical explanation for describing nucleation process. Nowadays more sophisticated approaches are under study (the EMLD-DNT model, the Density Functional Theory, the Diffuse Interface Theory, nonclassical nucleation pathways), especially for improving the description of nucleation in more complex systems, such as proteins, minerals, colloids, polymeric solutions [116].

Interestingly, it has been observed that ice homogeneously nucleating in atmosphere and vapour chamber experiments does not crystallize in the thermodynamically stable hexagonal polymorph, but it is mainly composed of cubic-rich and stacking disordered polymorphs [94, 118]. However, the molecular origin of this preference is still not clear because an improvement in spatio-temporal resolution of available experimental techniques should be needed. Quite recently a computational investigation using TIP4P/Ice water potential (the most accurate among existing molecular models for describing ice polymorphs) has been able to determine the ice homogeneous nucleation rate, pointing out that the early stage of freezing mechanism involves the competition between hexagonal and cubic ice [117]. As the nucleation carries on, the average number of water molecules participating in a cubic cage unit definitely exceeds that of molecules embedded in a hexagonal cage unit [117].

By contrast, as far as water undergoes the heterogeneous nucleation, it transforms to the hexagonal form of ice ( $I_h$ ). In nature heterogeneous nucleation is much more favoured: it is not a spontaneous process but induced by impurities or surfaces, and it is faster comparing to homogeneous nucleation. This is essentially due to the fact that droplets on a surface are not complete spheres (see section 2.2), so that the interfacial area is less than  $4\pi r^2$ , as instead assumed for homogeneous nucleation in CNT. In particular, the surface area decreases as the contact angle reduces. This geometrical factor lowers the interfacial area and the interfacial free energy contribution in eq.1.10, which in turn reduces the nucleation barrier  $\Delta G^*$ . Consequently, the reduction of the free energy barrier is expected to hasten the nucleation on surfaces with smaller contact angles. It is reasonable to assume that the flatness/curvature and the roughness of the contact surface are relevant parameters in the heterogeneous nucleation of ice, however a comprehensive and systematic understanding of the role of the surface and its properties is currently underway [119, 120]. For example planar but molecularly rough surfaces have been recently found not to promote heterogeneous nucleation, regardless of the hydrophilic or hydrophobic nature of the liquid under nucleation [121]. It seems rather that roughness prevents liquid water to arrange in layers or in fluctuating patches of hexagonal ice at the interface [121].

## 1.4 Interpretations of water anomalies

Many theories and conjectures have been proposed to account for the exotic phase behaviour of metastable water at low temperature. Three conjectures seem to have achieved more success midst the scientific community: the retracing spinodal [8], the singularity-free

scenario [10], and the second–critical point hypothesis [9]. Additionally, an original interpretation has been recently proposed by Moore and Molinero [122], as briefly discussed in the last part of the present section.

### 1.4.1 The retracing spinodal

The retracing spinodal conjecture (also regarded to as the *stability limit conjecture*) has a purely thermodynamic nature. According to this hypothesis, the anomalous increase of the response functions upon supercooling is due to the approach to the spinodal<sup>6</sup> curve, where superheated liquid water becomes unstable with respect to vapour.

In normal liquids, the liquid spinodal curve  $T_s$  (see fig.1.13) has a positive slope in the  $(P, T)$  plane and its trend is monotonic. In water, according to Speedy [8],  $T_s$  at negative pressures would instead retrace towards positive pressures, reaching the liquid-gas spinodal of superheated water (fig.1.13). In this way  $T_s$  may be crossed upon isobaric supercooling, providing a continuous boundary for superheated, stretched ( $P < 0$ ) and supercooled water states. The crucial point is that the spinodal line is characterized by divergence of both density and entropy fluctuations, so that retracing could explain the sharp increase in water compressibility and heat capacity that are experimentally observed. Since the spinodal line is essentially an envelope of isochores, its slope vanishes along the TMD curve (where density has a maximum in the  $(P, T)$  plane, that is  $\alpha_p = 0$ ), while the sign of its slope must change as intersect a curve along which the thermal expansivity is zero. As a consequence, points belonging to  $T_s$  must satisfy the following equation:

$$\left(\frac{\partial P}{\partial T}\right)_{spinodal} = \left(\frac{\partial P}{\partial T}\right)_{\rho} \quad (1.12)$$

### 1.4.2 The singularity-free scenario

According to this interpretation, water response functions do not diverge, whilst they do exhibit extremal points [10].

Let's go back to eqq.1.1, 1.2, 1.4. Starting from any point of the TMD, they imply: *i*) the isothermal compressibility of liquid increases upon isobaric cooling; *ii*) the thermal expansion coefficient increases upon isothermal compression and becomes negative upon isothermal decompression; *iii*) the isobaric heat capacity decreases upon isothermal compression; *iv*) the locus of  $\kappa_T$  extrema with respect to  $T$  along isobars coincides with the locus of  $\alpha_P$  extrema (where  $\alpha_P$  is the thermal expansion coefficient) with respect to pressure along isotherms.

The experimentally observed increase in the response functions is, therefore, to be linked to density anomalies, appearing in the form of a negative slope of TMD locus. Hence in the

<sup>6</sup>The spinodal line is the locus of points satisfying the condition:  $(\partial P/\partial V)_T = 0$ . It separates a metastable region from an unstable one in the coexistence region of the phase diagram. Above the spinodal line, the system approaches equilibrium by droplet nucleation, while below order parameter undergoes periodic modulations as a result of fluctuations. It is important to note that in real system spinodal line is not a sharp boundary [68, 123].

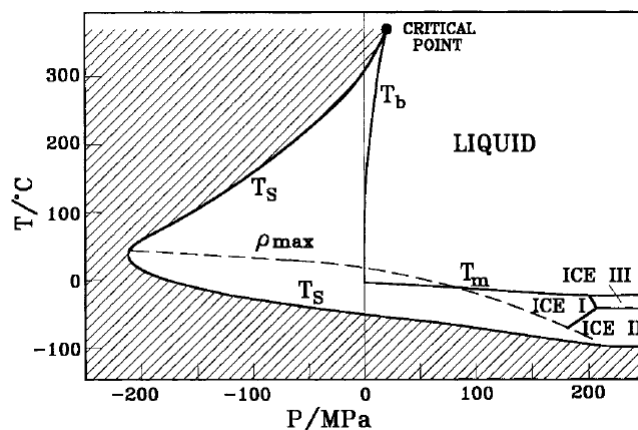


Figure 1.13: Water phase diagram showing the continuous retracing spinodal curve  $T_s$ , as postulated by Speedy's stability limit conjecture [8] (figure from [68]).

singularity-free scenario the response functions do not actually diverge but remain finite, so that no singularity needs to be invoked in order to explain the unusual behaviour of water.

Several theoretical models are able to account for water anomalies reproducing a scenario consistent with the singularity-free conjecture. One of the earliest attempts to reproduce the singularity-free scenario for supercooled water is due to Stanley and Teixeira [54]. They developed a microscopic correlated-site percolation model in which each site is occupied by an oxygen atom. Each  $i$  water molecule is assigned to another  $j$  water molecule, where the label  $j$  indicates the number of bonds that it can form<sup>7</sup>. Factors determining the probability that a bond is established are twofold: intermolecular distance and reciprocal orientation, so that a bond is formed only when the interaction between the two water molecules is stronger than an arbitrary cut-off. For a given probability of interaction, the density of  $j$ -sites is random, but the site connectivity depending on their species is not random; in particular, the probability that the site  $i$  belongs to  $j = 4$  species increases as the number of  $j = 4$  neighbours increases. This mechanism allows for simulating the cooperative nature characterizing hydrogen-bonding. The result is that, since volume site varies with the number of HB and the full-coordinated oxygen positions are strongly correlated, spatial correlations among molecules of a given species introduce corresponding spatial correlations in density fluctuations. This simple idea is able to provide qualitative predictions in agreement with experimental observations concerning, among the others, the increase in compressibility which reaches a maximum at low temperature with no divergence upon further cooling.

Another relevant example is given by the model introduced by Sastry *et al.* [10]. This is a lattice model based on nearest-neighbour attraction with directional and independent interactions, whose mean field solution yields the behaviour shown in fig.1.14 for the thermal expansion coefficient  $\alpha_P$ . At fixed pressure, lowering temperature induces a sharp but finite increase in  $\alpha_P$ , that exhibits a peak at a given temperature. Such a peak in the thermal expansion coefficient corresponds to a sudden increase in specific volume, that becomes more pronounced with increasing pressure. On the other hand, by fixing temperature, anomalies can be suppressed at higher pressures. A similar argument can be proposed for specific

<sup>7</sup>For example, in the case of a lattice with 4 coordination number, in any given configuration molecule  $i$  can form 0,1,2,3 or 4 bonds, thus  $j = 5$ .

heat: an abrupt increase in  $C_P$  causes entropy diminishes upon supercooling, being the effect more remarkable with increasing pressure. Anyway, beyond all the details, the crucial point to highlight is the ever finite increase of all response functions entailed in this model.

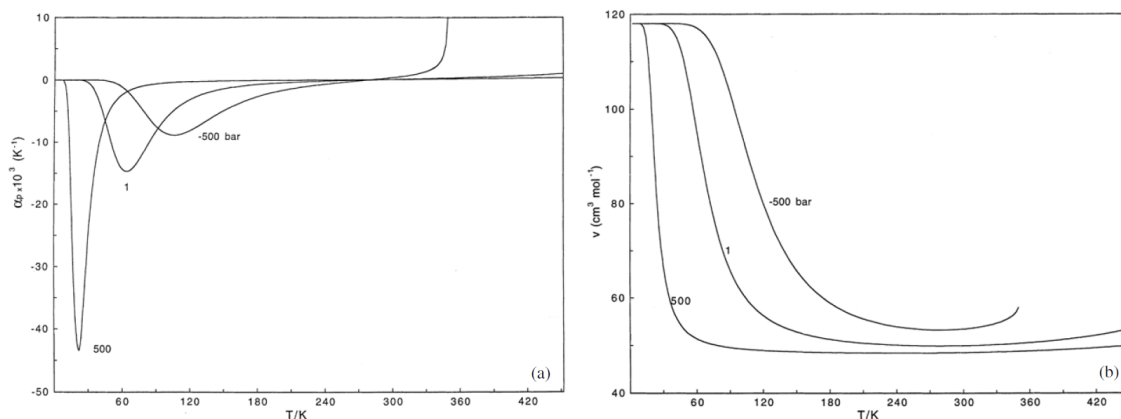


Figure 1.14: Example of response function for different pressures derived from the mean-field solution of the lattice-model by Sastry *et al* [10]. Figures display the temperature dependence of the thermal expansion coefficient  $\alpha_p$  (left panel) and molar volume  $v$  (right panel). At fixed pressure, a peak in  $\alpha_p$  results in a sharp increase in the change of volume with respect to temperature, such an increase becoming more abrupt upon supercooling and increasing pressure (figures from [17]).

### 1.4.3 The second critical point hypothesis

A possible explanation for the puzzling properties of supercooled water has been supplied in the hypothesis originally proposed by Poole and Sciortino in 1992 [9], who identified polymorphism as responsible for water anomalies, giving a thermodynamically consistent perspective on the global phase behaviour of metastable water (fig.1.15(a)). In particular, their hypothesis assumes the existence of a first-order phase transition between two different forms of liquid water, ending in a second critical point (distinct from the usual liquid-vapour critical point of the stable phase diagram). These two forms are addressed as low-density liquid (LDL) and high-density liquid (HDL), at low and high pressure respectively, and should be the thermodynamic continuation of the glassy forms LDA and HDA. From this point of view, the experimentally observed increase in response functions upon cooling is the macroscopic manifestation of the increase in density and entropy fluctuations associated to this critical point. Hence the experimentally observed transition between LDA and HDA is a signature of a structural arrest relative to a thermodynamic transition between these two forms of liquid water differing in density. Above the critical point LDL and HDL cannot be distinguished, whereas below it they become distinct and characterised by different values of specific volume and entropy. Consequently, the only way to recognise LDL and HDL as distinct forms of supercooled liquid water is moving along a thermodynamic path crossing the conjectured liquid-liquid coexistence line, where analytic discontinuity in the first derivatives of Gibbs energy is expected to be found [17].

The second-critical-point interpretation is the result of an extensive molecular dynamic simulation work based on the ST2 model of water <sup>8</sup>, showing that low-temperature isotherms exhibit an inflection point at high pressure whose trend in temperature is compatible with what is expected to be observed approaching a critical point. The location of the second critical point predicted by computer simulations is  $T_C \sim 220$  K and  $P_C \sim 100$  MPa = 1 kbar [17]. Furthermore, no low-temperature retracing of TMD was assessed under sufficiently high (in absolute value) negative pressures [9]. As a result, TMD does not intersect the spinodal line, whose slope is monotonically positive in the  $(P, T)$  plane and does not come back towards positive pressures (fig.1.15(b)). In particular, the negative slope of the liquid-liquid coexistence line implicates the lower density form (LDL) has a higher entropy with respect to HDL.

---

<sup>8</sup>ST2 is a rigid four-point-charge (two positive and two negative) model where every molecule has two positive charges  $+q$  ( $q < e$ , with  $e$  the modulus of a single electron charge) identified as partially shielded protons located at 1 Å from the oxygen atom  $O$ . The distance between  $O$  and each of the negative charges  $-q$  is 0.8 Å. The two couples of vectors connecting  $O$  with negative and positive charges are disposed forming a tetrahedral angle ( $109^\circ 28'$ ). Each pair of water molecules interacts via a potential consisting of a Lennard-Jones term between the oxygens, plus a modulated Coulomb term simulating the electrostatic attraction/repulsion for the 16 pairs of point charges [124].

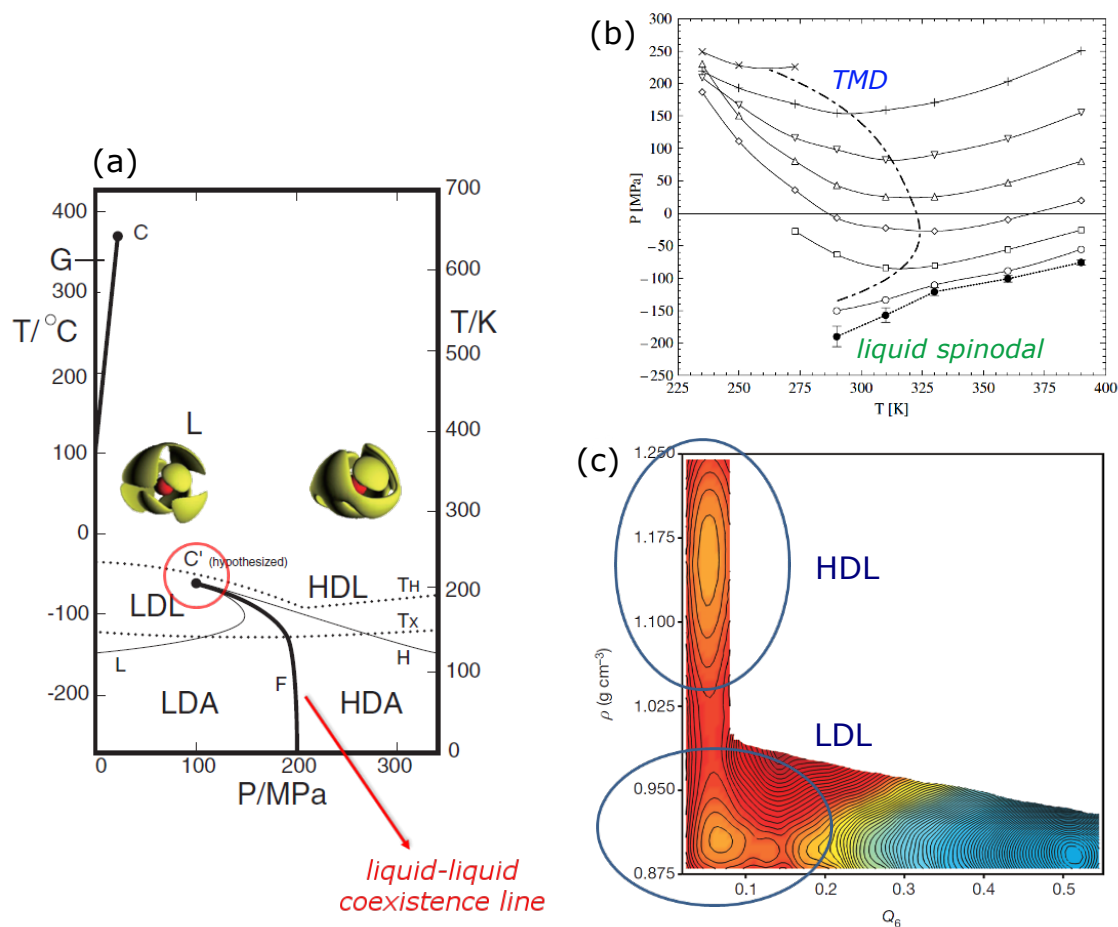


Figure 1.15: (a) Metastable phase diagram tracked following the second-critical-point interpretation [17, 125]. Inserts showing the spatial density functions for LDL and HDL are adapted from [51]. A new coexistence line, distinct from the liquid-gas one, appears estranging two phases analogous in structure to the amorphous forms LDA and HDA and terminating in a critical point  $C'$  (red circle). (b) Phase diagram of ST2 water. A series of isochores obtained for different values of density, with the TMD line connecting the minima along each of isochores curves. The bottom line indicates the spinodal  $P_s(T)$ , resulting from isotherm minima (figure from [9]). (c) The main result from the work of Palmer *et al.* [126]: free-energy isosurfaces show two minima corresponding to two distinct forms of liquid water differing in density, separated by a first-order phase transition. These two phases are metastable with respect to a crystalline state, being it more ordered and less energetic. The variable along the x-axis,  $Q_6$ , is an order parameter useful to distinguish highly ordered states (crystalline) from short-ordered configurations (liquid). The colour maps runs from red (high free energy) to blue (low free energy).

Over the years plenty of theoretical models and simulations have been performed, confirming<sup>9</sup> or ruling out the second critical point hypothesis as a possible explanation for gaining

<sup>9</sup>Even if simulations over non-crystallizing water models are able to prove the second-critical point hypothesis, finite-size problems introduce uncertainty in determining the exact location of the second critical point in the  $(P, T)$  plane.

insights into water metastable phase diagram. The multiparametric empirical model due to Jeffery and Austin [13], the theoretical contribution by Franzese and Stanley [14] based on a microscopic lattice model with directional interactions added to conventional nearest-neighbours ones, the modified Van der Waals model proposed by Poole [5], where the probability of HB formation is a function of the bulk density, the microscopic approach, due to Truskett *et al.* [12], with orientation-dependent interactions between water molecules leading to an equation of state with a mean field solution, are only a few examples that can be mentioned in order to hint the prolific research activity concerning this topic.

Up to now, one of the most recent and convincing theoretical proof of the existence of a transition between two liquid phases (L–L transition) is the work of Palmer *et al.* [126]. These authors, using a free-energy method specifically designed for studying phase transitions [127], have shown that ST2 water reveals two minima in the free-energy surface as a function of density and of the order parameter,  $Q_6$ , which allows to distinguish crystalline states from no long-range order configurations [126]. As shown in fig.1.15(c), two disordered phases (low  $Q_6$ ) are found to coexist in equilibrium: they differ in density, but have the same order parameter and are both metastable with respect to a crystalline phase (the minimum at higher  $Q_6$  and much lower free energy). Moreover, it has been demonstrated that supercooled water undergoes a first-order phase transition going from one to another liquid form. This is regarded as a first strong and unambiguous evidence for thermodynamic equilibrium between two *liquid* metastable polymorphs and liquid–liquid transition in ST2 model of water.

Unluckily, in bulk water identification of the liquid–liquid coexistence line proposed by Poole and Sciortino [9] and recently confirmed by Palmer [126] is not straightforward since the second-critical point is predicted to fall into the *No man's land*, thus in a region inaccessible to experiments on bulk water. As a consequence, despite some experimental evidence seem to be consistent with the second critical point hypothesis (see, for instance, [19, 128, 129]), at the best of our knowledge, no definitive experimental proof has been provided up to date. However, the first experimental support for the second-critical point hypothesis comes from Mishima and Stanley [19]: these authors demonstrated that, in the  $(T, P)$  plane, the extensions of the polymorphs ice IV and ice V display clear discontinuous changes in slope on crossing the hypothesized liquid–liquid phase transition (LLPT) line. Notwithstanding, no similar “kinks” could be reproduced for ice III. A more recent experimental proof is due to Winkel and co-workers [129]: by performing calorimetric and dielectric spectroscopy measurements on bulk water at ambient pressure, they have observed a double glass transition temperature for water and linked this result to the existence of two liquid phases. Nonetheless, since measurements have been carried out well below the *No man's land*, such a result may only support the two-liquid interpretation for supercooled water, but does not provide any direct answer to the question of whether there is a LLPT line ending in a second critical point or if LDL and HDL are distinct forms of supercooled water transforming into each other in a singularity-free scenario. In addition, no hints have been grasped about the possible thermodynamic connection with water at ambient conditions.

As firstly proposed by Ito *et al.* [130], from a dynamic point of view the existence of a low-temperature second critical point and the presence of a first-order liquid–liquid transition line are considered to be revealed by the observation of a fragile-to-strong dynamic crossover (FSC), occurring at  $\sim 225$  K on approaching  $T_g$  from the liquid side, as a consequence of a dramatic change in the hydrogen-bond structure of liquid water [64, 131]. According to molecular dynamic (MD) simulations, performed using different interaction

potentials for water, FSC is correlated with the *Widom line*, i.e. the locus of maximum correlation length in the  $P - T$  plane, springing from the hypothetical second critical point [132]. More precisely, crossing the Widom line gives rise to a change in the  $T$ -dependence of the diffusion coefficient  $D$  accordingly to the FSC, whereas structural and thermodynamic properties change from HDL-like to LDL-like. This means that the Widom line is associated with a sharp but continuous change in the value of the local order of the liquid which, in turn, induces a sharp but continuous change in entropy and its fluctuations, leading to a maximum in the specific heat ( $C_P^{\max}$ ) that can be easily highlighted by appropriated parameters defined by computer simulations.

What can be learned from this overview is that, at the actual state of art, both theoretical and experimental approaches are essential attempts to get through all the murky aspects relative to water. In fact, from one side, theoretical models and simulations allow to overcome the huge difficulties inherent experimental investigations. Though the prodigious number (about one hundred) of atomistic potentials of water developed since the 1930s<sup>10</sup> clearly admits the difficulty in properly modelling the complex physics of water (very popular and largely employed models for water are, for instance, SPC, SPC/E, TIP3P, TIP4P, TIP5P [133]). On the other hand, given this multiplicity and diversity of theoretical approaches, experiments appear to be the unique tool for directly investigating water behaviour and assessing which models are the most reliable.

Lastly, it is worth nothing that second-critical point hypothesis and singularity-free scenario have a relevant issue in common: they both suggest two forms of water do exist in the supercooled regime. Moreover, above the temperature at which the second-critical point is thought to exist, and under all thermodynamic conditions consistent with the singularity-free conjecture, these two forms of water will transform into each other with continuity along an isotherm, becoming indistinguishable. Hence the more pressing questions to answer are essentially two: *i*) do exist two distinct forms of supercooled liquid water? *ii*) if yes, does the coexistence line separating them ends in a critical point or no singularities occur in the *No man's land*?

This issue is still a matter of active debate and represents the framework within the present work is inserted.

#### 1.4.4 Relation between nucleation rate and water anomalies

It is not still clear what determines the lowest temperature to which water can be supercooled before it crystallizes ( $T_H \sim 232$  K). As discussed in section 1.2, what is known is that liquid water rapidly crystallizes below  $T_H$ , while thermodynamic and dynamic response functions anomalously increase in the supercooled region, according to a power law that would diverge around  $T_S \sim 225 - 228$  K [66, 134]. The small difference between these two temperatures ( $T_H$  and  $T_S$ ) suggests the likely existence of a link between the nucleation rate of ice and water anomalies. In recent years, much effort has been devoted to clarify this issue, especially exploiting the advantages of improved computer performance that have made affordable calculations that were unfeasible before. For example, few yers ago Moore

<sup>10</sup>The first model of liquid water is dated 1933 and was proposed by Bernal and Fowler [45]: they modelled water as an icelike disordered tetrahedral structure arising from the electrostatic interactions between close neighbours.

and Molinero [122] have performed a coarse-grained<sup>11</sup> simulation of supercooled water, finding out that the nucleation rate reaches a maximum at exactly 225 K: below this temperature ice nuclei formation happens more rapidly than the equilibration time of liquid water. By inspection of the time–temperature–transformation diagram (TTT), it can be seen that ice nucleation rate reaches a minimum around  $T_L = 200$  K (fig.1.16). Above  $T_L$  the system needs to overcome a high energy barrier, so that the formation of a critical nucleus is a very sporadic event. Under these conditions, crystallization is prevented and liquid water can be studied in its supercooled (metastable) state. Conversely, below  $T_L$  crystallization starts before liquid water has time to equilibrate, since nucleation barrier is similar to the thermal energy  $k_B T$  and the growth time of crystallites is comparable or shorter than the relaxation time of liquid water, being the growth rate proportional to the diffusivity of supercooled liquid water. This means that water exists in its liquid form for a time that is too short to allow it for reaching equilibrium. On the basis of this interpretation, the minimum crystallization time (corresponding to the limiting temperature  $T_L$ ) signs a crossover in the mechanism of ice crystallization, passing from a stage dominated by nucleation (above  $T_L$ ) to a regime dominated by growth (below  $T_L$ ). It can be concluded that the structural transformation and dynamic transition occurring at  $T_L$  establish an effective lower limit of metastability for supercooled water. This supports the kinetic limit previously set by Kauzmann [135], giving a solution to his entropy paradox.

Such an interpretation suggests that crystallization may occur faster than LDL's equilibration, ruling out the hypothesis of water that first converts to LDL and then crystallizes. Hence, in contrast with the three main theoretical scenarios presented in section 1.4 which assume that supercooled liquid water should exist also below  $T_H$ , the original interpretation of Moore and Molinero asserts the impossibility to obtain liquid water under  $T_H$  and finds that water crystallization in *No man's land* is limited only by the growth rate of the crystal nuclei, which is lowered on cooling [122].

---

<sup>11</sup>In [122] the mW water model was used, which describes each water molecule as a single particle interacting with its neighbours via anisotropic short-range interactions in order to mimic the effects of hydrogen bonds.

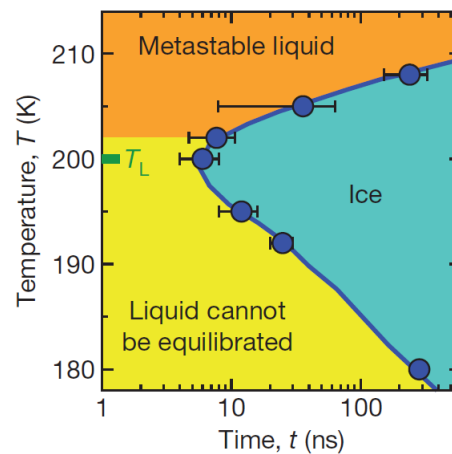


Figure 1.16: Time–temperature–transformation (TTT) diagram of mW water by Moore and Molinero [122]. Above  $T_L$  the dynamic is dominated by nucleation: crystallization is limited by the fact that critical nuclei formation is very rare, thus investigations on supercooled water in its metastable liquid state are feasible (orange area). Below  $T_L$  the dynamic is dominated by crystallites growth: crystallization proceeds faster than liquid water relaxation, thus the liquid has not enough time to equilibrate (yellow area). Nucleation and growth time scales become comparable at  $T_L$ . Blue circles indicate the average time needed to crystallize 70 % of water.



# Chapter 2

## Confined water

*Instead of being the biological center of the Universe, I believe our planet is just an assembly station, but one with a major advantage over most other places. The constant presence of liquid water almost everywhere on the Earth is a huge advantage for life, especially for assembling life into complex forms by the process we call "evolution".*

*Fred Hoyle - Astrophysicist*

### 2.1 Introduction

As introduced in the previous chapter (chapter 1), homogeneous nucleation and spontaneous crystallization hinder any attempt of direct access to the water phase diagram in the supercooled region known as *No man's land*. Over the years some strategies have been put in place to circumvent such an experimental difficulty. First of all, hyperquenching technique has revealed to be a very powerful solution [20, 21]: a rapid cooling of micrometer water droplets lets the system to directly transform into a glassy state; thus, by varying pressure and increasing temperature, the region of interest of the phase diagram can be explored until spontaneous nucleation occurs. Additionally, studying water as a solvent can represent another good trick [23, 24, 136, 137]: in particular, aqueous solutions of common salts (e.g. LiCl, KCl, NaCl, etc.) manifest a rich phase diagram where the presence of the solute lower the freezing point with respect to the pure solvent [138]; moreover, particular values of the salt concentration can be identified, such that crystallization is completely avoided<sup>1</sup>. At relatively low salt concentration, solute does not significantly affect the water network structure, which is subjected only to a weak electrostrictive effect due to ions (equivalent to an internal pressure) [25]. Another well-trodden track is the study of hydration water (i.e. few water layers in contact with surfaces) and water trapped in confined geometries. This latter strategy allows to obtain a downshift of the ice nucleation temperature  $T_H$  to an extent that depends on the size of the confining space [139], suggesting experiments on water into narrow volumes can represent a convenient framework to overcome the difficulties of

<sup>1</sup>For example, in the case of LiCl aqueous solution, this special feature is realized at the eutectic point, with  $R \sim 6$  ( $R = \text{mol}(\text{H}_2\text{O})/\text{mol}(\text{LiCl})$ ).

exploring the forbidden region of the phase diagram and give an experimental validation of models hitherto proposed (section 1.4).

However, a deeper comprehension of interfacial or confined water's structure, phase behaviour and dynamics is interesting also by itself, because water is commonly found in restricted geometries (e.g. living cells, food, soil, cloud nuclei, icy interstellar particles) and depressing of freezing point is even a mechanism naturally exploited by living organisms to survive in sub-freezing conditions. Successful steps forward in a better understanding of molecular structure and dynamics of water in spatially restricted environments might thus be crucial for an increasing awareness of its manifold role in chemical, biological and geological processes.

Over the years, several confining substrates have been investigated, both by experiments and simulations: emulsions and microemulsions [140, 141], natural and synthetic clays [142], globular proteins [143], micro- or nano-porous materials<sup>2</sup> [144–146]. Despite a great effort is still underway, 1D, 2D and 3D confined water's properties are far from being fully understood and still remain under-represented in research because of their sensitivity to confining surface features, such as roughness, hydrophilicity or hydrophobicity, chemical environment and topography of the confining geometry, that lead to a considerable deviation from what is expected in bulk water [147–151]. The crucial role played by the confining substrate properties and its interaction with water explains why is important to make well-defined confining media available, whose characteristics can be easily identified and modeled by computer simulations. Additionally, having the possibility to compare data coming from several different confining substrates is an important issue if some general perspectives (if any) are to be extracted about structure and dynamics of confined water. Among the "regular" confining media, self-ordered nanoporous aluminium oxide (AAO) [152, 153], Vycor-glass [149, 154, 155], Laponite [156] and other lamellar structures [157], spherical reverse micelles [158], zeolites [159], carbon nanotubes [160] and mesoporous silica matrices [161, 162] are some of the most widely employed.

In the following, special attention will be devoted to hydrophilic porous systems as confining media and relating physical processes, since all the results introduced in the present thesis have been achieved studying water trapped in MCM-41, that is indeed a hydrophilic mesoporous silica matrix. In particular, this chapter will describe the mechanisms by which water is adsorbed in confining media and the effects of confinement on its structure and dynamics, as reported in recent literature. At the end of the chapter, particular focus will be given to the description of MCM-41 substrates.

## 2.2 Capillary condensation in mesopores

Capillary<sup>3</sup> condensation is the process by which the vapour phase undergoes a multilayer adsorption into a porous medium proceeding until the pore volume becomes completely filled with the condensed liquid. The pressure of condensation is directly related to the liquid–vapor interfacial tension and to the pore geometry, size and shape. However, due to

---

<sup>2</sup>Porous materials can trap water into pores or channels. They are classified by IUPAC (International Union of Pure and Applied Chemistry) according to their size as *macropores* if the diameter is larger than 50 nm, *mesopores* if the diameter is between 2 and 50 nm, *micropores* if the diameter is less than 2 nm.

<sup>3</sup>A capillary does not necessarily have a tubular, closed shape, but can be any confined space with respect to its surroundings.

an increased number of Van der Waals interactions between vapour phase molecules inside the confined space, condensation always occurs below the saturation vapour pressure of the pure liquid at the given temperature, thanks to the formation of a meniscus at the liquid-vapour interface which allows for equilibrium below the saturation vapour pressure [163].

Generally speaking, when isolated molecules approach a surface, they experience Van der Waals attraction driving them to bind to the surface and to neighbour molecules. This starts the vapour-liquid transition. The equilibrium condition is described by the Young's equation:

$$\sigma_{lv} \cos(\theta) + \sigma_{sl} = \sigma_{sv} \quad (2.1)$$

where  $\sigma_{lv}$  is the liquid-vapour surface tension, i.e. the surface tension exerted by the droplet surface of the condensed liquid, while  $\sigma_{sl}$  and  $\sigma_{sv}$  are the interaction forces between the surface and the liquid and vapour phase, respectively. The term  $\sigma_{lv} \cos(\theta)$  describes the wettability of the surface (or the pore wall), being  $\theta$  the contact angle, i.e. the angle between the surface and the droplet interface (fig.2.1(a)).

From eq.2.1 an expression for the contact angle can be derived:

$$\cos(\theta) = \frac{\sigma_{sv} - \sigma_{sl}}{\sigma_{lv}} \quad (2.2)$$

If  $\theta < 90^\circ$  (*partial* wetting case), the liquid wets the surface because  $\sigma_{sv} > \sigma_{sl}$ , showing that the condensation process is promoted as the wall-vapour energy interaction is larger than the wall-liquid interaction; conversely, if  $\theta > 90^\circ$ , the liquid does not wet the surface being  $\sigma_{sl} > \sigma_{sv}$ . The limit case of  $\theta = 0$  is indicated as *complete* wetting case.

In the case of water molecules adsorbed into tiny pores (instead of an open and external surface) the same description is still valid, although eq.2.1 is a simplification for ideal surfaces, where *ideal* means perfectly flat and rigid. It is possible to obtain a more generalized and complete theory for real smooth surfaces, but this issue will not be detailed further as it falls outside the focus of this work.

What is interesting to remark is that, in the case of adsorption into small pores, water molecules keep condensing forming multilayers that grow up from the pore wall to the pore center, with the formation of a meniscus at the liquid-vapour interface (fig.2.1(b)). Corresponding to this interface, the difference between vapour ( $p_v$ ) and liquid ( $p_l$ ) pressure gives rise to the capillary pressure ( $p_c$ ), defined as:

$$p_c = \Delta p = p_v - p_l \quad (2.3)$$

A simple approach can be used to estimate this pressure by considering a spherical water droplet surrounded by water vapour. On the droplet surface, a capillary pressure  $\Delta p$  acts inducing a change  $dV$  in the droplet volume. Thus the work made by the capillary pressure on the water droplet can be expressed as:

$$W_p = \Delta p \cdot dV = \Delta p \cdot 4\pi R^2 dR \quad (2.4)$$

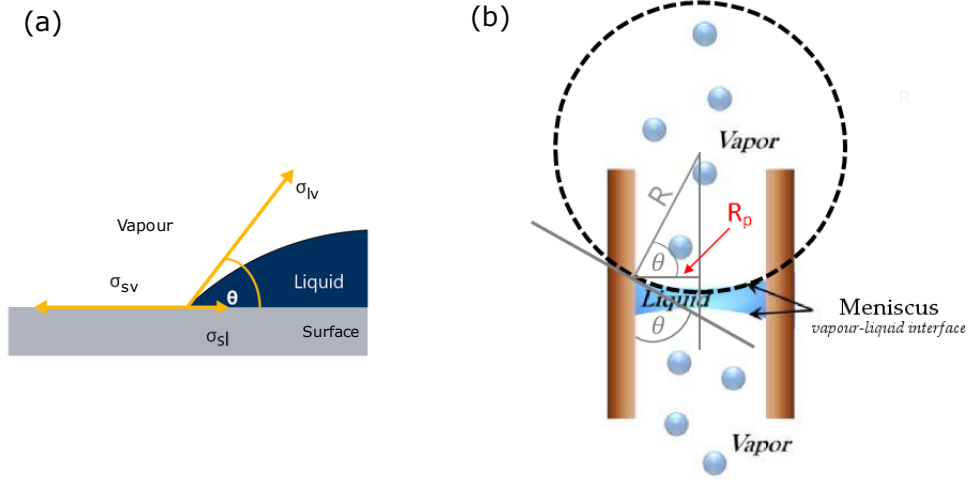


Figure 2.1: (a) Schematic diagram of contact angle of a liquid droplet adsorbed onto a solid surface. According to Young's equation (eq.2.1), there is a relationship between the liquid-vapour interfacial tension  $\sigma_{lv}$ , the interaction force between the surface (solid) and the liquid  $\sigma_{sl}$ , and the interaction force between the surface and the vapour  $\sigma_{sv}$ . If the contact angle  $\theta$  is between  $0^\circ$  and  $90^\circ$ , the surface is wettable, else ( $\theta > 90^\circ$ ) the surface is not wettable (hydrophobic) [figure from <https://www.kruss.de>]. (b) Water condensation on pore wall with the formation of a meniscus at the vapour-liquid interface. Water condensation carries on until the curvature of the meniscus,  $R$ , is given by the Kelvin equation (eq.2.11).

where  $R$  is the radius of the water droplet. The corresponding change in the droplet surface can be approximated as follows:

$$dS = (4\pi R^2 - 4\pi(R - dR)^2) = (4\pi R^2 - 4\pi(R^2 - 2RdR + dR^2)) \approx 8\pi R dR \quad (2.5)$$

This result allows to write the produced surface tension, defined as the work required to increase the surface unit area of the liquid, in the following form:

$$W_s = \sigma_{vl} \cdot dS = \sigma_{vl} \cdot 8\pi R dR \quad (2.6)$$

The system is in equilibrium when the right sides in eq.2.4 and eq.2.6 are equal:

$$\Delta p \cdot 4\pi R^2 dR = \sigma_{vl} \cdot 8\pi R dR \quad (2.7)$$

and this occurs when:

$$p_c = \Delta p = p_v - p_l = \frac{2\sigma_{vl}}{R} \quad (2.8)$$

The last equation is known as Young–Laplace equation and expresses the relation between the curvature of the surface,  $R$ , and the pressure difference between the vapour and liquid phase of water,  $\Delta p$ . In particular, in the case of an open surface with droplets immersed in their vapour,  $\Delta p$  is always positive because  $R$  has a positive sign. In the case of a concave

surface (meniscus formed during capillary condensation or bubbles in a liquid),  $R$  has a negative value and  $\Delta p < 0$ . For the limiting case of a flat surface,  $R \rightarrow \infty$ , implying  $\Delta p = 0$ .

The pressure change due to the curvature effects induces the molar Gibbs-free energy  $G$  to vary following the fundamental equation:

$$dG = V dp - S dT \rightarrow \Delta G = \int_0^{\Delta p} v dP = v \Delta p = v \frac{2\sigma_{vl}}{R} \quad (2.9)$$

where  $v$  is the molar volume of the liquid and eq.2.9 has been integrated at constant temperature along the curve surface of a spherical drop, exploiting the result of eq.2.8. By considering that  $\Delta G$  is the difference between molar Gibbs-free energy of the vapour in equilibrium with a curved surface ( $G^c$ ) and with a flat surface ( $G$ ), respectively,  $\Delta G$  can be also written as:

$$\Delta G = G^c - G = (G^0 + \mathcal{R}T \ln(p_0^c)) - (G^0 + \mathcal{R}T \ln(p_0)) = \mathcal{R}T \ln\left(\frac{p_0^c}{p_0}\right) \quad (2.10)$$

with  $p_0, p_0^c$  the vapour pressure in the two different configurations. By combining eq.2.9 and eq.2.10, we obtain the Kelvin equation:

$$\ln\left(\frac{p_0^c}{p_0}\right) = \frac{2\sigma_{vl} v}{R \cdot \mathcal{R}T} \quad (2.11)$$

that expresses the relation between the vapour pressure and the curvature of the liquid phase. By adding a negative sign<sup>4</sup> to the right side of eq.2.11, we can also obtain the applied pressure to the meniscus at the vapour-liquid interface of water in mesopores.

Eq.2.11 tells us that, at a given pressure  $p_0^c$ , once the meniscus is formed inside the pore, condensation continues until the radius of the liquid phase (the curvature of the meniscus) reaches the value  $R$  given in the Kelvin equation. We can thus conclude that capillary condensation drives the absorption of liquids (and water, in particular) into porous materials. It can be convenient to write the Kelvin equation as a function of the pore radius  $R_p = R \cdot \cos \theta$ , showing explicitly the dependence of the equilibrium pressure on the contact angle and the pore wall wettability:

$$\ln\left(\frac{p_0^c}{p_0}\right) = -\frac{2\sigma_{vl} \cos(\theta) v}{R_p \cdot \mathcal{R}T} \quad (2.12)$$

As a consequence, it can be concluded that condensation occurs below the saturation vapour pressure  $p_0$  if  $\theta < 90^\circ$ , while it happens above  $p_0$  if  $\theta > 90^\circ$ .

The Kelvin equation is often used for the experimental determination of the average pore size of porous media, exploiting the adsorption-desorption of a gas (e.g. nitrogen  $N_2$ ) within the pores of the material under study [164–168].

<sup>4</sup>The negative sign is required because the radius of a meniscus is conventionally measured on the vapour side.

## 2.3 Adsorption

The condensation of vapour onto the pore wall is an adsorption process, as the solute accumulates on the vapour–solid interface with no penetration inside the substrate. Adsorption is always a spontaneous process, thus it is associated with a decrease both in entropy and free energy of the system. Since the adsorption mechanism under investigation is dominated by physical interactions, it is called *physisorption*. This process is exothermic, non-selective and is characterized by relatively low interaction energies ( $\sim 1 - 50$  kJ/mol, typical of intermolecular weak bonds and Van der Waals interactions), that do not significantly modify the molecular structure at the interface and make the process easily reversible<sup>5</sup>. Because of the interaction weakness, adsorbed molecules are still relatively free to diffuse on the surface and migrate into the pore volume.

The number of molecules adsorbed to an interface can be described by functions called *adsorption isotherms*,  $\Gamma = f(P, T)$ , that are usually measured at constant temperature [163]. The simplest case is a linear increase of  $\Gamma$  with pressure and is described by the Henry equation [169]:

$$\Gamma = k_H \cdot P \quad (2.13)$$

with  $k_H$  constant. A more refined model is due to Freundlich [169], whose equation accounts for heterogeneous surfaces where there are regions with different affinity for the adsorbate:

$$\Gamma = k_F \cdot P^q \quad (2.14)$$

with both  $k_F$  and  $q$  constant and  $q < 1$ .

IUPAC classification of gas physisorption isotherms encompasses six isotherm types (fig.2.2) [170]. Type I (also known as Langmuir isotherm [169]) describes the adsorption process when just a monolayer can be adsorbed on the substrate. The corresponding equation is:

$$\frac{\Gamma}{\Gamma_1} = \left( \frac{k_L \cdot P}{1 + k_L \cdot P} \right) \quad (2.15)$$

with  $\Gamma_1$  the amount of molecules adsorbed in a single monolayer and  $k_L$  a constant. The possibility to rule out the presence of more than one layer is ensured by the hypothesis at the basis of Langmuir equation: *i*) the substrate is a very porous solid, *ii*) the adsorption process evolves at relatively high temperatures and low pressures. Furthermore, Langmuir theory assumes a uniform and homogeneous surface substrate (with all adsorption sites energetically identical, hence with the same probability to be occupied), with a negligible interaction between adsorbed molecules. Function in eq.2.15 is common for microporous substrates, filled at relative pressure less than 0.1 atm; it describes the fact that, if the number of binding sites is constant, the number of available sites decreases as the adsorption process goes on, until saturation occurs as a consequence of the complete covering of a monolayer. Type I is usually observed, for instance, with polar solute–substrate systems in apolar solvents.

---

<sup>5</sup>When adsorption engages strong intermolecular interactions, such as ionic or covalent bonds (50 – 500 kJ/mol), it is called *chemisorption*. In this case, molecules are adsorbed at specific sites on the substrate, likely causing changes in its structure.

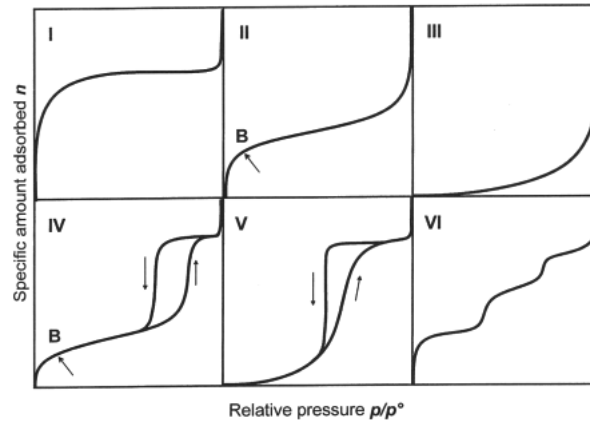


Figure 2.2: IUPAC classification of gas adsorption isotherms.

Type II can be obtained during adsorption on flat and homogeneous surfaces whereby cooperative effects take place. It is usually exhibited by non-porous or macroporous materials, where adsorption is not restricted and multilayers can be grown. In particular, the first step (point B in fig.2.2) describes the absorption of one monolayer; increasing pressure further, molecules are adsorbed forming a new layer over the previous one. Type III describes the same phenomenology as type II, but the binding of the first monolayer to the surface is weaker than the binding to the already adsorbed molecules. Type II and III represent an extension of the Langmuir theory and have been proposed by Brunauer, Emmett and Teller [171]: for this reason they are commonly addressed as BET isotherms. They thus describe the adsorption of multilayers by assuming a Langmuir adsorption for each monolayer and no interaction between single adsorbed layers, according to the following equation:

$$\frac{n}{n_1} = \frac{C}{\left(1 - \frac{P}{P_0}\right) \cdot \left[1 + \frac{P}{P_0}(C - 1)\right]} \cdot \left(\frac{P}{P_0}\right) \quad (2.16)$$

where  $n$  is the number of moles adsorbed per unit area,  $n_1$  is the number of moles adsorbed in one full monolayer per unit area,  $P_0$  is the equilibrium vapour pressure and  $C$  a constant taking into account the rate of adsorption/desorption of molecules to/from layers. Eq.2.16 can be rewritten as:

$$\frac{P}{V(P_0 - P)} = \frac{1}{CV_m} + \frac{C - 1}{CV_m} \left(\frac{P}{P_0}\right) \quad (2.17)$$

with  $V_m$  the adsorbate volume in a monolayer and  $V$  the total adsorbate volume. In particular, isotherm of type II is obtained if  $C \gg 1$ , while  $C \ll 1$  gives an adsorption of type III; when instead  $P/P_0 \ll 1$  and  $C \gg 1$  only a monolayer is adsorbed, recovering the Langmuir adsorption (type I). Eq.2.17 is largely used to determine the surface area of porous materials. To this aim, once data for gas (e.g.  $N_2$ ) adsorption-desorption to the pores of the material under investigation have been collected,  $P/V(P_0 - P)$  versus  $P/P_0$  can be plotted. Such a straight line has  $C - 1/CV_m$  as slope ( $m$ ) and  $1/CV_m$  as intercept ( $q$ ). Therefore the volume of a single monolayer can be calculated as  $V_m = 1/(m + q)$  and the BET surface area will be given by:

$$S_{BET} = \frac{V_m N_A A_{gas}}{MV} \quad (2.18)$$

where  $N_A$  is the Avogadro's number,  $A_{gas}$  the molecular cross-sectional area of the physisorbed gas and  $M$  its molecular weight.

Type IV and V are typical of capillary condensation in mesoporous solids. In particular, type IV is a step isotherm often observed in many industrial mesoporous materials, where the vertical region corresponds to pore-filling phenomena, while the step and flat region describe surface phenomena. More precisely, at low pressure one monolayer is adsorbed (as in the case of Langmuir adsorption), while at intermediate pressures multilayers are formed, until saturation occurs at high pressure when pores are completely filled. In porous materials a hysteresis phenomenon between adsorption and desorption may occur, because desorption is hindered for pores surrounded by other liquid-filled pores and evaporation is allowed only for molecules in contact with the vapour phase. This is the reason causing desorption to be delayed. Type V has a sigmoid shape and is a very uncommon isotherm, generally exhibited by non-porous or by certain mesoporous and macroporous adsorbent materials weakly interacting with the adsorbate; this isotherm looks like type III, but it usually shows hysteresis. Type VI is eventually a stepwise isotherm describing a multilayer adsorption which can be observed in non-porous materials with almost completely uniform surface (e.g. graphite/Kr); also type VI is not very frequent.

## 2.4 Effect of confinement on water

It is reasonable to wonder if and how confinement in narrow pores can affect water properties due to the interaction of water with the pore walls. Generally, confinement significantly influences phase transitions (gas/liquid and liquid/solid) and might modify water structure and dynamic with respect to the bulk, as discussed hereunder.

### 2.4.1 Freezing and melting under confinement

The outstanding advantage related to restricting water to tiny volumes has been hinted at the opening of the present chapter: confinement allows to decrease the melting temperature of water well below  $T_H$ , as it reduces the extent of the hydrogen bonded network [172] preserving the key tetrahedral local geometry (see section 2.4.2). The possibility to shift the melting temperature below  $T_H$  has paved the way to deal with water's well-known thermal and dynamic anomalies achieving more successful results. Thus it is not surprising that the effect of confinement on freezing and melting has stimulated plenty of works and discussions (see, for instance, [173] and references therein).

The shift of the phase transition temperature for the coexistence of solid and liquid phases in cylindrical pores of radius  $R$  is usually described by the Gibbs-Thomson equation [174]:

$$\Delta T_p(R) = T_0 - T_p(R) = \frac{C_{GT}}{R} \text{ with } C_{GT} = \frac{2T_0(\sigma_{ws} - \sigma_{wl})v}{\Delta h_{SL}} = \frac{2T_0\sigma_{SL} \cos(\theta)}{\Delta h_{SL}} \quad (2.19)$$

where  $T_0$  and  $T_p$  denote the melting temperatures in bulk and in the pore, respectively, and  $C_{GT}$  is the Gibbs-Thomson constant, depending on the surface free energies per unit area of the wall/solid ( $\sigma_{ws}$ ) and wall/liquid ( $\sigma_{wl}$ ) interfaces, the melting enthalpy ( $\Delta h_{SL}$ ) and the volume of the system ( $v$ , in its liquid or solid phase, depending on which has the lower free energy against the walls). As shown in eq.2.19, by using Young's equation  $C_{GT}$  can also be rewritten as a function of the interfacial free energy (interfacial tension) ice/water  $\sigma_{SL}$  and the contact angle  $\theta$ . The main information implied by eq.2.19 is that the smaller is the pore size, the lower is the freezing point of confined water, and thus the wider is the temperature interval over which supercooled water can be observed in its liquid form. This is true provided that the nanometric pore volume is not too narrow: in such a case supercooled water does not freeze at all [175–177].

Eq.2.19 does not take into account the wall pores effects to an extent suitable to describe the main consequences of interaction of water with the substrate. In fact, several studies employing a wide range of experimental techniques (e.g. vapour pressure measurements, NMR spectroscopy, dilatometry, calorimetry, neutron diffraction, small-angle and quasi-elastic neutron scattering) have pointed out the existence of a thin liquid-like layer of non-freezable water in contact with the hydrophilic pore walls [174, 178, 179]. This is often indicated as a boundary *premelted layer* (complete wetting case), with a thickness nearly independent of the pore size [174, 177, 179]. It starts to form at the solid/wall interface well below  $T_p$  and encompasses a fraction of water molecules that increases as the pore width is reduced. Water molecules situated in such a layer in contact with the pore wall remain in a state of lower mobility, up to temperatures above  $T_m$ , as evidenced by NMR cryoporometry experiments [174, 180] and ultrafast infrared polarization- and wavelength-selective pump-probe experiments [179]. This boundary layer is said to be non-freezable because, by lowering temperature below the freezing point, it does not assume the regular structure of ice. This may be due to water interaction with pore walls, even if the hypothesis of incommensurability of the crystal structure with that of the wall surface seems to be more plausible.

As a result, there are two types of water inside the pore: *free*<sup>6</sup> water in the middle of the pore, whose freezing and melting temperature is depressed with respect to the bulk, and *bound* interfacial water, confined between the surface of the pore wall and the frozen phase of the free water, that remains amorphous for all temperatures and physically acts as part of the pore wall [174, 177] (see fig.2.3, left panel). This finding requires to modify the actual pore radius rewriting eq.2.19 as follows:

$$\Delta T_p(R) = \frac{C}{R - \lambda} \quad (2.20)$$

that accounts for the dependence of the depression of the melting (and freezing) point on the thickness  $\lambda$  of the liquid-like layer at the pore/wall interface. Eq.2.20 is addressed in literature as the modified Gibbs–Thomson equation. It means that the radius of ice crystals in the pores is not  $R$  but  $R' = R - \lambda$ , where  $\lambda$  has been found to measure less than 1 nm [174, 175, 177, 181, 182], corresponding to one or two monolayers of water molecules. This simple approach provides reliable results over a temperature range of more than 50 K, with no need to take into account the temperature dependence of the thermodynamic quantities appearing in the definition of  $C_{GT}$ . We note that in the case of hydrophobic surface, the

<sup>6</sup>The water in the middle of the pore (not adjacent to the wall) is called *free* hereafter, in order to distinguish it from the bound non-freezable layer. However this does not have to get confused: water labelled as free is not bulk water, but always interpreted as confined into the pores.

non-freezable layer is superseded by a “void” layer due to repulsive interactions between water molecules and pore surface [183–185]. Thus, despite the physical and chemical details are completely different, the description given by eq.2.20 can be thought to be still valid.

Usually the melting and freezing temperatures ( $T_m$  and  $T_f$ , respectively) are not equal: the non-vanishing difference between them is usually referred to as thermal hysteresis, which is a signature of first-order phase transitions. The cause of this phenomenon is a matter of controversy [174]: for some materials it can be ascribed to a free-energy barrier between the metastable liquid and the ice inside the pore, or to pore-blocking effects on penetration of a solid front into the pores (the solid front can penetrate the pore only at a temperature somewhat below  $T_m$  for a given pore size). What is undoubtedly accepted is that hysteresis is markedly affected by the pore size: it is negligible in smaller pores and becomes remarkable in larger pores [174, 175].

Eq.2.20 conveniently describes the melting point depression as a function of the pore size, but its validity holds only until the pore diameter becomes too small [174, 177, 181]. It has been found that porous materials have a critical pore size  $D^*$  below which the melting and freezing of water as a first-order phase transition disappear. For example, the limiting pore diameter for MCM-41 is  $D^* \approx 2.9$  nm, as determined by [174]. The vanishing of the first-order phase transition at a specific pore size is believed to arise from the concurrence of two effects: increasing disorder in the ice phase as the pore size becomes narrower, and increasing short-range order in liquid water at the low-temperatures that can be reached inside very small pores [174]. As a result, the local structure of ice and liquid water in the pores becomes more and more similar as the pore size decreases, leading to the suppression of the thermal hysteresis. From a simple structural interpretation, we can argue that freezing does not occur when the pore volume becomes so small that it is not sufficiently large to accommodate the minimum size of stable nucleus and develop the long-range ice-like order [186].

### Hexagonal or cubic ice?

First hints about the appearance of cubic ice  $I_c$  in confined environments, instead of hexagonal ice  $I_h$  commonly observed in bulk samples, have been promoted since the early 1990s [154]. However, clear clues about the process of ice nucleation under confinement and the relative ice structure have been gained only in recent years. As seen above, it has emerged that nucleation is a size-dependent process. From this viewpoint, by studying water confined in nanoporous alumina (AAO) with pores of different diameters, a transition from heterogeneous nucleation of hexagonal ice  $I_h$  in larger pores to homogeneous nucleation of cubic ice  $I_c$  in smaller pores has been observed [152]. This result clearly suggests that confinement strongly influences the nucleation process, affecting the crystal structure (also introducing defects and disorder) as discussed in the following. This is probably due to the role played by the pore curvature in suppressing crystallization and to the simple fact that heterogeneous nucleation becomes less favoured as the pore size becomes smaller since impurities and heterogeneities are naturally excluded from the narrower environments. Interestingly, neutron and X-ray diffraction studies have revealed that nucleation in narrow pores leads the free water to transform in a defective form of ice  $I$ , that is predominantly cubic instead of hexagonal [91, 187–189]. This  $I$  form obtained upon confinement is not metastable to  $I_h$ , as observed in bulk water; it is rather a thermodynamically stable phase,

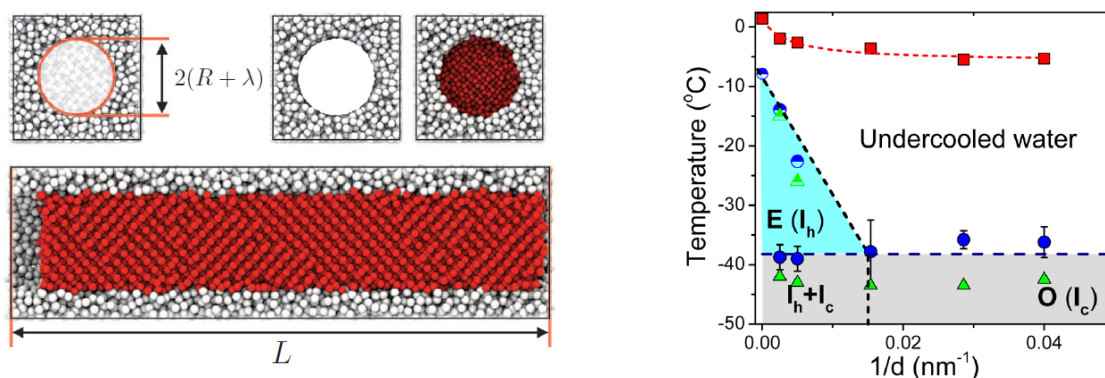


Figure 2.3: Left: Molecular simulation of water (red particles) confined within a nanopore of length  $L$ , radius  $R + \lambda$  and a disordered hydrophilic surface that mimic silica in the matrix named MCM-41.  $\lambda$  is the thickness of an amorphous water monolayer in contact with the pore inner surface (figure from [178]). Right: Phase diagram of water confined within self-ordered alumina nanopores (AAO), as depicted by [182]. The squares represent the melting temperature as a function of the inverse of the pore diameter, with the superimposition of a fit (red-dashed line) obtained using the modified Gibbs-Thomson equation. The half-filled and fully-filled circles indicate the heterogeneous and homogeneous nucleation, respectively, as obtained by dielectric spectroscopy. The corresponding triangular symbols (half-filled and full-filled) represent the same phenomena, but the respective transition temperatures are obtained from DSC.  $I_h$  is hexagonal ice,  $I_c$  predominantly cubic ice,  $I_h + I_c$  predominantly hexagonal ice, whereas  $E$  and  $O$  represent area of ice formation via heterogeneous and homogeneous nucleation, respectively.

persisting up to the melting point. The stabilization of cubic ice  $I_c$  under strong confinement makes easier to study supercooled water dynamics with no strict need for increasing pressure. More precisely, it has been found [94, 117, 187] that crystallization starts from a cluster of hydrogen-bonded molecules with no defined lattice planes. As far as the cluster grows up, a competition between the different growth axis emerges, resulting in no regular formation of hexagonal  $[\text{ABABAC}]_{\infty}$ <sup>7</sup> or cubic  $[\text{ABCABC}]_{\infty}$ <sup>8</sup> lattice planes, but a big concentration of stacking faults is shown. The resulting crystal structure appears to be hybrid with both cubic and hexagonal characteristics (see fig.2.3, right panel). This is a very general behaviour, even though detailed features are obviously influenced by pore size and shape, filling factor and thermal history [187].

Admittedly, the true cubic structure of ice  $I_c$  has been questioned also in the case of bulk water [91, 94, 190, 191]. In recent years several microscopic and computational data, supported by experimental diffraction patterns, have compellingly shown that ice which crystallizes from supercooled water has neither a purely cubic nor hexagonal structure, but is composed of randomly stacked layers of cubic and hexagonal sequences (fig.2.4). In literature it is usually referred to as *stacking-disordered ice I* [94]. Such an ice structure is only ordered in two dimensions (rather than three, as all purely crystalline solids), while it remains disordered along the direction of stacking of oxygen atom layers. As a consequence, differently from pure  $I_h$  and  $I_c$ , stacking disordered ice  $I$  is unlikely in the formation of macroscopic

<sup>7</sup>Ideal ice  $I_h$  is made of a regular hexagonally symmetric stacking of these building blocks, with a building block at the midpoint of a H-bond along the hexagonal  $c$  axis.

<sup>8</sup>Ideal ice  $I_c$  results from the stacking of these building blocks (with each block made of two H-bonded water molecules) centered at the midpoint of a H-bond along a cubic (111) direction.

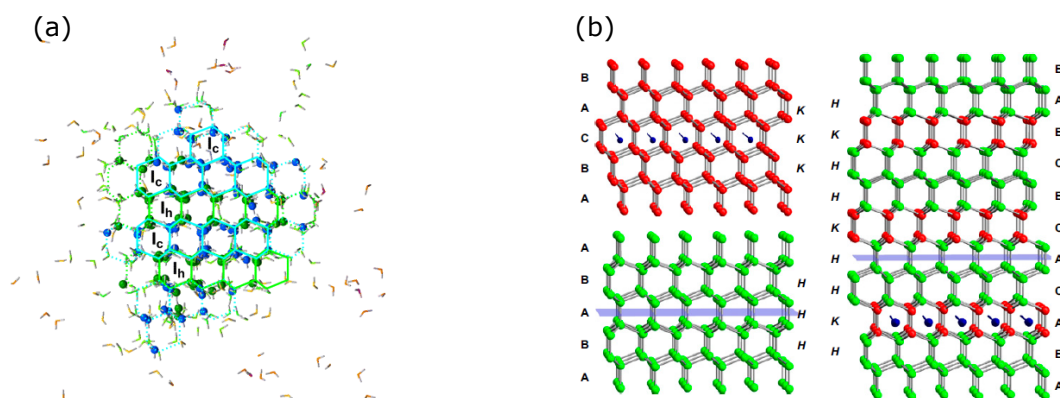


Figure 2.4: (a) Snapshot of ice crystal structure at 220 K as observed in Monte Carlo molecular simulations (figure from [91]). O atoms in the ice  $I_h$  environment are green, and those in the ice  $I_c$  configuration are blue. The spheres represent oxygen atoms involved in a well-ordered structure, whereas sticks indicate less correlated molecules. Dotted lines symbolize parts of the structure under development. (b) On the left side sequences of cubic (red) and hexagonal (green) ice with a regular (fault-free) structure are visible; only the oxygen atoms, connected by HBs, are shown. As indicated, there is an inversion center in the case of ice  $I_c$  and a horizontal mirror plane in the case of ice  $I_h$ . On the right side an example of a stacking-disordered arrangement is displayed: each layer formed by pairs of H-bonded water molecules have either a local mirror symmetry (H stacking, green atoms) or a local inversion center (K stacking, red atoms) (figure from [94]).

three-dimensional crystals of a distinct shape. Further confirmations of the structure of ice phases nucleating within a restricted geometry have been also provided by recent simulation works [192–194]. Leoni and Franzese, for instance, have performed a series of computer simulations on a water-like fluid confined in a slit pore with hydrophobic and hydrophilic walls, finding a clear layering effect in the density distribution between the walls [193, 194]. Moreover they have revealed that the fluid has an inhomogeneous structure because of the interaction with the walls, which induce the fluid to crystallize in mixed ice forms, often defective, distinctly different from a pure hexagonal or cubic lattice [193].

## 2.4.2 Structure and dynamics under confinement

Plenty of experimental and numerical studies have clearly confirmed that the properties of confined (interfacial) water significantly differ from those of bulk water [148, 195, 196]. However, interest residing in gaining even more and new insights into water's properties under confinement is not limited to the study of the depression of the melting point and the determination of the structure of the corresponding ice phases. On the contrary, throughout the years, extensive studies have been performed in order to reveal the microscopic structure and dynamics of liquid supercooled water in confined geometries, exploiting computer simulations and different experimental techniques, including IR and NMR spectroscopy, neutron scattering, dielectric spectroscopy and water sorption experiments [139, 144, 145, 147, 154, 161, 176, 180, 197–201].

The problem is that the interpretation of data aimed at the structural and dynamical characterization of a confined fluid is complicated by topological and chemical effects induced by the substrate, absent in bulk systems. Luckily the effects due to geometrical constraints can be handled by using highly ordered materials (e.g. MCM-41), with a well defined and controllable structure. The interaction between the fluid and the confining substrate is, by contrast, not so easily predictable without specific investigations, remaining one of the main problems to deal with in inspecting confined water.

### Structural modifications

What clearly emerges from various neutron scattering experiments probing water in mesoporous materials is that the microscopic structure of water under confinement is affected by its interaction with the substrate [151, 202, 203].

Let us consider silica matrices as a case study. First of all, strong water–substrate interactions, due to water–silica H–bonds, lead water molecules not to homogeneously occupy the whole available volume. Consequently, not only the average density of confined water results to be lower than in the bulk but, more importantly, density profile of water across the confining volume is not uniform and a density distribution can be observed along the radial and axial dimensions of the pore [151, 203]. In particular, water molecules are attracted towards the hydrophilic pore walls, thus a layer of denser water wets the silica surface, while a depletion of water molecules appears at the pore center. In addition, the density profile does not go abruptly to zero as the distance from the centre is equal to the pore radius [202]; this suggests that some water molecules may even penetrate into small pockets situated nearby the inner surface (fig.2.5(a)). Moreover, the water density distribution is temperature–dependent [203]: water molecules tend to occupy the pore volume more uniformly as temperature is lowered (fig.2.5(b)). Inhomogeneities are not peculiar to hydrophilic nanometric substrates, but may characterize also hydrophobic confining media. Indeed, many simulations have shown that by varying the strength of the interaction between water and substrate, the cohesion between water molecules could break with the formation of voids in the inner part of the pore in the case of hydrophilic walls; otherwise, if walls are hydrophobic, empty regions can form at the water–substrate interface [204]. These general findings imply that the structure of confined water is always neither homogeneous nor invariant under translations, even though homogeneity and translational symmetry have very often been assumed in numerous studies [195].

The density fluctuations (also known as “cohesive failure” effect) here discussed, due to interaction of water with the substrate (at least for hydrophilic walls), highlight changes in water molecular configurations [154, 202]. Whilst in the inner region of the pore volume water might recover a tetrahedral coordination, typical of bulk water, the structure of the interfacial water turns out to be significantly distorted compared to that of bulk water at the same temperature and pressure conditions, with a loss of order over the medium range [151, 195, 202]. Moreover, as the temperature decreases, the overall structure of water network becomes more tetrahedral with respect to ambient conditions [203]. Remarkably, this process of breaking of hydrogen bonds in confined water linked to the interaction of the first water layers with the confining surface would increase the entropy of the liquid compared to the bulk [149]. This may represent a significant factor for explaining the mechanism behind the possibility to obtain supercooled water under confinement over a wider temperature range. Finally, as long as the structure of water in confined environments is investigated by scattering experiments, an ever occurring phenomenon is the *pore size broadening*: the smaller the

pore, the broader the Bragg peaks [195]. As a consequence, the structure factor of a confined system can not be directly compared with that of the corresponding bulk phase whether the spatial constraints are not properly taken into account.

As a matter of fact, these results appear to be a common feature to all experiments and simulations, disregarding the specific structural and chemical characteristics of the confining medium (porous materials, emulsions, colloidal suspensions). Nevertheless, the degree of distortion of the hydrogen bond network on average depends on the particular confining geometry and the size of confinement [148], proving that the extent of the modifications affecting water structure originates from a complex interplay between water–substrate interaction forces and pore size.

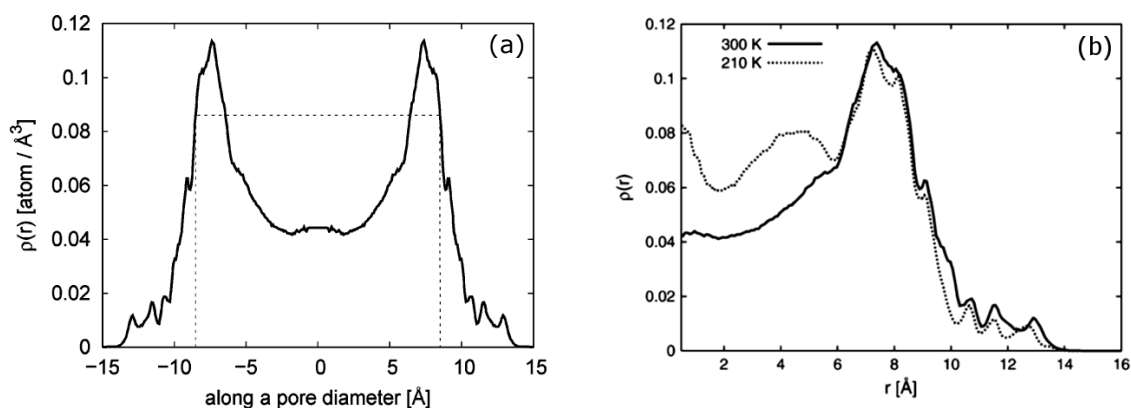


Figure 2.5: (a) Density profile,  $\rho(r)$ , of water confined in cylindrical pores, projected along the radial direction with respect to pore axis (solid line). The position  $r = 0$  corresponds to the pore center. The dashed lines delimit the density profile that would be obtained if water molecules were uniformly distributed in a pore of radius 8.5 Å [202]. (b) Density profile of water in conditions similar to those shown in (a); because of the symmetry with respect to the pore centre, only the density profile for positive values of  $r$  is shown. Solid line is referred to data at ambient temperature (300 K), dashed line is relative to deeply supercooled water (210 K) [203].

## Dynamic behaviour

As already mentioned in this section, in restricted environments water is subjected to both chemical and physical constraints. The former arise from the interaction forces established by water with the substrate molecules, the latter are due to the bare geometric confinement. Obviously this does not impact only the water structure, but also its dynamic behaviour. More specifically, the first effect that has been evidenced is a noticeable slowing down of the translational and rotational motion of water molecules upon confinement [161, 199].

Let us focus our attention on hydrophilic substrates. As a matter of fact, starting from ambient conditions and lowering the temperature, diffusion becomes progressively hindered because of confinement: on the one hand this is due to the favoured close interactions of interfacial water molecules with the pore wall, but on the other hand it is also the result of the roughness of the pore surface and in particular of the entrapment of water inside the small cavities of the pore wall [201]. To what extent translational and rotational motion are affected by confinement depends on the pore size, the pore surface composition [144, 205], and the

hydration level<sup>9</sup> [206]. More specifically, Quasi-Elastic Neutron Scattering (QENS) measurements have allowed to establish that a tighter confinement leads to a slower dynamics [144, 199, 206–208], and this result can be generalized to a large number of confining geometries. Thus, a smaller pore diameter yields an increasing fraction ( $\phi$ ) of water molecules influenced by the surface or the pore walls calculated with respect to the total number of water molecules under confinement; the bigger is  $\phi$  (or the lower the temperature), the slower the dynamics becomes as a more important fraction of water molecules are localized and cannot freely explore the volume surrounding them, causing the translational diffusion coefficient to be smaller. For example, in order to give some quantitative references, the self-diffusion coefficient of water protons in porous silica, determined by QENS experiments, has been shown to be slower by a factor of two in smaller pores (3.0 nm in radius) than in bigger ones (radius of 10.0 nm); in the latter case motion better resembles that of bulk water [144]. More recently similar results have also been pointed out by Osti and co-workers in their survey on the translational diffusion of water in different restricted environments [206], aimed to rationalize the impact of pore size and temperature on water dynamics. These authors have found that the smaller the pore size or the lower the temperature, the slower the dynamics becomes. Moreover, they have put in evidence that the dimensionality (1D, 2D or 3D) of the confining environment is another parameter that greatly affects water mobility.

So far the influence of confinement on diffusional dynamics of supercooled and interfacial water has been successfully described by means of the Relaxing Cage Model (RCM) [209]. The main idea at the basis of RCM is borrowed from Mode Coupling Theory (MCT): supercooled and interfacial water are characterized by a reduced thermal energy and by the formation of a more rigid H-bond cage around each water molecule; this implies that a molecule cannot freely move across the confining volume, but is able to translate only by rearranging the position of a certain number of molecules around it. As a result, water diffusion appears to be strongly coupled and influenced by the local structure and the structural relaxation of the system.

An extremely important result concerns the identification of a cuspid-like fragile-to-strong dynamic crossover (FSC) for water confined in the silica matrix MCM-41. As discussed in chapter 1, such a crossover should mark the transition of the water local structure from a mainly high-density liquid (HDL) to a low-density liquid (LDL), and is accounted for one of the strongest evidence of the existence of a second critical point. Chen and co-workers [128] have performed several investigations on deeply supercooled water confined in nanoporous silica matrices by using quasi-elastic and inelastic neutron scattering. They have extracted the translational relaxation time  $\tau_T$  from neutron data at different pore sizes and pressures. At high temperature  $\tau_T$  follows a VFT function, whereas at lower temperatures it is well fitted by an Arrhenius law. The crossover temperature  $T_L$  is around 225 K, and does not significantly change within error bars for different pore size samples. This is a very interesting result, suggesting that, when the confinement is sufficiently small (pore size  $< 1.8$  nm), the FSC temperature is size-independent. In other words, this means that the FSC appears to be a universal property of supercooled water, provided that the confinement length scale is of the order of nanometer.

The same temperature dependence, with a crossover temperature between 207 and 225 K, has been observed by varying pressure from ambient up to  $\sim 1.5$  kbar [128]. More precisely, the crossover temperature  $T_L$  has been shown to steadily decrease when pressure is increased up to 1.6 kbar, until it encounters the homogeneous nucleation temperature of

<sup>9</sup>The hydration level can be defined as the fractional mass of water uptake per mass of sample:  $h = m_{\text{water}}/m_{\text{dry sample}}$ . This is the definition we will adopt hereafter.

bulk water at that pressure. Above 1.6 kbar, it is no longer possible to recognize the characteristic feature of FSC. This outcome is of particular relevance because the existence of the FSC is linked to the predicted first-order liquid-liquid coexistence line and its end point, the second critical point [17]. More specifically, the FSC should occur as the Widom line is crossed. As introduced in section 1.4.3 and according to [132], the Widom line is an imaginary line in the  $P$ – $T$  plane where many thermodynamic quantities and transport coefficient show a peak when crossing it at a constant pressure. The Widom line should originate from the low temperature critical point ( $P_C, T_C$ ) and extend into the one-phase region, with the same slope as that of the liquid–liquid coexistence line at ( $P_C, T_C$ ). Consequently, what is expected is that moving along the Widom line by increasing pressure, the hypothesized second critical point should be approached. Indeed the idea is that the end point of the Widom line may anticipate the second critical point of water in its metastable phase diagram [128, 210] (fig.2.6).

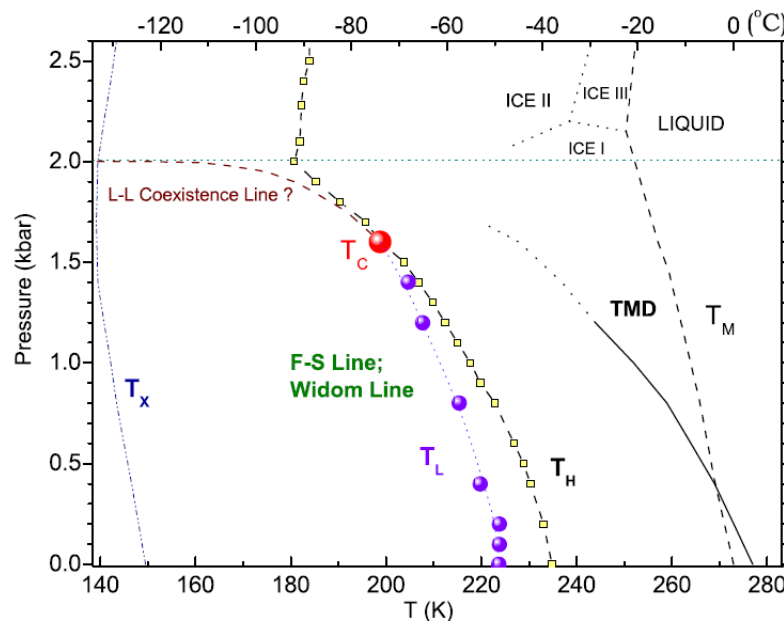


Figure 2.6: The fragile-to-strong crossover temperature,  $T_L$  (solid circles), plotted as a function of pressure in a  $(P, T)$  plane. The homogeneous nucleation temperature line of bulk water, denoted as  $T_H$ , is also shown. In addition, the crystallization temperatures of amorphous solid water,  $T_X$ , and the temperature of maximum density line,  $TMD$ , are reported (figure from [210]).

### 2.4.3 From confined to bulk water: does it make sense?

In the present section has come to light that interfacial and confined water present clearly different properties compared to bulk water, encompassing both structure and dynamics. Hence the claim to extend findings relative to confined water to deduce something about bulk water deserves some comments and caution. In order to get an idea about this issue, it can be helpful to summarize what has been discussed in the previous sections.

First of all, we have seen that regarding confined and bulk water as the same system could be quite misleading since materials in restricted volumes may exhibit a different physical

behaviour with respect to bulk, with the emergence of new phase transitions or new location of the phase transitions in the phase diagram.

Furthermore, as far as microscopic structure is concerned, bulk supercooled water and water under confinement cannot be considered the same liquid, even if some similarities may be found at a local scale. Nonetheless the overall structure of the two liquids shows relevant differences in the coordination number (number of H-bonds per water molecule) and in the interstitial water molecules, that are severely reduced under confinement. In addition the extended HB network appears to be more distorted, with a loss of order over the medium range and a transition from a more ordered to a more disordered configuration as temperature is lowered.

Another relevant feature being worth mentioning is that confined supercooled water is an inhomogeneous system, regardless of the hydrophilic or the hydrophobic character of the interaction of water molecules with the confining surface. Some authors also claim that the traditional distinction between the inner free (unperturbed) water and the bounded (perturbed) water close to the surface, is even too simplified and a layer-by-layer description should be more adequate [195]. These observations suggest that confined water needs to be specifically treated in order to account for the lack of isotropy and translational symmetry with respect to the bulk case.

The observations arising from all these outcomes make clear that an accurate determination of the microscopic structure and dynamics of confined water assumes a relevant role if one wants to answer the question about differences and similarities between bulk and confined water. However, whether information on confined water can be used to extrapolate properties of supercooled bulk water in the *No man's land* remains a matter of debate.

## 2.5 MCM-41

Among the various confining systems, we focus our attention on the silica matrix named MCM-41. In the following a brief description of the main structural properties of such a medium is reported, in order to explain why literature describes it as one of the best material to perform studies in restricted environments [28, 202, 211].

MCM-41 is a mesoporous silicate<sup>10</sup> material, often presented as an excellent molecular sieve because of its very regular and ordered structure. MCM is an acronymous standing for "Mobile Composition of Matter". In particular, MCM-41 has attracted great attention and it is often regarded as the most suitable model adsorbent mesoporous system currently available. Being an excellent model medium, it allows the best comparison between experiments and Molecular Dynamics (MD) simulations. The distinctive features making MCM-41 so unique are to be essentially sought in its very regular and relatively simple structure. Indeed it consists of an array of uniform hexagonal channels of tunable and quite monodispersed size (ranging from 2 to 10 nm), arranged in a honeycomb type lattice (fig.2.7). In addition the pore size distribution is very narrow and the length is significantly greater than the pore diameter, so that it becomes reasonable to study it as a 1D or 2D system. Then the absence of pore channel intersections ensures pore-networking effects (likely responsible for the hysteresis frequently observed in the conventional mesoporous systems) are negligible

<sup>10</sup>The term *silica* is generally used to refer to the silicon dioxide, SiO<sub>2</sub>, in its various forms, including crystalline, amorphous, hydrated and hydroxylated ones.

[175]. These properties explain why MCM-41, since its discovery, has been immediately preferred to Vycor glass, another conventional porous material largely employed as confining medium [149]. In fact Vycor exhibits bigger pores and a rather wide distribution of pore sizes and shapes, with a significant pore connectivity, which may lead to blurring in the interpretation of the experimental results.

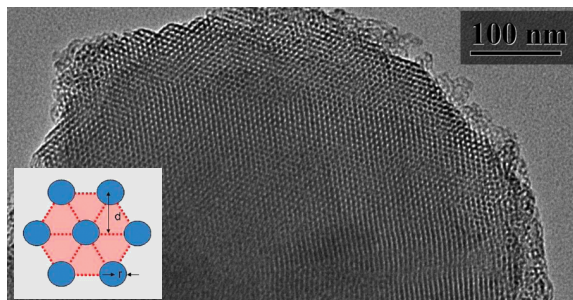


Figure 2.7: TEM image of MCM-41 produced by ACS Material (<http://www.acsmaterial.com>). The inset on the lower left displays a schematic representation of the MCM-41 honeycomb lattice: the blue circles are the pores,  $r$  indicates the pore radius and  $d$  the interplanar distance [202].

The main advantages of MCM-41, compared to other substrates, are that it guarantees a relative ease of synthesis and modelling, it does not swell upon hydration and the hexagonal array of cylinders produces a well-defined and well-identifiable Bragg peaks both in Small Angle Neutron Scattering (SANS) and neutron diffraction experiments over the wide range of exchanged momentum accessible on instruments currently available at the European facilities (e.g. ISIS, ESRF, SOLEIL, ILL).

MCM-41 belongs to the family named M41S, classified into three main groups with well defined ordered mesostructures:

- MCM-41, with a hexagonal array of unidirectional and non-interconnecting pores;
- MCM-48, with three-dimensional cubic pore structure;
- MCM-50, with a lamellar (but unstable) structure.

MCM-41 is by far the most studied member of M41S family. Beside its highly regular and ordered structure with tunable pore diameter, MCM-41 is appreciated also for large pore volumes, hydrocarbon sorption capacities, high BET surface areas (in the range 600 – 1300 m<sup>2</sup>/g), high thermal and mechanical stability, and hydrophilicity of the inner pore walls.

### 2.5.1 Synthesis of MCM-41

MCM-41 and its promising features are one of the most successful examples of the great effort dedicated to the fabrication of ever new materials with tailored properties suitable for specific applications, extending from pure science to geology, environmental and food technology, biotechnology, chemical and construction industries.

Since its original discovery, a variety of synthesis routes have been attempted for MCM-41 type materials. In particular, three different molecular mechanisms have been proposed

in order to explain the formation of the nanosized mesopore structures [31]: *i*) the liquid-crystal templating (LCT), where an organic species acts as a central structure surrounded by inorganic oxides forming a framework, *ii*) the self-assembly mechanism, *iii*) the cooperative self-assembly mechanism.

Regardless the particular strategy adopted, basically a typical synthesis requires a minimum of four reagents: a silica precursor, a solvent (water and/or ethanol), an ionic or non-charged surfactant acting as a *templating agent*, whose chain length determines the pore size of the porous matrix, and a catalyst [211].

We will give some more details about the former mechanism (LCT), being it presented in literature as the most likely responsible for the mesoporous structure formation in the case of an ionic surfactant. As discussed in the experimental section (section 5.2), the MCM-41 silica matrix used as confining medium in our experiments has indeed been synthesized by following this route.

As depicted in fig.2.8, in the LCT process the large hydrophobic alkyl chains of the surfactant cause the template ions to aggregate together in order to minimize the energetically unfavourable interactions between apolar chains and the polar solvent. The resulting aggregates are called *micelles*, and have a spheric shape with a hydrophobic core containing the large alkyl chains of the surfactant. This is what is regarded as liquid-crystal phase. Increasing the amount of template, the spherical micelles gradually evolve to long tubes (rod-like micelles); increasing further, the rod-like micelles aggregate into hexagonal liquid-crystalline units. Silicate species deposit between surfactant rods, condensing into an inorganic network with hexagonal ordering stabilized by the electrostatic interaction between surfactant molecules and silicate species. This engenders the formation of the basic framework of MCM, resembling the MCM-41 structure. If the template concentration is further increased, this hexagonal liquid crystal phase first transforms into a cubic liquid crystalline phase (MCM-48) and then, at higher concentration, to a lamellar liquid crystalline phase (MCM-50). The template can be removed by repeatedly washing the material with de-ionized water and by calcination at high temperature (500 – 600° C).

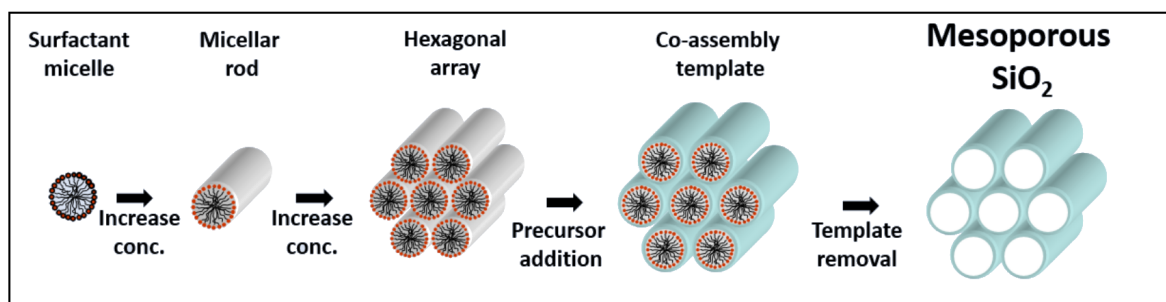


Figure 2.8: Sketch of the synthesis pathway of MCM-41 via the liquid-crystal templating (LCT) mechanism. The reaction starts with the formation of single spherical micelles evolving in rod-like aggregates, further arranging in a network of regular arrays of hexagonal ordering. The template is finally removed by calcination (“Mesoporous Materials for Energy Storage”, teaching material by John To, Stanford University).

During the synthesis, silanol groups (SiOH) are formed, due to hydrolysis reaction with water and humid atmosphere. Silanols bind to the inner surface of MCM-41 and are responsible for the highly hydrophilic character of this kind of substrates. When water is introduced into the pores, it firstly attaches to the hydration sites offered by silanol groups via hydrogen bonds, until all adsorption sites are occupied and hydrogen-bonded clusters of water

molecules may start to form, binding to the previously adsorbed water layer. Density of water in this first layer adjacent to the pore wall is determined by the density and orientation of silanol groups [174]. The density of silanol groups on the pore surface of MCM-41 varies with the template removal method, and ranges between 2.5 and 5 silanol groups  $\text{nm}^{-2}$ . Silanol groups play an important role in various behaviours of water in porous silica as they are the main responsible for the water-pore wall interactions altering water structure and dynamics. Moreover they are also suitable for chemical bonding with other inorganic species or organic ligands, making relatively easy to modify the inner surface of MCM-41. Another strategy to change the surface properties of MCM-41 materials is by introduction of heteroatoms such as boron, titanium, vanadium, and gallium [30].

Parameters involved in and influencing the reaction of formation of MCM-41 are multiple, such as temperature, solvent, pH, stirring rates, silica precursor. In particular, the surfactant composition and its concentration (silicate:surfactant ratio) have been found to play a major role in controlling the final shape, size and inner structure of the porous material [31]. From this point of view, computer simulations can offer an important and useful instrument for rapidly screening and tuning large sets of candidate materials with different properties (pore radius, wall thickness, surface structure and chemistry) and selecting those that seem more promising for a further experimental synthesis and test. This is an obviously cost- and time-saving strategy. The problem is that a reliable atomic model of MCM-41 is needed for such a purpose, but, although the MCM-41 structure results to be well-known at the mesoscale, information available at the nanoscale are not sufficiently accurate. Uncertainties remain over the thickness of the pore walls, their degree of structural order (whether they are completely amorphous or partially crystalline), the surface roughness, the possible presence of surface irregularities and micropores. This has given rise to the development of a plethora of computational models, more or less complex, aimed to achieved an ever better and truthful representation of MCM-41 structure at the atomic scale [150, 212].

# Chapter 3

## Experimental techniques: Neutron scattering

*In one drop of water are found all the secrets of all the oceans; in one aspect of You are found all the aspects of existence.*

*Kahlil Gibran*

Neutron scattering<sup>1</sup> has been used to investigate the structure of our sample (water confined in a mesoporous silica matrix) over a wide range of length scales, in order to capture structural features of both the substrate and the intermolecular water network. This has been possible thanks to NIMROD [213], a new diffractometer installed at the neutron spallation source ISIS (Rutherford Appleton Laboratory, near Oxford, UK) in 2008. It was specifically conceived to cover a very wide range of momentum transfer  $Q$ , ranging from atomic interactions to distances typically explored by small angle scattering techniques.

In this chapter, basics of neutron scattering theory will be given, with reference to an ideal experiment. Then some of the principal aspects that make a real experiment departing from an ideal one will be discussed. Lastly, some space will be devoted to the description of the instrumentation used for performing our experiments.

---

<sup>1</sup>In order to prevent any confusion, we believe it may be useful to specify that, traditionally, in a *scattering* experiment neutrons interacting with sample are collected with a scan both in energy and in momentum transfer  $Q$  (see section 3.1); on the contrary, when we speak about *diffraction*, we mean that outgoing neutrons are collected only as a function of their  $Q$ . Notwithstanding, in the everyday language, these two terms, namely *scattering* and *diffraction*, are often mixed up and used with no particular attention to their original meaning. For this reason, in the following, as far as no particular reference is given, the two terms will be used indifferently as synonyms to indicate, in general terms, any experiment based on the interaction of neutrons with matter over the entire accessible  $Q$  range.

### 3.1 Theoretical background

#### 3.1.1 Basic principles of neutron scattering

A scattering experiment is essentially a collision between a probe particle and a target. In general, collision results in a change both in momentum ( $\mathbf{p}$ ) and energy ( $E$ ) of the probe particle. A scheme of the process is shown in fig.3.1: the incident particle hits the sample with a wavevector  $\mathbf{k}_i$  and frequency  $\omega_i$ , emerging with a final wavevector  $\mathbf{k}_f$  and frequency  $\omega_f$ , where  $|\mathbf{k}| = 2\pi/\lambda$ , being  $\lambda$  the wavelength of the incident beam. We can thus express the *momentum transfer* and the *energy transfer* during the collision process as follows:

$$\mathbf{Q} = \mathbf{k}_i - \mathbf{k}_f \quad (3.1)$$

$$E = \hbar\omega \quad \text{with} \quad \omega = \omega_i - \omega_f \quad (3.2)$$

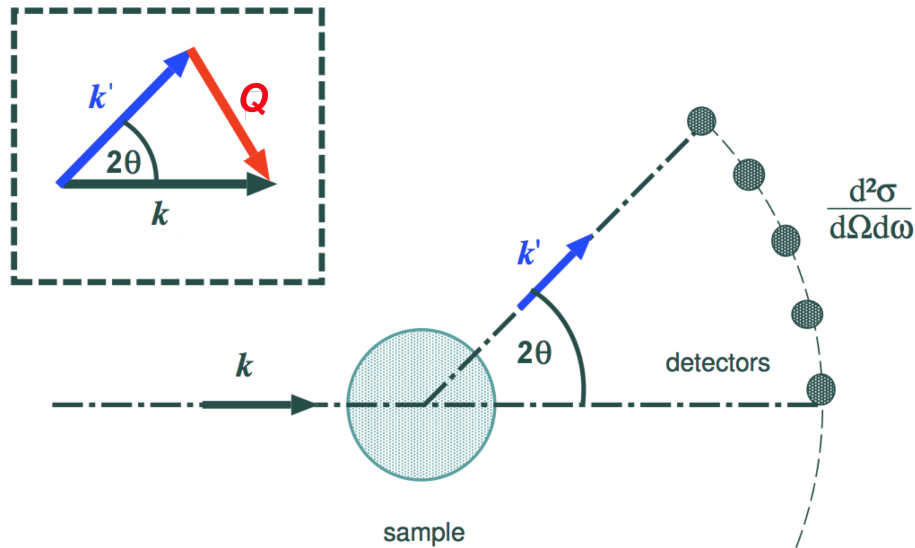


Figure 3.1: Schematic representation of a neutron scattering experiment.

In the case of our experiments the probe was represented by neutrons, subatomic particles whose basic properties are listed in table 3.1. The interest is focused on thermal neutrons (with kinetic energy comparable with thermal) because of their usefulness that comes to light if we look at their energy and wavelength.

Mass	939.57 MeV/c <sup>2</sup>
Charge	0
Spin	1/2
Magnetic dipole moment	-1.913μ <sub>N</sub>

Table 3.1: Basic properties of the neutron. μ<sub>N</sub> is the nuclear magneton.

In fact, bearing in mind that a particle of mass  $m$  and velocity  $v$  (moving in the same direction as the wavevector  $\mathbf{k}$ ) is represented by a plane wave of wavelength  $\lambda$  given by the De Broglie equation  $\lambda = \frac{h}{mv}$ , and reminding that its momentum is  $\mathbf{p} = \hbar\mathbf{k}$ , the relation linking the kinetic energy to the momentum of the incident particle becomes:

$$E = \frac{1}{2}mv^2 = \frac{p^2}{2m} = \frac{\hbar^2 k^2}{2m} \sim k_B T \quad (3.3)$$

After inserting the values of the neutron mass and the other constants in eq.3.3, we obtain:

$$\lambda = \frac{6.283}{k} = \frac{3.956}{v} = \frac{9.045}{\sqrt{E}} \sim \frac{30.81}{\sqrt{T}} \quad (3.4)$$

$$E = 5.227v^2 = \frac{81.81}{\lambda^2} = 2.072 k^2 \sim 0.08617 T \quad (3.5)$$

where  $\lambda$  is in  $\text{\AA}$ ,  $k$  in  $\text{\AA}^{-1}$ ,  $v$  in km/s,  $E$  in meV, and  $T$  in K. Generally, a thermal neutron is characterized by  $E \approx 25$  meV,  $v \approx 20$  km/s and  $\lambda \sim 2$   $\text{\AA}$ .

Hence the main characteristics we can take advantage of in neutron scattering experiments are:

- The mass of a thermal neutron has a De Broglie wavelength of the same order of the interatomic distances in solids and liquids. This allows to exploit the interference phenomenon to yield information about the atomic structure of the system (as well as with X-ray diffraction).
- Since neutrons are uncharged, they are able to deeply penetrate into the sample, interacting with atomic nuclei via nuclear forces (there is no Coulomb repulsion to overcome). More importantly, the dependence of the scattering cross section on the mass number (isotope) is completely random, and this enables to distinguish between different isotopes of the same chemical element, to detect light elements to which X-rays are not sensible due to their low atomic number (e.g. hydrogen), and to discriminate between elements close in the periodic table.
- The energy of thermal neutrons is of the same order as that of many excitations in condensed matter. Measurements of neutron energies in inelastic scattering experiments provide information on dynamics and energy of the excitations, and thus about interatomic forces.
- The neutron has a magnetic moment which allows it to interact with unpaired electrons in magnetic atoms. This feature enables to study both nuclear and magnetic properties of materials.

### 3.1.2 The scattering cross section

In an ideal scattering experiment we want to measure how many neutrons emerge from the sample, with a given momentum transfer and a given energy, with respect to the number of incident neutrons which are assumed to be monochromatic [214]. A scheme of the geometry of a scattering experiment is depicted in fig.3.2. Let us consider a beam of thermal neutrons

with energy  $E_i$ , incident on a target, and a detector that counts how many neutrons have been scattered in a given direction as a function of their energy  $E_f$ . The important requirement is that the detector–target distance is large compared to the dimensions of the target and the detector, so that the small solid angle  $d\Omega$  subtended by the detector at the target is well defined. It is convenient to describe the scattering geometry in terms of polar coordinates  $(r, \theta, \phi)$  with respect to the  $z$  axis which defines the direction of the incident neutron beam. Given these conditions, we can define the *partial differential cross section* as the number of neutrons scattered per second into a small solid angle  $d\Omega(\theta, \phi)$  with final energy between  $E_f$  and  $E_f + dE_f$ , normalized for the incident flux  $\Phi^2$ , and the accepted angular and energy range  $d\Omega$  and  $dE_f$ . If we count the scattered neutrons into the solid angle  $d\theta$  along the direction  $(\theta, \phi)$ , regardless of their energy, we can measure the so-called *differential cross section* (DCS), defined as:

$$\begin{aligned} \frac{d\sigma}{d\Omega} &= \frac{\text{number of neutrons scattered per second into } d\Omega \text{ in direction } (\theta, \phi)}{\Phi^2 d\Omega} = \\ &= \int_0^\infty \frac{d^2\sigma}{d\Omega dE_f} dE_f \end{aligned} \quad (3.6)$$

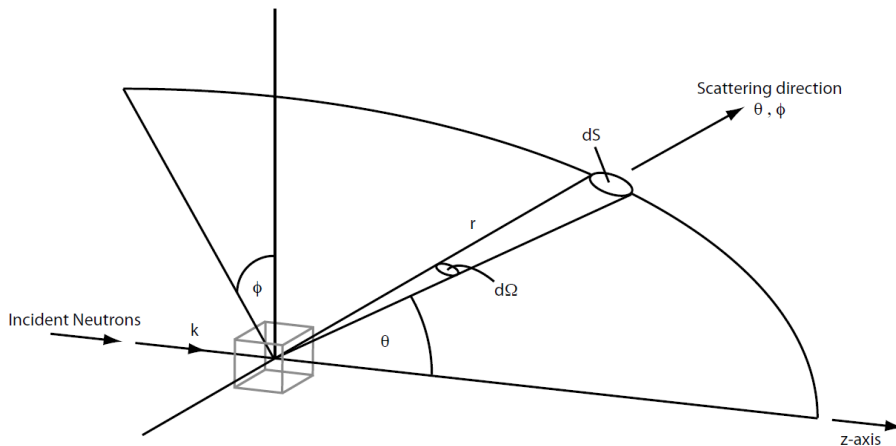


Figure 3.2: Geometry of a typical scattering experiment [214].

Now, if we want to determine the total number of neutrons scattered per second by the sample,  $\sigma_{tot}$ , we just need to integrate the DCS over all the directions, obtaining the *total scattering cross section*. The cross-sections are what we actually measure with experiments and, usually, they are quoted per atom or molecule (the expressions above need to be divided by the number of atoms or molecules in the sample). These physical quantities have to be linked to their corresponding theoretical expressions, in order to understand how they relate to the description of the sample at atomic level.

For the sake of simplicity, it is convenient to start by considering the cross-section of a point scattering center in the Born approximation [215]. The nuclear forces inducing the scattering

<sup>2</sup>The flux of the incident neutrons is defined as the number of neutrons through unit area per second, being the area perpendicular to the direction of the neutron beam.

act over a range of about  $10^{-14} - 10^{-15}$  m, while the wavelength of thermal neutrons is of the order of  $10^{-10}$  m, thus much larger than the range of nuclear forces. This circumstance implies that the entire scattering process can be described in terms of s-waves ( $l = 0$ , with  $l$  the azimuthal quantum number), whose angular scattering distribution is spherically symmetric.

If we assume that the origin is at the position of the nucleus and that the incident neutrons travel along  $\mathbf{k}$ , the monochromatic incident flux can be written as a plane wave:

$$\Psi_i = \exp(i\mathbf{k}_i \cdot \mathbf{r}) \quad (3.7)$$

As the scattering is spherically symmetric, the scattered wave can be described as a spherical wave centred in  $\mathbf{r}'$  with scattering amplitude  $f$ :

$$\Psi_f = \frac{f(\lambda, \theta)}{R} \exp(i\mathbf{k}_f \cdot \mathbf{R}) \quad (3.8)$$

with  $\mathbf{R} = \mathbf{r} - \mathbf{r}'$  the position of the scatterer. The neutron case is straightforward because  $f(\lambda, \theta)$  does not significantly depends on wavelength and scattering angle [215], so that we can write it as a constant, named *scattering length*:

$$f(\lambda, \theta) = -b \quad (3.9)$$

where the minus sign is a matter of convention aimed to have a repulsive interaction potential when  $b$  is positive. The scattering length is a complex number in principle, but its imaginary part is generally negligible, allowing for treating it as a real number. The only exception is represented by nuclei with high absorption coefficient, such as cadmium, gadolinium, boron, whose scattering length varies rapidly with neutron energy and can give rise to *resonance* phenomena. The scattering length of a specific atom is influenced by the coupling of angular momentum of nucleus and that of neutrons and by the corresponding multiplicity.

If  $v$  is the neutron velocity, the number of scattered neutrons passing through the elementary area  $dS$  per second is (see fig.3.2):

$$v dS |\Psi_f|^2 = v dS \frac{b^2}{R^2} = v b^2 d\Omega \quad (3.10)$$

Since the incident flux is  $\Phi = v |\Psi_i|^2 = v$ , the DCS becomes:

$$\frac{d\sigma}{d\Omega} = \frac{v b^2 d\Omega}{\Phi d\Omega} = b^2 \quad (3.11)$$

and, by integrating over the entire solid angle, we obtain the total cross section:

$$\sigma_{tot} = 4\pi b^2 \quad (3.12)$$

A unit commonly used for  $\sigma$  is the barn ( $1 \text{ barn} = 10^{-28} \text{ m}^2$ ).

If we have a nucleus with non-zero spin or a sample containing a natural mixture of isotopes for a given atom, the scattering length is defined by an average value and a standard deviation:  $b = \langle b \rangle \pm \Delta b$ , with  $\Delta b = \sqrt{\langle (b - \langle b \rangle)^2 \rangle} = \sqrt{\langle b^2 \rangle - \langle b \rangle^2}$ . Thus, by rewriting the variance in the form  $\langle b^2 \rangle = \langle b \rangle^2 + (\Delta b)^2$ , the scattering cross-section can be expressed as the sum of two quantities:

$$\sigma_{tot} = 4\pi \langle b^2 \rangle = \sigma_{coh} + \sigma_{inc} \quad (3.13)$$

where  $\sigma_{coh} = 4\pi \langle b \rangle^2$  and  $\sigma_{inc} = 4\pi (\langle b^2 \rangle - \langle b \rangle^2)$ . The coherent and incoherent contributions to the total cross section depend on the specific nucleus we consider and change for different isotopes. One of the most useful example is represented by hydrogen ( $^1\text{H}$ ) and deuterium ( $^2\text{H}$  or D), as reported in table 3.2.

Isotope	$b_{coh}$	$b_{inc}$	$\sigma_{tot}$	$\sigma_{coh}$	$\sigma_{inc}$
H	-3.74	25.27	82.03	1.76	80.26
D	6.67	4.04	7.64	5.59	2.05

Table 3.2: Comparison between the coherent and incoherent scattering lengths ( $b_{coh}$  and  $b_{inc}$ , respectively) and the total, coherent and incoherent cross-sections ( $\sigma_{tot}$ ,  $\sigma_{coh}$  and  $\sigma_{inc}$ , respectively) of two largely used isotopes: hydrogen (H) and deuterium (D). The table clearly shows that hydrogen scatters neutrons mainly incoherently, whereas scattering from deuterium is predominately coherent. Moreover the total cross-section of H is much higher than that of D. All scattering lengths are given in fm, while cross-sections are expressed in barns.

As a handy approximation, we can restrict our treatise to the special case of elastic scattering:  $E = 0$ , i.e. the collision causes no energy exchange being the nucleus fixed at the origin of the coordinates. This is also known as *static approximation* and means that incident and scattered neutrons have the same energy. Such a hypothesis will be taken for granted hereafter and it is at the basis of corrections required at the stage of data analysis. The elastic approximation implies that the amplitude of the wavevector is regarded as constant upon scattering:  $|\mathbf{k}_i| = |\mathbf{k}_f| = 2\pi/\lambda$ , meaning that  $\hbar\omega \ll E_i$ . On the basis of elementary trigonometric considerations (fig.3.1), we can write the intensity of momentum transfer as follows:

$$Q = \frac{4\pi \sin(\theta)}{\lambda} \quad (3.14)$$

where  $2\theta$  is the angle between the incident and scattered wavevector.

Under the hypothesis of elastic scattering, the resultant scattered wave in the more general case of a three-dimensional assembly of nuclei becomes:

$$\Psi_f = - \sum_i \left( \frac{b_i}{r} e^{i\mathbf{k}_f \cdot \mathbf{r}} e^{i\mathbf{Q} \cdot \mathbf{r}} \right) \quad (3.15)$$

where  $\mathbf{Q} = \mathbf{k}_i - \mathbf{k}_f$  is the momentum transfer defined in eq.3.1.

### 3.1.3 The Fermi pseudopotential

Let's start by ignoring the spin of the neutron; in this case, the neutron state is completely defined by its momentum, i.e. by the wavevector. An expression of cross sections in terms of microscopic quantities can be given by using the *Fermi's golden rule*, a fundamental result of first order perturbation theory in quantum-mechanics [216]. Let us consider a neutron with wavevector  $\mathbf{k}_i$  incident on a scattering system in a state characterized by a quantum number  $l$ : the neutron interacts with the system via a potential  $V$  and is scattered with a final wavenumber  $\mathbf{k}_f$ , changing the state of the scattering system from  $l$  to  $l'$ . On the basis of the Fermi's golden rule, the DCS, which is the sum of all processes leading the state of scattering system from  $l$  to  $l'$  and that of neutron from  $\mathbf{k}_i$  to  $\mathbf{k}_f$ , can be evaluated as:

$$\left(\frac{d\sigma}{d\Omega}\right)_{l \rightarrow l'} = \frac{k_f}{k_i} \left(\frac{m}{2\pi\hbar^2}\right)^2 |\langle \mathbf{k}_f l' | V | \mathbf{k}_i l \rangle|^2 \quad (3.16)$$

It is not easy to obtain a theoretical expression for the potential  $V$ , so a heuristic approach results to be more affordable. The unique analytical model that is able to well reproduce the features of a scattering experiment is the *Fermi's pseudopotential*, defined as follows:

$$V(\mathbf{r}) = \frac{2\pi\hbar^2}{m} \sum_{i=1}^N b_i \delta(\mathbf{r} - \mathbf{R}_i) \quad (3.17)$$

where  $b_i$  and  $\mathbf{R}_i$  are the scattering length and the position of the  $i^{\text{th}}$ -nucleus. Eq.3.17 defines a local potential describing the short-range strong interaction between neutrons and nuclei. The physical justification to use a so simplified model relies on the big difference between the range of the nuclear forces driving the interaction ( $\sim 10^{-15}$  m) and the typical wavelength of a thermal neutron ( $\sim 10^{-10}$  m): the neutron-nucleus interaction goes rapidly to zero without extending outside the nucleus dimension and incident neutrons actually see the nucleus as a point.

Inserting the pseudopotential 3.17 into the golden rule and considering the more general case of neutrons scattered by an assembly of nuclei in the static approximation, after some passages [214], the DCS for  $N$  scattering centres results:

$$\left(\frac{d\sigma}{d\Omega}\right) = \overline{\left\langle \left| \sum_{j=1}^N b_j e^{i\mathbf{Q}\cdot\mathbf{r}_j} \right|^2 \right\rangle} = \left\langle \sum_{i,j=1}^N \overline{b_j b_i^*} e^{i\mathbf{Q}\cdot\mathbf{r}_{ij}} \right\rangle \quad (3.18)$$

where it has been assumed that the distance to the detector is much larger than the typical size of the sample, i.e.  $|\mathbf{r} - \mathbf{R}_j| \approx |\mathbf{r}| = r$ , and  $\mathbf{r}_{ij} = \mathbf{r}_i - \mathbf{r}_j$  gives the relative position between the scattering centres  $i$  and  $j$ . Moreover, the horizontal bar indicates the thermal average over the positions of atoms during the experiment, while the  $\langle \rangle$  is an average over the isotope distribution, the orientation of nuclear spins and the scattering lengths  $b_j$ . We note that, despite the perturbation theory holds only in the case of a linear response (weak probe-sample interaction), the results given for neutrons are satisfactory, albeit the interaction is strong. This means that the sample remains weakly perturbed.

### 3.1.4 Coherent and incoherent cross sections

The DCS 3.18 can be written as the sum of two distinct terms [214, 215]:

$$\left(\frac{d\sigma}{d\Omega}\right) = \left(\frac{d\sigma}{d\Omega}\right)_{coh} + \left(\frac{d\sigma}{d\Omega}\right)_{inc} \quad (3.19)$$

where

$$\left(\frac{d\sigma}{d\Omega}\right)_{coh} = \langle b \rangle^2 \left| \sum_{k=1}^N \exp(i \mathbf{Q} \cdot \mathbf{r}_k) \right|^2 \quad (3.20)$$

$$\left(\frac{d\sigma}{d\Omega}\right)_{inc} = N \left( \langle b^2 \rangle - \langle b \rangle^2 \right) \quad (3.21)$$

The coherent scattering results from the interference between the waves scattered by different nuclei and provides information about the structure of the sample. On the other hand, the incoherent scattering is related to the motion of a single particle and describes how a single scattering length  $b_j$  is different from the average; this term originates from the interference of a single wave with itself in two different time instants and is due to the scattering atoms being not perfectly fixed. We can thus interpret the coherent as the “average” contribution (that we would have if the neutron saw the sample as a perfect crystal) and the incoherent as an expression of fluctuations.

### 3.1.5 Correlation functions

The cross section can be related to the thermal average of operators describing the scattering system, which can be expressed in terms of *correlation functions* (CFs). These functions, originally introduced by Van Hove, give insights into the physical meaning of the terms occurring in the scattering cross sections [214]. They take into account only pair-wise interactions (i.e. interactions between any two particles in the system), neglecting correlations of higher orders which introduce terms of interaction between three or more particles. These latter terms are much less relevant for the description of correlations in a fluid system and are even not accessible by conventional scattering techniques.

In particular, the structure of a fluid can be described by means of  $g(\mathbf{r})$ , namely the static Pair Distribution Function (PDF) of the sample<sup>3</sup>. It is an average particle density with respect to any particle at the origin, and represents the quantity that we want to extract from a neutron diffraction experiment. It defines the correlation length of the system and is the Fourier transform of the Static Structure Factor (SSF)  $S(\mathbf{Q})$ , defined as follows:

<sup>3</sup>From a more general point of view, the pair distribution function of a system of  $N$  particles is the second-order correlation function  $g^{(2)}(\mathbf{r}_1, \mathbf{r}_2)$ . If the system consists of spherically symmetric particles (as in our case),  $g^{(2)}(\mathbf{r}_1, \mathbf{r}_2)$  depends only on the relative distance  $\mathbf{r}_{12} = \mathbf{r}_2 - \mathbf{r}_1$  between the couple of particles, hence it is common to write  $g^{(2)}(\mathbf{r}_1, \mathbf{r}_2) = g^{(2)}(\mathbf{r}_{12}) \equiv g(\mathbf{r})$

$$\begin{aligned}
S(\mathbf{Q}) &= \frac{1}{N} \left\langle \sum_{i,j}^N \exp(i\mathbf{Q} \cdot \mathbf{r}_{ij}) \right\rangle = \\
&= \int_{-\infty}^{\infty} S(Q, \omega) d\omega = 1 + \rho \int \exp(i\mathbf{Q} \cdot \mathbf{r}) [g(\mathbf{r}) - 1] d\mathbf{r} \quad (3.22)
\end{aligned}$$

where  $N$  is the total number of nuclei and  $\rho$  the average particle density of the sample. It can be demonstrated that  $g(\mathbf{r})$  is connected to the Pair Correlation Function  $G(\mathbf{r}, t)$  (evaluated at  $t = 0$ ), which is in turn the Fourier transform of the Intermediate Scattering Function (ISF) of the system, defined as:

$$I(\mathbf{Q}, t) = \frac{1}{N} \sum_{ij} \langle \exp[-i\mathbf{Q} \cdot \mathbf{R}_j(0)] \exp[i\mathbf{Q} \cdot \mathbf{R}_i(t)] \rangle \quad (3.23)$$

Since in a fluid the average structure is isotropic, only the modulus of  $\mathbf{Q}$  and  $\mathbf{r}$  is relevant; if the particle orientation is random, we can average over the all orientations of  $\mathbf{Q}$  and the structure factor can be written in terms of the spherical Bessel functions of zero order:

$$S(Q) = 1 + \frac{1}{N} \left\langle \sum_{i,j \neq i} \frac{\sin(Q r_{ij})}{Q r_{ij}} \right\rangle \quad (3.24)$$

At high  $Q$  ( $Qa \gg 1$ , where  $a$  is the average atomic distance),  $S(Q)$  oscillates around 1 until this is approached as a limiting value ( $S(Q \rightarrow \infty) = 1$ ), whereas for  $Q \rightarrow 0$  the SSF is related to the density fluctuations in the sample, and thus to its isothermal compressibility  $\kappa_T$ :  $S(0) = \rho \kappa_T k_B T$ . This last equality implies that  $S(0) = 1$  for a perfect gas, while it is expected to be  $S(0) \ll 1$  for a liquid system.

The function  $g(r)$  is called *radial distribution function* (fig.3.3) and is proportional to the probability to find an atom at distance  $r$  from another atom located at the origin (in other terms, given a tagged particle at the origin,  $\rho g(r)$  represents the conditional probability to find another particle at distance  $r$  away from the origin). Under these hypothesis,  $S(Q)$  is given by:

$$S(Q) = 1 + 4\pi\rho \int_0^{\infty} r^2 [g(r) - 1] \frac{\sin(Qr)}{Qr} dr \quad (3.25)$$

The first peak of  $g(r)$  indicates the average distance between first neighbour atoms and defines the first coordination shell with respect to an atom at the origin. In addition,  $g(r)$  can be used to calculate the average number of particles that can be found in a spherical shell of radius  $r$  and thickness  $dr$  around a reference particle:

$$\langle n(r) \rangle = \rho g(r) 4\pi r^2 dr \quad (3.26)$$

From eq.3.26 the coordination number of the particle located at the origin of the reference system, that is the average number of neighbour particles within a distance  $R$ , is given by:

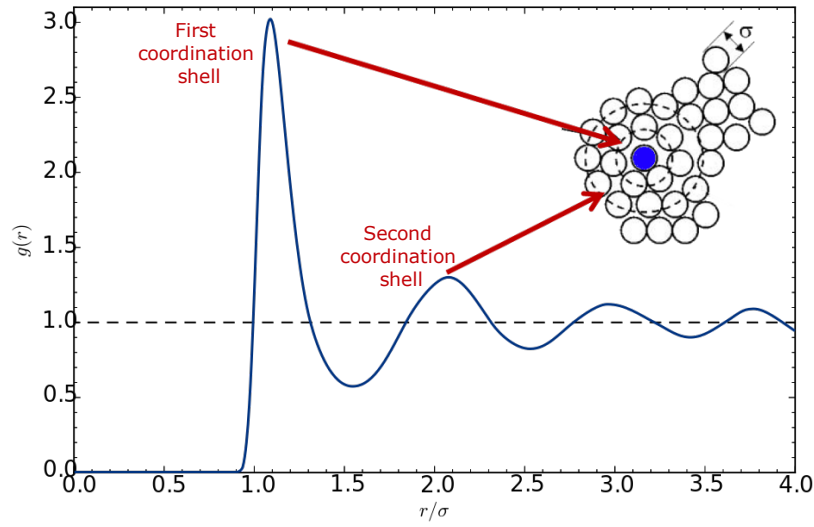


Figure 3.3: Radial distribution function for a typical Lennard–Jones liquid of diameter  $\sigma$ , whose atomic configuration is schematically depicted in the inset.  $g(r)$  shows some peaks corresponding to the coordination shells of the particle at the origin. Red arrows point at the first and second coordination shells.

$$\langle n(R) \rangle = 4\pi\rho \int_0^R r^2 g(r) dr. \quad (3.27)$$

### 3.1.6 Molecular fluids and multicomponent systems

If we have a molecular fluid, we need to take under consideration more than one SSF. In particular, we have a *Partial Structure Factor* (PSF) for every couple of atomic species in the molecule. A generic PSF is defined as follows:

$$S_{\alpha\beta}(Q) = \sum_{\alpha,\beta} \langle \exp(i\mathbf{Q} \cdot [\mathbf{R}_\alpha(0) - \mathbf{R}_\beta(0)]) \rangle \quad (3.28)$$

where  $\alpha$  and  $\beta$  are the two atomic species. At each of the PSF corresponds a site-site *Radial Distribution Function* (RDF)  $g_{\alpha\beta}$ , according to the following expression:

$$S_{\alpha\beta}(Q) = 1 + 4\pi\rho \int r^2 [g_{\alpha\beta}(r) - 1] \frac{\sin(Qr)}{Qr} dr \quad (3.29)$$

which is the probability that, given a nucleus of species  $\alpha$  at the origin, a nucleus of species  $\beta$  is found at distance  $r$ . In this case the DCS per atom is a linear combination of all the PSFs, weighted by the concentration and the scattering length of the nuclei:

$$\frac{d\sigma}{d\Omega} = \sum_{\alpha} c_{\alpha} \frac{\sigma_{tot}^{\alpha}}{4\pi} + \sum_{\alpha\beta} c_{\alpha} c_{\beta} b_{\alpha} b_{\beta} S_{\alpha\beta}(Q) \quad (3.30)$$

where the first term is the atomic self-scattering contribution, while the second represents the interference scattering term; its Fourier transform gives the so-called neutron weighted radial distribution function. This function contains all the structural information about the sample, albeit its interpretation may be demanding.

### 3.1.7 The isotopic substitution and EPSR simulations

In order to extract from neutron scattering data structural information not immediately accessible by experiments, e.g. orientational correlations of a system, is necessary to separate the total scattering function into the individual  $S_{\alpha\beta}(Q)$ . This result can be achieved by exploiting the fact that different isotopes of the same atom have a different scattering length (see, for instance, table 3.2), therefore they are "seen" differently by neutrons. This means that it is possible to apply the Isotopic Contrast Method (with first and second order difference), consisting in performing a series of experiments on samples with different isotopic concentration of a given species.

For example, for water or water-based molecular systems, the H/D isotopic substitution is the most convenient probe for revealing the intermolecular structural correlations. In this case, the total structure factor  $F(Q)$  can be written in terms of three partial structure factors, namely  $S_{XX}$ ,  $S_{XH}$  and  $S_{HH}$ , where the label H refers to substituted atoms and X to the unsubstituted ones. They can be extracted by simply reversing a system of three equations in three unknown variables. The important hypothesis at the basis of this technique is that the substitution of an atom with another isotope within the molecule does not alter the structural properties of the sample, at least within the experimental sensitivity. In other words, we accept that  $S_{HH} = S_{DD}$  and  $S_{XH} = S_{XD}$ .

Notwithstanding, in a real experiment the situation described before is not likely very frequent. More often the number of partial structure factors to determine (unknown quantities) is greater than the number of measures that is possible to perform (equations). In such a case, the system is under-determined and computer simulations represent a powerful instrument to overcome this difficulty. In particular, in 1996 the EPSR (Empirical Potential Structure Refinement) method has been introduced [217, 218]: it is based on Monte Carlo simulations with the fundamental constraint of being consistent with results from neutron scattering experiments. The basic idea is to build up a simulation box with a pair interaction potential model (reference potential, e.g. Lennard-Jones 12-6) able to reproduce the main structural features of the real system (such as the hydrogen bond for water). Then the simulation can start: the total energy potential of the system is written as the sum of two contributions, the reference potential ( $U_{ref}$ ) and an empirical one ( $U_{emp}$ ). For a single component of the sample (e.g. a molecule) four types of "motions" are allowed, casually chosen: translation of the molecule, rotation of the molecule, rotation of atomic groups within the molecule, and movements of individual atoms within the molecule. For each step, the molecule coordinates undergo a slight random change and the new configuration is evaluated on the basis of the Metropolis condition: if the change in energy, weighted by a factor  $\exp(-\Delta U)/k_B T$  (where  $\Delta U$  is the variation of the potential energy of the system after the motion) is negative, the new configuration is accepted, otherwise it is ruled out. The energy change after

each of the accepted steps is used to update  $U_{\text{emp}}$ . Then the structural factors calculated starting by the new simulated potential are compared with the experimental ones: if the difference does not overcome a specific threshold, i.e. if the simulation approaches the data sufficiently closely (the residues calculated by fitting the experimental data with the simulated structural factors do not show any significant structure)<sup>4</sup>, the simulation proceeds with a new step; when the accordance between simulation and experiment is satisfactory and the empirical potential does not change any more (or else the modulus of the empirical potential energy<sup>5</sup> reaches a predefined limit), a number of equivalent configurations are accumulated in order to have a good statistics [219].

Since in the experiments shown in the present thesis we did not take advantage of EPSR simulations, no further details will be provided concerning this issue. More and in-depth information can be found, for instance, in [220].

### 3.1.8 Small Angle Neutron Scattering (SANS)

We have discussed so far the determination of the structure of the sample on atomic scale. However many are the samples for which the length scales we are interested in are much bigger, of the order of the mesoscale. In this case it is necessary to collect scattered neutrons at small angles (and thus at small  $Q$  values) to explore distances  $d$  of the order of nanometer ( $\sim 1 - 300$  nm), because  $d \sim 2\pi/Q$  [221]. Even though the atomic detail is lost, meaning that in the expression of the DCS we do not need to sum over the all  $i, j$  atoms, we are allowed to tend to the continuum limit. As far as these conditions stand, the *density scattering length* is defined as:

$$\rho(\mathbf{r}) = b_i \delta(\mathbf{r} - \mathbf{r}_i) = \frac{\sum_{i=1}^N b_i}{V} \quad (3.31)$$

where  $b_i$  is the scattering length of the atom  $i$  and  $V$  is the volume occupied by the  $N$  atoms. Let us consider only the coherent contribution to the scattered intensity, as it contains information about the distribution of matter in the sample, that is what we want to investigate. We note that it is reasonable to replace atomic properties with a mesoscopic quantity because the density scattering length of a molecule as a function of distance ( $r$ ) from a given atom becomes essentially constant beyond a certain radius  $r^*$ , thus for  $Q < 1/r^*$  the atomic structure details are lost. Therefore, if we are observing the structure of the sample over lengths much larger than atomic distances, the sum in eq.3.18 can be replaced by an integral over the whole sample (normalised by the volume):

$$\frac{d\Sigma}{d\Omega}(\mathbf{Q}) = \frac{N}{V} \frac{d\sigma}{d\Omega}(\mathbf{Q}) = \frac{1}{V} \left| \int_V \rho(\mathbf{r}) \exp(i\mathbf{Q} \cdot \mathbf{r}) d\mathbf{r} \right|^2 \quad (3.32)$$

where  $\frac{d\Sigma}{d\Omega}$  is the macroscopic cross-section. Eq.3.32, known as *Rayleigh-Gans equation* [222], shows that small angle scattering arises from inhomogeneities in the distribution of the density scattering length  $\rho(\mathbf{r})$ . Since the macroscopic cross-section is proportional to the square

<sup>4</sup>Ideally, the difference between simulated and experimental structure factors should go to zero when the simulation well reproduces the data.

<sup>5</sup>The empirical potential energy is defined by  $\bar{U} = \sum_{r,j=1}^N |U_{\text{emp}}^{(j)}|$ , where  $j$  labels any particular pair of atoms.

of the amplitude of the Fourier transform of  $\rho(\mathbf{r})$ , all phase information are lost, implying that it is impossible to obtain from the macroscopic cross-section the density scattering length distribution by simply performing the inverse Fourier transform.

In the case of a biphasic system (e.g. a colloidal solution or water confined in a porous matrix), the total volume  $V$  can be divided in two regions,  $V_1$  and  $V_2$  so that  $V = V_1 + V_2$ , with two different density scattering lengths,  $\rho_1$  and  $\rho_2$  respectively. The application of the Rayleigh-Gans equation leads to (for  $\mathbf{Q} \neq 0$ ):

$$\frac{d\Sigma}{d\Omega} = \frac{1}{V}(\rho_1 - \rho_2)^2 \left| \int_{V_1} \exp(i \mathbf{Q} \cdot \mathbf{r}) d\mathbf{r}_1 \right|^2 \quad (3.33)$$

showing that the macroscopic cross-section, and thus the scattering intensity, depends on the *contrast*, namely on the difference between the density scattering lengths of the two phases. Such a difference comprises the properties of both the material (density, chemical composition) and the probe (via the scattering lengths), whilst the right-most term in eq.3.33 describes the spatial arrangement of the system under investigation. Eq.3.33 also leads to the *Babinet principle* [222], stating that two samples with the same structure but phases with inverted density scattering lengths produce the same coherent scattering. This hides again a loss of information: we have no possibility to discern whether  $\rho_1 > \rho_2$  or vice-versa. As seen before, the isotopic substitution technique allows to change the scattering cross-section of a molecule by replacing one of its atom with a suitable isotope. In principle, this can be made for tuning the contrast and matching the density scattering length of some specific components of the system (in order to highlight only the components we are interested to see). For this reason a good strategy is to plan experiments that exploit the contrast variation technique, representing one of the key advantages of neutron scattering over X-rays and light.

### SANS data analysis

Depending on the  $Q$ -range of interest, the integral cross-section can be conveniently approximated in order to gather information focusing on different physical aspects. For instance, at very low  $Q$  ( $Q \rightarrow 0$ ), the Guinier approximation allows to extract the gyration radius of the scattering particles, giving the average dimensions of the scattering centres. In particular, over the low- $Q$  range accessible by our experiments (with  $Q \gg 1/d$ , being  $d$  is the characteristic size of the scattering object), the scattered intensity is proportional to a negative power of the momentum transfer  $Q$ :

$$I(Q) \sim A Q^{-D} + B \quad (3.34)$$

where  $A$  and  $B$  are constants, while  $D$  is the *Porod exponent* [223]. If there are sharp boundaries between the phases of the system, eq.3.34 provides indications about the dimensionality of the system (regardless if we have a single particle or an aggregate) which can be obtained as the slope of the "Porod plot" ( $\log I$  vs  $Q$ ). In the simplest case of a single particle, we have  $D = 1$  for a rod,  $D = 2$  for a plate,  $D = 4$  for a sphere. Rough surfaces are characterized by  $D$  between 3 and 4, that indicates a fractal dimension  $F$ , with  $D = 6 - F$ .

An in-depth description of small angle scattering data over the  $Q$ -range commonly accessible at neutron facilities can be found, for example, in [221, 223].

## 3.2 From an ideal to a real scattering experiment

The scattering theory presented in the previous section relies on some simplifications with respect to a real experiment. Therefore some important issues need to be considered when a real experiment is performed and data require to be conveniently corrected.

The main aspects to deal with are listed in the following:

- The neutron beam is never truly monochromatic, implying that the diffraction pattern can only be measured with a *finite resolution* function. Moreover there is a highly non-linear relationship between the wavelength range allowed to get through the collimator and the final radiation flux incident on the sample.
- Not all the neutrons reaching the detector have been scattered by the sample. Some of the radiation comes from the *background* and has to be removed from the counts of the detector.
- Samples are normally surrounded by one or more containers (the sample holder, the thermal radiation shields, etc.), which inevitably attenuate the scattered radiation to some extent. Therefore the measured intensity has to be corrected for *attenuation* due to both the sample and any surrounding containers.
- In a real scattering pattern, structural information coming from the *container* are superimposed to those relative to the sample. Often the Bragg reflections due to the container can be hard to subtract completely from the experimental signal. This points out the importance of the choice of the container material. Ideally, in order to make the corrections easily feasible, a container should be made of a purely incoherent scattering medium (such as Vanadium) or at least of a material with a small coherent cross-section (such as Titanium–Zirconium alloy).
- A fraction of the scattered signal comes from *multiple* scattering events, that are neglected in the theory and contribute to the scattering pattern with a signal lacking useful structural information [224].
- In order to calculate useful structural quantities about the sample, it is essential to put the scattered data onto an *absolute* scattering cross-section scale. This means that the instrument needs to be calibrated in absolute units by means of a preliminary measurement performed on a purely incoherent standard sample (e.g. polycrystal of Vanadium).
- The theory developed in the previous section rests on the validity of the static approximation. On the basis of this fundamental assumption, the neutron beam scattered by the sample is so energetic that the loss or gain of energy occurring as a result of the scattering event is negligible. Unfortunately this circumstance can never be realised in practice, especially for light atoms that can easily recoil and undergo a large exchange of energy due to the comparable mass of the scattering nucleus and the probe. This means that the scattering is never truly elastic and *inelasticity* effects, leading to

distortions in the diffraction pattern, need to be corrected for [225]. Inelasticity affects primarily the self-scattering, leaving the interference contribution only weakly influenced. The first attempt to remove inelasticity distortions is due to Placzek, who proposed a method for calculating the corrections to the static approximations based on the Taylor expansion of the dynamic structure factor about its elastic value [226]. However this method is valid only when  $\hbar\omega$  is small compared to the incident energy, thus it does not work when the scattering sample contains light atoms. Alternative strategies are very difficult to be implemented in practice, therefore experimenters typically use an *ad hoc* polynomial method to remove the inelastic scattering by empirically fitting a smooth background to the experimental data. Obviously such a background subtraction has to be done with caution because it may introduce artifacts in the diffraction pattern that do not represent real structures of the sample.

### 3.3 The experimental apparatus

#### 3.3.1 The neutron source

A real experiment can be performed either at a reactor or a pulsed neutron source. The difference is obviously in the way by which the neutron beam is produced [215]. In the first case neutrons are produced by *fission*, a chain reaction whereby a cold neutron collides with a heavy nucleus that splits into two lighter ones, releasing  $\gamma$ -rays, neutrons and other subatomic particles. Neutrons are produced in a continuous flux, but their kinetic energy is too high ( $\sim$  MeV), thus they are moderated to the energies (meV  $\div$  eV) useful for applications in condensed matter through collisions with light atoms (usually heavy water,  $D_2O$ , or graphite kept at  $T \approx 300$  K). The resulting distribution of neutron speeds approaches the Maxwell-Boltzmann function corresponding to the temperature of the moderating material. With a reactor's diffractometer we select the incoming neutron wavelength  $\lambda_i$  (usually by means of a monochromator) and measure the function  $I(\theta|\lambda)$ , i.e. the scattering intensity as a function of the diffraction angle  $2\theta$ , with no analysis in energy. By assuming elastic scattering ( $|\mathbf{k}_i| = |\mathbf{k}_f| \Rightarrow Q = 2k_i \sin \theta$ , with  $k_i = 2\pi/\lambda_i$ ), we obtain that the dynamical range of  $Q$  and its resolution are determined by the range of covered angles and the angular resolution, respectively.

An alternative source of neutrons, which has become increasingly exploited since the 1990s, is based on accelerator technology, similar to that found in synchrotron facilities. In essence, a proton beam is accelerated up to 800 MeV – 1 GeV in a synchrotron and then deflected out to a target made of heavy elements, such as tungsten, mercury or tantalum. This collision results in the excitation of the target nuclei, which, recovering their fundamental state, produce high energy neutrons (*cascade*) and other sub-atomic particles (*evaporation*), including less energetic neutrons. The total reaction is called *spallation* and the neutrons produced need to be slowed down to the thermal energy by means of a moderator. Since the injection and extraction processes are repeated periodically (typically 10–60 times a second), the neutron beam produced via spallation is pulsed. Each incident proton produces approximately 15 neutrons (much more efficient than fission). The heat dissipated in each spallation process is  $\sim 55$  MeV, while fission dissipates  $\sim 180$  MeV: this reduces the cooling problems and allows for the production of intense neutron fluxes. With respect to reactors, spallation sources offer a clear advantage also in terms of security and environmental impact (they do

not generate nuclear waste), and this is why their construction is always less controversial. The energy of a pulsed neutron beam is selected by the *Time of Flight* (TOF) technique, that exploits the kinematic relation between the neutron time of flight over a known distance and its velocity to determine the neutron energy before or after the scattering event. In fact, if we assume that a neutron is elastically scattered, its velocity is  $v = (L_0 + L_1)/t$ , its wavelength is  $\lambda = h/mv$  and the corresponding momentum transfer is  $Q = ht/m(L_0 + L_1)$ , being  $L_0$  and  $L_1$  the primary (moderator–sample) and the second (sample–detector) flight paths. Therefore, in comparison with a reactor, the dynamic range accessible with a spallation source is wider, because the scanning in  $Q$  is not determined by the angular position of the detectors, but by the neutron time of flight itself and what we measure is the function  $I(\theta|t)$ , again with no analysis in energy. In principle, for a diffractometer installed in a spallation source, only one detector would be sufficient to perform a scattering experiment (but having more than one detector is more advisable for achieving a better statistics). Comparing with the reactor sources, the use of the TOF technique dramatically reduces the duration of a typical scattering experiment and, at the same time, the loss in neutron flux due to the monochromator, which rejects 95% of the incoming beam and does not permit to reveal different wavelengths.

The measured functions  $I(\theta|\lambda)$  and  $I(\theta|t)$  need to be converted into a function of the momentum transfer  $Q$ , namely the Measured Differential Cross Section (MDCS)  $\Sigma(Q)$ , by performing corrections discussed in sec.3.2 (subtraction of the background and sample container contribution, correction for the multiple scattering and absorptions, calibration of the instrument in absolute units).

### 3.3.2 The NIMROD diffractometer at ISIS

Our neutron scattering experiments were performed at the ISIS neutron spallation source, located at the *Rutherford Appleton Laboratory* (Harwell Oxford, Didcot, UK). More specifically, the instrument we opted for is NIMROD (Near and InterMediate Range Order Diffractometer), a time–of–flight diffractometer installed few years ago at the ISIS Second Target Station (TS2) that produces a neutron beam with a broad spectral range, also including very slow neutrons (with  $\lambda$  down to  $\sim 10$  Å). It is this property of the TS2 that allows NIMROD to bridge the traditional gap between SANS experiments and wide-angle neutron scattering, providing a continuous access to length scales ranging from the interatomic ( $< 1$  Å) up to mesoscopic ( $\gtrsim 300$  Å), while maintaining a structural subatomic resolution thanks to the relatively high  $Q$  values accessible [213]. A scheme of NIMROD is displayed in fig.3.4.

NIMROD diffractometer makes use of a forward scattering geometry to minimize inelastic scattering effects. The heart of the instrument, where the sample holder is inserted, is occupied by a large vacuum vessel (high vacuum,  $\sim 10^{-5}$  mbar) aimed at removing parasitic air-scattering from around the sample and from the second neutron flight path. This is a markedly important issue because allows to minimize the sample dependent background scattering, otherwise impossible to correct in the data analysis procedures. The neutron intensity is measured by two monitors, one for the incident beam and one for the transmitted beam, located right before and after the sample.

In total NIMROD has 1854 detector elements, based on ZnS(Ag) scintillation technology and organized in two arrays: the wider angle one covers scattering angles ( $2\theta$ ) from  $3.5^\circ$  to

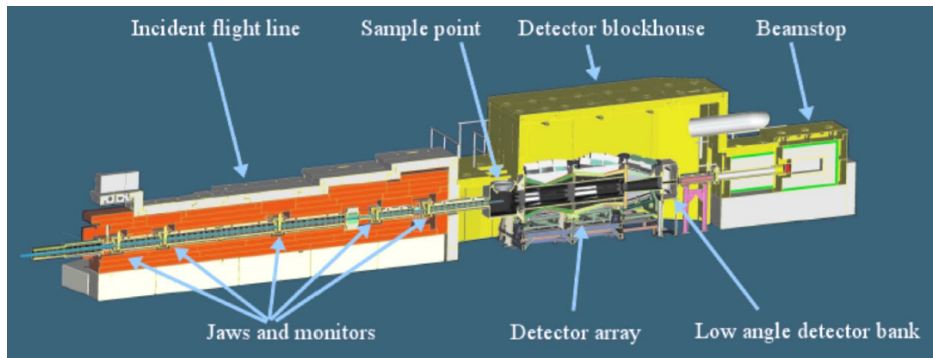


Figure 3.4: Cutaway diagram of NIMROD with an overview of its key components [213].

$40^\circ$  and consists of 1098 elements grouped in 18 modules and arranged over a cylindrical surface of radius 70 cm about the neutron beam axis; instead, the low angle detector array covers an angular distribution from  $0.5^\circ$  to  $2.2^\circ$  and consists of 756 elements divided into 24 segments around the beam axis. The standard grouping of the detector modules sums up the counts of all the detector elements around the beam axis corresponding to their position in the scattering angle, sharply improving the statistical quality of the output data. However, as each detector can be probed individually, also other more complex detector groupings are possible, accordingly with specific sample geometries. The main technical characteristics of NIMROD are listed in table 3.3.

As in all the instrument based on TOF technique, the incident and final wavevectors are determined by requiring that all neutrons reaching the detector in a given time channel have the same time-of-flight from the source. This constraint is satisfied by the condition

$$\frac{1+L}{k_e} = \frac{1}{k_i} + \frac{1}{k_f} \quad (3.35)$$

where  $k_e$  is the wavevector of the elastic scattering event (i.e.  $k_i = k_f$ ) and  $L$  is the ratio of scattered to incident flight paths. In other words,  $k_e$  can be determined knowing the total time-of-flight for a particular time channel and the elastic momentum transfer can be defined as  $Q_e = 2k_e \sin(\theta/2)$ . The inelasticity corrections for a TOF experiment result to be larger at low  $Q_e$  values.

The peculiar NIMROD's properties and its wide  $Q$  range make it particularly suitable for studying the structure of liquids, disordered, and nanostructured materials. For instance, it finds ideal application in the study of biomolecules in solution, complex and confined fluids, functional and composite materials (e.g. porous media, intercalates, Sol-Gels and colloidal dispersions).

We opted for NIMROD because it better met our needs: *i*) obtaining structural details about both the porous silica matrix (MCM-41) and the supercooled water confined within, *ii*) probing structural changes experienced by both confining substrate and confined liquid as temperature is lowered. For achieving such a goal, we needed to assess simultaneously structural changes at mesoscopic (porous matrix) and interatomic (supercooled water) length scales. Indeed, as stated above, NIMROD offers the possibility to correlate structural information at interatomic and mesoscopic distances, with a single measurement over a wide  $Q$  range.

Incident wavelengths	0.05 Å– 10 Å
Q-range	0.01 Å <sup>-1</sup> – 50 Å <sup>-1</sup>
Resolution	2θ = 0.5° – 10° ⇒ < 10% ΔQ/Q 2θ = 10° – 40° ⇒ ~ 2% ΔQ/Q
Flight path	Incident (primary): 20 m Final (second): 1–5.5 m
Moderator	Coupled cold
Detectors	1854 ZnS scintillator elements, in rows parallel to the beam
Angular range	0.5° – 40°
Beam size	30mm wide x 30mm high

Table 3.3: Main nominal characteristics of the diffractometer NIMROD (<http://www.isis.stfc.ac.uk/instruments/nimrod>).

# Chapter 4

## Experimental techniques: Infrared spectroscopy

*Nothing has such power to broaden the mind as the ability to investigate systematically and truly all that comes under thy observation in life.*

*Marcus Aurelius*

Infrared spectroscopy permits to analyse the interaction of infrared electromagnetic radiation (energy between  $\sim 10^{-3}$  and  $\sim 1$  eV) with the sample, detecting vibrational and rotational motions whose transitions can give insights on structure, dynamics, and chemical processes at atomic and molecular level.

For our aims, this technique has proven to be extremely helpful to probe changes in vibrational frequencies of hydrogen bonds of confined water as a function of temperature and pressure. In particular, we have taken advantage of infrared spectroscopy to combine dynamical information with structural data obtained by neutron scattering experiments. More specifically, we have investigated the response of our sample in two frequency ranges: the middle infrared (MID) region, typical of the vibration of water OH bonds, and the far infrared (FIR) region, where the low energies involved are descriptive of the vibrations of clusters of hydrogen bonds. This has given us the possibility to get an overall picture of the changes experienced by our sample and the structural and dynamical behaviour of supercooled water in a confined environment. We performed our experiments at the synchrotron Soleil (Saint-Aubin, France), exploiting the new high-pressure/low-temperature set-up available at the AILES beamline [227].

In this chapter basics of vibrational spectroscopy theory will be given, with particular focus on infrared radiation. Subsequently, a brief description of a synchrotron light source and some details about the main features of the instrumentation used in our experiments will be provided.

## 4.1 Theoretical background

As demonstrated by quantum mechanic theory, the absorption of infrared (IR) radiation promotes the transition of a molecule from a fundamental to an excited state. In particular, the energy content of IR radiation is able to activate vibrational and rotational transitions but not electronic excitations, as in a molecule we typically have  $\Delta E_{el} \gg \Delta E_{vib} \gg \Delta E_{rot}$ , where  $\Delta E_{el}$ ,  $\Delta E_{vib}$ ,  $\Delta E_{rot}$  are the energy gaps between electronic, vibrational and rotational levels respectively. This means that the absorption of IR photons induces transitions resulting from roto-vibrational motions of the molecules, being their energy not enough to allow electronic transitions (as seen with UV radiation), dissociation of molecules or removal of electrons.

The IR electromagnetic spectrum can be subdivided into three regions: the *Near-IR* (NIR,  $\sim 12800 \div 4000 \text{ cm}^{-1}$ ), that excites overtones or harmonic vibrations; the *Mid-IR* (MIR,  $\sim 4000 \div 400 \text{ cm}^{-1}$ ), that may be used to probe the fundamental vibrations and associated roto-vibrational structures; the *Far-IR* (FIR,  $\sim 400 \div 30 \text{ cm}^{-1}$ ), that is suitable for rotational spectroscopy [228].

Each transition produces a band in the IR absorption spectrum of the molecule, whose assignment and full comprehension requires a good knowledge of molecular symmetry and group theory. Furthermore, IR absorption bands do not appear in the spectrum as very narrow peaks, but undergo a broadening effect mainly due to collisions between molecules and finite lifetime of the states involved in the transition.

### 4.1.1 Vibrational transitions

For the sake of simplicity, we can start by consider a diatomic molecule. This is the simplest case: the two atoms and the connecting bond are treated as a simple harmonic oscillator, composed of two masses joined by a spring. The corresponding Schrödinger equation has a known solution, whose eigenvalues lead to the following quantized vibrational energy [229]:

$$E_{vib} = \left( n + \frac{1}{2} \right) h\nu \quad (4.1)$$

where  $n$  is an integer ( $n = 0, 1, 2, \dots$ ) denoting the vibrational level and  $\nu$  the frequency of the absorbed photon. The energy levels are equally spaced by  $h\nu$  and the energy associated to each level increases with  $n$ . The harmonic oscillator is a good approximation only for the lowest energy levels ( $n = 0, 1$ ). As  $n$  becomes greater than 1, the potential in the Hamiltonian of the system departs from the harmonic oscillator because of dissociation (occurring when the two atoms move away from each other) as well as repulsion (occurring when the atoms get too close). In order to take these effects into account, the interaction can be better described by the Morse potential:

$$V_{\text{Morse}} = D_e \left( 1 - e^{-\beta q} \right)^2 \quad (4.2)$$

where  $D_e$  is the dissociation constant,  $\beta = \sqrt{k/2D_e}$  (with  $k$  the force constant of the oscillator), and  $q = R - R_0$  is the coordinate of the vibration motion of the molecule (with  $R_0$  the interatomic distance at equilibrium). The Morse potential in eq.4.2 entails the following vibrational energy:

$$E_{vib} = \left(n + \frac{1}{2}\right) h\nu - \left(n + \frac{1}{2}\right)^2 \gamma_{an} h\nu \quad (4.3)$$

with  $\gamma_{an} = \frac{h\nu}{4D_e}$  the anharmonicity constant. By including the anharmonic terms, the vibrational energy levels are not equally spaced. Conversely, the spacing decreases as  $n$  increases, until it approaches zero (continuum of states).

Not all the energy levels can be reached via a vibrational transition. Actually, a transition between two vibrational levels is allowed only if the so-called *selection rules* are fulfilled [229]. They descend from two fundamental conditions: *i*) the amount of energy brought by electromagnetic radiation must be equal to the gap between the final and the initial vibrational levels involved in the transition ( $h\nu = E_f - E_i$ ), *ii*) the dipole moment of the molecule must change, that is to say that the transition moment integral must be non-zero, namely  $[\mu]_{if} = \int dq \phi_f^*(q) \mu \phi_i(q) \neq 0$ , where  $\mu$  is the dipole moment operator and  $\phi_f$  and  $\phi_i$  are the wave functions of the final and initial state respectively. By assuming the harmonic approximation and expanding the dipole moment  $\mu$  of the molecule<sup>1</sup> in Taylor series using the vibrational coordinate  $q$ , it can be demonstrated that the only condition making  $[\mu]_{if}$  non-zero is  $\Delta n = \pm 1$ . This means that the initial and final state must be just one level apart to cause a change in the dipole moment. When these conditions occur, a molecule is said to be "IR-active". If anharmonic effects are not negligible, also quadratic terms of the series expansion of the dipole moment are required, so that transitions with  $\Delta n = \pm 2, \pm 3, \dots$  are allowed as well.

In order to evaluate if a vibrational transition can be induced, we need to know not only the selection rules, but also how energy levels are populated. The distribution of particles among energy levels depends on temperature  $T$  and follows the Boltzmann distribution:

$$\frac{N_f}{N_i} = \exp\left(\frac{E_f - E_i}{k_B T}\right) \quad (4.4)$$

where  $N_f$  and  $N_i$  are the number of particles in the excited (final) and initial state, while  $E_f$  and  $E_i$  are their respective energies (with  $E_f > E_i$ ). Hence it is possible to state that at low temperature only the lowest energy levels are significantly populated and, at room temperature, the most probable transitions are from  $n = 0$  (ground state) to  $n = 1$ .

### 4.1.2 Rotational transitions

The Schrödinger equation for a rotational motion can be easily solved by approximating a diatomic molecule as a rigid rotor [229]. In this case, the only non-zero contribution to the

<sup>1</sup>The dipole moment of a molecule is defined as  $\mu = q \cdot \mathbf{d}$ , where  $q$  is the amount of charge at either end of the dipole and  $\mathbf{d}$  is the distance between the charge centres.

Hamiltonian of the system is the kinetic one, and the resulting rotational energy is (in the centre of mass reference frame):

$$E_{rot} = \frac{p^2}{2I} = \frac{h^2}{8\pi^2 I} \cdot J(J+1) = BJ(J+1) \quad (4.5)$$

where  $I$  is the momentum of inertia,  $J$  the angular momentum operator and  $B$  the rotational constant. A better description of the rotational energy levels can be obtained by adding a centrifugal distortion term, taking into account the bond stretching occurring as the molecule rotates. However this represents a minor correction, being the centrifugal distortion constant several orders of magnitude smaller than  $B$ . Rotational energy levels are separated by  $\sim 10^{-4} - 10^{-3}$  eV, so that rotational transitions are easily excited by electromagnetic radiation in the FIR range. Notably, selection rules for symmetric rotators allow only transitions with  $\Delta J = +1$ , while asymmetric rotators permit transitions also when  $\Delta J = 0, \pm 1$ .

### 4.1.3 Vibrational modes of water molecule

For a polyatomic molecule the theory summarized above is still valid, but much more complex because there is more than one bond to consider to describe vibrational motions and more than two atoms to account for rotational transitions. Moreover, for complex molecules vibrations can be conjugated, leading to infrared absorptions at characteristic frequencies that may be related to whole chemical groups, rather than single atom pairs.

Usually, in the case of a polyatomic molecule, vibrations can be summed up or resolved into *normal modes* of vibration [229]. In general a non-linear molecule with  $N$  atoms has  $3N$  degrees of freedom describing the movement of each atom along the  $x$ ,  $y$  and  $z$  directions. Such a movement can generate:

- 3 translations of the whole molecule (along  $x$ ,  $y$  and  $z$ );
- 3 rotations (about  $x$ ,  $y$  and  $z$ );
- $3N-6$  vibrations.

Vibrations can involve either a change in bond length (*stretching*) or bond angle (*bending*). A further distinction can be done between bonds which stretch in-phase or out-of-phase, defined as *symmetric* or *asymmetric* stretching respectively.

A number of factors may complicate the interpretation of the IR spectra of polyatomic molecules. As an example, *overtones* and *combination* bands can be mentioned: while the first case is represented by absorption bands located at positions that are multiples of a fundamental absorption frequency, combination bands arise when two different fundamental bands (with frequency  $\nu_1$  and  $\nu_2$ ) absorb simultaneously and only a single band appears at a frequency equal to  $(\nu_1 + \nu_2)$ . Also the presence of a *Fermi resonance* can affect the IR spectrum of a polyatomic molecule: this happens when an overtone or a combination band absorbs nearly at the same frequency of another fundamental. The result is that two relatively strong bands, usually of about the same intensity, appear close together when only one is expected, at somewhat higher and lower frequencies with respect to the position of the expected band.

Our interest is focused on water, which is indeed a non-linear planar molecule. Since it

has three atoms, the number of its vibrational modes is  $3N - 6 = 3$ , as depicted in fig.4.1 (left side). The first two are stretching modes and occur when the OH bonds are stretched or compressed. We can observe either a symmetric stretching ( $\nu_1$  or  $\nu_s(\text{H}_2\text{O})$ ) or an asymmetric stretching ( $\nu_3$  or  $\nu_{as}(\text{H}_2\text{O})$ ). In the former case the two hydrogens move away and towards the oxygen atom at the same time and the dipole moment<sup>2</sup> does not change in direction but only in magnitude, whilst the latter case corresponds to hydrogen atoms stretching simultaneously but in opposite way, causing the dipole moment changing in both magnitude and direction and switching from left to right. The symmetric stretch is an easier deformation to obtain than the asymmetric one, thus it occurs at lower wavenumbers<sup>3</sup>. The third vibrational mode is a bending ( $\nu_2$  or  $\delta(\text{H}_2\text{O})$ ) and describes the motion of the two hydrogens getting closer and further apart from each other, changing the  $\text{H}\hat{\text{O}}\text{H}$  angle of the molecule. The dipole moment does not change in direction (it always lies in the plane of the molecule), but it does change in magnitude, increasing with bending. It is important to note that bending always requires less energy than stretching.

As seen in chapter 1, water molecules are bonded forming a network of HBs. This prevents  $\text{H}_2\text{O}$  molecules to freely rotate or translate, undergoing frustrated rotations and translations that result in small amplitude oscillations. As a consequence of frustrated rotations, three additional vibrational modes arises (fig.4.1, right side): the rocking mode ( $r(\text{H}_2\text{O})$ ), due to hydrogens oscillating about the  $z$  axis going back and forth like a pendulum (by keeping the same mutual distance); the wiggling mode ( $\omega(\text{H}_2\text{O})$ ), that arises from the hydrogen atoms that oscillate about the  $x$  axis, moving together above and below the plane of the molecule; the twisting mode ( $\tau(\text{H}_2\text{O})$ ), due to hydrogens oscillating about the  $y$  axis, moving in opposite way above and below the plane of the molecule. However, since this latter mode does not imply dipole moment changing, it is IR-inactive. Frustrated translations provoke small oscillations that manifest as a stretching vibration between molecules (inter-molecular stretching mode).

Actually, unlike other liquids, water's inter-molecular vibrations span a very wide frequency range, making vibrational energy relaxation in liquid  $\text{H}_2\text{O}$  considerably complex, with a strong interplay between intra- and inter-molecular relaxation motions influenced by anharmonic vibrations, hydrogen-bonding interactions and dielectric fluctuations [230]. As a consequence, the timescales and pathways involved in the relaxation of vibrational excitation in  $\text{H}_2\text{O}$  are the subject of numerous recent experimental [230–236] and theoretical [237–241] investigations. Deficiency of experimental techniques in achieving a sufficiently high time resolution has led so far to consider contributions from stretching, bending and inter-molecular modes as independently evolving [230]. Nonetheless some recent works, relying on the new possibilities offered by femtosecond lasers and ultrafast broadband spectroscopy [230, 232, 235, 242], have established that the OH stretching vibration cannot be described in terms of a simple local bond stretching or a symmetric/asymmetric vibration, but needs to be regarded as a result of the collective excitation of several molecules.

Summarizing what has been here presented about roto-vibrational dynamics of  $\text{H}_2\text{O}$ , in a typical IR spectrum of liquid water we can recognise the following absorption features (fig.4.2): the OH stretch vibration, centred at  $\sim 3400 \text{ cm}^{-1}$ ; the  $\text{H}_2\text{O}$  bend vibration, centred at  $\sim 1650 \text{ cm}^{-1}$ ; intermolecular vibrations such as librations (hindered rotations) between  $700$  and  $400 \text{ cm}^{-1}$  and stretching and deformations of the hydrogen-bond network at even

<sup>2</sup>The dipole moment of a molecule can be calculated as  $\boldsymbol{\mu} = \sum_i^N q_i \mathbf{r}_i$ , where  $q_i$  is the magnitude of the  $i^{\text{th}}$  charge and  $\mathbf{r}_i$  is its position with respect to the origin of the reference system.

<sup>3</sup>The linear wavenumber  $\tilde{\nu}$  is defined as the inverse of the wavelength  $\lambda$  of the incident radiation,  $\tilde{\nu} = 1/\lambda$ , and it is usually expressed in  $\text{cm}^{-1}$ .

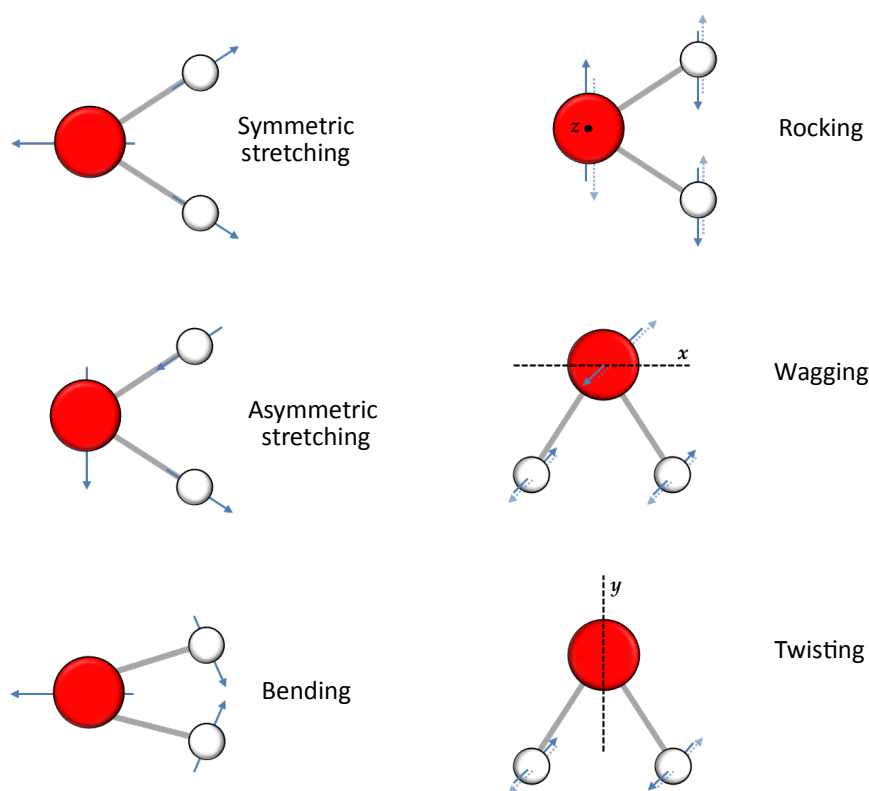


Figure 4.1: Left: vibrational modes of water molecule. Movement of oxygen atom (red) and hydrogens (white) gives rise to symmetric and asymmetric stretching and bending. Right: additional vibrational modes of H-bonded water molecules, giving rise to small oscillations about  $x$ ,  $y$  and  $z$  axis (rocking, wagging, and twisting respectively).

lower frequencies (the so-called *connectivity band*) [243, 244].

## 4.2 The experimental apparatus

### 4.2.1 The synchrotron radiation

Synchrotron radiation plays a key role in fundamental research as well as in technological applications. It has represented a huge step forward in X-rays spectroscopy and since its first development (less than one century ago) has allowed to overcome the most restrictive experimental limitations imposed by X-ray production based on vacuum tube technology. Today it provides new perspectives in the study of condensed matter with very high spatial resolution (down to the atomic scale) [245–248].

Synchrotron radiation is produced by accelerated charged particles travelling at velocities very close to the speed of light. Their trajectory is forced to curve as they go through a magnetic field, thus experiencing a centripetal acceleration. Joseph Larmor, in 1897, was the first to predict that a charged particle should emit energy upon acceleration. His theory was

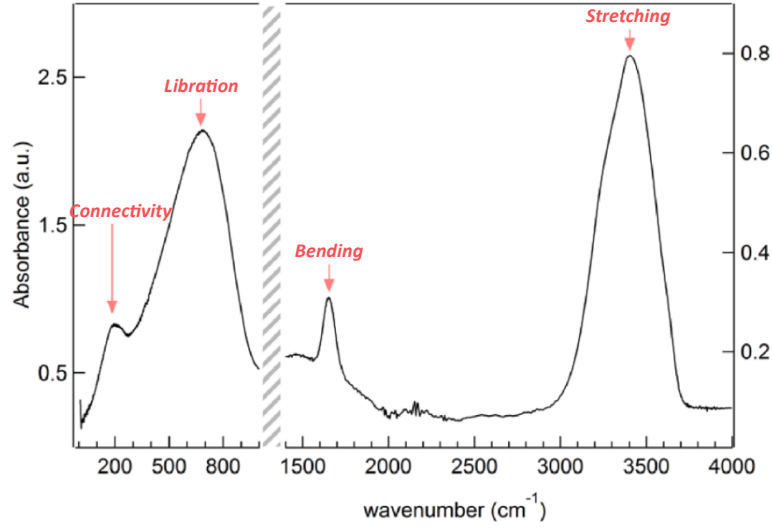


Figure 4.2: FIR and MIR spectra of liquid water at 298 K [244]. Starting from higher wavenumbers, we find the band corresponding to the OH stretching vibration (at  $\sim 3400 \text{ cm}^{-1}$ ) and the much less intense bending band (at  $\sim 1650 \text{ cm}^{-1}$ ). At lower frequencies the libration band is visible (at  $\sim 700 \text{ cm}^{-1}$ ), together with the connectivity band (at  $\sim 185 \text{ cm}^{-1}$ ), due to the collective motion of hydrogen bond network and its deformations. Notably, these last two bands are plotted on a different ordinate axis with respect to the bending and stretching bands because of the much lower intensity of these latter bands.

firstly developed for classical particles (with a velocity  $v \ll c$ , being  $c$  the speed of light) and then extended by Alfred-Marie Liénard to the case of a relativistic particle ( $v \rightarrow c$ ) moving along a circular trajectory. At low velocity ( $v \ll c$ ) a charged particle emits electromagnetic radiation isotropically, whereas an observer in the laboratory frame sees a relativistic particle emitting the whole radiation in a narrow beam of photons aligned with the forward direction of the particle. The angular divergence (expressed in radians) of the emitted cone beam is related to the Lorentz factor  $\gamma$  as follows [215]:

$$\frac{1}{\gamma} = \sqrt{1 - \left(\frac{v}{c}\right)^2} \ll 1 \quad (4.6)$$

The beam sweeps tangentially around the circumference of the storage ring along which the relativistic particles travel. The resulting electromagnetic radiation source is pulsed [215]: in fact an observer in the plane of the orbit sees the emitted radiation as brief flushes of duration given by  $\tau \approx R/2c\gamma^3$ . The corresponding spectrum is continuum with a lower bound of  $\lambda_{\min} \approx c\tau$  and a critical (or median) wavelength  $\lambda_c = 4\pi R/3\gamma^3$ .

The energy loss,  $\Delta E$  (corresponding to the energy of the emitted radiation), in one tour around the circular trajectory is given by:

$$\Delta E = \frac{4\pi e^2}{3R} \gamma^4 \propto \frac{E^4}{m_0^4 R} \quad (4.7)$$

with  $R$  the curvature radius of the trajectory,  $m_0$  the rest mass particle (given in the common units of multiples of eV),  $e$  the elementary charge. According to the last equation, the lighter

is the particle the more is the outgoing energy, being it inversely proportional to the fourth power of the mass particle. This is why synchrotron facilities are commonly injected with electrons.

The remarkable success of synchrotron X-ray radiation primarily relies on its highly collimated nature, which allows for fluxes of photons that are several orders of magnitude more intense than those from vacuum tube sources. In addition, synchrotron radiation is intrinsically polarized, a characteristic that no other X-ray source can provide.

A real synchrotron is not perfectly circular. In practice, a storage ring consists of a combination of curved regions, where a magnetic field perpendicular to the orbital plane is applied in order to accelerate the charged particles (bending magnets), and straight regions, where magnetic quadrupoles and radio-frequency cavities provide the beam focusing and supply the energy lost by particles in the radiative process, respectively. The modern X-ray facilities, known as third generation sources, were introduced in the 1990s and are characterized by a significantly higher brilliance (or brightness)<sup>4</sup> and the capability to enhance the emission of specific harmonic modes. This has been achieved through the use of insertion devices called *wigglers* and *undulators* [215]. Nowadays the goal is to go towards the fourth-generation synchrotron, based on free electron laser (FEL) sources. Its peak brightness in the X-rays range is expected to be many orders of magnitude larger than a third-generation synchrotron source. Synchrotron radiation is suitable for manifold applications, such as X-ray diffraction (XRD) experiments for the structural analysis of crystalline and amorphous materials (also under extreme conditions, i.e. low temperature–high pressure), X-ray crystallography of proteins, characterization of surfaces, interfaces, and thin films at atomic to nano-scale detail, as well as high resolution imaging. Nevertheless, the use of synchrotron radiation is not limited to applications requiring high energy photons or high spatial resolution. In fact, as shown by eq.4.7, a synchrotron facility gives the possibility to access a wide energy range, extending from the infrared to the X-rays. The opportunity to exploit the high flux of this radiation source over the whole spectral range opens interesting perspectives also for other techniques that do not require X-rays. Infrared spectroscopy represents a proper example, as shown in the next section.

#### 4.2.2 The AILES beamline at synchrotron SOLEIL

SOLEIL (Saint-Aubin, France), an acronym for *Source Optimisée de Lumière d'Énergie Intermédiaire de LURE*<sup>5</sup>, is a third-generation synchrotron radiation source, with a wide spectral range varying from infrared (1 eV) to hard X-rays (50 keV), largely appreciated for its high stability. The maximum nominal energy of electrons is 2.75 GeV and 29 beamlines are currently open (even if a total of 43 slots are available around the storage ring).

As discussed before, infrared spectroscopy affords high sensitivity for water vibrational modes. Moreover it usually needs only small amounts of sample and can be exploited for studying water in different environments and under several experimental conditions.

<sup>4</sup>*Brilliance* is a parameter that quantifies the quality of a source. It represents the photon flux per unit area and per unit solid angle, divided by 0.1% of the bandwidth, in order to account also for the spectral distribution of the emitted photons. Synchrotron sources have an extremely high brilliance, also ten thousands times greater than sunlight.

<sup>5</sup>LURE (Laboratoire d'Utilisation du Rayonnement Électromagnétique) is the precursor of SOLEIL and was a pioneering laboratory in the field of synchrotron radiation. It closed in 2003.

For these reasons, we have performed our experiments at the AILES beamline (Advanced Infrared Line Exploited for Spectroscopy), that indeed is dedicated to infrared absorption spectroscopy. It covers a wide electromagnetic spectral region, ranging from the far to the near infrared ( $5 - 10000 \text{ cm}^{-1}$ ), with an extension into the THz domain. The beamline has been specifically designed for a high level of mechanical stability, in order to minimize the background noise, and offers the possibility to perform measures by varying both pressure and temperature.

These specific advantages have allowed us to investigate the vibrational motion of water molecules in our confined geometry by changing the experimental conditions and exploring a frequency range that is wider with respect to that covered by the most up-to-date literature [249, 250]. In fact, the peculiar characteristics of a synchrotron light (high flux and brilliance), combined with the dedicated design of AILES, have made possible to obtain absorption spectra with a good signal-to-noise ratio not only in the MIR frequency domain, but also in the FIR range (table 4.1), allowing an investigation of the connectivity band, otherwise impossible to assess with laboratory sources.

IR range	$\text{cm}^{-1}$
THz	20–60
FIR	50–600
MIR	500–9000

Table 4.1: Spectral acquisition ranges available at the beamline AILES.

Two spectroscopic stations can be fed by synchrotron light at AILES [249]: a high resolution ( $0.001 \text{ cm}^{-1}$ ) interferometer mainly dedicated to gas phase experiments (this first interferometer will not be described further as it was not used for our experiments) and a lower resolution interferometer used for condensed matter studies, based on a Michelson interferometer (fig.4.3). The AILES interferometers are also equipped with internal sources, useful when the synchrotron light is not available. In particular, we benefited from the internal Globalbar source for measuring in the MIR domain [251]. The Globalbar, whose name is simply a combination of *glow* and *bar*, is a silicon carbide rod, electrically heated at 1200 K and emitting continuously in the MIR range ( $300 - 4500 \text{ cm}^{-1}$ ). Even though its brilliance is several orders of magnitude lower than that of synchrotron radiation, we could obtain spectra of satisfying quality in the MIR region as well.

The temperature can be reduced from 353 K down to 4 K, thanks to a helium closed cycle cryostat.

Concerning the detectors, two different types are installed depending on the frequency range of the absorbed radiation. In the FIR and THz domain a thermal bolometer is used. It consists of an extremely sensitive thermistor made of boron-doped silicon, connected to a heat reservoir by a resistance. Any thermal radiation reaching the detector causes a temperature change which, in turn, generates a change in resistance that is then amplified and measured as a voltage difference. In order to reduce the contribution coming from the thermal background, the bolometer is cooled down at liquid helium (4.2 K). Conversely, the liquid nitrogen cooled mercury-cadmium-tellurium MCT photodetector is more efficient for measures in the MIR region.

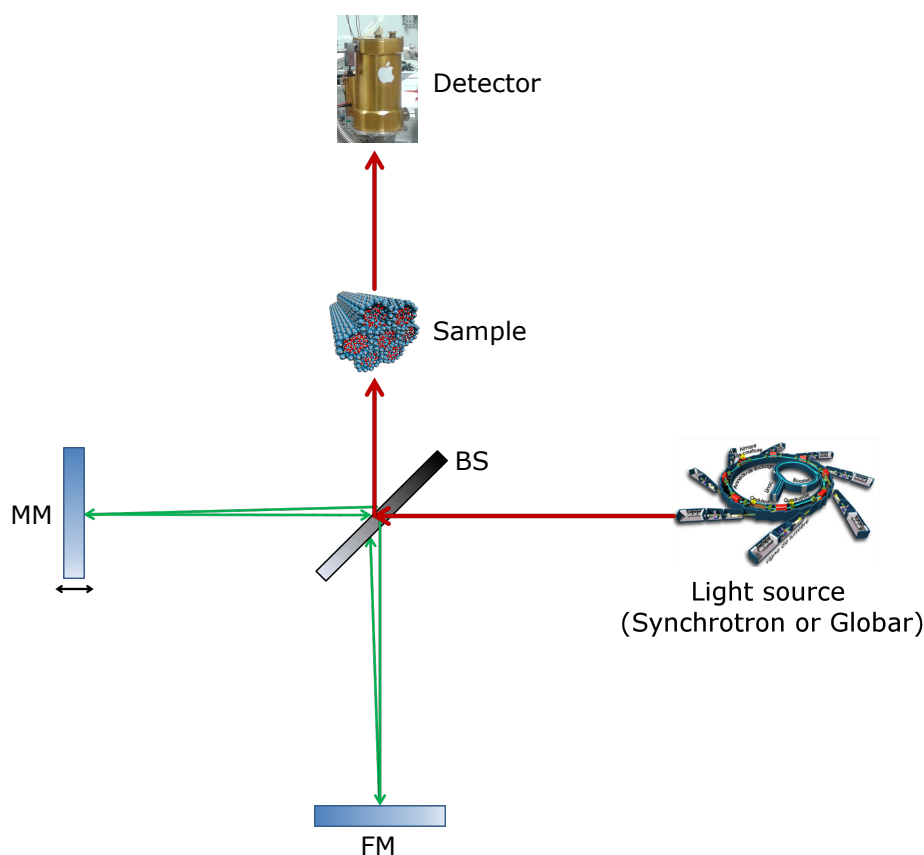


Figure 4.3: Schematic representation of a Michelson interferometer unit (FTIR). The infrared beam hits a beam splitter (BS), that is a semitransparent mirror which splits the incoming beam into two perpendicular beams; the BS is positioned at an incident angle of  $\sim 45^\circ$ , and, ideally, 45% of the incident light is transmitted and 45% is reflected. The two beams travel separate paths: one is transmitted to a moving mirror (MM), the other one is reflected and conveyed to a fixed mirror (FM). After being reflected by the respective mirrors, the first beam is reflected by the BS while the second beam is transmitted through it. Then the two beams recombine and are conveyed to the sample compartment and the detector. Before to recombine, the two beams travel a different optical path and the difference ( $\delta$ ) can give rise to constructive or destructive interference of the two beams. In particular, we have constructive interference if the optical paths differ by an integer multiple of the photon wavelength ( $\delta = n\lambda_0$  with  $n = 0, 1, 2, \dots$ ); on the contrary, the interference is destructive if the optical paths differ by an odd integer of half a wavelength ( $\delta = (2n + 1)\frac{\lambda_0}{2}$  with  $n = 0, 1, 2, \dots$ ). The translating mirror moves at constant velocity, thus the intensity of the recombined beam (for a monochromatic source) is a sinusoidal signal oscillating between zero (destructive interference) to a maximum (constructive interference).

### The high-pressure/low-temperature (HPLT) set-up

In addition, the AILES beamline offers several set-ups and well-controlled sample environments, with two working configurations available: transmission and reflectivity. For our experiments we have exploited only the high-pressure/low-temperature (HPLT) set-up in transmission configuration [227], hence the description hereunder will be focused on it (fig.4.4).

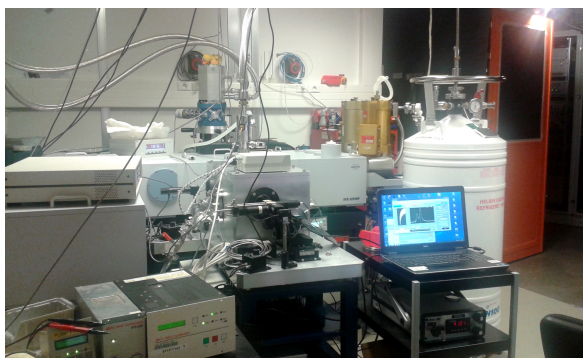


Figure 4.4: External view of the HPLT set-up at the AILES beamline. In the picture the vacuum chamber containing all the elements along the light path (described in the text), the cryostat, and the temperature controller are visible. Also a portable computer is shown: it represents the workstation with the Labview program (developed by the beamline scientific staff) able to tune the cassegrains and mirror positions in order to obtain an alignment as fine as possible and correct it during the measurement. This program has been developed also for fitting the fluorescence lines of ruby and hence provide a direct measurement and registration of the pressure inside the cell.

The AILES HPLT set-up is equipped with a diamond anvil cell (DAC), being the diamond extremely hard and transparent in the IR and THz range (fig.4.5(a)). Nevertheless, such a sample environment requires very small samples (size of the order of hundreds of microns), since the sample is placed into a hole of  $100 - 200 \mu\text{m}$  in diameter and  $60 \mu\text{m}$  in thickness, inserted into a thin metal slab, named *gasket*<sup>6</sup>, and then accommodated between the diamond faces. This restriction to small volume samples makes synchrotron radiation, several orders of magnitude more brilliant than commercial IR source, essential to obtain good signals under pressure over the complete IR range and specifically in the far infrared. The sample is loaded into the cell together with a transmitting medium and few ruby chips. The transmitting medium has to be chosen on the basis of the sample type and the desired spectral range and is necessary to realize a pressure distribution as homogeneous as possible within the sample. Instead ruby is used for the *in situ* calibration of the pressure, by exploiting its fluorescence emission lines, whose wavelength varies with pressure (apart from a temperature-dependent shift that can be easily corrected). It is preferable to have more than one ruby chip, inserted at different positions, in order to evaluate the homogeneity of the pressure inside the cell, being the laser spot much smaller than the sample area. The maximum pressure reachable is  $\sim 20 \text{ GPa}$ . The temperature during cooling is registered by a thermocouple probe (Chromel/Alumel), placed inside the metal body of the cell. The available temperature range is  $\sim 35 - 320 \text{ K}$ .

The interferometer mounted on the AILES branch dedicated to condensed matter studies is a FTIR Bruker IFS 125 HR. It is accommodated in a vacuum chamber, pumped down to  $\sim 10^{-5} \text{ mbar}$ , with a system of 12 gold coated mirrors that direct the light beam through a collimator and a double condenser system (the Cassegrain objectives) [227], which conveys the beam to the the DAC with a focusing spot of  $\sim 300 \mu\text{m}$ . The position along  $x$ ,  $y$  and  $z$ -axis of both Cassegrains and DAC can be finely adjusted by means of motorized stages, remotely controlled, allowing their repositioning and tuning the alignment *in situ* during measurements under vacuum. The light path in transmission configuration is shown in

<sup>6</sup>The gasket wraps the two diamond faces as a ring, avoiding sample leaking and preventing the diamond faces to be too closely approaching.

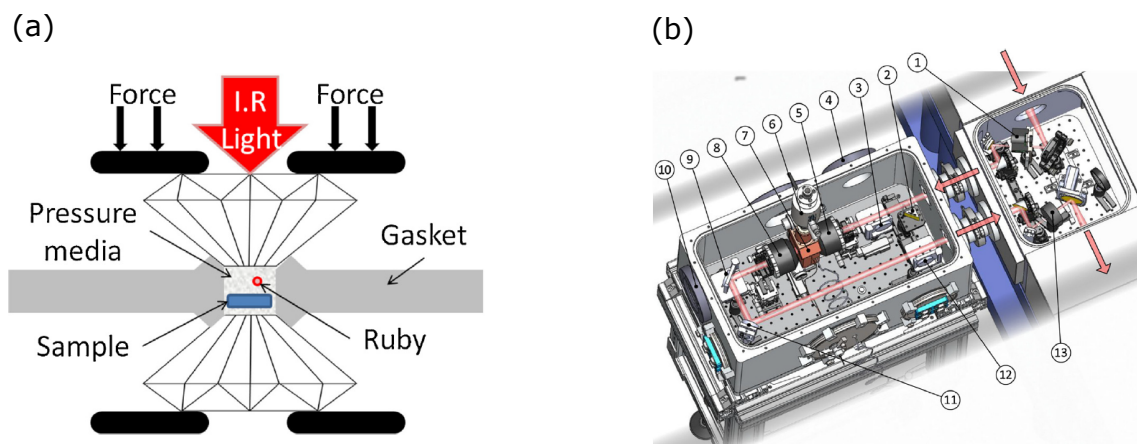


Figure 4.5: (a) Schematic view of a DAC [227]; the sample is loaded in the gasket hole between diamonds, together with the transmitting pressure medium and ruby chips. (b) Layout of the HPLT setup and the spectrometer [227]: (1) polarizer, (2, 3, 9, 11, 12) mirrors, (4, 10) viewports, (5, 8) Cassegrain reflective objectives, (6) cryostat, (7) DAC, (13) aperture.

fig.4.5(b). Additional primary and turbomolecular pumps placed under the chamber ensure a even better vacuum ( $\sim 2 \cdot 10^{-6}$  mbar), necessary for measurements at very low temperatures to prevent the condensation of residual water molecules onto the external walls of the cell or on the cold finger of the cryostat.

# Chapter 5

## Experimental results: Neutron Scattering

*Science, my lad, is made up of mistakes, but they are mistakes which it is useful to make, because they lead little by little to the truth.*

*Jules Verne*

### 5.1 Overview and motivations

Neutron scattering has been applied to investigate modifications occurring in the microscopic structure of water when confined in a mesoporous silica matrix across the supercooled region of its phase diagram. In particular, we were interested in testing the hypothesised existence of a Widom line, i.e. the line where the correlation lengths (or specific heat) exhibit their maxima in the  $P - T$  plane, as it should imply the existence of a Second Critical Point (section 1.4.3) [128, 132, 252, 253]. With this aim, we also wanted to assess the existence of a density minimum in confined water at  $\sim 200 - 210$  K, as purported by Chen and co-workers [70]. Such a result, questioned by part of the scientific community [176, 195, 254, 255], has been invoked as a proof of the existence of two water polymorphs below its homogeneous nucleation temperature. How is a density minimum related to the second critical point hypothesis? A thermodynamic quantity useful to understand this point is the thermal expansion coefficient  $\alpha_P$  (or isobaric expansivity), that is related to the temperature derivative of the density. At temperatures above the density maximum,  $\alpha_P$  is positive for water and for the vast majority of liquids. As the temperature decreases,  $\alpha_P$  drops, crosses zero and becomes negative (the liquid expands on cooling). An open question concerns what happens as the temperature is lowered further: does  $\alpha_P$  remain negative, or return to positive values? If the latter case occurs, the temperature at which  $\alpha_P$  crosses zero again and becomes positive is that of a density minimum.

This means that if an inflection point appears in the density vs temperature profile, a distinct peak is expected in the thermal expansion coefficient between the temperatures of minimum and maximum density. Chen's group claims to have found such a peak in  $\alpha_P$  at  $\sim 230$  K

[256, 257]. Coincidentally, some other studies on confined water have shown that the transport coefficients reveal a fragile-to-strong dynamic crossover (FSC) at  $225 \pm 5$  K [210, 258], and the Stokes-Einstein relation breaks down at the same temperature [64, 259]. As discussed previously, this feature has been explained by the hypothesis of a liquid-liquid critical point (LLCP) at high pressure. The occurrence of the  $\alpha_P$  maximum and the FSC has led to argue that a single thermodynamic and dynamic crossover temperature may exist, and it is around 230 K. Many computer simulations of water infer the existence of a density minimum [253, 260–262], but convincing experimental observations are not so abundant and date back to just a few years ago [70, 256, 257, 263, 264]. However, an interesting and complete overview of the recent experimental investigations focused on the density minimum and the FSC in deeply supercooled water under strong confinement, and the connection with the LLCP picture, can be found in [265].

This thesis has therefore allowed us to take part in the vivid debate about the thermodynamic models able to rationalize the anomalous behaviour of water, especially in its supercooled phases, attempting to shed light on this controversial topic.

For this purpose, we used two MCM-41 substrates with different confining sizes, investigated at ambient pressure along a path from room temperature to the deeply supercooled region. One of the two substrates had a pore size able to induce a severe-confinement effect suppressing ice nucleation, as expected from results reported in literature [70, 266, 267]. By contrast, in the other confining medium the pores were large enough to have ice formation below the homogeneous nucleation temperature  $T_H$ , and it has been used as the reference against which the enhancement of density fluctuations was assessed. We made use of isotopic substitution in the filling liquid: the substrates were hydrated with heavy water ( $D_2O$ ) and a light/heavy water mixture. Heavy water was preferred to light water because  $D_2O$  is less affected by inelastic effects with respect to  $H_2O$ . In addition,  $D_2O$  provides a more marked scattering contrast, allowing for an easier identification of changes in diffraction pattern as temperature decreases [255].

Thanks to the new NIMROD diffractometer installed at ISIS, the wide  $Q$ -range accessible for each sample has made possible to investigate, by a single measurement, the microscopic correlations in the confined liquid at larger  $Q$ , the mesoscopic ordered structure of the substrate giving rise to Bragg peaks at low  $Q$  values and the density fluctuations possibly occurring at even lower  $Q$  range.

## 5.2 Sample preparation

As already specified, we chose MCM-41 as confining medium because it offers several peculiar advantages when compared to other substrates, i.e. a very regular geometrical shape giving Bragg peaks clearly visible in SANS and neutron diffraction experiments, a regular distribution of pore size, tunable pore size with nanometric dimensions, a high hydrophilicity, and lack of swelling upon hydration. As stated in advance, we used two preparations of MCM-41, differing in the pore diameter. The samples appeared as a white powder and were synthesized by Prof. Gérald Lelong (IMPMC, Université Pierre et Marie Curie, Paris), following the procedure described, for instance, in [31]. The main properties of the two preparations are listed in table 5.1.

Sample	Pore diameter $\Phi$	TPV
MCM-41/C10TMABr	2.8 nm	0.5 mL/g
MCM-41/C18TMABr	4.5 nm	1.1 mL/g

Table 5.1: Main properties of the two MCM-41 preparations used for our samples. TPV stands for *Total Pore Volume*, given by the ratio between the empty space inside the matrix (i.e. the volume occupied by pores) and the mass of MCM powder. It has been determined by means of the BET model for the adsorption isotherms [164, 171, 268].

The matrix with narrower and wider pores will be addressed hereafter as C10 and C18, respectively.

First of all, as close as possible to the experiment days (in order to reduce the possibility of hydrolysis of the pore surface), MCM-41 powder needed to be calcinated to remove the surfactant molecule used for the synthesis and left inside for protecting the pore structure. Calcination consisted in heating the MCM-41 powder in air at 550°C (with a rate of 1 K/min). After that, the hydration procedure was accomplished by using a sealed desiccator at room temperature ( $\sim 298$  K), with an open source of water to provide a saturated humidity environment. Both confining media were loaded with pure D<sub>2</sub>O and with a mixture of 92% H<sub>2</sub>O and 8% D<sub>2</sub>O (labelled as HD mixture), which gives no structural signal from water at low  $Q$  and thus was used to test that the hydrated matrix did not experience significant structural changes as a function of temperature. In the case of C10 sample (smaller pore size), particular attention was paid in setting the time of exposure to the water vapour in order to achieve  $\sim 90\%$  of pore filling. A complete filling of the pore volume was considered unsafe, because of the expected volume expansion experienced by water on cooling. On the other hand, for C18 the hydration level was a less crucial parameter and we were only interested in not to overload the matrix for avoiding a huge amount of hexagonal ice from water pushed out of the pores below the freezing temperature. Hence a partial or at least a complete filling was considered as satisfactory, with no particular regard for the exact value of the hydration level. The resulting hydration level,  $h$ , is reported in table 5.2, where  $h$  is defined as the grams of water (D<sub>2</sub>O or HD mixture) per gram of dry MCM, namely:

$$h = \frac{\text{mass of water (g)}}{\text{mass of dry powder (g)}} \quad (5.1)$$

where the mass of the adsorbed water can be easily determined by a difference between the mass of the hydrated sample and the mass of the dry matrix, that is to say by measuring the mass gain after the hydration procedure.

Generally speaking, the adsorbed species in MCM-41 samples are characterized by type IV adsorption isotherms (see fig.2.2). But water has a special behaviour. In fact, whatever the pore diameter, water sorption phenomenon in MCM-41 samples looks like a capillary condensation phase transition and adsorption isotherms are expected to be of type III or V [188].

	$h$ (D <sub>2</sub> O)	$h$ (HD mixture)
MCM-41/C10TMABr	0.39 g/g	0.38 g/g
MCM-41/C18TMABr	0.48 g/g	0.48 g/g

Table 5.2: Hydration level  $h$  (defined as in eq.5.1) obtained for the two MCM-41 matrices when loaded with pure D<sub>2</sub>O and the HD mixture made of 92% H<sub>2</sub>O and 8% D<sub>2</sub>O.

In the remainder of this thesis MCM-41 matrix filled with  $D_2O$  and HD mixture will be addressed as  $wet_{D_2O}$  and  $wet_{HD}$ , respectively.

## 5.3 Neutron diffraction experiments

### 5.3.1 Experimental details

The neutron diffraction experiments have been performed at the NIMROD time-of-flight diffractometer installed at the ISIS spallation neutron source. As stated before, NIMROD is particularly recommended for our purposes and is well suited to evidence at the same time critical fluctuations and/or crystallization events.

Both the hydrated and dry MCM-41 samples were loaded into a standard Ti-Zr cell (2 mm internal spacing and 1 mm wall thickness), with a flat geometry. The Ti-Zr alloy is a good material for sample containers in neutron experiments because its contribution to the cross-section is essentially incoherent. Titanium has a bound coherent scattering length of  $-3.44$  fm and zirconium  $+7.16$  fm; if these two elements are alloyed in the mass ratio  $Ti:Zr=7.16:3.44$ , i.e. 2.1:1, then the total coherent scattering length should equal zero. Sample environment consisted of a CCR (Closed-Cycle Refrigerator) cryostat, as we were interested in bringing the sample to low temperatures at ambient pressure.

Neutron diffraction measurements were collected on both wet and dry substrates, thus we measured six samples: C10 (small pores) hydrated with  $D_2O$ , C10 hydrated with HD mixture, C18 (big pores) hydrated with  $D_2O$ , C18 hydrated with HD mixture, dry C10 matrix, dry C18 matrix. In the case of wet samples, temperature range ran from ambient down to 160 K, in a step of about 10 K. Dry matrices were measured at room temperature and at 209 K, temperature chosen as a reference to check if any significant modification occurs upon cooling. Moreover, measurements were carried out both on warming and cooling paths, in order to test the presence of thermal hysteresis. For each measurement at a given temperature the sample was exposed to the neutron beam for  $\sim 150$  minutes (after the thermalization time), enough to gain a good statistics.

As required for data reduction (section 5.3.2), in addition to the measurements of the samples loaded into the container ( $I_{SC}$ ), three further data sets were collected: the intensity diffracted by the empty container ( $I_C$ ), the background intensity ( $I_B$ ), measured leaving the scattering position empty with the radiation beam on, and the intensity scattered by a vanadium polycrystalline slab ( $I_V$ ), used for putting the data on an absolute scale of scattering cross-section.

### 5.3.2 Raw data reduction

The raw diffraction patterns coming from a typical neutron diffraction experiment are not immediately ready for data analysis, but need to be properly corrected to obtain the true DCS containing the meaningful structural information about the sample. As a matter of fact the raw scattered intensity does not represent the differential cross-section introduced in chapter 3 and the incoherent (or self) component depends on the scattering angle because of the inelastic distortions introduced by the nuclei recoil (and neglected in the theoretical description).

Raw data correction has been performed by using the software GudrunN [269], that permits to obtain differential cross sections from the experimental patterns measured (total scattering data). The procedure demands the following main steps:

**Check of detectors' efficiency.** Since TOF diffractometers have large arrays of detectors, it is likely that some of them do not work perfectly (they may be unstable or too noisy). If the number of neutrons counted by a detector bank is out the range defined by  $\langle n \rangle \pm \sigma_n$  (where  $\langle n \rangle$  and  $\sigma_n$  are the average and standard deviation of revealed neutrons, respectively), the information given by such a detector must be removed from the data analysis.

**Normalisation to the incident flux.** The measured intensities for the background, sample and container must be normalised to the number of incident neutrons they have received, measured by a monitor placed after the moderator. This step is essential if different measured datasets need to be compared.

**Background subtraction.** The background intensity  $I_B$ , resulting from neutrons which reach the detector without interacting with the sample, is subtracted from the  $I_C$  and  $I_{SC}$  spectra.

**Calibration to the vanadium spectrum.** Vanadium is used to put the diffraction data on an absolute scale. It is characterized by a very small coherent cross-section, producing very weak Bragg reflections. Vanadium is a solid metal with a precisely known density, it is stable (does not need a container) and can have a highly simple and regular geometry (a cylinder or a flat plate). Thanks to the heavy mass of vanadium nucleus, also the inelasticity corrections can be easily evaluated using an approximate model. Vanadium is measured at the beginning of the experiment, with the same beamline conditions used for the samples. Since its cross-section is purely incoherent,  $I_V$  results proportional to the density of the polycrystal, thus allowing to calibrate  $I_C$  and  $I_{SC}$  spectra to absolute units. Therefore, after the background subtraction is accomplished, the experimental pattern is divided by the vanadium spectrum and the absolute scale is measured in barns atom<sup>-1</sup> sr<sup>-1</sup>.

**Calculation of the multiple scattering correction.** Multiple scattering arises when the neutron is scattered by more than one nucleus before reaching the detector. This process invalidates the biunivocal correspondence between the scattering angle  $\theta$  and the momentum transfer  $Q$  ( $Q = 4\pi \sin(\theta/2)/\lambda$ , with  $\lambda$  computed from the neutron TOF), that concerns a single event of elastic scattering. Multiple scattering appears in the experimental pattern as a smooth function decreasing towards higher scattering angles and increasing with the cross section intensity. In fact, multiple scattering usually affects the spectrum at low  $Q$ , as the double scattering is the most probable event and neutron is deflected towards small angles. The multiple scattering corrections are calculated by Monte Carlo simulations that model the structure factor of the sample, usually neglecting the inelastic scattering contributions [270]. The multiple scattering contribution to the signal comes mostly from slow neutrons, which have higher probability to interact with nuclei more than once before emerging from the sample. Since NIMROD receives the beam from the TS2, whose energy spectrum has a greater number of neutrons with relatively low energy, the multiple scattering correction becomes particularly important for this instrument.

**Calculation of the absorption correction.** The attenuation given by absorption events from both the sample and the container is obtained using an algorithm developed by Paalman and Pings (for cylindrical samples and annular sample cells) [271], that calculates the attenuation coefficients only as a function of the scatterer shape and its total average cross section.

**Deadtime correction.** Most detectors have an intrinsic deadtime  $\tau$ , that indicates the minimum time interval between two events needed for the detector to be able to resolve them as two separate events. When two consecutive events reach the detector with a time delay shorter than  $\tau$ , they are counted as a single event.

**Detectors grouping.** Typically detectors at similar scattering angles are grouped together, since they have similar resolution functions. Multiple detectors can be combined by simply calculating the arithmetic mean of the counts in each detector at a given angle, or by computing an average weighted by the counting statistics. Generally, this latter strategy provides better results as poorly counting detectors have a reduced weight in the average calculation.

**Can subtraction.** After the  $I_C$  and  $I_{SC}$  spectra have been properly corrected following the aforementioned steps, the empty cell signal can be subtracted from the sample spectrum in order to obtain the experimental cross section we seek,  $\Sigma(Q)$ .

**Inelastic scattering correction.** As stated in section 3.2, the inelastic scattering is corrected by empirically subtracting a smooth function from the data. Actually, the diffraction scattering cross-section in a TOF experiment is an integral of the double differential cross section evaluated along paths of constant time-of-flight. If the incident neutrons do not strictly conserve their energy but exchange it at some extent with the target nuclei during the scattering events, the integral to be evaluated is not trivial:

$$\frac{d\sigma}{d\Omega} = \int_{\Gamma} \frac{\Phi(k_i)}{\Phi(k_e)} \left( \frac{\partial k_i}{\partial k_e} \right) \frac{\epsilon_d(k_f) k_f}{\epsilon_d(k_e) k_i} F_n(Q, \omega) d\omega \quad (5.2)$$

where  $\Gamma$  is the constant  $Q$  path,  $\Phi(k_i)$  is the flux of incoming neutrons,  $\epsilon_d(k_f)$  is the detector efficiency at the energy of the scattered neutron, and the product  $\Phi(k_e)\epsilon_d(k_e)$  comes from the instrument calibration. The factor  $\partial k_i/\partial k_e$  for a TOF experiment is given by  $(a+1)/[a+(k_i/k_f)^3]$  (with  $a = L_0/L_1$ , being  $L_0$  and  $L_1$  the primary and the second flight path respectively). It represents the Jacobian accounting for the change of integration variable from  $2\pi/k_f$  to  $\omega$ . Unfortunately, there are several systematic errors in a real experiment that make difficult to calculate the corrected DCS. The principal error source is the integration path which in a real experiment departs from constant  $Q$ . In a TOF experiment the inelastic distortions are more important at low  $Q$  and increase with the scattering angle (fig.5.1).

The total differential scattering cross section obtained after the correction procedures is normalized to the number of nuclei hit by the beam. This is possible also in the case of powder samples, by considering the *tweak factor*, being it the inverse of packing fraction. The packing fraction affects the calculation of the attenuation and multiple scattering because in this case the sample atomic density is the specified atomic density divided by the tweak factor. As a result, what we obtain is a pattern given by the scattered intensity as a function of the momentum transfer  $Q$ . Notwithstanding, we can also be interested in seeing how scattered

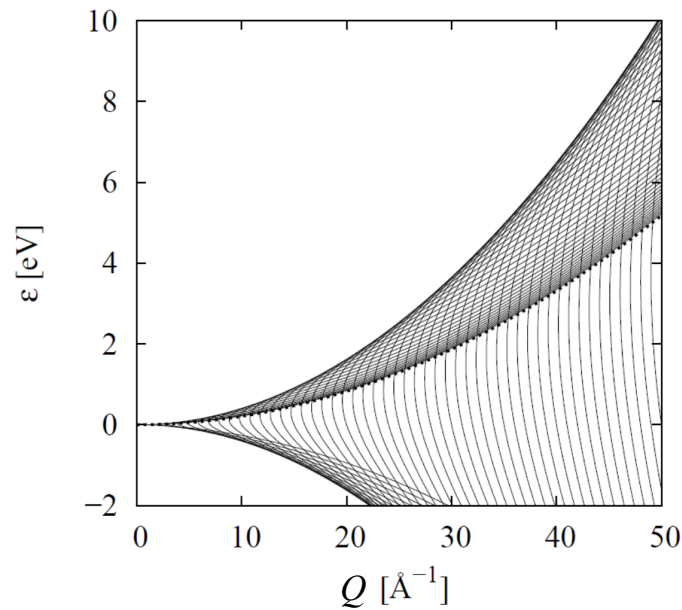


Figure 5.1: Constant time-of-flight trajectories in  $(Q, \epsilon)$  space sampled in a time-of-flight diffractometer (SANDALS at ISIS) at a scattering angle of  $30.71^\circ$  ( $Q$  and  $\epsilon$  are the momentum and the energy transfer respectively). The dashed line represents the recoil energy of a proton. At high  $Q$  values the trajectories approach the ideal constant  $Q$  condition (trajectories are more parallel to the  $\epsilon$ -axis) in the recoil energy region. Conversely, at low  $Q$  the trajectories become highly curve, especially near  $Q = Q_e$  ( $\epsilon = 0$ ) and this is why in a TOF experiment inelastic corrections are expected to be more relevant at low  $Q$  (figure from [269]).

intensity looks like in the real space ( $r$ -space). The software GudrunN performs the transformation from the  $Q$ - to  $r$ -space by means of Fourier transform computed using the top hat convolution method [225] or the revised Lorch truncation function<sup>1</sup>.

In addition to the standard correction procedure described in the present section, some of our diffraction patterns required a further adjustment. Indeed they showed small "steps" at specific  $Q$  values (fig.5.2) or big "holes" similar to those expected in case of a resonance. We found that such defects in the experimental DCS were ascribable to slightly different levels at the maximum elastic  $Q$  for each NIMROD's detector group, causing a bad merge of the signal [225].

### 5.3.3 Substrate characterization and determination of the sample density

In order to suitably correct and analyse the data, GudrunN needs to know the composition and the density of each sample, including the MCM-41 substrate. As far as the composition is concerned, we know that MCM-41 is made of amorphous silica, thus we can write it as  $\text{SiO}_2$ . The relative molar composition of the sample in terms of  $\text{SiO}_2$  and water ( $\text{D}_2\text{O}$  or HD mixture) can be easily set from the hydration level  $h$  experimentally determined, as reported in section 5.2. Indeed we have:

<sup>1</sup>A direct Fourier transform of the diffraction data is unfeasible because it is traditionally affected by unphysical oscillations due to truncation.

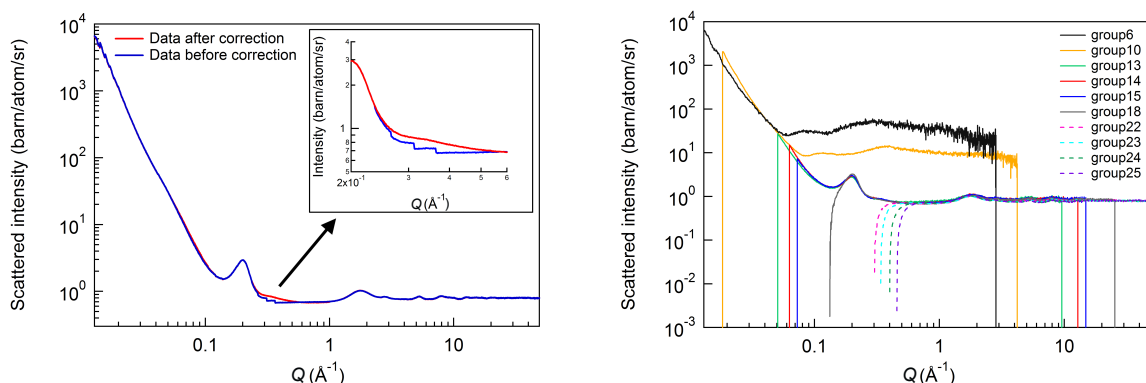


Figure 5.2: Left: Example of "steps" in the DCS of C10 sample filled with D<sub>2</sub>O at 284 K, due to an unfitting merge of the scattered intensity revealed by different detector groups. The graph reports the comparison between the scattering pattern before and after the application of the procedure adopted for removing the small "steps" arising around 0.2 – 0.5 Å<sup>-1</sup>. Right: Some of the 25 NIMROD detector groups are individually represented. In particular, the groups accountable for the bad merge of the signal are indicated by dashed lines (groups from 22 to 25); the signals coming from those groups have been cut or removed in order to obtain a proper merge of all the detectors in the final DCS.

$$h = \frac{m_w}{m_{SiO_2}} = \frac{PM_w \cdot n_w}{PM_{SiO_2} \cdot n_{SiO_2}} \quad (5.3)$$

where  $m_w$  and  $m_{SiO_2}$  is the mass of water and silica matrix respectively, and PM and  $n$  indicate their molar mass and the number of moles. Since the molar masses and  $h$  are known quantities, eq.5.3 can be used to determine the ratio between the molar amount of filling water and that of substrate as  $n_w/n_{SiO_2} = (PM_{SiO_2}/PM_w) \cdot h$ .

What is unknown is the exact number of silanol groups (-SiOH) on the inner pore surface, because it may vary for each sample, depending on the particular preparation route and the hydration/dehydration cycles endured by the substrate. Moreover, by comparing the diffraction pattern from pure silica (measured in a previous experiment) [202, 203] with that from dry MCM-41 substrate, it arises that the latter misses pure amorphous silica by a factor of several units. Such a discrepancy can only be explained admitting that there was additional non-exchangeable light hydrogen present which had not been removed during the sample preparation. In particular, by requiring that the diffraction pattern of MCM-41 matrix after normalisation had the same amplitude oscillations as pure silica, the estimated fraction of light hydrogen not exchanging with the adsorbed water was around 48% (compared to the number of Si atoms) for the smaller pores (C10) and 24% for the bigger pores (C18).

Regarding the density of dry MCM-41 substrates, the problem is not easy as for a bulk sample. In the case of confining matrices, a multiscale approach is required [202]. This means that at each level of description (macroscopic, nanoscopic, or microscopic) a corresponding density can be defined:

- the density of the pore walls, also known as local density  $\rho_l$ ;
- the density of a single grain,  $\rho_g$ ;
- the density of the macroscopic powder in the sample container exposed to the neutron beam,  $\rho_m$ .

Since we do not have the possibility to directly measure the local density of MCM-41 during the experiment, we took advantage of literature data, assuming  $\rho_l = 2.11 \text{ g/cm}^3$  [30]. The density of a single grain is related to the local density by the following expression:

$$\rho_g = \frac{\rho_l}{1 + \rho_l \cdot \text{TPV}} \quad (5.4)$$

where TPV is the total pore volume, i.e. the volume occupied by the pores within 1 g of powder. Finally, the macroscopic powder density  $\rho_m$  is proportional to the grain density  $\rho_g$  and to the packing fraction of the sample,  $\eta$ , inside the sample container. The packing fraction is defined as the ratio between the volume occupied by the powder grains,  $V_g$ , and the total volume of the sample container,  $V$ , thus we can write  $\rho_m = \rho_g \cdot \eta = \rho_g \cdot \frac{V_g}{V}$ . This latter quantity, once expressed in  $\text{\AA}^{-3}$ , is the number density required by GudrunN to yield the correct DCS.

In the case of wet substrates, the average density of the sample can be obtained with the following steps:

- Determination of the MCM grain density, as expressed in eq.5.4.
- Determination of the local density of the filling liquid ( $\text{D}_2\text{O}$  or HD mixture), given by  $\rho_w = h/\text{TPV}$ .
- Evaluation of the average density of the filling liquid inside the grain, given by:  $\rho_{w,g} = \frac{\rho_w}{1 + (\rho_l \cdot \text{TPV})^{-1}}$ .
- Assessment of the average density of the hydrated sample expressed as  $\bar{\rho} = \rho_g + \rho_{w,g}$ .
- Determination of the corresponding number density, by means of the packing fraction, as explained above.

The packing fraction,  $\eta$ , along with the silanol number, are not known *a priori*, but can be determined by the diffraction data following a *trial and error* procedure. Essentially, one tries to give a reasonable estimate of the sample density and silanol number able to obtain a satisfactory match of the simulated pattern with the experimental one at high  $Q$ . In other words, one firstly sets the right composition of the sample, that is the concentration of species known with the largest accuracy, i.e. Si and O (from the silica matrix  $\text{SiO}_2$ ), and D, O, H (from the absorbed water and the additional non-exchangeable H); then all the other parameters are evaluated accordingly, to have a DCS oscillating around the expected self-scattering level at high  $Q$ . It is worth noting that an exact determination of the sample density, the powder packing fraction and the number of silanol groups was not particularly important for our aims, as we did not need to perform computer simulations to characterize the structure of our samples from an atomistic point of view. Thus we calculated the macroscopic powder density by means of the aforementioned relations and we could adjust the other unknown parameters with no particular refinement, but simply bearing in mind we wanted to obtain a reasonable DCS level at high  $Q$ .

## 5.4 Experimental results

### 5.4.1 Dry substrates

At the mesoscopic scale, MCM-41 appears as a honeycomb array of cylindrical pores in a silica matrix, characterized by two lengths: the interplanar distance,  $d$ , and the pore radius,  $r$ . The interplanar distance determines the position of the low- $Q$  Bragg peak in the DCS of the dry matrix (fig. 5.3). As expected, lowering the temperature the MCM structure does not change; this holds true for both C10 and C18 substrates, as shown by measuring the DCS of dry matrices at high and low temperature (285 K and 209 K, respectively) and verifying the almost perfect overlapping of the two spectra for both substrates (fig. 5.3).

In the case of C10 sample, the (100) Bragg peak visible at  $Q_{100} = 0.192 \text{ \AA}^{-1}$  yields an interplanar distance equal to  $d_{100} = 2\pi/Q_{100} = 3.27 \text{ nm}$ . Starting from the knowledge of the total pore volume of the substrate (table 5.1) and the interplanar distance calculated above, the matrix pore radius can be assessed by means of a relation involving only geometric parameters:

$$r_{\text{geom}} = d_{100} \sqrt{\frac{2}{\pi\sqrt{3}} \cdot \frac{\rho_l \cdot TPV}{1 + \rho_l \cdot TPV}} \quad (5.5)$$

The last equation gives for pore radius a value of 1.42 nm, corresponding to a pore diameter  $\Phi = 2 \cdot r_{\text{geom}} = 2.84 \text{ nm}$ , which is in excellent agreement with the size listed in table 5.1.

Concerning C18 sample, the (100) Bragg peak is positioned at  $Q_{100} = 0.120 \text{ \AA}^{-1}$ , resulting in an interplanar distance  $d_{100} = 5.24 \text{ nm}$ . The pore radius calculated according to eq. 5.5 leads to a pore diameter of 5.29 nm. This result shows a much less satisfactory accord with the expected value of  $\Phi$  reported in table 5.1. This discrepancy may be due to an inaccurate evaluation of TPV or pore radius in the sample preparation stage. However it should be noted that for MCM-41 conventional thermodynamical methods (such as BJH method, based on the capillary condensation of nitrogen gas inside the pore volume) often underestimate the pore size [202]; on the other hand, geometrical descriptions, which do not take into account the real structure of the sample but rely on a regular and defect-less model of the system (for instance, the pore roughness is neglected), may in some cases overestimate the matrix pore size. Therefore, the pore sizes given in table 5.1 (2.8 nm for C10 and 4.5 nm for C18) should be regarded as nominal diameters, given the intrinsic dependence of their measurement on the method employed. Despite these uncertainties, we can conclude that C10 sample ensures a pore size sufficiently small to be suitable for probing the possible suppression of the freezing/melting phase transition in confined water, whereas C18 has a pore size big enough to allow a nucleation process at low temperature. This outcome guarantees that we can regard the bigger size sample as a reference to understand and interpret the scattering pattern obtained from the smaller size sample, which represents the focus of our study.

Furthermore, with the idea to use C18 sample as a reference, we notice that a bigger pore size (5.29 nm) comparing to the nominal diameter (4.5 nm) would not represent a disadvantage. If the hydration procedure is properly performed, since the vapour pressure is the same at the same temperature, we expect that with a bigger core volume it is less likely that water is pushed outside the pore. Hence, we can be confident that in the case of scattering

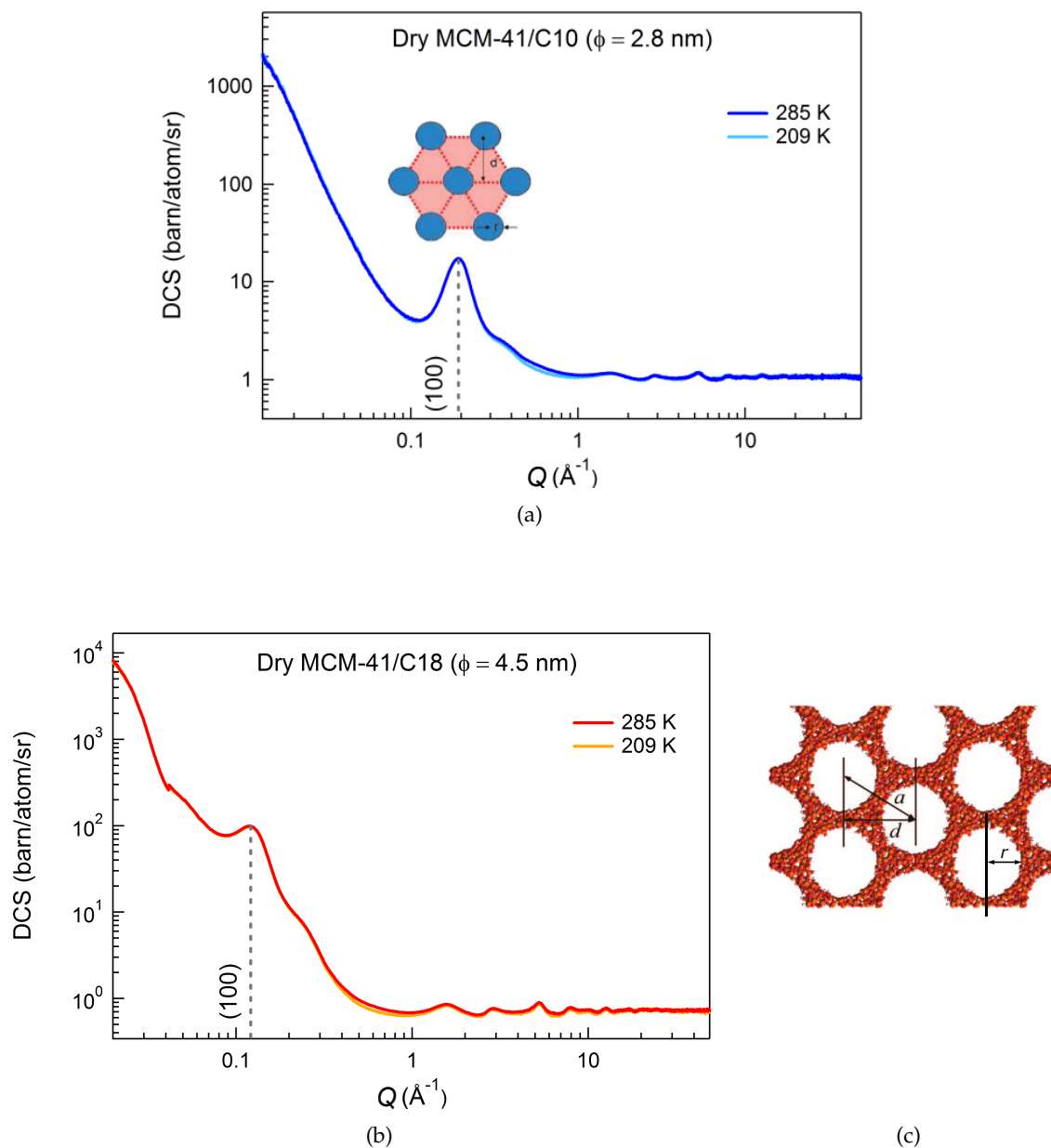


Figure 5.3: Differential scattering cross section for dry C10 (a) and C18 (b) MCM-41 at ambient and low temperature (285 K and 209 K, respectively). The structure of the porous medium is clearly temperature-independent. A pronounced Bragg peak (convoluted with the instrumental resolution function) is visible at low  $Q$ , corresponding to the reflection by (100) plane of the 2D hexagonal array of cylinders. The position of this peak allows for determining the interplanar distance  $d$  and the pore radius  $r$ , as described in the text. The other reflections, i.e. (110) and (200), which should be found on the right side of the main peak (100), are not visible because of their low intensity and the broadening effect at low- $Q$  due to the finite resolution of the instrument. (c) Two dimensional hexagonal structure of MCM-41 material. The inter-pore and interplanar distance are labelled as " $a$ " and " $d$ ", respectively. The former is related to the Bragg peak (110), the latter to the (100) Bragg reflection visible in (a) and (b) (figure from [272]).

patterns revealing the presence of ice, such a solid phase would be found within the pore volume, even if the pore size was actually bigger.

## 5.4.2 Hydrated samples

The typical scattering pattern of the hydrated MCM-41 silica matrix, obtained after the data correction procedures previously described, is displayed in fig.5.4.

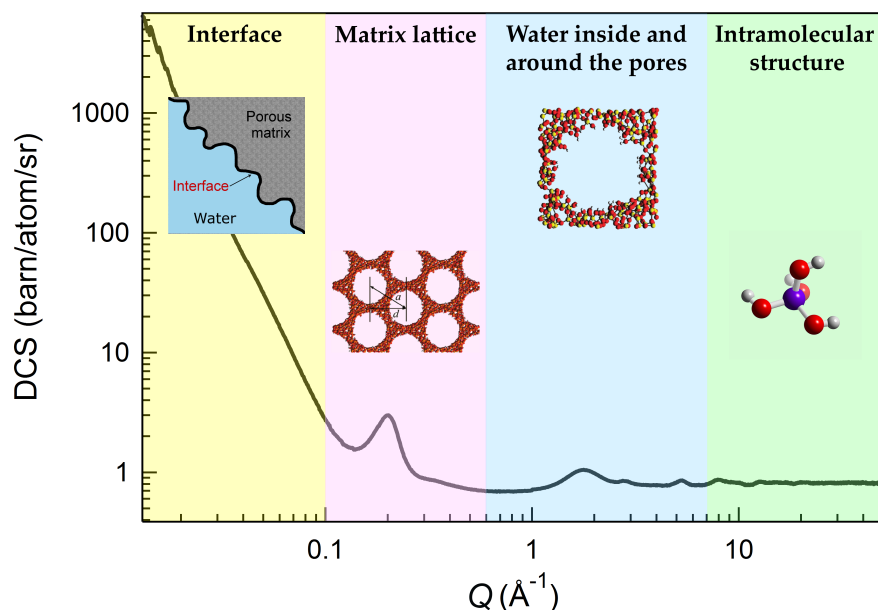


Figure 5.4: Example of neutron differential cross section of C10 hydrated with  $\text{D}_2\text{O}$  at 284 K, measured at the NIMROD diffractometer. In the graph four  $Q$ -ranges are evidenced with different colours, corresponding to the different size scales accessible. At very low  $Q$  (yellow) a steep rise gives information about the intergrain interfacial scattering (Porod region); data at low  $Q$  (pink) can be used to extract information on the matrix lattice, as shown in section 5.4.1; the intermediate  $Q$  region (blue) provides structural information about adsorbed water, giving insights into the arrangement of molecules within and around the pore in the matrix; at larger  $Q$  (green) structural intramolecular information are accessible.

As discussed at the opening of the present chapter, the diffractometer NIMROD offers the important advantage of exploring, with a single experiment, a wide  $Q$ -range spanning from the mesoscopic to the microscopic scale, as shown in fig.5.4. At very large  $Q$  we gain structural intermolecular information, at intermediate  $Q$ -range the structure of the confined water is accessible, at low  $Q$  we can investigate the 2D hexagonal internal structure of the confining MCM-41 system, and at very low  $Q$  density fluctuations (if present) occur and should become visible along the steep rise of the signal. The latter represents the intergrain interfacial scattering, also known as Porod region, and owes the main contribution to its intensity to the grain fractal packing, coming from the scattering length density (SLD) contrast between air and MCM grains.

First of all, we must ascertain that the substrate does not undergo any significant modification with temperature when hydrated. This can be achieved by observing the DCS of the wet<sub>HD</sub> C10 and C18 samples at different temperatures over intermediate and high  $Q$ -range, as shown in fig.5.5 and 5.6. As expected, contributions to DCS mostly come from the dry

matrix, being the coherent signal relative to water properly suppressed. Furthermore, the diffraction patterns of  $wet_{HD}$  collected at different temperatures (from 285 K down to 209 K) are well superimposed throughout the investigated  $Q$ -range: this demonstrates that the hydrated substrate does not change when temperature is lowered.

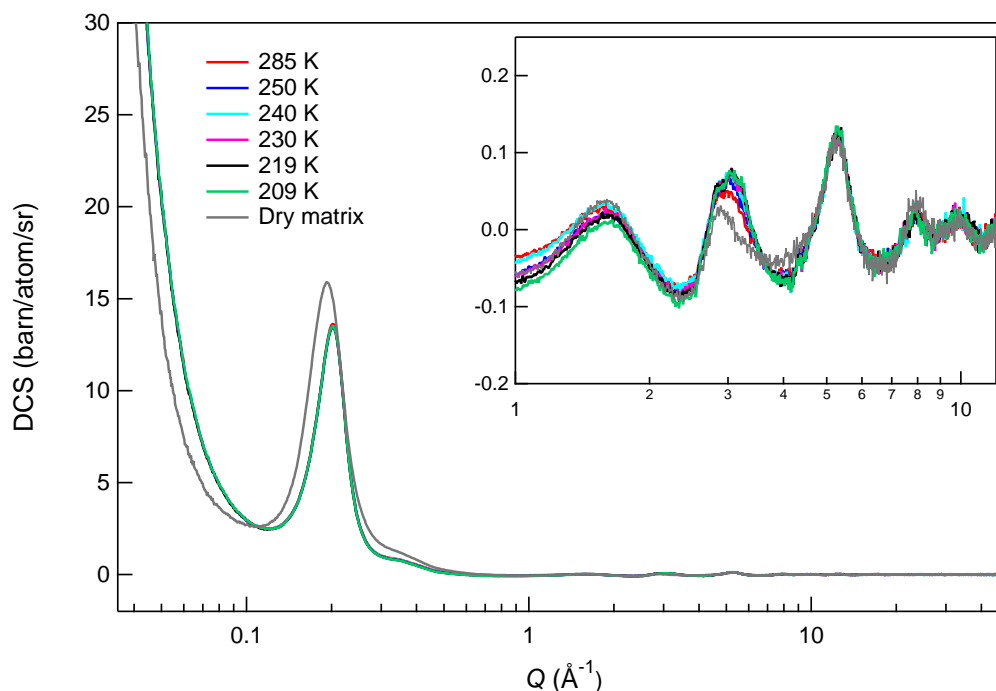


Figure 5.5: DCS of C10 sample (pore size 2.8 nm), hydrated with the HD mixture. The DCS of dry matrix has been reported for comparison. Only slight differences can be addressed between the Bragg peaks of dry matrix and those of the hydrated one; the little change in intensity is due to a different contrast between silica/vacuum and silica/HD mixture configurations. The HD mixture has been prepared with a concentration of light and heavy water specifically calculated to suppress the signal from water inside the pores. This strategy ensures that any possible change in DCS must be ascribed to the porous matrix structure. The inset shows the  $Q$ -range interested by the suppression of water peaks and reveals that no significant modifications of the porous matrix structure occur when hydrated.

After this preliminary check, it can be convenient to analyse the water structure and its modifications by subdividing the entire  $Q$ -range of the differential cross section of hydrated samples in three main subregions: the short-range correlation region, including the  $D_2O$  peak (blue area in fig.5.4), the medium-correlation domain, which encompasses the silica peak (fig.5.4, pink area), and the long-range correlation zone, corresponding to the Porod region (fig.5.4, yellow area). It should be useful to remind that our attention will be focused almost exclusively on the  $wet_{D_2O}$  C10 sample. The bigger pores matrix will be simply regarded as a reference for pinpointing the ice nucleation occurrence, whereas the HD mixture has completed its function in probing the temperature–independence of hydrated substrate structure, as addressed above.

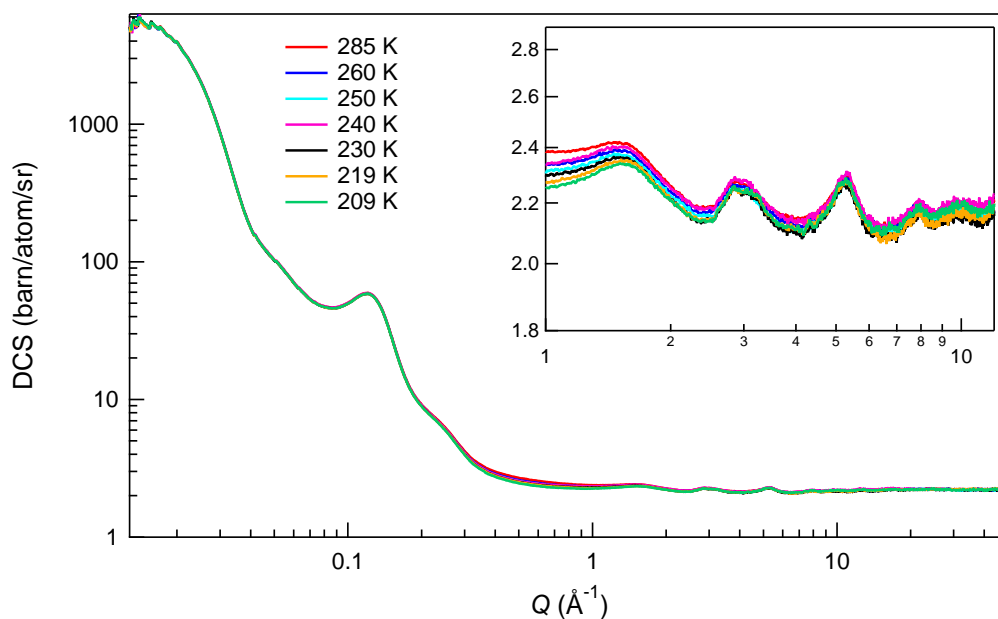


Figure 5.6: DCS of C18 sample (pore size 4.5 nm), hydrated with the HD mixture. The HD mixture has been prepared with a concentration of light and heavy water specifically calculated to suppress the signal from water inside the pores. This strategy ensures that any possible change in DCS must be ascribed to the porous matrix structure. The inset shows the  $Q$ -range interested by the suppression of water peaks and reveals that no significant modifications of the porous matrix structure occur when hydrated.

### 5.4.3 Short-range correlations: D<sub>2</sub>O peak

Let us consider the differential cross sections of wet<sub>D<sub>2</sub>O</sub> C10 sample over a  $Q$ -range restricted to the region comprising information about water structure (fig.5.7), bearing in mind that possible modifications of the diffraction profile mainly come from changes in the phase state of the pore water<sup>2</sup> [175]. In addition, C10 substrates were carefully hydrated not more than 90% of the total pore volume, thus we can rule out the possibility to observe relevant contributions to the diffraction pattern coming from  $I_h$  or  $I_c$  which could result from the crystallization of inter-grain water, i.e. water outside the pores and trapped within pockets in the silica grains.

Since it is by far the most prominent feature of the DCS in the  $Q$ -range here examined, we will focus our attention on the first diffraction peak (FDP) of D<sub>2</sub>O, because the other peaks are much less instructive as they are less intense than FDP by about an order of magnitude. At ambient temperature (284 K) the diffraction pattern of D<sub>2</sub>O is that typical of liquid state, with a broad FDP centered at  $1.78 \text{ \AA}^{-1}$ . As long as the temperature is higher than around 250 K, the DCS does not exhibit any relevant change, except for a slight intensity increase. This demonstrates that from ambient temperature down to (at least) 250 K confined heavy water is in a supercooled state. The most significant modification occurs between 250 K and 239 K, when the signal of ice formation can be observed. Indeed the FDP is distinctly more intense, sharpened and steeply shifted towards lower  $Q$  as the temperature decreases, moving from  $1.78 \text{ \AA}^{-1}$  at 284 K to  $1.69 \text{ \AA}^{-1}$  at 239 K. Both values are significantly below  $\sim 1.95 \text{ \AA}^{-1}$ , that

<sup>2</sup>As discussed in chapter 2, in a porous environment we can distinguish between two types of water: *free* water, that is the water in the middle of the pore volume, and *bound* water, that is the non-freezable water layer adjacent to the pore walls. In the present section we use the expression *pore water* to address free water.

is the position of the main peak for bulk water at 298 K [176, 254, 264]. The fact that in confined water the main diffraction peak is always below the position in the bulk is a first and simple indication that the density of confined water is lower than that of the bulk [151]. This view that water confined in porous silica MCM-41 has lower density than the bulk is also supported by other works [176, 177], including structural studies (neutron diffraction experiments assisted by EPSR simulations) [149, 151], that evidence a large decrease in the number of triangular water conformations (OW-OW-OW<sup>3</sup> angle equal to about 60°) [149]. Such a result is particularly meaningful as it suggests a more open structure of water network upon confinement. How much the density of confined water is below that of bulk is still a matter of debate, but several evidences suggest a decrease of order 6 – 10% in the core region [151]. We remark that, since water is not expelled from pores, a variation in density is due to a different local arrangement of water molecules and not to a change in their number. For the sake of completeness, we notice that in [256, 273] an opposite conclusion is reached, namely that, for full hydrated pores, confined water has a density  $\sim 8\%$  higher than the bulk density. However, no further evidences confirming this result have been reported in literature so far, and it seems to be an artifact of data analysis rather than a physical feature. In addition, other studies based on molecular dynamics simulations of deeply supercooled H<sub>2</sub>O confined in MCM-41 are at odds with results presented in [151], as they find that the effective water density is around 0.98 g/cm<sup>3</sup> and reaches the value of the bulk density (1.0 g/cm<sup>3</sup>) in the inner part of the pore volume [274]. The FDP width, calculated at the FWHM of a Lorentzian fit<sup>4</sup>, shrinks from 0.97 Å<sup>-1</sup> at 284 K to 0.62 Å<sup>-1</sup> at 239 K, when the onset of crystallization appears. We notice that 239 K is consistent with the homogeneous nucleation temperature expected for bulk D<sub>2</sub>O, taking into account the isotopic effect due to the presence of deuterium. Since in the literature it has been pointed out that the main peak of water moves to lower  $Q$  as the density falls (whatever the temperature and pressure), the behaviour exhibited by our neutron diffraction patterns indicates that (i) confined water has always a lower density than the bulk, and (ii) a rapid decrease in the pore water local density is observed, due to an increasing order of the tetrahedrally hydrogen-bonded network in supercooled D<sub>2</sub>O, which can be regarded as a signature of the formation of the crystalline solid phase. This observation is also confirmed by [176], where the radial distribution functions derived from neutron diffraction data of D<sub>2</sub>O confined in MCM-41 clearly show interatomic correlations indicative of an increasing hydrogen bonding upon cooling. Comparing DCS obtained in small pores with those measured in the larger pore substrate strengthens this interpretation. Fig. 5.8 displays such a comparison between selected temperatures of both small ( $\Phi = 2.8$  nm) and large ( $\Phi = 4.5$  nm) pore samples. On the basis of the results reported in literature about porous media with pore size larger than around 3 nm (see [177], for instance), water nucleation cannot be avoided. According to the Gibbs-Thomson equation (section 2.4.1) the depression of the the freezing temperature ( $\Delta T_p$ ) is smaller as the pore radius becomes bigger, thus water in the larger pore sample should transform into crystalline ice at a higher temperature (i.e. a temperature closer to the freezing point of bulk water). This is indeed what we observe in wet<sub>D<sub>2</sub>O</sub> C18 sample: D<sub>2</sub>O undergoes a complete solidification at around 230 K. Conversely, C10 substrate should have a pore size small enough to prevent ice nucleation. But this does not correspond to our findings, as a behaviour similar to that arising in wet<sub>D<sub>2</sub>O</sub> C18 is evidenced in the smaller pore sample as well, even though a coexistence of supercooled water and ice nuclei is likely to be conjectured [275]. Remarkably, the FDP of experimental DCS obtained from wet<sub>D<sub>2</sub>O</sub> C10,

<sup>3</sup>OW labels the oxygen atom in a water molecule. Thus OW-OW-OW stands for the angle formed by three hydrogen-bonded water molecules.

<sup>4</sup>The FDP peak has been fitted by a Lorentzian function with the addition of a linear background.

centred at  $\sim 1.68 \text{ \AA}^{-1}$ , does not appear as a single peak. It rather looks like the convolution of three substructures, located approximately between  $1.5$  and  $1.9 \text{ \AA}^{-1}$ , which are not present in the liquid phase. Obviously, ice peaks arising in DCS of larger pore sample has a narrower shape and is more intense. The former fact is due to the less severe confinement experienced by water within pores of  $4.5 \text{ nm}$  in diameter, that leads to a less pronounced peak broadening effect [195] (section 2.4.2). On the other hand, the difference in intensity of DCS referred to the two distinct kinds of sample has to be ascribed to the larger amount of water that can be adsorbed into C18 pores, offering a bigger internal volume.

Hence we can argue that  $\text{D}_2\text{O}$  confined in pores of  $2.8 \text{ nm}$  in diameter experiences a liquid–solid (ice) phase transition probably starting around  $239 \text{ K}$ . It is worth noting that to establish the exact onset of freezing for  $\text{D}_2\text{O}$  in a restricted environment is not straightforward, as nanoconfined water/ice does not freeze/melts as sharply as bulk water/ice (a temperature spread of several degrees is expected, depending on the cooling/heating rate) [275]. Some other authors have found consistent results working on MCM-41 and other porous silica materials with pore size similar to our C10 sample [144, 176].

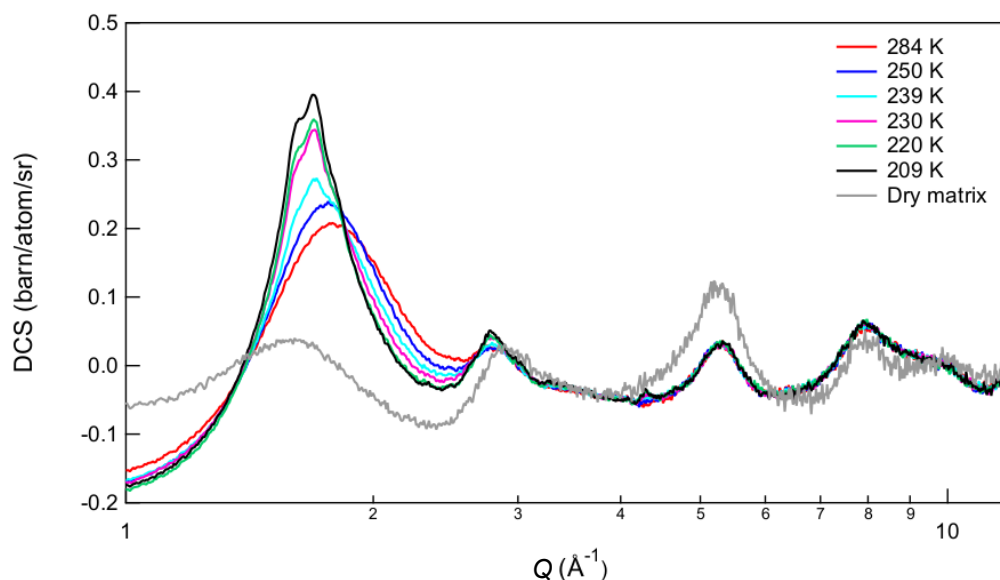


Figure 5.7: Differential cross sections of C10 sample (pore size  $2.8 \text{ nm}$ ), hydrated with  $\text{D}_2\text{O}$  at different temperatures. The diffraction pattern of dry matrix has been reported for comparison.

It is interesting to ask if the freezing temperature depression here found is in agreement with prediction of the modified Gibbs-Thomson equation (eq.2.20). Some sources of uncertainty have to be taken into account, e.g. the determination of the non-freezable water layer ( $\lambda$ ) which is indirect, is assumed to be independent of the pore radius, and relies on the true value of the pore diameter. But it is impossible to gain an absolute value of the pore radius, being it strongly dependent on the experimental technique used for its measurement<sup>5</sup>. Moreover, a reliable determination of the Gibbs-Thomson constant ( $C$ ) is also required and several different values are available in the literature, mostly depending on

<sup>5</sup>There exists a variety of methods for estimating pore radius: geometrical considerations, diffraction data, adsorption isotherms, etc. The latter is the most widely employed method, but it encompasses some uncertainty also by itself because information extracted from isotherms and the amount of gas adsorbed strongly depend on the nature of gas-surface or liquid-surface interaction.

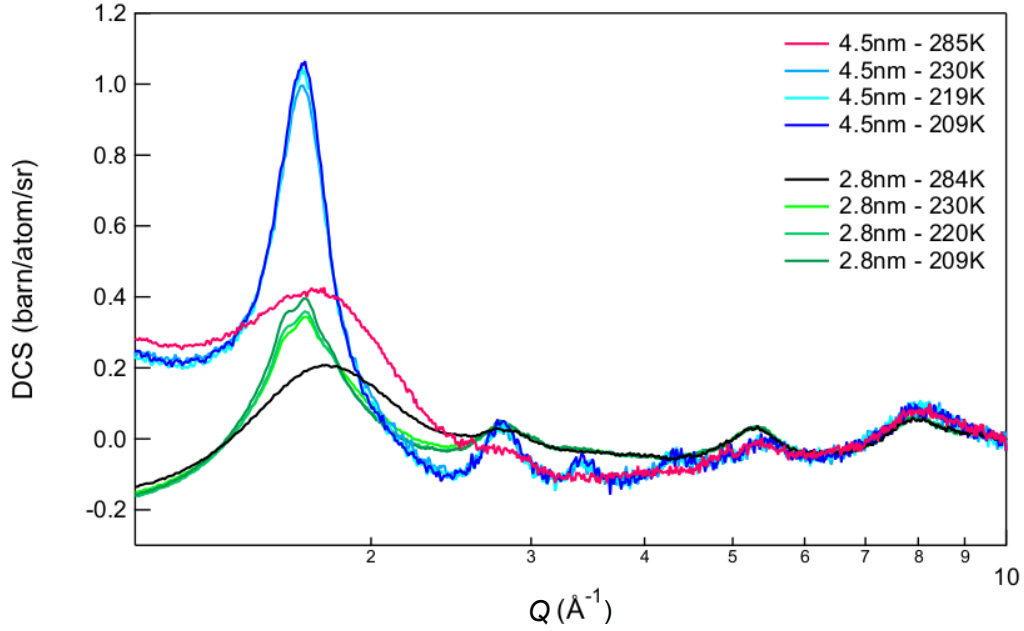


Figure 5.8: Comparison between DCS of C10 and C18 samples, hydrated with  $D_2O$  at different temperatures. Only some selected temperatures have been reported in order to make the graph easier to read. Data from the two different substrates have been labelled in terms of their pore size (2.8 nm for C10 and 4.5 nm for C18).

the particular confining medium under investigation. In our specific case, we can take advantage of the extensive and systematic studies carried out by Findenegg and co-workers on water confined in MCM-41 substrates with different pore sizes and based on vapor sorption deposition, calorimetry, and NMR spectroscopy [174, 177, 181]. In particular, Findenegg *et al.* have measured the depression of melting/freezing point,  $\Delta T_p$ , of both  $H_2O$  and  $D_2O$  for pores with different diameters in the range 2-10 nm. The plot of  $\Delta T_p$  against the inverse of the core radius  $R' = R - \lambda$  is reported in fig.5.9. Data follow linear trends: the slope of the linear fit relative to the depression of freezing point of  $D_2O$  (open circles along the green line in fig.5.9) is equal to the constant  $C$  that we are looking for. It results to be  $C \approx 34.5$  Knm.

The non-freezable layer thickness  $\lambda$  remains unknown, but we have no reliable instruments to determine it unambiguously. Despite this, we can use the experimental evidence of ice nucleation event as resulting from neutron diffraction cross-sections and apply eq.2.20 to give a reasonable estimate for  $\lambda$ . Given that  $\lambda = R - (C/\Delta T_p)$  and knowing from experiment that  $\Delta T_p = 34$  K, for  $R = 1.4$  nm, we find  $\lambda \sim 0.38$  nm, that is very reasonable and in agreement with data reported in literature for this sort of porous media (between 1 and 2 monolayers of non-freezable water at the pore wall, on average) [177, 181]. By a rough estimate, a layer thickness  $\lambda \approx 0.38$  nm corresponds to a fraction of non-freezable molecules in the contact layer,  $\varphi = 1 - (1 - \lambda/R)^2$  [177], equal to around 47%. This outcome suggests that the modified Gibbs-Thomson equation provides a good description of the depression of the freezing/melting temperature of water when confined in cylindrical pores with a size of few nanometres, assuming a non-freezable layer of  $\sim 0.38$  nm next to the pore walls. The conclusion is therefore that changes in shape and position of the first peak of  $D_2O$  confined in C10 matrix may be interpreted as a freezing phase transition. In order to assess the occurrence of a hysteresis phenomenon, as claimed by several authors, we measured

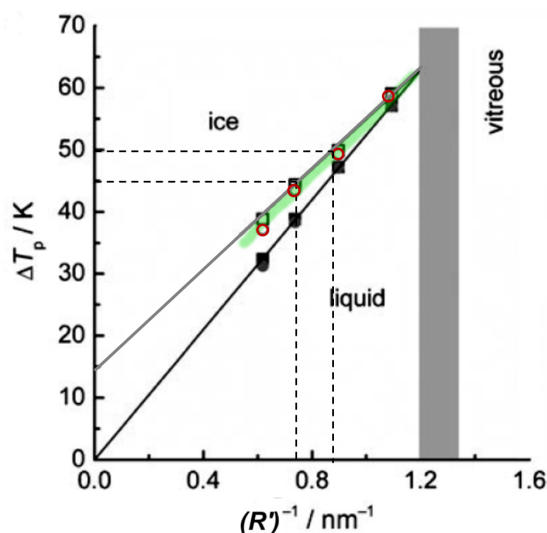


Figure 5.9: Results obtained from light and heavy water confined in MCM-41 matrix by [174]. The plot shows the temperature difference between melting/freezing transition in bulk and confined water ( $\Delta T_p$ ) as a function of the inverse pore radius ( $R' = R - \lambda$ ), also accounting for the non-freezable interfacial water layer ( $\lambda$ ), as explained in the text. Melting point depression is represented by full symbols, while freezing point depression is given by open symbols. Squares and circles are referred to data for  $\text{H}_2\text{O}$  and  $\text{D}_2\text{O}$ , respectively. Straight lines are best fits of the data. The stability regions for liquid, ice, and vitreous water are labelled. Figure from [174] has been modified highlighting the data of our interest relative to the freezing point depression of  $\text{D}_2\text{O}$  (red open circles along the green line), fitted by the grey straight line. The dashed horizontal and vertical lines identify the points we have used to calculate the slope of the fit line, corresponding to the Gibbs-Thomson equation constant  $C$ .

dry $_{\text{D}_2\text{O}}$  C10 sample again, starting from 220 K up to 284 K. If we look at the silica Bragg peak (fig.5.10), no significant differences emerge between diffraction patterns collected at the same temperature upon cooling or warming. Conversely,  $\text{D}_2\text{O}$  peak measured in warming at 239 K and 250 K is more intense with respect to that obtained upon cooling; such a difference affects only the maximum of the peak and can be regarded as the signature of an ordinary nucleation process. In fact, throughout the cooling path ice nuclei release energy to grow up, whereas they need to absorb energy to melt along the warming path. This means that upon cooling ice nuclei fluctuate between forming and melting (liquid-ice coexistence), vice-versa ice nuclei melt and form again during warming. In this case, the system has more difficulty in exceeding the nucleation potential barrier and a few more ice nuclei persist with respect to the cooling phase. This interpretation is further confirmed by observing that the melting and cooling patterns come to overlap at 284 K and below 239 K: liquid-ice coexistence is no longer observed, because  $\text{D}_2\text{O}$  is completely liquid (at 284 K) or fully crystallised (below 239 K).

Since MCM-41 does not present pore channel intersections, our outcome is also corroborated by previous studies [175, 276] suggesting that pore networking may be accountable for the thermal hysteresis frequently observed in conventional mesoporous systems. Moreover, absence of hysteresis (or the presence of a negligible hysteresis effect) for water confined in MCM-41 substrates with pore radius less than 2.1 nm was also confirmed by [175] and [263]. Findenegg *et al.* [174] have suggested that hysteresis may be a consequence of homogeneous nucleation (existence of a free-energy barrier between the metastable liquid and pore ice), or pore-blocking effects on penetration of a solid water phase front into the

pores. These authors have found a systematic decrease of the hysteresis width with decreasing pore radius<sup>6</sup>. This behaviour has been verified by reducing the pore radius in the range  $\sim 1.40 - 1.45$  nm, where hysteresis effect becomes noticeably small. Since hysteresis is a signature of first-order phase transitions, this result indicates that there exists a limiting pore diameter near  $D^* \approx 2.80 - 2.90$  nm at which melting and freezing of confined water as a first-order phase transition disappears in MCM-41 materials [174, 177]. This phenomenon likely results from a combination of two effects: *i*) the increasing disorder of the ice phase as the pore size becomes smaller; *ii*) the increasing of the short-range order in liquid water as the temperature decreases due to local bond-ordering.

It must be noted that the pore size of our C10 sample is very close to  $D^*$ , so that *a priori* determination of the character of freezing/melting transition of confined water was not easily predictable and the finding of a very weak hysteresis effect is in accordance with the interpretation and conclusions given by [174]. In addition Moore *et al.* [277], in their study on freezing/melting and structure of ice in hydrophilic nanopores, have pointed out that the nucleation of ice is homogeneous (the pore wall surface does not intervene in the ice formation) and have estimated that the critical nucleus contains about  $\sim 75 - 100$  molecules, with a radius of gyration of  $\sim 1$  nm. This value is not far from  $R = 1.4$  nm of our mesoporous sample. This finding suggests that nucleation starts to be hindered in pores with size close to ours (even though we already observe crystallization in our C10 sample), confirming the reliability of  $D^*$  experimentally found by other authors [174, 177].

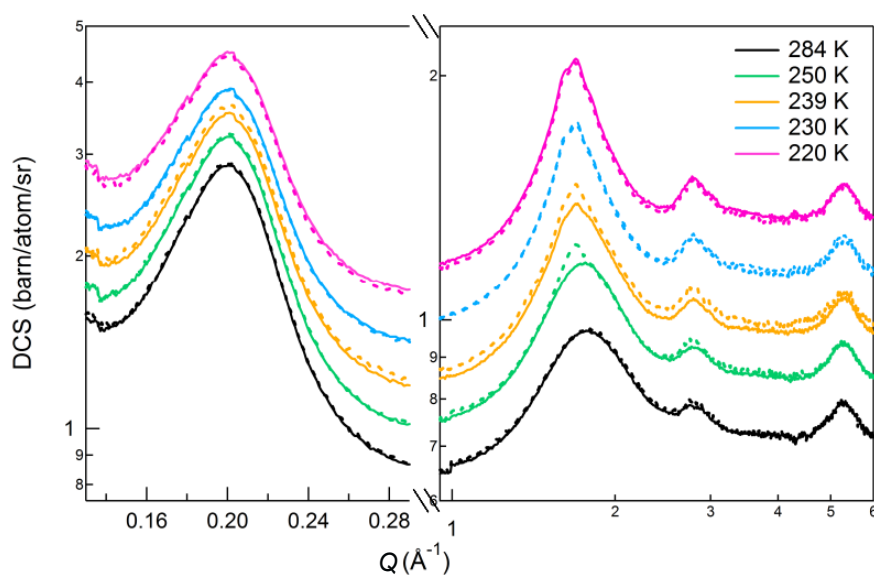


Figure 5.10: Differential cross-sections of wet- $D_2O$  C10 at different temperatures: solid lines represent scattering patterns obtained along the cooling path (from 284 K to 220 K), dashed lines indicate scattering patterns measured along the warming path (from 220 K to 284 K); each colour corresponds to a different temperature. The graph is restricted to the Bragg peak of silica matrix (left side) and to the  $Q$ -region concerning the water structure (right side); the two spectral regions are plotted on a different ordinate axis. Slight differences between DCS obtained upon cooling and warming can be noticed only in water structure. Curves at the same temperatures have been arbitrarily shifted along the vertical axis.

<sup>6</sup>It should be noted that Findenegg and co-workers find a hysteresis width of about 2 K for a pore diameter equal to 2.5 nm (close to the pore diameter of our sample) [174]. We would not have been able to appreciate this difference because we measured neutron diffraction patterns in steps of 10 K each.

Once ice nucleation has been pointed out in our sample, it may be appropriate to identify which species of ice structure is formed in this confined environment. For this aim, we attempted to benefit of computer simulations. More specifically, hexagonal and cubic ice structures were simulated by using EPSR code [219] over the same  $Q$ -range covered by our experiment and the result was compared to experimental DCS obtained from wet<sub>D<sub>2</sub>O</sub> C10 at low temperature (209 K), at which we claim to observe ice nucleation. The result is shown in fig.5.11.

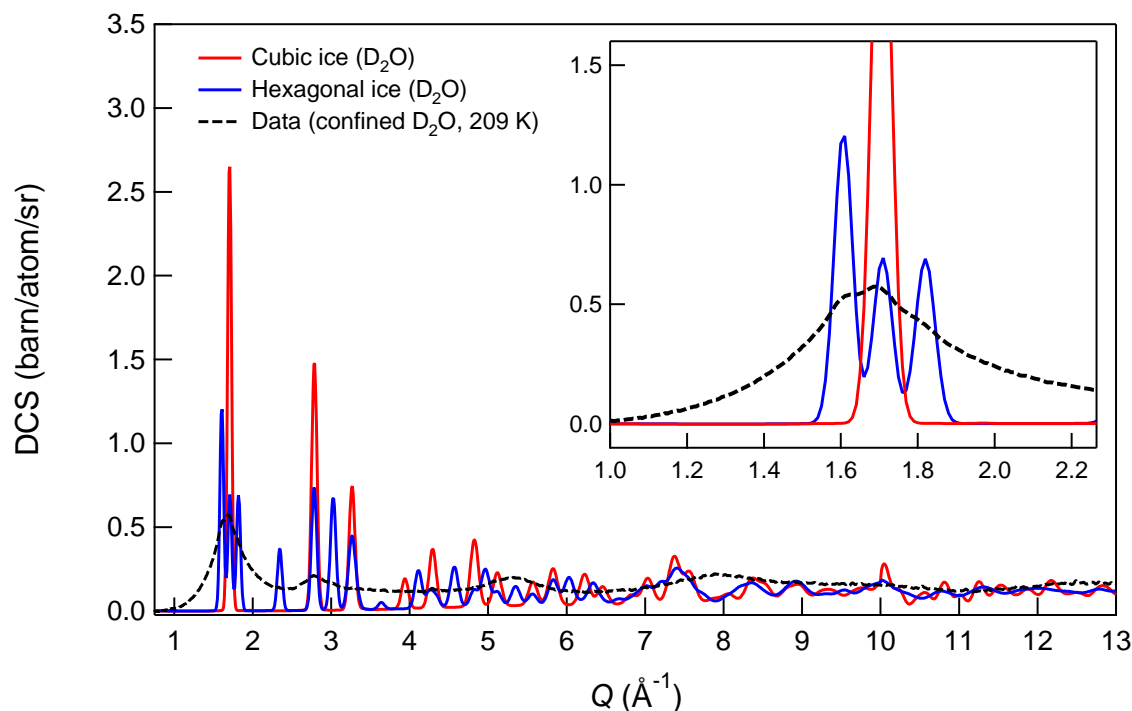


Figure 5.11: EPSR simulations of cubic and hexagonal ice, performed employing the SPC/E water model (courtesy of Alan Soper), compared to the experimental differential cross-section of  $\text{D}_2\text{O}$  (dashed line) confined in C10 matrix (pore size 2.8 nm). The diffraction patterns have been arbitrarily shifted along the vertical axis in order to have the same offset with respect to the origin. The inset shows an enlargement of the main peak (FDP) of  $\text{D}_2\text{O}$ .

We want to focus our attention to the the  $Q$ -region included between 1.0 and 3.5  $\text{\AA}^{-1}$ , where the main three or four peaks of ice DCS come out. Cubic ice is characterized by three intense and sharp peaks, first of which is centred at  $\sim 1.70$   $\text{\AA}^{-1}$ . This is also the position of the central feature in the experimental DCS, as evidenced in the inset of fig.5.11. A further correspondence can be found between the second peak of cubic ice, at  $\sim 2.78$   $\text{\AA}^{-1}$ , and the second peak of experimental DCS. The first peak of hexagonal ice diffraction pattern exhibits an easily distinguishable feature: it is split in three adjacent peaks, whose positions follow those of the aforementioned small features of the experimental DCS, taking also into account the peak broadening effect due to water confinement [188, 195, 278]. The second peak of hexagonal ice does not find any correspondence in our data, but the third peak of  $I_h$  (that overlaps the second peak of  $I_c$ ) falls on the same position of the second peak of experimental DCS. All these observations alongside literature data (section 2.4.1) contribute to reach the conclusion that ice nucleated in the small pores of MCM-41/C10 is neither pure  $I_c$  nor  $I_h$ . It rather appears as a mixture of cubic ice, probably coexisting with some hexagonal ice nuclei. This induces to confirm that the best description of ice structure inside small pores is given

by the *stacking-disordered ice I* model, according also to result recently presented by [91, 94] combining X-ray diffraction data and Monte Carlo simulations. As noted by [94], the unambiguous assignment of the degree of stacking disorder requires very high quality diffraction data, currently not obtainable for confined water by conventional diffraction methods. In fact, difference of "disordered" ice  $I_c$  with respect to ice  $I_h$  are very small and easily unnoticed in the range from 200 to 240 K. For the same reason, we are not able to quantify accurately the fraction of  $I_h$  and  $I_c$  within our pores. We can only gather that ice is present in a stacking-disordered phase, supposing that the amount of  $I_c$  is likely predominant because the formation of ice  $I_c$  is known to be favoured in nanometer-sized confined geometry.

#### 5.4.4 Medium-range correlations: silica peak

If we move to lower  $Q$ -values, we find a well-defined Bragg diffraction peak relative to the (100) plane of 2D hexagonal lattice of water cylinders in the grains of the confining matrix. This  $Q$ -region allows to probe the medium-range order and corresponds to the same momentum transfer domain accessible by a typical SANS experiment<sup>7</sup>. As introduced in section 3.1.8, in a small-angle diffraction experiment the neutron scattering intensity distribution depends on the *contrast*, namely on the difference between the density scattering lengths of the two phases. In this case, the two phases are the silica matrix and water ( $D_2O$ ) filling the pores. Heavy water is particularly suitable for being used as a filling liquid because it has a considerably different scattering length density (a factor of 2 larger) with respect to the silica matrix.

In particular, while the silica peak of wet<sub>HD</sub> C10 sample is constant with temperature, evident changes in intensity arise in the wet<sub>D<sub>2</sub>O</sub> C10 sample. Since we know that the HD mixture suppresses the coherent contribution coming from water, this last observation suggests that the contrast variation as a function of temperature is exclusively due to modifications in water structure upon cooling (fig. 5.12). Moreover, it can be immediately noticed that the width and the position of the Bragg peak do not change with temperature. This contributes to prove that the structure of the confining medium can be regarded as unaffected by temperature (at least over the temperature range explored by our experiments).

In 2007, Chen and his co-workers presented the results of their SANS experiments performed on a fully hydrated ( $D_2O$ ) MCM-41-S-15 powder [70]. The  $Q$ -range covered by their measurements goes from about 0.1 to 0.4  $\text{\AA}^{-1}$ : this means that it only encompasses the interfacial scattering and the Bragg peak due the hexagonal array of silica pores, with a lack of information about water structure at higher momentum transfer. On the basis of this work, they claimed to have identified a density minimum in deeply supercooled confined water at a temperature  $T_{\min} = (210 \pm 5)$  K (fig. 5.13). This finding would reinforce the plausibility of the existence of a Widom line emanating from the liquid-liquid critical point and passing between  $T_{\min}$  and  $T_{\max}$  (the temperature of maximum density).

It should be noted here that all the results provided by Chen and his colleagues [64, 70, 128] are relative to samples of MCM-41-S15, with a nominal pore diameter of  $(1.5 \pm 0.1)$  nm and a hydration level equal to 0.5 g  $D_2O$ /g substrate. However, this information appear to

<sup>7</sup>Usually, a typical small angle neutron scattering experiment gives access to the  $Q$ -domain corresponding to both medium and long-range correlations. The latter  $Q$ -range is known as the Porod region and is analysed in the next section.

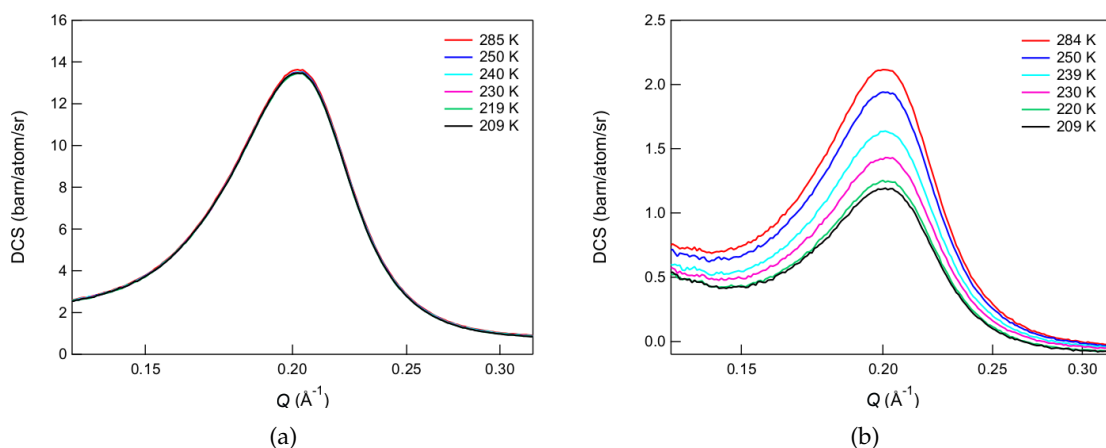


Figure 5.12:  $Q$ -region corresponding to the silica peak (i.e. the porous substrate) in  $wet_{HD}$  (a) and  $wet_{D_2O}$  (b) MCM-41/C10 samples (pore size 2.8 nm). In (a) all the DCS curves are superimposed, with no temperature-dependence. Since we know that in this sample the signal coming from water has been properly suppressed, this observation confirms that the porous substrate structure does not change upon cooling, as expected. Such an outcome implies that the difference in DCS shown in (b), that arise from the different contrast between water inside the pore and the silica matrix, is only due to changes in the  $D_2O$  structure as temperature is lowered.

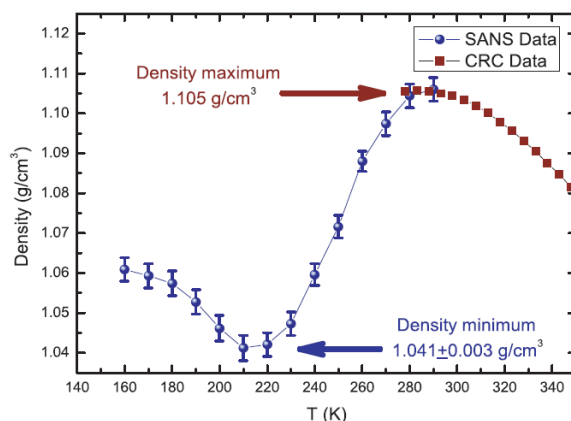


Figure 5.13: Figure from [70] showing the average  $D_2O$  density inside MCM-41-S-15 measured by SANS technique as a function of temperature. Alongside the experimental points (filled circles), also density data for bulk heavy water are reported (filled squares). The latter were taken from the *CRC Handbook of Chemistry and Physics*.

be unreliable, as demonstrated in [255]. In fact, for the specified pore radius of 0.75 nm the maximum amount of water that can be adsorbed is less than 0.2 g  $D_2O$ /g substrate. This and other factors conduce to assert that the correct pore radius for this material is near 1.25 nm, that would depict a very different scenario. Such a value is indeed not far from the limit of pore diameters at which water would show a feature in the differential scanning calorimetry trace corresponding to freezing on supercooling [177]. In addition, considering the intrinsic uncertainties in the determination of the pore radius, 1.25 nm is close enough to the pore radius of our C10 sample ( $r = 1.4$  nm), thus  $wet_{D_2O}$  C10 is expected to behave in a manner similar to that investigated in [70]. Therefore, in order to compare our results with those

presented in [70], we have restricted our attention to the silica Bragg peak alone reproducing the same analysis performed by Chen, as described in the following.

### Background subtraction

First of all, a power law decay (linear in log-log scale) has been subtracted from each diffraction pattern, in order to remove the contribution from the asymptotic part of the interfacial scattering. This procedure was essential for a comparison between the silica Bragg peaks of our sample with those obtained in [70]. After the normalization of the intensity of each diffraction pattern to its maximum, the  $Q$ -region from the onset of the silica Bragg peak downward has been fitted by a power law decay ( $I(Q) = A \cdot Q^p$ , with  $p < 0$ ), as displayed in fig.5.14.

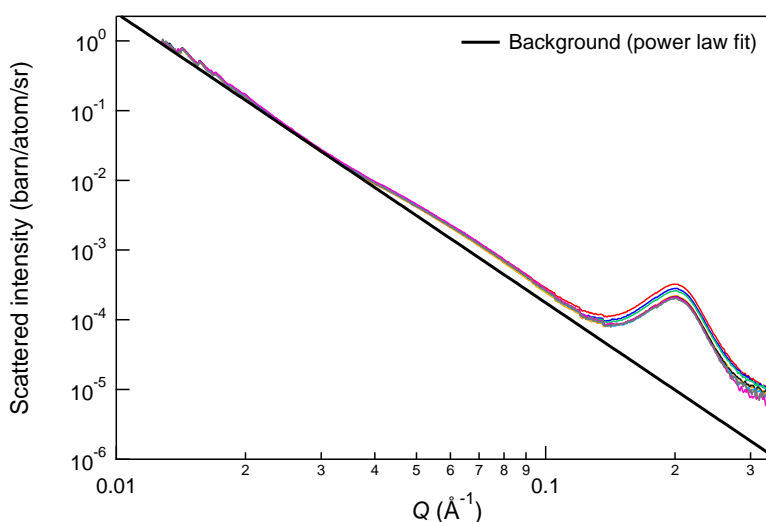


Figure 5.14: Background at low  $Q$ ,  $I(Q) = A \cdot Q^p$ , with  $p < 0$ , modelled as a power law decay for each DCS obtained from wet<sub>D<sub>2</sub>O</sub> C10. Coloured curves represent the experimental diffraction patterns at different temperatures, whereas the black line (in log-log scale) indicates the power law fit function modelling the background which we want to subtract.

For each temperature the best fit gives an exponent  $p$  close to  $-4$  ( $p = -4.13 \pm 0.14$ ), corresponding to a Porod exponent (section 3.1.8)  $D = 4$ . This result is in good agreement with the fractal dimension,  $F = 2$ , expected for a quite smooth surface [223]. Since the fit parameters are really weakly dependent on temperature, we subtracted the same background<sup>8</sup> to all the diffraction patterns shown in fig.5.14. This procedure leads to the result shown in fig.5.15A.

A direct comparison between our results with those presented in [70] (fig.5.15B) clearly points out an important issue. Qualitatively speaking, the temperature evolution of silica Bragg peak in the left panel of fig.5.15 closely resembles the diffraction patterns reported on the right side (figure from [70]): the peak intensity decreases on lowering temperature, but

<sup>8</sup>We selected as background the fit function with the smallest slope (in absolute value) in the log-log scale. This choice ensured that all the experimental points lie above the fit curve.

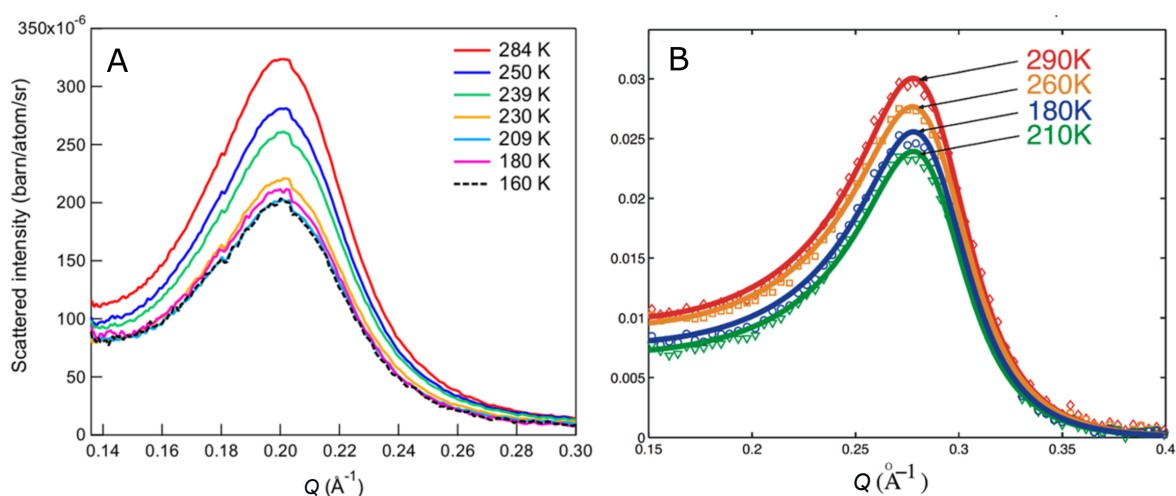


Figure 5.15: (A) Silica Bragg peak at different temperatures after background subtraction. For the sake of clarity, only some selected temperatures have been reported. The intensity monotonically decreases on lowering temperature, but at 180 K an apparent inversion of this trend is observed: the amplitude of the pink curve (180 K) becomes higher than that of the light blue one (209 K). A similar behaviour is shown in (B), where the same plot taken from [70] is visible. Despite this similarity, if we also plot the diffraction pattern measured at an even lower temperature (160 K, dashed black line in A), then we can notice that the peak intensity starts decreasing again and drops on the DCS obtained at 209 K.

at 180 K an apparent inversion of this trend is observed. In fact, the intensity of the silica Bragg peak measured at 180 K results higher than that obtained at 210 K. In [70] it was observed that the amplitude of the silica Bragg peak starts to increase again as the temperature is lowered below 180 K. Contrarily, our experiment shows that cooling the system below 180 K does not cause a further increase in the Bragg peak amplitude. Actually, the diffraction pattern measured at 160 K falls down on that obtained at 209 K. Hence, although we observe the same phenomenology as that presented in [70], the presence of a minimum is not unambiguously clear. Indeed, as evidenced in fig.5.15A, data at 209, 180 and 160 K can be considered practically coincident within the experimental uncertainty.

### Data analysis

According to the literature [70, 256, 263], the evidence of a minimum in the amplitude of the silica Bragg peak on cooling is directly related to the presence of a minimum in density of the confined water. Reasons behind this statement become clear if we explicitly write the model describing the diffraction intensity in the  $Q$ -range between  $\sim 0.1$  and  $\sim 0.3 \text{ \AA}^{-1}$  (typical for a SANS experiment). This is what we have done, following the same procedure for data analysis presented in [70, 256, 263].

The small-angle diffraction intensity distribution can be modelled as follows:

$$I(Q) = nV_p^2(\Delta\rho_{\text{SLD}})^2\bar{P}(Q)S(Q) \quad (5.6)$$

where  $n$  is the number of scattering units (i.e. water cylinders) per unit volume,  $V_p$  is the volume of a single scattering unit,  $\Delta\rho_{\text{SLD}} = \rho_{\text{SLD}}^{\text{D}_2\text{O}} - \rho_{\text{SLD}}^{\text{MCM}}$  is the neutron contrast, i.e. the difference of the coherent scattering length density between heavy water and the environment (silica substrate),  $\bar{P}(Q)$  is the normalized particle structure factor (or form factor) of the scattering unit, and  $S(Q)$  is the interparticle structure factor of a 2D hexagonal lattice. It should be noted that the scattering geometry (an array of long cylinders with a small circular cross section, as in the case of MCM-41 matrix) essentially selects only those cylinders whose axis is parallel to the incident neutron direction, so that the direction of the measured  $Q$ -vector is nearly perpendicular to the cylindrical axis.

Since the thermal expansivity of the silica substrate is negligible compare to that of water in this temperature range, eq.5.6 tells us that the scattered intensity is proportional to the square of the difference of the SLD between the confined liquid and the substrate,  $\Delta\rho_{\text{SLD}}$ . The term  $\Delta\rho_{\text{SLD}}$  in eq.5.6 contains the *contrast* contribution to the scattered intensity. In fact,  $\rho_{\text{SLD}}^{\text{D}_2\text{O}}$  is proportional to the mass density of  $\text{D}_2\text{O}$ , as  $\rho_{\text{SLD}}^{\text{D}_2\text{O}} = \alpha\rho_m^{\text{D}_2\text{O}}$ , where  $\alpha = (N_A \sum b_i)/M$ , being  $N_A$  the Avogadro's number,  $M$  the  $\text{D}_2\text{O}$  molecular weight and  $b_i$  the coherent scattering length of the  $i$ -th atom in the scattering unit<sup>9</sup>. The form factor  $\bar{P}(Q)$  of a long cylinder is given by

$$\bar{P}(Q) = \frac{\pi}{QL} \left( \frac{2J_1(QR)}{QR} \right)^2 \quad (5.7)$$

where  $L$  and  $R$  represent the length and radius of the cylinder, respectively (with  $QL > 2\pi$ ), and  $J_1(x)$  is the first-order Bessel function of the first kind. Finally, the structure factor  $S(Q)$  of a perfect 2D hexagonal lattice is a series of Delta functions (Bragg peaks) located at  $Q_1 = 2\pi/a$ ,  $Q_2 = 2\sqrt{3}\pi/a, \dots$ , where  $a$  is the length of the primitive lattice vector of the hexagonal lattice. In this case we have to take into account the unavoidable broadening of the Bragg peaks do to defects in the real lattice and the finite size of the grains. As a result, the structure factor  $S(Q)$  can be well approximated by a Lorentzian function. Summarizing, the measured neutron scattering intensity after background subtraction can be expressed as:

$$I(Q) = nV_p^2 (\alpha\rho_m^{\text{D}_2\text{O}} - \rho_{\text{SLD}}^{\text{MCM}})^2 \frac{\pi}{QL} \left( \frac{2J_1(QR)}{QR} \right)^2 \left( \frac{\frac{1}{2}\Gamma}{(Q - Q_0)^2 + (\frac{1}{2}\Gamma)^2} \right) \quad (5.8)$$

where  $Q_0$  is the Bragg peak position. In the relation above all the variables are independent of temperature<sup>10</sup>, except for  $\rho_m^{\text{D}_2\text{O}}$ , that accounts for the differences arising in the diffraction patterns shown in fig.5.12(b). On the basis of this observation, it is therefore possible to determine the density of confined  $\text{D}_2\text{O}$  by measuring the temperature-dependent neutron scattering intensity at the Bragg peak [70, 263]. However, we will demonstrate that this approach can lead to misleading conclusions. In addition, it is important to notice that in this model the density  $\rho_m^{\text{D}_2\text{O}}$  is assumed to be constant across the pore. Nonetheless, the assumption of a uniform water density upon confinement has been shown not to hold true [151, 195, 254, 255, 279].

We have fitted the model described above to our diffraction data (after the background subtraction), rewriting eq.5.8 in a simpler form:

<sup>9</sup>In general, the SLD of a molecular liquid is equal to the number density of the liquid times the scattering length of the molecule.

<sup>10</sup>Note that the scattering length of a nucleus does not change with temperature.

$$I(Q) = C \frac{J_1(QR)^2}{Q^3 R^2} \left( \frac{\frac{1}{2}\Gamma}{(Q - Q_0)^2 + (\frac{1}{2}\Gamma)^2} \right) \quad (5.9)$$

with the prefactor

$$C = I(Q_0) = A \cdot (\rho_m^{\text{D}_2\text{O}} - C_0)^2. \quad (5.10)$$

The temperature-independent parameter  $C_0$ , related to the SLD of the silica matrix, has been estimated by applying the same fitting function (eq.5.9) to the diffraction pattern obtained from wet<sub>HD</sub> C10 sample at ambient temperature (fig.5.16(a)), bearing in mind that HD mixture here used suppresses any structural signal from water and makes visible only the contribution from the confining medium. Before fitting the neutron scattering intensity using eq.5.9 to extract the value of D<sub>2</sub>O density at each temperature, we need to determine the last unknown temperature independent constant  $A$  in eq.5.10. According to [70, 257, 263, 280], we achieved this goal by normalizing the density of the highest temperature to that of bulk D<sub>2</sub>O at ambient pressure taken from NIST Scientific and Technical Database (NIST Chemistry WebBook <http://webbook.nist.gov/chemistry/fluid/>). It is known that the absolute values of interfacial and core densities of confined water at ambient temperature (298 K) are already significantly lower than bulk density, as shown in [151, 195, 202]. This implies that the normalization procedure reported above is not strictly correct. Despite this, we decided to normalize our data to the density of bulk D<sub>2</sub>O (1.11 g/cm<sup>3</sup>), instead of considering its reduction due to confinement, in order to directly compare our results to those reported in [70] (fig.5.18).

The fitted curves for different temperatures are displayed in fig.5.16(b), and show the good agreement of the model with the experimental data. The parameters of interest (Bragg peak position, Lorentzian width, and mass density of D<sub>2</sub>O) extracted from the fitting procedure are listed in table 5.3 as a function of temperature. In the last column of table 5.3 are also reported the values of D<sub>2</sub>O density obtained by normalizing the density of the highest temperature to that of confined D<sub>2</sub>O. According to [151], this latter value has been estimated as 6% lower than bulk D<sub>2</sub>O density at ambient temperature, namely 1.043 g/cm<sup>3</sup>. Fig.5.17 shows that, by normalizing to the confined D<sub>2</sub>O density at ambient temperature, D<sub>2</sub>O density values obtained as fit parameters (table 5.3, last column) are much more reasonable and consistent with the average density corresponding to the density profiles calculated by recent simulations works [151, 195, 202]. At the same time, fig.5.17 points out that changing the normalization only affects the *absolute* values of D<sub>2</sub>O density, but its temperature evolution remains the same.

Fig.5.18(a) shows the temperature evolution of the mass density of confined D<sub>2</sub>O (red circles) obtained as fit parameter from the model analysis described above. The measured D<sub>2</sub>O density shows a smooth transition from a high-density level (at high temperature) to a low-density level (at low temperature). It should be noted that, in principle, the accuracy of the absolute density we can determine with this method depends on the background subtraction. Moreover, also the unavoidable uncertainties in the determination of the pore diameter have an important impact on the calculated density. However, the shape of the density-temperature profile is independent of the data treatment before the application of the fitting model, and the qualitative features are expected to be independent of the absolute

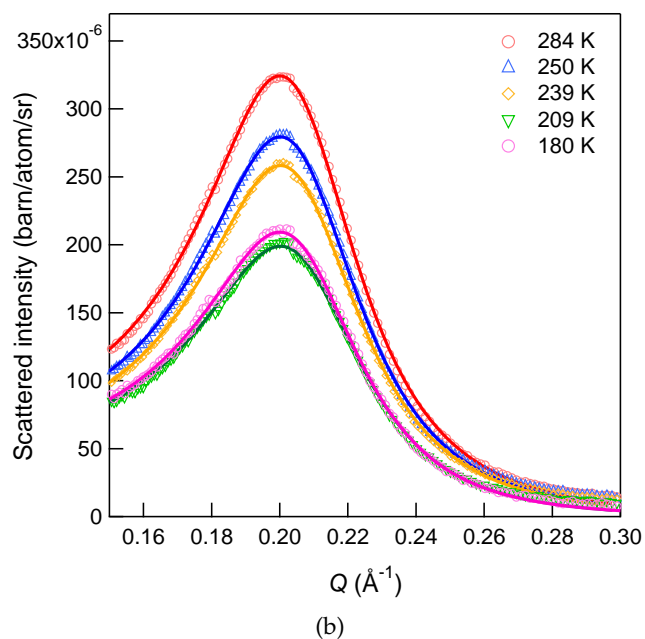
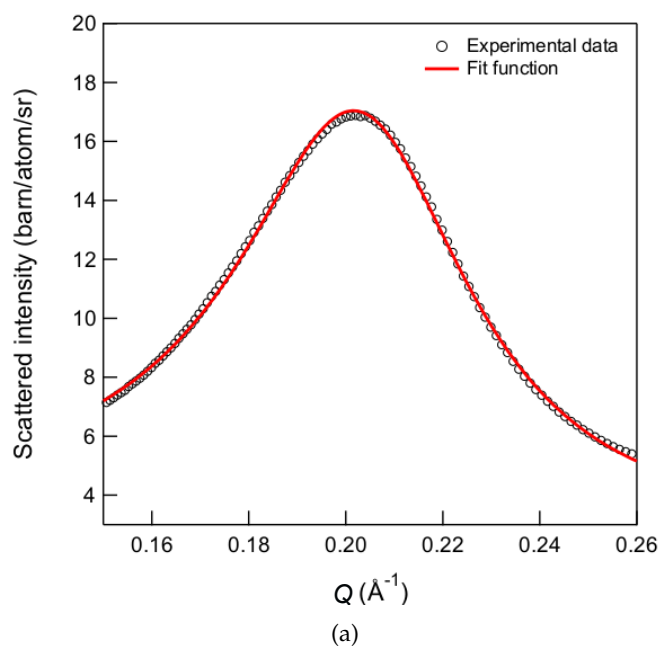


Figure 5.16: Analysis of the Bragg peak intensity distribution by using the model given by eq.5.9. (a) Fit of the diffraction pattern intensity measured from  $\text{wet}_{\text{HD}}$  C10 sample at 285 K. Density extracted as a fit parameter has been used to evaluate the constant  $C_0$ . (b) Experimental neutron scattering intensity (open symbols) obtained from  $\text{wet}_{\text{D}_2\text{O}}$  C10 sample and their fitted curves (solid lines) for different temperatures. To make the figure clearer, only some selected temperatures have been shown. However, the same good agreement between the model and the experimental data is observed at all the measured temperatures.

Temperature (K)	$Q_0$ ( $\text{\AA}^{-1}$ )	$\Gamma$ ( $\text{\AA}^{-1}$ )	$\rho_m^{\text{D}_2\text{O}}$ ( $\text{g}/\text{cm}^3$ ) [a]	$\rho_m^{\text{D}_2\text{O}}$ ( $\text{g}/\text{cm}^3$ ) [b]
284	0.204	0.0289	$1.104 \pm 0.003$	$1.043 \pm 0.003$
250	0.204	0.0292	$1.070 \pm 0.003$	$1.015 \pm 0.003$
239	0.204	0.0292	$1.060 \pm 0.003$	$0.999 \pm 0.003$
230	0.205	0.0294	$1.047 \pm 0.004$	$0.988 \pm 0.004$
220	0.205	0.0298	$1.042 \pm 0.004$	$0.985 \pm 0.004$
209	0.205	0.0299	$1.041 \pm 0.005$	$0.976 \pm 0.005$
180	0.205	0.0291	$1.044 \pm 0.004$	$0.985 \pm 0.004$
160	0.205	0.0295	$1.041 \pm 0.005$	$0.970 \pm 0.005$

Table 5.3: Principal fitted model parameters (Bragg peak position, Lorentzian width and  $\text{D}_2\text{O}$  mass density) as a function of temperature. Values reported in this table are obtained using eq.5.9 at fixed  $C_0$  ( $C_0 = 0.612 \text{ g}/\text{cm}^3$ ). The column  $\rho_m^{\text{D}_2\text{O}}$  labelled as [a] shows the values of  $\text{D}_2\text{O}$  density calculated by normalizing to the density of *bulk*  $\text{D}_2\text{O}$  at 284 K ( $\rho_{\text{D}_2\text{O}}^{\text{bulk}} = 1.11 \text{ g}/\text{cm}^3$ ), according to [70]. Instead, the column  $\rho_m^{\text{D}_2\text{O}}$  labelled as [b] reports the values of the  $\text{D}_2\text{O}$  density obtained by normalizing to the density of *confined* heavy water at 284 K. This latter parameter has been estimated as 6% lower than the bulk ( $\rho_{\text{D}_2\text{O}} = \rho_{\text{D}_2\text{O}}^{\text{bulk}} - 6\% \rho_{\text{D}_2\text{O}}^{\text{bulk}}$ ) [151]. Where not reported, uncertainties are less than 1%.

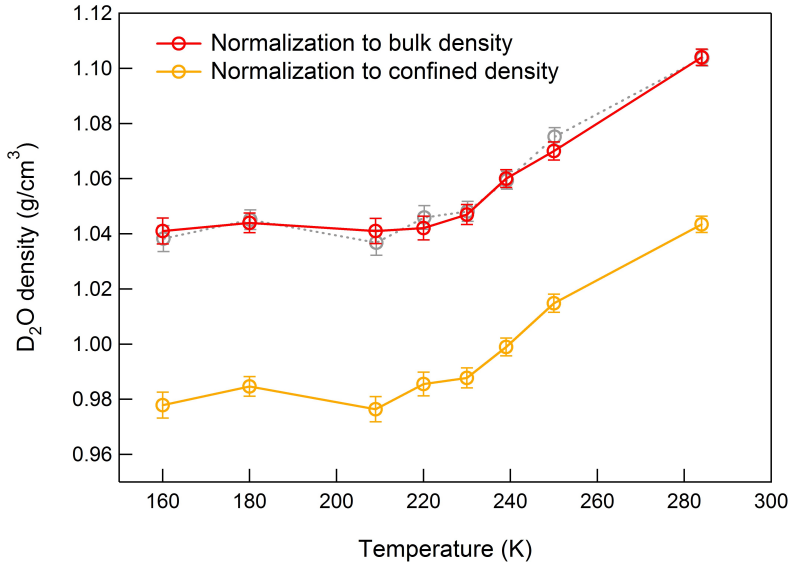


Figure 5.17: Temperature evolution of  $\text{D}_2\text{O}$  density upon cooling, calculated as a fit parameter obtained by eq.5.9. Red points have been obtained by normalizing the density of the highest temperature to that of bulk  $\text{D}_2\text{O}$  ( $1.11 \text{ g}/\text{cm}^3$ ), while the orange points are the result of normalization computed by using the density of confined  $\text{D}_2\text{O}$  ( $1.043 \text{ g}/\text{cm}^3$ ), according to [151]. The orange points have been vertically shifted and overlapped to the red ones (grey dotted line), showing that the temperature evolution of confined  $\text{D}_2\text{O}$  density remains the same within the experimental uncertainties. Lines connecting symbols are guides for eyes.

density scale. Fig.5.18(b) shows the temperature dependence of the thermal expansion coefficient  $\alpha_P$  ( $\alpha_P = -\rho_m^{-1}(\partial\rho_m/\partial T)_P$ ), derived from the  $\rho_m$  vs  $T$  curve reported in fig.5.18(a). If we now compare our results with those obtained in [70, 256] (blue triangles), we can evidence a good accordance from  $\sim 285 \text{ K}$  down to  $\sim 210 \text{ K}$ , while the agreement is less good at lower temperatures. In particular, [70, 256] find a minimum in  $\rho_m^{\text{D}_2\text{O}}$  at 210 K, asserting that this high density–low density transition in the supposed liquid water can be regarded as

the mirror of the transition between the low density (LDA) and high density (HDA) amorphous solid phases of water at even lower temperatures. Moreover, it was claimed that the method illustrated above represents a good strategy to measure density of confined water and to locate the LLC (if it exists). By contrast, our data seem to reach a limiting value ( $\rho_m^{\text{D}_2\text{O}}(\text{lim}) \approx 1.04 \text{ g/cm}^3$ ), instead of a minimum in  $\text{D}_2\text{O}$  density at  $\sim 210 \text{ K}$ . The calculated  $\rho_m^{\text{D}_2\text{O}}(\text{lim})$  is close to the density of bulk  $\text{D}_2\text{O}$  stacking-disordered ice<sup>11</sup> (that is the ice polymorph expected to be found within the core pore).

Once the  $\text{D}_2\text{O}$  density has been determined, one can calculate the corresponding thermal expansion coefficient  $\alpha_P$ : since the absolute value of  $\alpha_P$  is known to exhibit a peak crossing the Widom line above the critical point, a maximum in  $-\alpha_P$  at a given temperature  $T^*$  could be interpreted as the signature of the Widom line crossing at  $T^*$  for ambient pressure. However, if we look at the temperature dependence of  $\alpha_P$  (fig.5.18(b)), we note that the thermal expansion coefficient exhibits a maximum, but the peak is much less pronounced than that found, for instance, in [256, 257, 280]. Such a broad maximum in  $-\alpha_P$  appears at 239 K, namely at the same temperature where a transition from liquid-like to ice-like structure has been observed in the  $Q$ -range corresponding to short-range correlations. The absence of a sharp and well defined peak in the red curve in fig.5.18(b) makes us not able to identify the exact temperature at which  $-\alpha_P$  has its maximum. What we can conclude is just that the absolute value of  $\alpha_P$  likely reaches its highest value at around 230 – 240 K. Despite data shown in [70] exhibit a similar  $\alpha_P$  vs temperature behaviour, those results are interpreted by the authors as an evidence for the existence of the Widom line and the associated LLPT. In view of the above, we do not agree with this conclusion, as will be discussed in section 5.4.6.

Irrespective of the comparison with results shown in [70], we observe a marked reduction in density of confined  $\text{D}_2\text{O}$  (table 5.3) with respect to the bulk upon cooling ( $\text{D}_2\text{O}$  bulk density at ambient temperature is  $1.11 \text{ g/cm}^3$ ), giving a further confirmation of the hints gained from the analysis of the water main peak. The density decreases with lowering temperature down to  $\sim 220 - 210 \text{ K}$ , where it seems to reach a limiting value. More specifically,  $\text{D}_2\text{O}$  density falls by approximately 6% when going from 284 K to 209 K. A quite similar result is confirmed also in [257], where the density change for  $\text{D}_2\text{O}$  between the maximum and the (purported) minimum value is stated to be 5.8%. We remark again that the density drop we observe is due to changes in the local arrangement of water molecules within the pore, and not to a change in their number.

#### 5.4.5 Long-range correlations: Porod region

If water can be described, even at ambient temperature, as a mixture of two liquids differing in density [51, 114, 126, 260, 265, 273, 281], then concentration fluctuations between the two liquids are expected. In principle, this should, in turn, give rise to enhancement and fluctuations in scattering intensity at very low  $Q$  [51]. However, the analysis of the Porod region in the DCS here presented does not reveal any evidence of this circumstance. In fact, a steep rise in DCS intensity is visible at very low  $Q$ , but all data are superimposed in that

<sup>11</sup>The  $\text{H}_2\text{O}$  stacking-disordered ice, hexagonal ice and cubic ice densities are available from [http://www1.lsbu.ac.uk/water/ice\\_phases.html](http://www1.lsbu.ac.uk/water/ice_phases.html). The corresponding densities for  $\text{D}_2\text{O}$  can be calculated by accounting for the fact that the density of  $\text{D}_2\text{O}$  phases is 20/18 times as much as water.

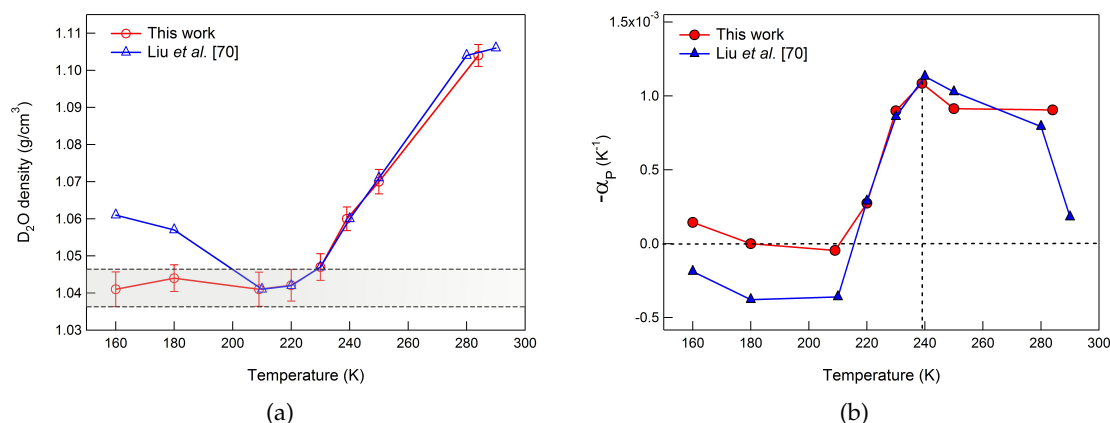


Figure 5.18: Comparison between data calculated in the present work (red symbols) and those reported in [70] (blue symbols). (a) Temperature evolution of  $D_2O$  density upon cooling. Heavy water was confined within MCM-41 of 2.8 nm pore size and its density was calculated as a fit parameter obtained by eq.5.9. The experimental points in the grey strip are consistent within the experimental uncertainty. (b) Thermal expansion coefficient,  $-\alpha_P = \rho_m^{-1}(\partial\rho/\partial T)$  as a function of temperature, where  $\rho_m$  is the  $D_2O$  density shown in (a). Red circles have been obtained from our experimental data, while for the blue triangles we have calculated  $\alpha_P$  exploiting data reported in [70] and shown in (a). The temperature of the density minimum is where  $\alpha_P$  is equal to zero. Lines connecting symbols are guides for eyes.

region, as evident from fig.5.19. In particular, the intensity continuously increases moving towards low  $Q$  values, but the diffraction patterns remain essentially parallel (within the experimental uncertainty) for all the measured temperatures.

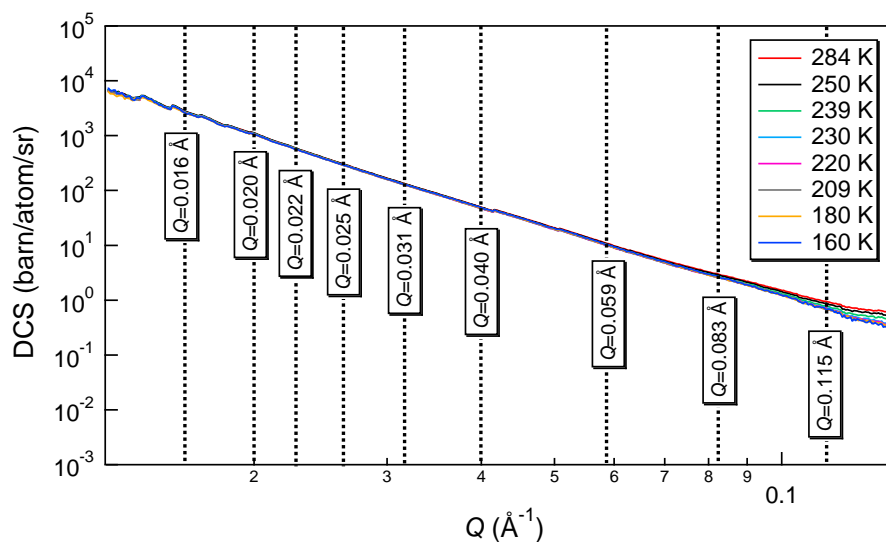


Figure 5.19: Porod region of DCS obtained from  $wet_{D_2O}$  C10 sample at different temperatures. The figure shows that all data are superimposed. The selected  $Q$  values indicated in the graph are used to perform the analysis described in the text.

In order to make this point clearer, we have accomplished a more quantitative analysis of the Porod region. First of all, we have plotted the scattering intensity at selected  $Q$  values as

a function of temperature. The selected  $Q$  spread out the entire Porod region and are those indicated in fig.5.19. The result is displayed in fig.5.20 and shows a smooth and continuous decrease of the scattered intensity with temperature. For each  $Q$  value the temperature evolution of the scattered intensity has been fitted by means of a linear function.

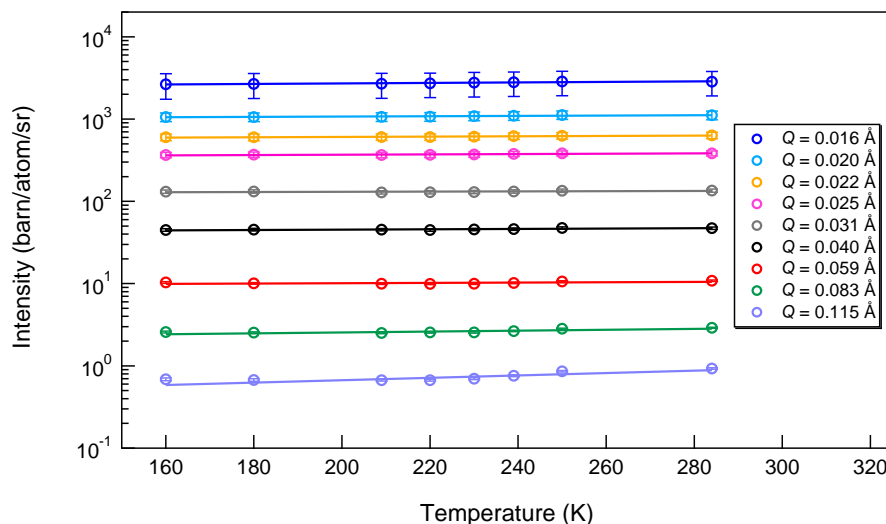


Figure 5.20: Scattered intensity as a function of temperature for selected  $Q$  values in the Porod region. Straight lines represent linear fits of the experimental data.

As visible in fig.5.20, all the fit functions are nearly horizontal and their slope is the same, within errors, for each  $Q$  value. This result is useful to emphasize that there is not any inversion in the temperature trend of the scattered intensity over the entire  $Q$  range corresponding to the Porod region. Such a result is particularly remarkable because it proves that we are not crossing a Widom line upon cooling confined  $D_2O$  at ambient pressure.

#### 5.4.6 Discussion and conclusions

As said above, the purpose behind our neutron diffraction experiments was to contribute to the open debate about the existence of a phase transition between a low-density and a high-density supercooled water phase, as proposed by a number of computer simulation studies [14, 126, 253, 260, 282]. From an experimental point of view, this effort results in trying to assess the hypothesized existence of a Widom line in the phase diagram of confined water, which should represent the extension of the liquid-liquid coexistence line above the second critical point (fig.2.6) and should intersect the temperature axis for ambient pressure at  $\sim 210 - 220$  K [128, 132, 253]. Such a hypothesis relies on two observations: *i*) the general finding that confined water appears to undergo a dynamical fragile-to-strong cross-over at a temperature around  $220 - 225$  K (for  $H_2O$ )<sup>12</sup>, *ii*) the apparent observation of a density minimum in confined water at a temperature near  $200 - 210$  K, with the lowest density occurring at temperatures below that of the Widom line. Such a minimum in water density,

<sup>12</sup>When results for  $H_2O$  and  $D_2O$  are compared, it must be reminded that the thermodynamic quantities of  $D_2O$  are usually shifted of several degrees towards higher temperatures compared to that of  $H_2O$ .

especially in the case of a hydrophilic confinement, is believed as the result of the full development of a defect-free random tetrahedral network (RTN) of hydrogen bonds, whose structure should sign the lower limit of water density [257]. In view of this considerations, the idea was to design an experiment aimed to go through the phase diagram of confined supercooled water, attempting to cross the purported Widom line on lowering temperature at fixed pressure.

As a matter of fact, the evidence of a temperature of minimum density in deeply supercooled confined water is still controversial. From one side, there are claims pointing out the existence of a minimum in confined water density [70, 256, 257, 263, 264]; on the other side, there are other studies that question the interpretation of experimental results in terms of a water density minimum and its link to the second critical point [176, 195, 254, 255, 279]. Other authors have also cast doubt upon the interpretation of dynamic data in terms of a FSC [283–287].

As shown in fig. 5.18(a), our experiments do not reveal any density minimum in heavy water confined within MCM-41/C10 silica substrate. On lowering temperature, D<sub>2</sub>O density reaches a limiting value but does not rise again when the temperature is lowered further below  $T \sim 210$  K, as the data comprised within the grey strip can be regarded as consistent within the experimental uncertainty (also considering the dependence on the background subtraction). Such a result is at odds with [70, 254, 256, 257].

Since this outcome stems from the specific data analysis we performed on the silica Bragg peak intensity, this aspect deserves a more in-depth discussion.

The traditional formalism of SANS data analysis is valid only as far as two conditions are verified: *i*) water within the pore does not crystallize and remains liquid at all temperatures, and *ii*) the density of *both* confining and confined systems are constant, implicitly implying that water is supposed to uniformly occupy the pore volume. But this condition is not verified, because the density of D<sub>2</sub>O confined in MCM-41 silica matrix is not homogeneous across the pore volume, as recently proved by several investigations based on experiments and simulations (see section 2.4) [151, 195, 255]. Consequently, changes in the Bragg peak intensity cannot be interpreted as evidence for density changes, as the form factor is modulated by the density fluctuations and the neutron contrast term needs to be numerically evaluated [279].

Actually, a uniform density profile of water appears to be implausible also at atomistic level, if we take into consideration the highly charged nature of the silica surface, the roughness and disordered structure of the internal pore walls, and the method of formation of these materials from cylindrical micelles [255]. On the basis of what has been observed about density inside the pore, we can argue that the standard definition of average density is clearly an unrealistic assumption. After all, the DCS at high  $Q$ , where the intramolecular contributions are dominant, are almost perfectly superimposed for different temperatures (fig. 5.7). This should not happen if the average density at high and low temperature was different.

The inhomogeneous and anisotropic character of confined water distribution seems to be the effect of a non-negligible and temperature-dependent interaction between water and the confining walls [195]. That is to say that the mesoscopic arrangement of water molecules in the pores may also be affected by modifications in the interactions involving both water and substrate as the temperature is lowered. In particular, supercooling makes HBs between water molecules stronger and those between water molecules and the pore walls weaker [195]. It is worth noting here that the importance of water-confining surface interaction in very narrow pores (1.4 nm in diameter) has been also evidenced recently by some authors reporting that supercooled water confined in hydrophobic media does not exhibit any density minimum [71, 280]. They explained such a result assuming that hydrophobic interactions

of water with the pore walls may lead to a different density profile compared to that of hydrophilic confinement.

As a consequence, the model described in section 5.4.4 does not allow to extract the confined water density from the intensity of the silica (100) Bragg peak. This means that marked modifications in Bragg peak intensity cannot be unambiguously interpreted as evidence for changes in the average density of the sample, because the intensity of the (100) Bragg peak depends not only on the average density of water within the core pore, but also on how water is spatially distributed across the pore. Such a consideration entails that SANS experiments are not a reliable strategy to obtain a straightforward measure of the density of confined water.

Our results may be better explained in the light of atomistic simulations of the structure of a system very similar to wet MCM-41/C10 studied over a wide  $Q$ -range [151, 195, 203, 255]: changes in molecular configurations experienced by confined water on lowering temperature suggest that at 210 K water molecules occupy the pore volume more uniformly than at ambient temperature. The reduction of the pore regions inhomogeneously occupied by water can be due to a change in the balance between water cohesive interaction with respect to the adhesive interaction<sup>13</sup> of water with the substrate [279]. This picture not only is consistent with a more ordered structure as the temperature is lowered, according to [151, 195, 202, 203, 279], but it also accounts for the modifications occurring in the Bragg peak intensity. Indeed, the scenario depicted above would result in the reduction of the scattering intensity with decreasing temperature (i.e. the reduction of the neutron contrast), whereas the level of DCS at high  $Q$  would remain unchanged, being it proportional only to the average sample density [267]. In principle, different molecular arrangements at constant density or changes in density at a mesoscopic scale may affect the SANS peak intensity in the same manner [195]. On the basis of this interpretation, the intensity of Bragg peak does not necessarily change because the average density is changed, but because water molecules arrange differently at a local scale within the silica pores. In particular, a less intense Bragg peak can be equally explained as a more homogeneous density profile on cooling [203]. In other words,  $T \sim 210$  K is the temperature where density fluctuations are minima, but it cannot be regarded as the temperature of water density minimum. This interpretation can solve the apparent contradiction previously highlighted. In this context, this conclusion holds true irrespective of ice formation at low temperatures.

In addition, it should be emphasized that a density minimum is not always related with a thermal expansion coefficient ( $\alpha_P$ ) maximum. This is pointed out, for instance, by some recent X-ray and neutron scattering studies on water under hydrophobic confinement [71, 280]. Even though the present investigation concerns water in a hydrophilic substrate, results here shown are quite similar to those by [71, 280]: we have found a broad peak in  $\alpha_P$  as well, but no density minimum has been detected. From the one hand, such a remark suggests that the evidence of the  $\alpha_P$  peak is an intrinsic property of water, which does not depend on the nature of the confining surface, apparently reinforcing the Widom line interpretation and its crossing as a demonstration of the existence of the proposed LLCP at higher pressure. On the other hand, it indicates that the existence of a density minimum and a maximum in thermal expansion coefficient are not to be regarded as necessarily correlated, as suggested by other studies [70, 256]. In other words, studies on hydrophobic

---

<sup>13</sup>Density profiles calculated for water confined in a mesoporous silica matrix at ambient conditions are well accounted for by conjecturing the existence of regions of cohesive failure [279]. Such a result seems to be supported also by molecular dynamics simulations of water confined between hydrophilic planar walls [204]. Changes in the density profile as the temperature decreases may thus reflect a change in the balance between water-water and water-substrate interactions.

confinement evidence that a density minimum is a sufficient, but not necessary condition for an inflection point.

Moving to higher  $Q$ , where the structure of confined water can be assessed, we have attested that  $D_2O$  remains in a supercooled state within MCM-41 silica matrix ( $\Phi = 2.8$  nm) down to about 239 K: below this temperature water in the core pores starts to crystallize, as pointed out by marked changes occurring in the differential cross-sections at short-order  $Q$ -range, which clearly demonstrate an abrupt structural change at  $\sim 239$  K. Furthermore, comparison with simulated neutron diffraction patterns has suggested that the ice phase observed upon confinement in wet- $D_2O$ -C10 is neither purely hexagonal nor purely cubic, but looks like a randomly defective lattice whose structure is known in literature as stacking-disordered ice I [91, 94].

Qualitatively, such a description is consistent with the picture of a higher-density phase transforming to a lower-density phase, but nothing actually suggests we can interpret these phases as HDL and LDL. In our opinion, the higher-density phase from 284 K down to  $\sim 239$  K and the lower-density phase from  $\sim 239$  K downward are to be simply regarded as liquid supercooled water and solid ice, respectively. A fact that reinforces the rationality of this interpretation is the density decrease we calculated in section 5.4.4: we measured a difference of  $\sim 6\%$  from  $D_2O$  at ambient temperature to  $D_2O$  at 209 K, where the density reaches its limiting value. Although the limiting density is close to the density of  $D_2O$  LDA ( $\approx 1.04$  g/cm<sup>3</sup>), such a difference is much smaller than the 26% difference expected between HDA and LDA, but is absolutely comparable to the  $\sim 7\%$  variation from ordinary liquid  $D_2O$  to ice  $I_c$ .

It may be questioned that a sharp phase transition in systems with pore size comparable to C10 has been seldom evidenced by other techniques, such as the differential scanning calorimetry (DSC) [161, 174, 176, 177, 181, 288]. This inconsistency can be explained invoking the sensitivity of the experimental technique which is employed: even clusters of few ice nuclei can be revealed by neutrons, but they are likely not enough to be detected by DSC. Moreover  $\Phi = 2.8$  nm is really close to the limiting size to observe crystallization in porous environments. Consequently, the possible DCS trace revealing a freezing/melting event is expected to be very weak and probably not easily detectable with respect to the background.

Similar results were reached by Erko *et al.* [254] combining SAXS, SANS and WAXS data scattering suggesting the necessity to assume an inhomogeneous density profile of confined water. Although they actually identify a low-temperature density minimum of water confined in cylindrical pores of ordered mesoporous MCM-41 materials, they attribute this phenomenology to a liquid-solid transition of water, whose structure is considerably influenced by confinement. This statement is further reinforced by the observation that the temperature at which the density minimum occurs is shifted to lower temperatures as the pore size decreases.

Lastly, a pronounced increase of the scattering intensity at very low  $Q$  as a result of enhanced density fluctuations inside the pore should have been visible in the NIMROD data on crossing the Widom line, if it exists. Instead, no intensity fluctuations appear in the steeply rise at very low  $Q$  (Porod region), providing a proof of the absence of density fluctuations in the liquid phase. We want to specify that, as we speak about density fluctuations, we intend for fluctuations *across* the pore, because no density fluctuations are expected to be found *along* the pore axis, as shown in [151].

Although this approach is correct in principle, we believe it should be appropriate to focus on the length scales involved in the  $Q$ -range corresponding to the Porod region, comparing it to the 2D space accessible to water molecules in the restricted geometry here investigated. If we want to study the water behaviour on length scales comparable to the pore size of C10 sample, then we need to explore a momentum transfer given by  $Q = 2\pi/\Phi \approx 0.2 \text{ \AA}^{-1}$  (with  $\Phi = 2.8 \text{ nm}$ ). However, as depicted in fig.5.4, the corresponding  $Q$  region is occupied by the Bragg peak due to the silica matrix. The conclusion is that the  $Q$  region spanning up to  $\sim 0.1 \text{ \AA}^{-1}$  does not include the density fluctuations between two liquid phases we are looking for. They are to be sought at higher  $Q$  values, but, even if they do exist, would be covered up by the first Bragg peak of the silica matrix. In addition, it is worth mentioning that pores, creating a confined geometry, by construction suppress (at least partially) the possibility of finding density fluctuations with length scales larger than the pore diameter. As a consequence, the only information which might be inferred is that, on decreasing temperature, the interface does not change while the water inside the core pore is experiencing structural modifications.

By putting together results, observations, and comments given in this chapter, we can confirm that our neutron diffraction experiments on hydrated and dry MCM-41 mesoporous substrates bolster the idea that the earlier reports of a possible liquid–liquid transition in supercooled confined water are rather to be regarded as a liquid–solid transition. Hence our results suggest that linking this structural transition to the dynamic cross-over from fragile-to-strong liquid would need more cautions. In particular, if no enhancement of density fluctuations are visible crossing the Widom line (as it is indeed in our case), the crossover observed in several structural and dynamical quantities [128, 143, 210, 258, 259] is likely due to instrumental artifacts or to crystallization transition involving at least a fraction of the confined water.

Another relevant issue here highlighted is the importance of analysing neutron scattering patterns over a sufficiently wide  $Q$  range, and not simply relying on information which can be extracted from a single region, as done by [70, 256]. Indeed we have seen that the silica Bragg peak by itself cannot provide any conclusive evidence for the existence of water density minimum in a restricted geometry, but we need also to investigate what happens to water structure. Hence we have demonstrated that a simultaneous analysis of the temperature evolution of the Porod region features, the hexagonal Bragg peak intensity, and the region of the scattering patterns relative to water structure plays a key role in a correct interpretation of diffraction data without settling in misleading conclusions. To the best of our knowledge, this is the first time that the phenomenology occurring in confined environments is interpreted on the basis of neutron scattering data spanning a wide  $Q$ -range, including both the substrate and the confined liquid. This is true except for the recent work by Kamitakahara *et al.* [264], where neutron diffraction has been used to track the temperature dependence of structural properties of heavy water confined in MCM-41-S (another member of the MCM family) with very narrow pores (the nominal pore diameter was 1.61 nm). They have combined data from low  $Q$  ( $0.1 - 0.4 \text{ \AA}^{-1}$ , corresponding to the silica Bragg peak) and from higher  $Q$  ( $1.0 - 3.0 \text{ \AA}^{-1}$ , corresponding to the first diffraction peak of  $\text{D}_2\text{O}$ ). Although the approach is similar to ours, the conclusions are totally different. In fact, the authors believe in the validity of the method of calculation of the  $\text{D}_2\text{O}$  density based on the temperature evolution of the first Bragg peak of silica matrix, as proposed by [70], thus they claim that a comparison between the diffraction patterns of the two selected  $Q$ -ranges allows for the identification of  $\text{D}_2\text{O}$  structural changes strongly correlated with changes in density. In

particular, they state to have found a density minimum in D<sub>2</sub>O at 190 K and recognise a structural change in D<sub>2</sub>O that takes place at around  $(240 \pm 10)$  K, consistent with our observations within the experimental uncertainty. However, they interpret such a change as the signature of the transition from a mostly HDL-like structure to a mostly LDL-like structure, rather than as a liquid-solid phase transition. Moreover, in their diffraction patterns at low temperatures ( $T < 250$  K) the signature of hexagonal ice  $I_h$  is clearly visible (three intense and sharp peaks between  $\sim 1.5$  and  $2.0 \text{ \AA}^{-1}$ ), arising from water expelled from the pore and crystallizing outside the pore volume, between the MCM-41 powder grains. We therefore argue that, even if the diffraction patterns showed any hint of a liquid-solid transition *within* the pore, it would be hidden by the much more intense signal coming from the hexagonal ice outside the pores, and would not be detected.

Finally, we have learned that any conclusions regarding the structural, dynamic and thermodynamic behaviour of supercooled confined water based on scattering experiments require a full and detailed characterization of the sample if they presume to be reliable.

To sum up, the results presented in this chapter do not provide proofs for the existence of a second critical point in the metastable phase diagram of water. By contrast, they seem to be more consistent with the singularity-free (SF) model. However, information extracted from our experimental data are not sufficient to clearly distinguish between these two scenarios, nor to reach definitive conclusions about this issue.

# Chapter 6

## Experimental results: Infrared spectroscopy

*L'essentiel est invisible pour les yeux.*

*Antoine de Saint-Exupéry (Le Petit Prince)*

### 6.1 Overview and motivations

The purpose behind our experiments using infrared (IR) radiation was to give more insights into the metastable phase diagram of supercooled confined water from a different viewpoint with respect to that offered by neutron diffraction experiments. In the case of water, IR spectroscopy comes across as a particularly suitable tool, being it able to probe bonds oscillations because of the large transition dipole moment of water molecules and thanks to its sensitivity to the molecular *local* environment. Its high capability to detect H<sub>2</sub>O vibrational modes pinpoints IR spectroscopy as an ideal technique which can be exploited to study even small amount of water in different environments and under several conditions. In particular, we focused our attention on the vibrational motion of hydrogen bond, that is the key element of the supramolecular connectivity.

It is generally admitted, indeed, that water properties (at least in its bulk configuration) originate from a delicate balance of interactions on different length scales covering several order of magnitude: the H-bond at the molecular (local) scale, and the extension of the HB network on larger scales up to the mesoscopic level.

Bringing in mind this peculiar trait, IR spectroscopy measurements were performed over a broad frequency range, which encompasses both the mid-infrared (MIR) region ( $1000 < \omega < 6000 \text{ cm}^{-1}$ ) and the low-frequencies domain known as far-infrared (FIR) region ( $\omega < 600 \text{ cm}^{-1}$ ). This allowed us to monitor the evolution of intramolecular and intermolecular vibrational modes in water as a function of temperature and pressure, with particular emphasis on the high-frequency OH-stretching band (in the MIR range) and the so-called connectivity band (in the FIR range), arising from the collective motion of the hydrogen-bond network.

The IR absorption spectrum of confined water is expected to change somehow with respect to that of bulk water and the most significant modifications are predicted to arise upon cooling. In particular, some authors claim that in confined water the temperature and pressure evolution of the OH-stretching and H $\hat{O}$ H bending bands, investigated by IR spectroscopy, show a structural change from a predominantly high-density phase (HDL) to a lower-density phase (LDL) as the Widom line is crossed [264, 289].

In setting the experimental conditions (temperature and pressure) to properly investigate our system, we were guided by previous experimental works on deeply supercooled water supporting the existence of the second critical point [128].

The idea is that, if the second critical point and liquid-liquid coexistence line exist, below the critical pressure  $P_C$  and for temperature  $T > T_C$  a unique liquid phase is expected to be found (fig.6.1, green area). If we perform an experiment by varying temperature at constant pressure  $P < P_C$ , we should move from a high density phase (HDL) at high temperature to a low density phase (LDL) at sufficiently low temperature (fig.6.1, blue area). Since a fragile behaviour is assigned to HDL, whereas a strong behaviour is associated with LDL, a clear fragile-to-strong crossover is expected to be observed by measuring the sample at constant pressure and decreasing temperature. Conversely, if the experiment is carried out in the two-phase region at  $P > P_C$  by varying temperature, we should observe a mixture of different proportions of HDL and LDL as the liquid-liquid coexistence line is crossed (fig.6.1, pink area). This mixed state should result in the absence of a clear-cut crossover.

Relying of this picture, Liu and co-workers [128] have exploited the capabilities of quasi-elastic and inelastic neutron scattering techniques to assert that a clear fragile-to-strong crossover (FSC) is observed up to  $\sim 1.2$  kbar, at temperatures ( $T_L$  line) closely tracking the homogeneous nucleation temperature line (fig.2.6). The upper end of this  $T_L$  line should be located at 1.6 kbar and 200 K, when intersecting the  $T_H$  line. That point signs a change in the character of the dynamic transition: beyond 1.6 kbar the FSC disappears. According to these authors, the presence of a FSC can be regarded as a consequence of the crossing of the Widom line and the liquid-liquid coexistence line. On the basis of these findings, the idea was to explore the phase diagram of supercooled confined water trying to cross the supposed Widom line by varying temperature at constant pressure. Therefore we established four pressure points, ranging from  $\sim 1.0$  kbar up to  $\sim 2.5 - 3.0$  kbar: if the Widom line exists and we can cross it, a significant change in water vibration dynamics is expected around  $\sim 1.5 - 2.0$  kbar. The temperature range, going from ambient down to  $\sim 140$  K, was chosen in order to explore, at each pressure, both below and above the supposed FSC temperature.

We applied infrared spectroscopy to the same system investigated by neutron scattering experiments (chapter 5). In particular, we studied the behaviour of pure water (H $_2$ O) confined in MCM-41/C10 silica substrate (pore diameter  $\Phi = 2.8$  nm). No measurements were carried out on the MCM-41/C18 matrix (pore diameter  $\Phi = 4.5$  nm), because of the limited beam time available. In addition, on the basis of the findings presented in the previous chapter, no interesting information was expected to be gathered from the confinement in the bigger size substrate.

All IR spectra were collected on the AILES beamline, at the French synchrotron SOLEIL (Saint-Aubin, near Paris). The possibility to exploit the high brilliance of a synchrotron radiation source made us capable of exploring also the very low-frequency domain (FIR range) obtaining spectra with a satisfactory signal-to-noise ratio. This remarks the importance of our results extending over a wide frequency range, which includes *both* the MIR and FIR

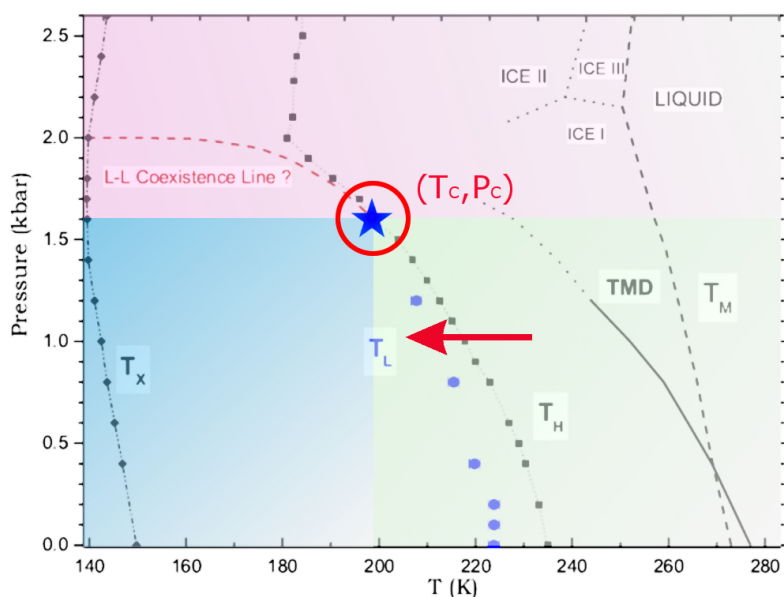


Figure 6.1:  $P - T$  phase diagram of water confined in mesoporous silica matrix MCM-41-S (with  $14 \text{ \AA}$  nominal pore diameter).  $T_L$  (solid circles) denotes the pressure dependence of the dynamic transition temperature linked to the FSC;  $T_H$  and  $T_X$  indicate the homogeneous nucleation temperature line and the crystallization temperature of amorphous solid water, respectively;  $TMD$  depicts the temperature of maximum density line (figure from [128]). The hypothesized second critical point is located at  $(T_C, P_C)$ , as highlighted by the red circle. When the system is investigated below the critical pressure  $P_C$  and above the critical temperature  $T_C$  (green area), a one-phase liquid is expected to be found. If we perform an experiment following the red arrow, i.e. by varying temperature at fixed pressure below  $P_C$  (blue area), we should detect a density change, moving from a liquid phase with higher density (HDL, on the high temperature side of the phase diagram) to a lower density phase (LDL, on the lower temperature side). This transition should reflect the dynamical FSC. On the other hand, if the experiment is performed above the critical pressure  $P_C$  (pink area), we should enter the two-phase region crossing the liquid-liquid coexistence line: the system is thus a mixture of HDL and LDL phases and the dynamical transition linked to the FSC does not longer occur.

domain. The literature shows that the number of studies concerning the water behaviour in the MIR region dramatically overwhelms those related to the FIR domain. Such a lack of experimental studies dedicated to the supramolecular connectivity of water is due to the low intensity of the conventional laboratory IR sources, which makes particularly difficult to distinctly probe the vibrational features of water at very low frequencies. Therefore we have taken advantage of IR measurements to support and integrate the structural information and their interpretation given in chapter 5, in order to better understand if and how they might be correlated to the existence of the LLPT and the second critical point.

## 6.2 Sample preparation

The investigated system is the same probed by neutron spectroscopy (chapter 5), i.e. water confined in MCM-41 silica matrix. In order to compare results coming from IR experiments with the structural information gathered from neutron scattering data, we chose to investigate only the C10 substrate ( $\Phi = 2.8 \text{ nm}$ ), as in the previous chapter it revealed to offer the

most interesting findings. MCM-41/C10 sample was prepared following the same procedure described in section 5.2. In this case, the silica matrix was hydrated by pure (deionized)  $\text{H}_2\text{O}$ , because the probe was a photon beam that is insensitive to different isotopes of the same element, thus no reasons held for using heavy water. The hydration level reached after the completion of the hydration procedure is  $h \approx 0.51$  grams of  $\text{H}_2\text{O}$ /grams of dry MCM. This corresponds to a pore filling slightly greater than 90% as in the neutron scattering experiments, but still not too high to expect a significant amount of water pushed outside the pore volume on cooling. Moreover, the sample has been probed under pressure, and in such a case a full pore filling should be preferred in order to avoid that empty space could cause the collapse of the pore structure as the pressure is applied.

## 6.3 Infrared spectroscopy experiments

### 6.3.1 Experimental details

Infrared spectra were collected on the AILES beamline, at the synchrotron SOLEIL. Measurements were carried out using a Bruker IFS 125 Fourier transform spectrometer (FT-IR) and all the IR spectra were collected in transmission mode. All the experiments were performed by using a bolometer detector (even though in the mid-infrared region a MCT photodetector is often preferred), with a resolution of  $2\text{ cm}^{-1}$  and 100 scans per spectrum (enough to get a good statistics).

In particular, the mid-infrared region ( $1000 < \omega < 6000\text{ cm}^{-1}$ ) was investigated by means of a Globar lamp (internal source), in combination with a KBr beam splitter, whereas for the far-infrared region ( $50 < \omega < 600\text{ cm}^{-1}$ ) it was necessary to resort to the infrared emission of the synchrotron radiation in order to obtain a sufficiently high signal-to-noise ratio, thanks to its much higher brilliance with respect to a laboratory source. The synchrotron light was used in combination with a composite Si beam splitter. Details of the experimental set-up can be found in chapter 4.

Over both the mid- and far-infrared domain the spectra were collected by varying temperature and pressure. For this reason, we used a diamond anvil cell (DAC), described in chapter 4. After hydration, a small amount of powder sample was loaded within the micrometer-sized hole between the diamond faces. Then it was dispersed in a few drops of oil, used as pressure transmitting medium (see below for details), adding the ruby chips needed for pressure calibration.

In this context, the fundamental requirement for a pressure transmitting medium is to be IR-transparent, i.e. not to have significant spectral features in the frequency domain over which the sample is investigated. This assures that vibrational bands have necessarily to be ascribed to the vibrational motions of the sample. On the basis of this observation, as long as the mid-infrared region was investigated, we used Fluorolube<sup>®</sup> as transmitting medium. Fluorolube<sup>®</sup> is a saturated, hydrogen-free, low-molecular weight polymer of chlorotrifluoroethylene (CTFE) that is chemically inert under many demanding conditions. It is ideal for preparation of samples to be investigated from  $4000$  to  $1360\text{ cm}^{-1}$ , where it is non-absorbing, except at around  $2300\text{ cm}^{-1}$ . In this latter restricted spectral region Fluorolube<sup>®</sup> shows a very weak absorption band, but it is out of the spectral range of our interest (fig. 6.2). For the far-infrared range we made use of Nujol, a mineral oil with a high molecular weight. It is chemically inert, being it essentially a heavy paraffin oil, i.e. a long chain alkane ( $\text{C}_n\text{H}_{2n+2}$

where  $n$  is very large). Its IR spectrum shows major peaks at 2950-2800, 1465-1450, and 1380-1370  $\text{cm}^{-1}$ , thus it is ideal for wavenumbers less than 1000  $\text{cm}^{-1}$ .

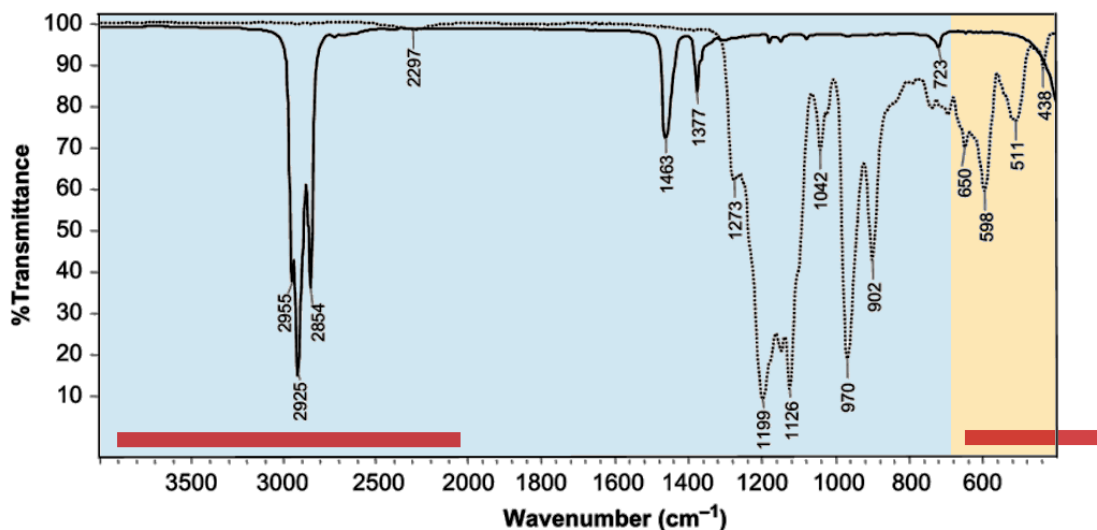


Figure 6.2: The FT-IR transmission spectrum of Nujol and Fluorolube<sup>®</sup> (figure adapted from [290]). The Nujol spectrum is shown as a solid line and the Fluorolube<sup>®</sup> one is represented as a dotted line. Colours approximately indicate the spectral regions corresponding to MIR (blue) and FIR (orange). The red bars specify the spectral ranges involved in our measurements (for FIR measurements, the spectral range was extended at even lower wavenumbers). As can be seen in the wavenumber range of the MIR domain, Fluorolube<sup>®</sup> does not exhibit any spectral features, while no significant absorbance bands due to Nujol can be found in the FIR domain.

The mixture consisting of powder sample, oil and ruby was then sandwiched between DAC and exposed to the infrared beam. As required by any scattering or transmission experiment, the cell environment was kept under vacuum ( $\sim 10^{-5} - 10^{-6}$  mbar) for the duration of the entire experiment (about two days for each measurement).

The pressures at which MIR spectra were recorded are  $(0.07 \pm 0.03)$  GPa,  $(0.15 \pm 0.01)$  GPa,  $(0.200 \pm 0.003)$  GPa,  $(0.250 \pm 0.006)$  GPa, while the FIR spectra were acquired at  $(0.11 \pm 0.02)$  GPa,  $(0.16 \pm 0.01)$  GPa,  $(0.21 \pm 0.02)$  GPa,  $(0.300 \pm 0.001)$  GPa. At each pressure, the temperature ranged from 143 to 293 K, in steps of  $\sim 10$  K. It has to be noted that pressure values are approximate and a different uncertainty is associated to each one. This is because we worked at relatively low pressures, and this led us to experience some difficulties to make the pressure stable for the duration of the entire experiment. For this reason, the reported value results from the average of the pressure measured at the beginning of the experiment (at room temperature, as the sample started to be cooled) and the end (after bringing back the sample to room temperature on warming). We note that even the lowest pressure is higher than 1 bar and no measurements were performed at ambient pressure. This is due to the DAC, that needs to be pressurized at least a little bit in order to prevent the loss of water loaded within the matrix pores as it is under vacuum.

For each pressure, IR spectra were acquired both on cooling and warming, in order to check whether measurements were reproducible along the two opposite paths or a phenomenon due to thermal hysteresis occurred. An example is given in fig.6.3, where spectra obtained upon cooling are compared to spectra collected on warming for some selected temperatures at 0.11 GPa over the FIR frequency domain. For similar temperatures the spectra seem

well reproducible: although some slight differences can be detected in intensity due to unavoidable little changes in the alignment of the optical components, the spectral shape is essentially the same for close temperatures. For this reason, we have decided to ignore hereinafter all data collected upon warming. Therefore data analysis has been performed only on IR spectra recorded on cooling, being them reliable and reproducible for all temperatures and pressures here investigated.

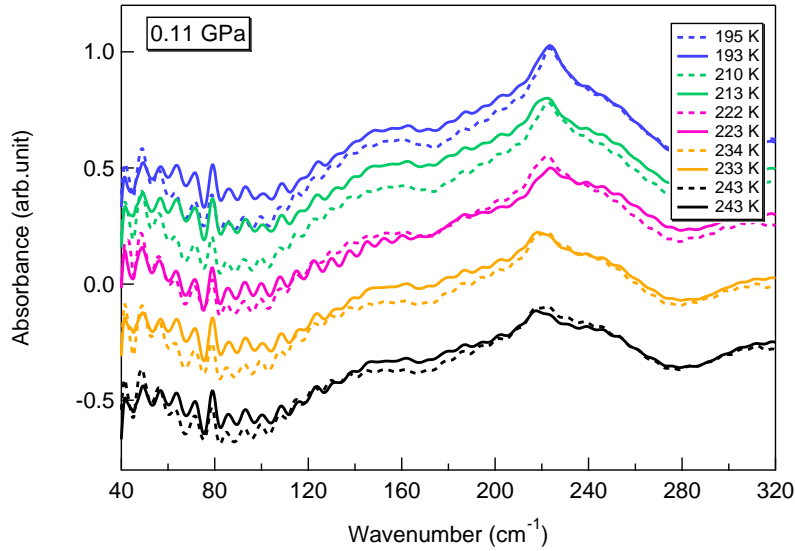


Figure 6.3: Comparison between FIR spectra acquired along cooling and warming paths for some selected temperatures at 0.11 GPa. Solid lines represent spectra obtained by lowering the temperature, whereas dashed curves are obtained by increasing temperature. Very similar response resulted from the other temperatures and pressures and for the MIR spectral region (data not shown). It clearly emerges that no signatures of thermal hysteresis occur, as spectra are perfectly reproducible on cooling and warming. Some slight differences in intensity can be noticed. However, they are simply ascribable to small modifications in the alignment of the optical components throughout the experiment. Curves have been arbitrarily shifted along the vertical axis for clarity.

The data acquired from a single measurement is an interferogram, namely the modulated transmitted intensity of the IR beam as a function of the moving mirror position (or of the optical path difference between the two recombining beams) of the Michelson interferometer unit (chapter 4). Each position of the moving mirror corresponds to a temporal delay between the two beams exiting from the beam splitter. The transmitted intensities are therefore measured in the time domain. A fast Fourier transform algorithm is applied in order to obtain a spectrum in the frequency domain. Usually one is interested in getting a transmittance or absorbance spectrum of the sample. This requires two measurements: a reference measurement (i.e. the light intensity distribution before it interacts with the sample) and the sample measurement (i.e. the light intensity distribution after the interaction with the sample loaded into the cell). The transmittance,  $T$ , and the absorbance,  $A$ , of the sample are defined as:

$$T = \frac{I_S}{I_0} \quad (6.1)$$

$$A = \log_{10} \left( \frac{I_0}{I_S} \right) \quad (6.2)$$

where  $I_S$  and  $I_0$  are the transmitted intensity of the sample and the reference, respectively. It needs to be noted that, for each sample, the reference was recorded by measuring the IR spectrum of the DAC loaded only with the pressure transmitting medium, rather than using the IR spectrum of the empty cell. In the following, all the experimental spectra will show the IR absorbance as a function of the wavenumber.

Before collecting IR spectra of the hydrated sample, it was tested that the dry C10 matrix did not introduce any relevant absorbance band in the spectral range where interesting features relative to water were expected to be found.

### 6.3.2 Data treatment

For the MIR frequency domain, the raw data obtained from the interferograms collected at AILES needed some corrections before being analysed. Indeed all MIR spectra were affected by big oscillations superimposed to the signal we were interested in, as shown in fig.6.4. The whole spectral window measured in the mid-infrared domain has been limited to the wavenumber range relevant for the OH-stretching vibration of water ( $\sim 2500 - 4500 \text{ cm}^{-1}$ ).

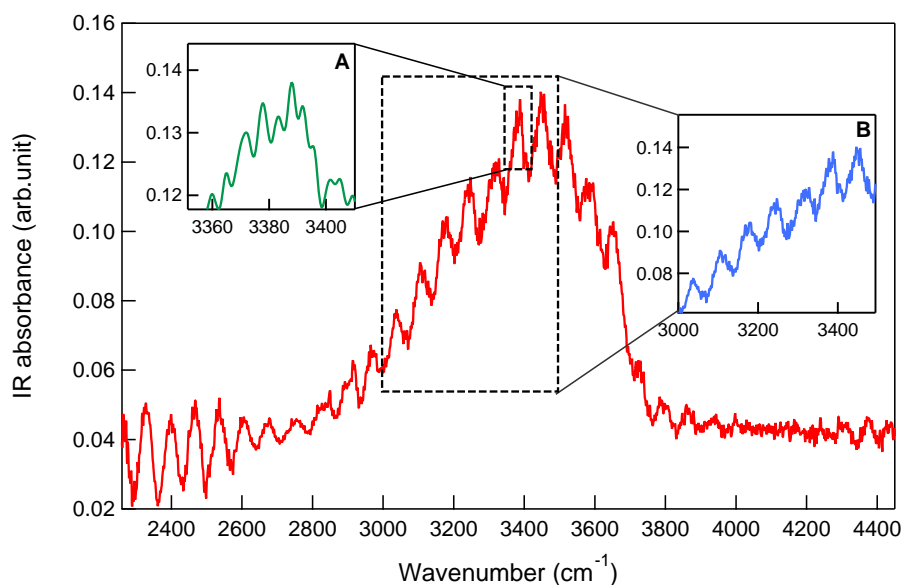


Figure 6.4: Example of raw data in the MIR frequency domain. The absorbance intensity obtained from the interferogram recorded at the AILES beamline presents some evident oscillations superimposed to the signal containing information we were interested in. Inset A indicates very high frequency fluctuations giving rise to a statistical noise component of the raw signal, which can be removed by means of tools specifically designed for signal denoising and available in several software of common use (e.g. MATLAB<sup>®</sup>, IgorPro<sup>®</sup>, etc.). Inset B highlights the “big” oscillations that have been found superimposed to the experimental MIR signal. Removal of such a component was a much more demanding task as the common tools dedicated to statistical denoising were not efficient. This task has thus requested a specific strategy in order to obtain good quality MIR signals, as described in the text.

Before dealing with data analysis, we needed to remove these “big” oscillations that do not carry any information about the temperature- and pressure-evolution of our sample. Unfortunately, tools commonly available for signal denoising are able to remove just the statistical

noise component, i.e. the very high frequency fringes clearly visible in the spectra (fig.6.4, inset A). To the best of our knowledge, such an issue has never been raised in literature, thus no indication could be found from other authors; when similar features have been identified in IR spectra (see for instance [60], where the FIR spectra, collected at the AILES beamline, exhibit visible fringes which the authors ascribe to multiple reflections in between the two sample windows), no specific solution has been proposed.

As a first attempt to solve this problem, we tried to fit the raw signal by a sum of  $n$  Gaussians ( $G_i(\omega)$ ), adding a sinusoidal term ( $S(\omega)$ ) to reproduce the "big" oscillations displayed in inset B of fig.6.4. Therefore we wrote the following fit function:

$$y(\omega) = B + \sum_{i=1}^n G_i(\omega) + S(\omega) \quad (6.3)$$

with

$$G_i(\omega) = A_i \cdot \exp\left(-\frac{(\omega - \omega_i)^2}{s_i^2}\right) \quad (6.4)$$

$$S(\omega) = A_0 \cdot \sin(f\omega + \phi) \quad (6.5)$$

where  $A_0, A_i, s_i, f, \phi, B$  are the fit parameters and  $\omega$  is the wavenumber reported on the horizontal axis. The result is visible in fig.6.5, where a raw MIR signal has been fitted by using eq.6.3 with  $n = 3$ . The outcome can be considered quite satisfactory, at least for the wavenumbers corresponding to the band center, but the quality of the fit is not good enough along the tails. This observation becomes clearer if we subtract the sinusoidal term  $S(\omega)$  of the fit function reported in fig.6.5 (blue line) from the experimental raw data (red line). The result is shown in fig.6.6.

The two oscillating tails shown in fig.6.6 can be fitted separately by means of two different damped sine functions, as displayed in fig.6.7.

It clearly results that, if we now subtract the two damped sine terms, used as fitting functions in fig.6.7 from the signal reported in fig.6.6, the big oscillations arising in the original MIR signal presented in fig.6.4 might be properly removed, leaving just the very high-frequency and low-amplitude oscillations due to the intrinsic statistical noise. Nonetheless, the strategy here proposed requires to find, for each measured absorbance spectrum, three fitting functions (at least) to subtract from the original MIR signal. As a matter of fact, this procedure could be serviceable for our purposes, but it appears to be rather intricate and time-consuming if all the collected data are wanted to be properly corrected. Also the application of a Fourier filter was unsuccessful as it did not provide an adequate correction. In order to circumvent such a drawback, a better strategy for signal denoising was identified and described hereunder.

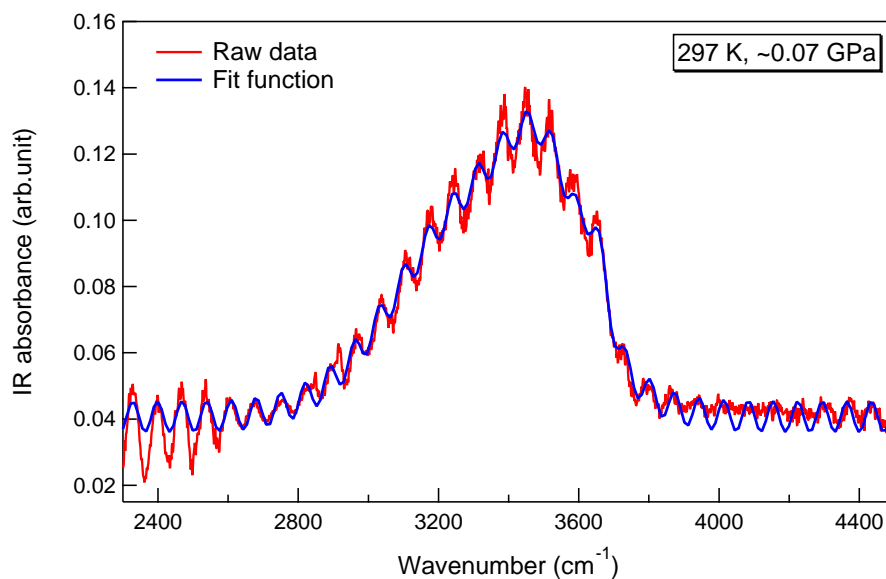


Figure 6.5: Example of MIR absorbance (red line), recorded at 297 K and 0.07 GPa, fitted by using eq.6.3 with  $n = 3$  (blue line) in order to remove the “big” oscillations, which represent the undesired component in the experimental signal.

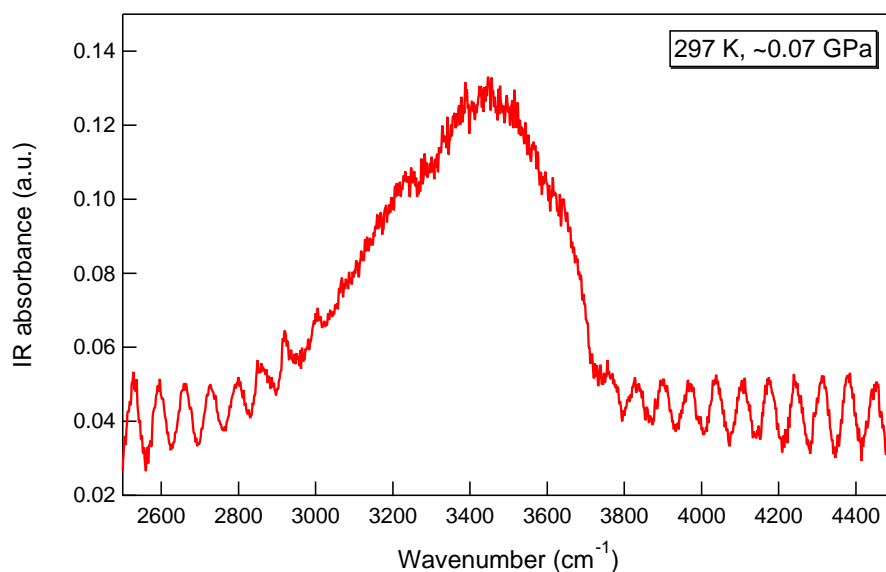


Figure 6.6: Signal obtained as the subtraction of the sinusoid term  $S(\omega)$  of the fit function reported in fig.6.5 (blue line) from the raw data (red line). A satisfactory result is visible only in the region corresponding to the peak, where the residual oscillations are those due to the statistical noise. Unfortunately, big oscillations are still present along the right and left tail of the signal.

### Wavelet denoising

A markedly more powerful strategy to clean up our MIR absorption spectra is the Stationary Wavelet Decomposition (SWT Denoising 1D) technique, performed by adapting the MATLAB<sup>®</sup> dedicated toolbox to our problem.

Wavelets are a relatively recent instrument developed in applied mathematics around thirty

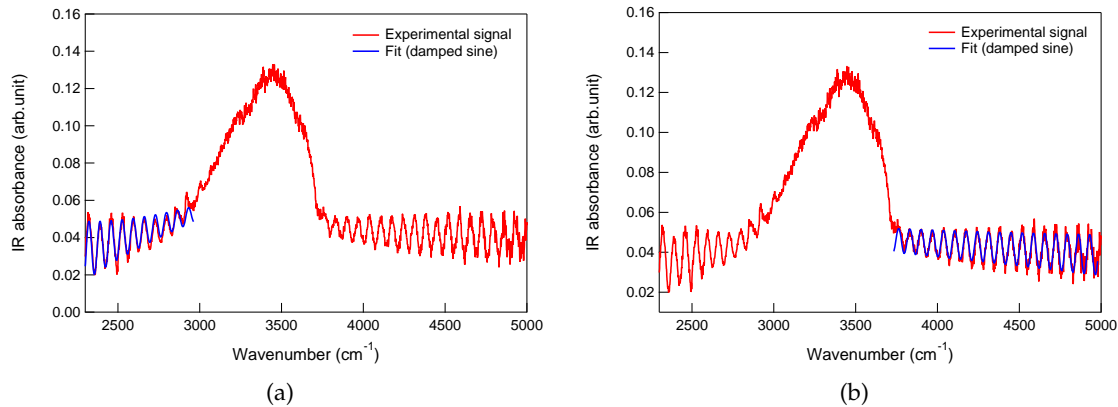


Figure 6.7: Fit of the left (a) and right (b) tail of the signal (red line) obtained as the subtraction of the sinusoidal term in eq.6.3 from the experimental raw data (fig.6.6). The fitting functions are two damped sine (with different parameters), shown as blue line in the figures.

years ago [291]. Wavelet analysis is particularly useful for the decomposition time series into time–frequency space, to determine both the dominant modes of variability and how those modes vary in time [292]. Thus it is not a coincidence that wavelet analysis is finding large and numerous applications especially in engineering, geophysics, and meteorology [293–295]. Comprehensive reviews on mathematical aspects of wavelet transforms and their applications may be found in [291, 292, 296, 297].

The continuous wavelet transform (CWT) of a time signal  $x(t)$  consists of a projection over a basis of compact support functions obtained by dilations and translations of the so-called *mother wavelet*  $\Psi(t)$ <sup>1</sup>. The wavelet coefficients resulting from the signal decomposition are function of the time  $t$  and the scale  $s$ , which is inversely proportional to the frequency [298]. Therefore, the CWT of a time signal  $x(t)$  can be defined as follows:

$$W_x(t, s) = C_\Psi^{-1/2} \int_{-\infty}^{+\infty} x(\tau) \Psi^* \left( \frac{t - \tau}{s} \right) d\tau \quad (6.6)$$

where  $C_\Psi^{-1/2}$  is a constant characteristic of each wavelet function (it is necessary to take into account the mean of  $\Psi(t)$ ) and  $\Psi^*((t - \tau)/s)$  is the complex conjugate of the dilated and translated mother wavelet  $\Psi(t)$ .

Essentially, the wavelet transform decomposes a time signal into basis functions (*wavelets*) and is calculated separately for different segments of the time-domain signal at different frequencies. The main hallmark of the wavelet transforms is indeed that they offer “variable time–frequency” resolution, in contrast with Fourier transform of a signal which only offers frequency resolution.

The wavelet function (also called as wavelet kernel) can be either *real* or *complex*. In the former case, it is more suitable to capture oscillatory behaviour in the signal, whereas in the latter better performances are obtained in isolating peaks or discontinuities. There exists a huge number of wavelet basis and functions; for examples and detailed descriptions we refer to [299, 300].

A discrete version of wavelet transform can be also adopted to decompose a time signal

<sup>1</sup>A *mother wavelet*  $\Psi$  can be an orthogonal or nonorthogonal set of functions (basis). Wavelet functions are always *finite*.

$x(t)$ , where  $t = n\delta t$  is the discretized time variable (with  $n$  an integer localized time index). According to [301], if the discretized scales  $s_j$  are arranged on a dyadic distribution, i.e.  $s_j = 2^j$ , and the translations are multiple of the scale  $s_j$ , the orthonormal basis  $\psi(t)$  obtained by dilations and translations of the mother wavelet  $\Psi(t)$  can be expressed as:

$$\psi_{[k]}^{(j)}(t) = 2^{-j/2} \Psi\left(\frac{t - 2^j k}{2^j}\right) \quad (6.7)$$

Hence, the discrete wavelet coefficients are obtained as follows:

$$w_x^{(s)}(n) = \sum_{k=-\infty}^{+\infty} \Psi^{(s)}(n - 2^s k) x(k) \quad (6.8)$$

Eq.6.8 tells us that, by varying the wavelet scale  $s$  and translating  $\Psi$  along the localized time index  $n$ , it is possible to build up a picture showing both the amplitude of any features versus the scale and how this amplitude varies with time. Therefore, the wavelet transform is simply a series of bandpass filters with a known response function (the wavelet function), of uniform shape and varying location and width.

The discrete wavelet transform can represent a valuable tool to realize filtering algorithms, likewise the Fourier transform can be employed to filter signals in the space and time domains. For the intrinsic characteristics of wavelet transforms, filtering can be performed on the scale and time simultaneously. This technique offers an important advantage over the traditional filtering: it removes noise (or undesired structures in the signal) at *all* frequencies and allows to isolate single events that have a broad power spectrum and multiple events that have different or varying frequency. A complete description of the Wavelet filtering technique can be found in [302], along with a practical and brief guide to wavelet analysis given by [297].

Generally, noise is a low amplitude-high frequency signal,  $N(n)$ , imposed on the higher amplitude-lower frequency signal,  $S(n)$ . The recorded signal,  $V(n)$ , can thus be written as  $V(n) = S(n) + N(n)$  and the purpose of any denoising procedure is to remove the higher frequency components in order to extract  $S(n)$  (which includes the information we want to analyse) from  $V(n)$ .

In particular, the denoising technique here employed is based on the reconstruction of the original signal by means of the discrete inverse wavelet transform (IWT) [303].

Essentially, the discrete wavelet transform (DWT) is used to convert a series  $a_0, a_1, \dots, a_m$  (the experimental signal) into two coefficient series: one low pass series known as "approximation" and one high pass series known as "detail", where the length of each series is  $m/2$ . Usually, this transformation is applied recursively on the low-pass series until the desired number of iterations is reached. First of all, the original signal, that must be a vector of  $N = 2^n$  elements, is numerically transformed into two vectors with  $2^{n-1}$  elements each. One vector contains the "approximate" or smooth coefficients, the other gets the detail coefficients. The former serves as an input for each iteration. After applying the selected wavelet transform to the input vector, the detail coefficients are obtained: the unwanted signal components can thus be removed from the original signal by setting the detail coefficients related to those particular components to zero. Otherwise, the contribution of a component can be reduced setting a proper threshold on the corresponding detail coefficients. Obviously, the selection of the threshold represents a crucial step in the separation procedure and in the final result. Finally, the inverse wavelet transform can be applied on the semi-processed

signal to get back to the original signal which now is free from noise or other unwanted components.

The procedure described above is the same we have followed to treat our MIR spectra. In fact, the wavelet decomposition technique appears to be particularly suited for our aim, as it allows to analyse the noise level separately at each wavelet scale and adapt the denoising algorithm accordingly, with no particular assumptions on the structure of the signal. Since the filtered signal was verified to be independent of the particular wavelet basis used for denoising decomposition, we used the simplest wavelet function, known as "Haar"<sup>2</sup>. Obviously, the final result is strongly dependent on the filtering level (the number of detail coefficient used for decomposition) and on the threshold established for each level. We opted for level 7 (fig.6.8). In particular, level 8 does not look like noise but as a significant part of the signal. Indeed, if it was removed from the reconstructed signal, some physical features we wanted to analyse would be lost<sup>3</sup>, hence it was completely included in the signal reconstruction. Levels 5-7 represent the undesired "big" oscillations that we wanted to remove, thus the corresponding coefficients were set to zero. Levels 1-4 reproduce the very high frequency noise (statistical noise) that we do not really need to remove; for this reason, we did not set them to zero, but defined a threshold able to remove from the coefficients only the high amplitude oscillations occurring at the lowest wavenumbers.

This denoising algorithm has made us capable to remove the undesired oscillations visible in fig.6.4, preserving the statistical noise component. An example of the result obtained by the application of the Stationary Wavelet Decomposition technique (with approximation at the 7<sup>th</sup> level) to our MIR spectra is displayed in fig.6.9.

## Detrending

The denoising algorithm based on the wavelet transform returns a really satisfactory result: the MIR signals are smooth and only the genuine features relative to the sample vibrations are preserved. However, MIR spectra are not ready yet for data analysis because they show a linear trend which needs to be removed. MATLAB<sup>®</sup> provides several functions already implemented to take on this task (e.g. *detrend*, *polyfit/polyval*, etc.) but none of them offers the user a full control. For this reason, we produced a simple and home-made code, which finds the best straight-line passing through the two points defining the selected window corresponding to the wavenumbers where the IR band appears. Such a line must always lie under the signal and is subtracted from the denoised spectrum. The result is shown in fig.6.10.

---

<sup>2</sup>The Haar wavelet function is the first basis introduced for wavelet analysis and was proposed in 1909 by Alfréd Haar.

<sup>3</sup>A good hint in this sense can be found by observing the residuals between the original signal and the reconstructed one (fig.6.8): if we have correctly removed just the noisy components, the residuals are expected to be structureless.

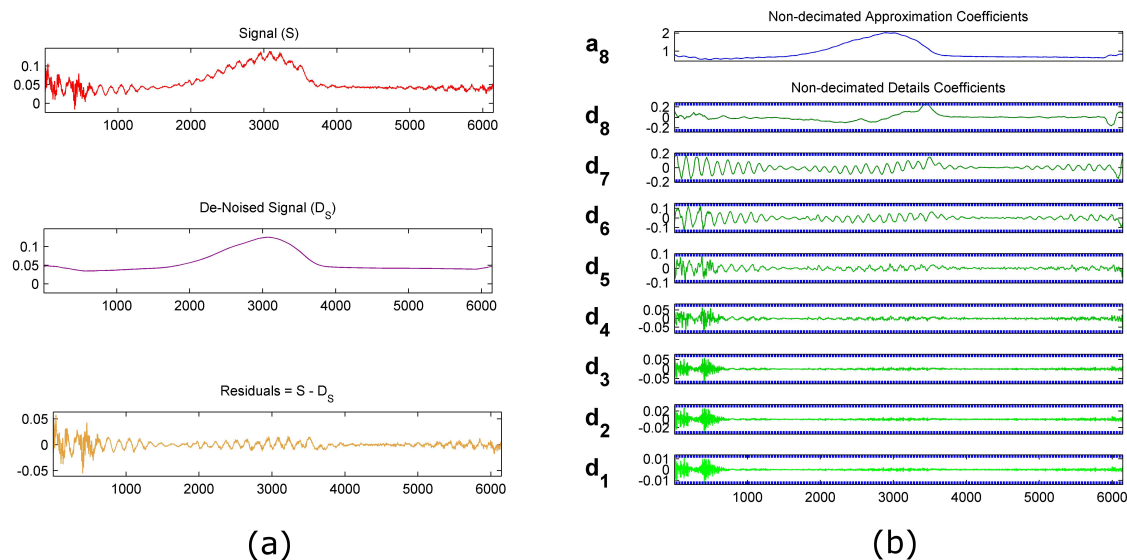


Figure 6.8: In panel (a) there are the original signal (red), the denoised signal as a result of the application of the Stationary Wavelet Decomposition technique described in the text (purple), and the residuals calculated as the difference between original and denoised signal (yellow). In panel (b) all the coefficients of the wavelet decomposition are shown. In particular,  $d_1 - d_8$  are the detail coefficients at respective levels;  $a_8$  is the approximation at 8<sup>th</sup> level, obtained setting to 0 levels 5-7 which include the unwanted "big" oscillations that we need to remove. As can be seen from 8<sup>th</sup> level, it produces a too strong smoothing as removes some "real" structures from the signal. For this reason, we actually decided to stop the approximation of the denoising procedure to the 7<sup>th</sup> level. Levels 1-4 mainly include the statistical noise, that we do not necessary want to remove from the original signal.

### Background subtraction

In principle, wavelet denoising combined with detrending would accomplish a good pre-processing of the collected spectra. However, on closer inspection it appears that most signals still present a background not completely flat. Hence, such a non-flat background has been traced for each spectrum performing a polynomial fit (computed by IGORPro<sup>®</sup>, using the Multipeak Fitting Package) and subtracted from the detrended signal. An example of the result obtained by means of background subtraction is pointed out in fig.6.11.

After the data treatment described above (wavelet denoising, signal detrending and polynomial background subtraction), MIR spectra are ready for analysis in terms of Gaussian deconvolution, in order to find the different water "populations" contributing to the OH-stretching band. This issue is discussed in the next sections.

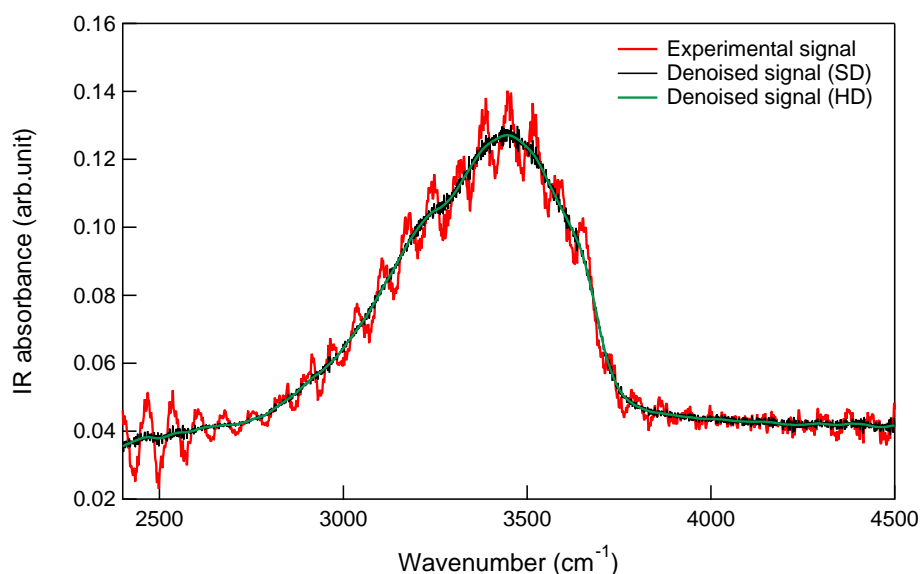


Figure 6.9: Example of the application of the Stationary Wavelet Decomposition (SWD) technique to filter the MIR spectra collected at the AILES beamline. The original signal is depicted in red; the black line represents the signal reconstructed after "soft" filtering (SD) by means of discrete wavelet analysis (level 7), that preserves the statistical noise component removing all undesired oscillations. Also the result of a "hard" denoising (HD, level 7) is superimposed to the original signal as a green line, where the statistical noise has been removed as well. We notice that this spectrum has been measured at relatively high temperature (297 K) and low pressure (0.07 GPa), and has been shown as an example because it does not really need the other corrections discussed in the text (i.e. linear detrending and subtraction of a polynomial background).

## 6.4 Experimental results

### 6.4.1 Mid-infrared data (MIR)

MIR spectroscopy allowed us to explore the spectral range corresponding to the OH-stretching band of confined water ( $2800 \lesssim \omega \lesssim 3800 \text{ cm}^{-1}$ ). In principle, the frequency range accessible by MIR spectroscopy should allow to observe also the HOH-bending band ( $\sim 1650 \text{ cm}^{-1}$  for bulk water). However, the time interval in the interferogram corresponding to that spectral region was heavily affected by noise and artifacts, which have irretrievably compromised the original signal. Moreover, according to [227], a strong two-phonon absorption band at approximately  $1900 - 2300 \text{ cm}^{-1}$  can degrade the signal in that spectral range, which is the same where the bending band of  $\text{H}_2\text{O}$  arises. In addition, it should be emphasized that the bending band has a low intensity and MIR spectra were collected through the internal source, that has a far lower brilliance than the synchrotron beam. The low signal-to-noise ratio, together with the other sources of signal degradation, may explain why we were not able to detect and analyse the bending band of  $\text{H}_2\text{O}$ . Consequently, since no information could be extracted from the MIR spectra about bending modes, we focused our attention on the OH-stretching bend.

MIR spectra were collected by varying temperature at fixed pressure, and measurements were repeated for four different pressures. In order to discuss our results in the light of the phase diagram reported in fig.6.1, we remind that  $1 \text{ kbar} = 0.1 \text{ GPa}$ .

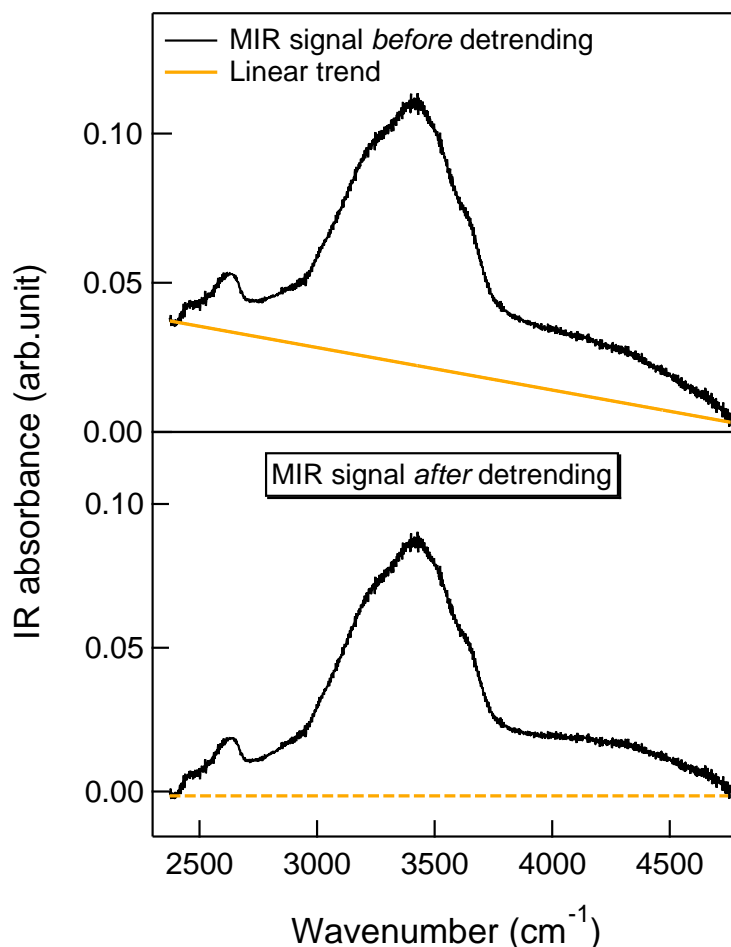


Figure 6.10: Example of detrending procedure applied to MIR signals after wavelet denoising. Detrending consists in the subtraction of the best straight-line from the experimental data (upper panel). In this context, the best straight-line is defined as the line passing through the two points at the extremes of the selected window, laying below the signal. The result is reported in the bottom panel. For clarity, a case where the linear trend to subtract was particularly evident has been shown.

As expected, visible modifications in the shape and intensity of the OH-stretching band occur as the temperature decreases. An overview of the MIR spectra collected as a function of temperature is displayed in fig.6.12 for each pressure. For the sake of clarity, the statistical noise has been removed from all spectra.

As can be noticed in fig.6.12, at the lowest pressure (0.07 GPa) the temperature range is wider. We indeed attempted to cool the sample further (down to 118 K), but at  $\sim 143$  K the absorbance profile shows the onset of a new intense and sharp sub-band, shifted towards the low-wavenumber tail of the OH-stretching band. By lowering the temperature, the intensity of this new sub-band starts to significantly and rapidly increase and the spectral shape is markedly modified. We believe that such a component can be ascribed to bulk ice probably grown onto the outer walls of the cell because such low temperature requires a better vacuum than that available in our experimental set-up. Since the MIR signal obtained between 118 K and 143 K did not come from confined water, it was likely not interesting for our purposes. Therefore, at higher pressures the sample was investigated over a restricted

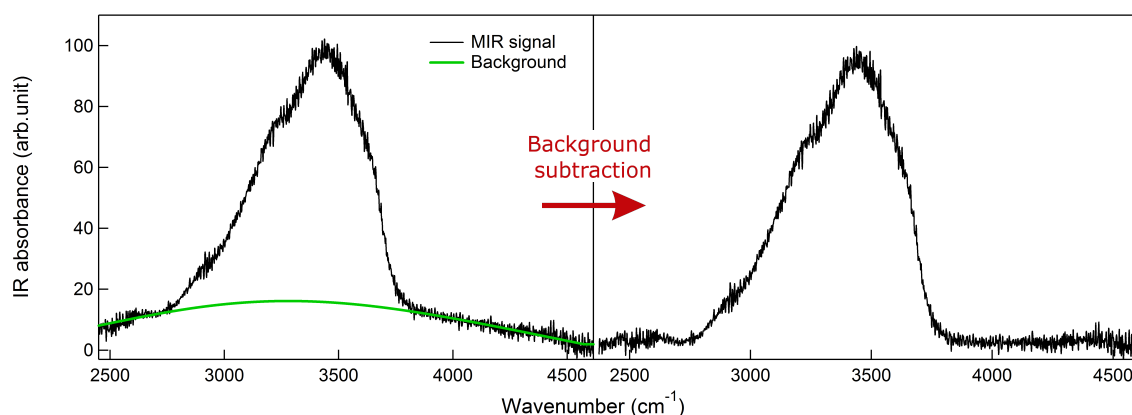


Figure 6.11: Example of background subtraction procedure. The MIR signal obtained after wavelet denoising and detrending still exhibits a non-flat background that needs to be removed (left side). Such a background has been modelled by means of a polynomial fit and subtracted from the signal. The result is displayed in the right panel. Also in this case, we have shown a spectrum where the polynomial background was particularly evident, in order to make the result of the correction better visible.

temperature range, between 293 and 153 K.

The physical origin of the small feature arising at about  $2600\text{ cm}^{-1}$  is not clear. Excluding the presence of hydrocarbon impurities in the substrate remaining from the surfactant after calcination (they could have given rise to a small spectral feature at around  $2800 - 2900\text{ cm}^{-1}$  due to CH stretching), a comparison with reports in the literature suggests that it should be caused by beam radiation-induced defects or be linked to the mesoporous silica matrix structure [200]. However, this small band is temperature-independent and was not associated with the spectrum of water. For this reason, it was not included in the spectral analysis of the OH-stretching band described in the following.

Fig. 6.13 shows the temperature evolution of the maximum of the OH-stretching band of confined  $\text{H}_2\text{O}$ . The position of the OH-stretching band maximum shifts towards higher frequencies as the temperature increases. This behaviour is followed at each pressure and is perfectly in line with previous deep inelastic neutron scattering measurements [304]. As demonstrated by IR and Raman studies under pressure [305], a shift of the intra-molecular stretching of the OH-bond towards higher energy is correlated with a decrease of the H-bond strength. Furthermore, for pressures lower than  $\sim 0.2\text{ GPa}$  two changes in the slope occur (at  $\sim 170\text{ K}$  and  $\sim 250\text{ K}$ ). A similar result has been found in [306] studying the vibrational dynamics of interfacial water at ambient pressure. These authors have interpreted such an outcome as the signature of two dynamical transitions in the H-bond strength. However, in our case, the two changes in slope merge into one (at around  $200\text{ K}$ ) at pressures equal or higher than  $\sim 0.2\text{ GPa}$ .

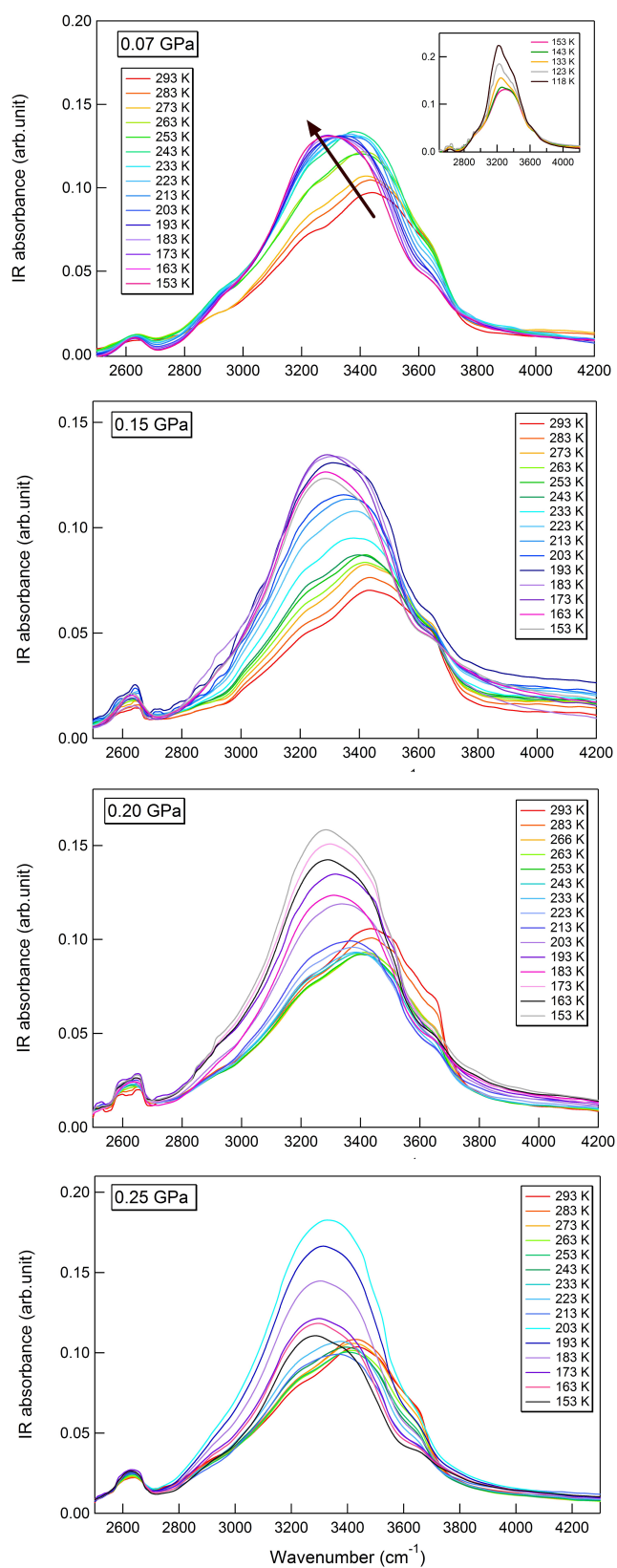


Figure 6.12: Temperature evolution of the OH-stretching band of  $\text{H}_2\text{O}$  trapped in MCM-41/C10 at different pressures (0.07, 0.15, 0.20, 0.25 GPa). Vibration of the OH-bond was investigated starting from ambient temperature (293 K) down to 153 K, where water is deeply supercooled. At the lowest pressure (0.07 GPa, upper graph) we attempted to lower the temperature further (the black arrow points out the way of decreasing temperature). However, an intense and sharp component arises, as shown in the inset: this has been ascribed to bulk ice forming on the outer walls of the cell.

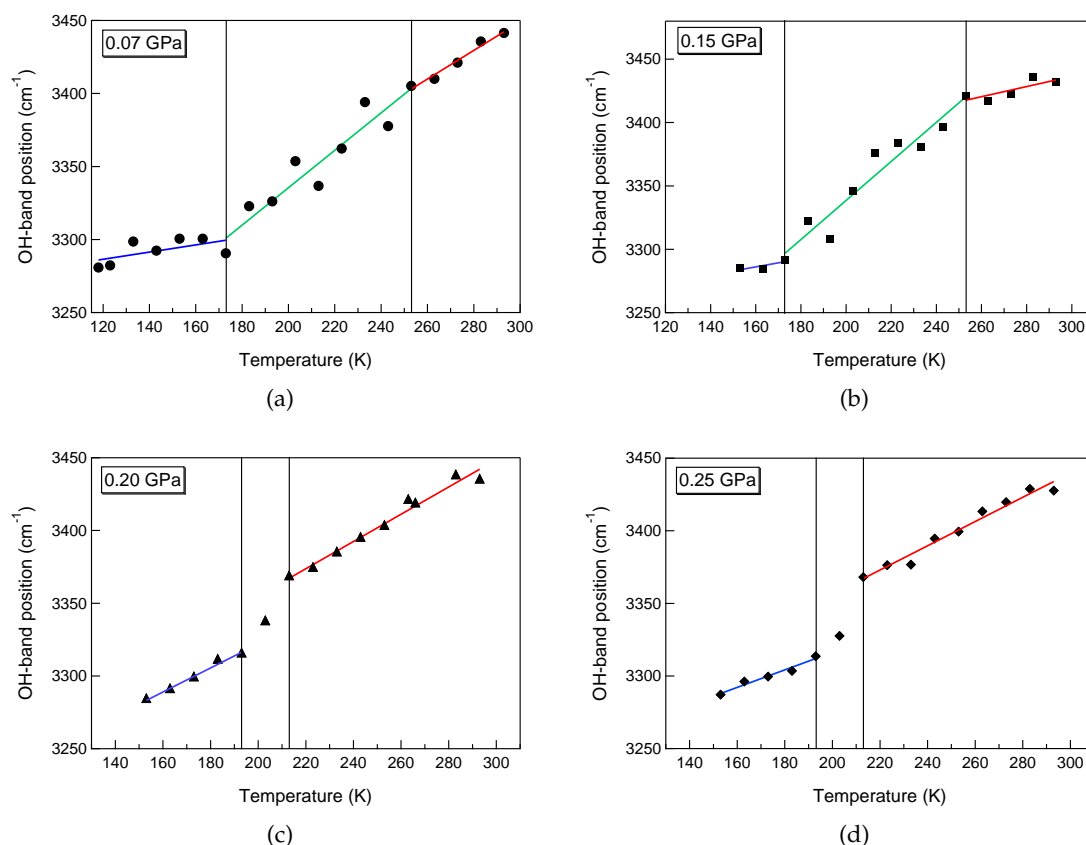


Figure 6.13: Position of the maximum of the OH-stretching band of confined water as a function of temperature, for different pressures. The frequency of the OH-stretching band maximum shifts towards higher values as the temperature increases, regardless of the pressure. However, for pressures below  $\sim 0.20$  GPa a double change of slope seems to occur (at  $\sim 170$  K and  $\sim 250$  K), while slope changes once at 0.20 GPa upwards (around 200 K).

Despite huge literature is actually available about analysis of Raman and IR spectra of OH-stretching band of water (see, for instance, [60, 69, 157, 158, 200, 289, 306–311] and references therein), a consistent and complete interpretation is still lacking. We have found that the spectral profile in the restricted MIR region reported in fig.6.12 can be satisfactorily described by the superposition of several Gaussian components (after signal pre-processing, as described in the previous section) over the whole investigated temperature range. In particular, we tried to minimize the number of parameters, i.e. Gaussian curves reproducing the experimental signal, with a satisfactory  $\chi^2$ . According to this criterion and some other authors' works on Raman and FTIR spectra (see, for instance, [289]), a deconvolution of the OH-stretching band of water using four Gaussians seems to be a reasonable choice. An example of the fitting procedure is reported in fig.6.14.

The same deconvolution procedure depicted in fig.6.14 has been applied to all collected spectra. For each pressure, MIR spectra were analysed in sequence starting from 293 K down to the lowest recorded temperature. Subsequently, the same procedure has been repeated on the opposite way, decomposing the MIR signal starting from the lowest temperature up to 293 K. This strategy has allowed us to have a "double check", in order to verify the reliability of the parameters found from the fitting procedure and of their evolution with

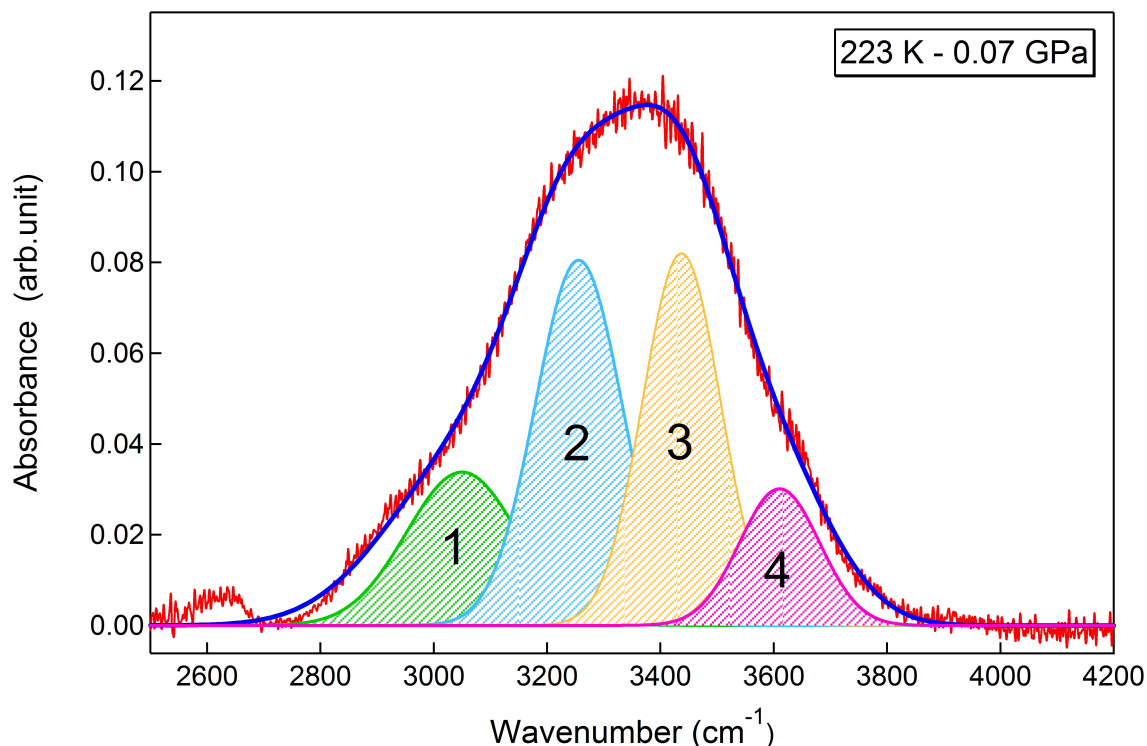


Figure 6.14: Example of the spectral deconvolution of the OH-stretching band of confined water in the MIR frequency range, collected at 223 K and 0.07 GPa. For all temperatures, the OH-stretching band has been decomposed in four distinct intramolecular sub-bands modelled as Gaussian curves, centred around  $\sim 3080 \text{ cm}^{-1}$  (green band, number 1),  $\sim 3200 \text{ cm}^{-1}$  (blue band, number 2),  $\sim 3450 \text{ cm}^{-1}$  (yellow band, number 3),  $\sim 3630 \text{ cm}^{-1}$  (magenta band, number 4). The red line represents the experimental data, whereas the overall fit (obtained as the sum of the four Gaussian components) is shown in the solid blue curve. The Gaussian positions have been initialized by using hints coming from [289] and [60], then the position of the 1<sup>st</sup> and 4<sup>th</sup> bands have been forced to not exchange with the adjacent bands. The interpretation that we propose for the four components of the OH-stretching band (see section 6.5) has suggested to require that these two sub-bands occupied the extrema of the spectral range investigated. No other constraint has been imposed.

temperature. The strategy developed for MIR data analysis has made us capable of monitoring the temperature and pressure evolution of each sub-band, which we have interpreted as representative of “populations” of water molecules with a different dynamic behaviour. At a first glance, it can be assessed that the temperature evolution of each sub-band position is quite similar for all pressures. Moreover, it distinctly emerges that increasing pressure does not dramatically change the position of the different components, as no swap between adjacent bands occurs (fig.6.15). More in-depth discussion about this argument will be given in the next section.

In order to provide a more quantitative interpretation of information extracted from MIR spectra analysis, we have identified the fractional area of each sub-band (i.e. the integrated area under the single band relative to the total area) as a suitable parameter for a description of the temperature and pressure evolution of our system. The contribution of each sub-band is assumed to be proportional to the relative abundance of that particular water molecule population. In this way, we could observe, at a given pressure, how the relative number of

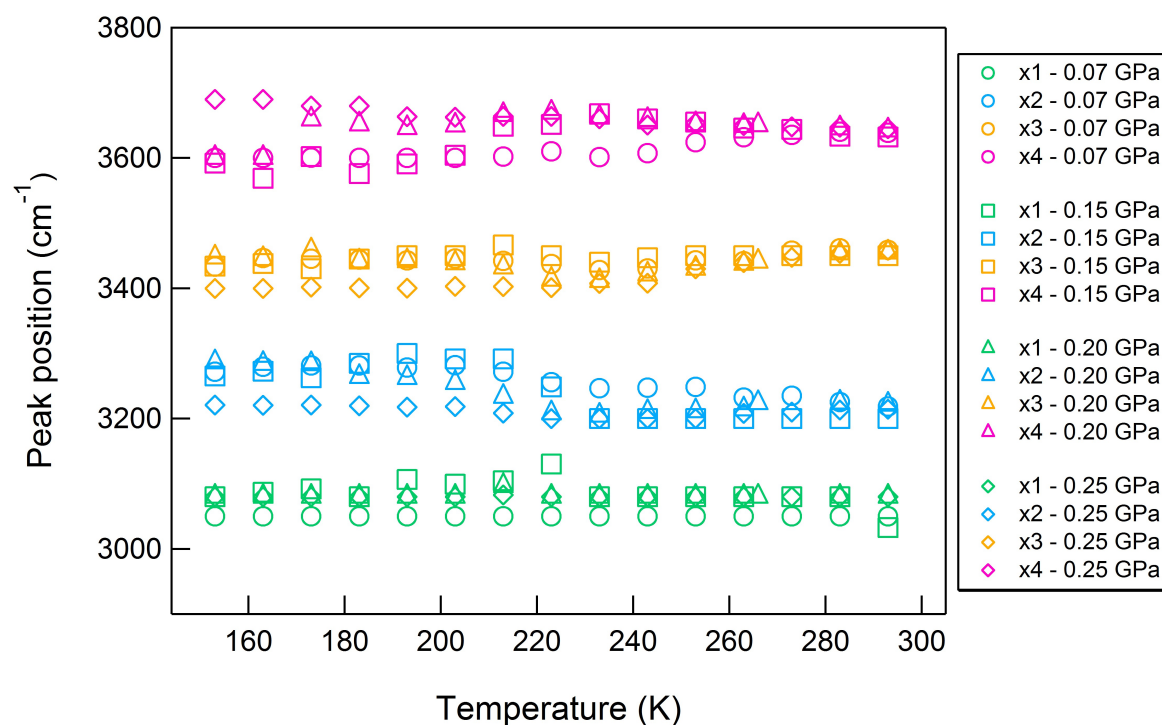


Figure 6.15: Position of the centre of the peaks relative to the four sub-bands coming from the decomposition of the OH-stretching band of confined water as a function of temperature. The results are provided for different values of the pressure applied to the system, showing that pressurizing the sample cell does not induce dramatical changes in the temperature evolution of the peak position of each component. The peak position of single bands are indicated as x1, x2, x3, x4 (referring to the same labels reported in fig.6.14).

water molecules belonging to each population changes as the temperature decreases from the ambient to the deeply supercooled regime. The result of this calculation is displayed in fig.6.16 for all pressures. The numbers 1, 2, 3, 4 labelling each water population refer to those reported on the sub-bands in fig.6.14.

The highest (4) and lowest (1) components correspond to the stronger and weaker H-bonds, respectively. As clearly emerges from fig.6.16, the effect of temperature on such components is practically negligible. By considering that the error on the calculated fractional areas is around 20%<sup>4</sup>, the fractional areas relative to components 1 and 4 can be regarded as constant over the investigated temperature range for all pressures. By contrast, the two dominant components (2 and 3) appear to be heavily affected by temperature: their fractional areas follow opposite trends on decreasing temperature, varying between  $\sim 0.1$  and  $\sim 0.6$ . Moreover, a temperature can be identified at which the fractional areas relative to the two dominant sub-bands cross each other, and the temperature where the crossing is observed decreases as the pressure increases. This behaviour is verified for all pressures, except for the highest one (0.25 GPa).

<sup>4</sup>This estimate is meant as an upper limit of the experimental error associated with the fractional area subtended by each sub-band obtained as the result of the Gaussian deconvolution of the OH-stretching band.

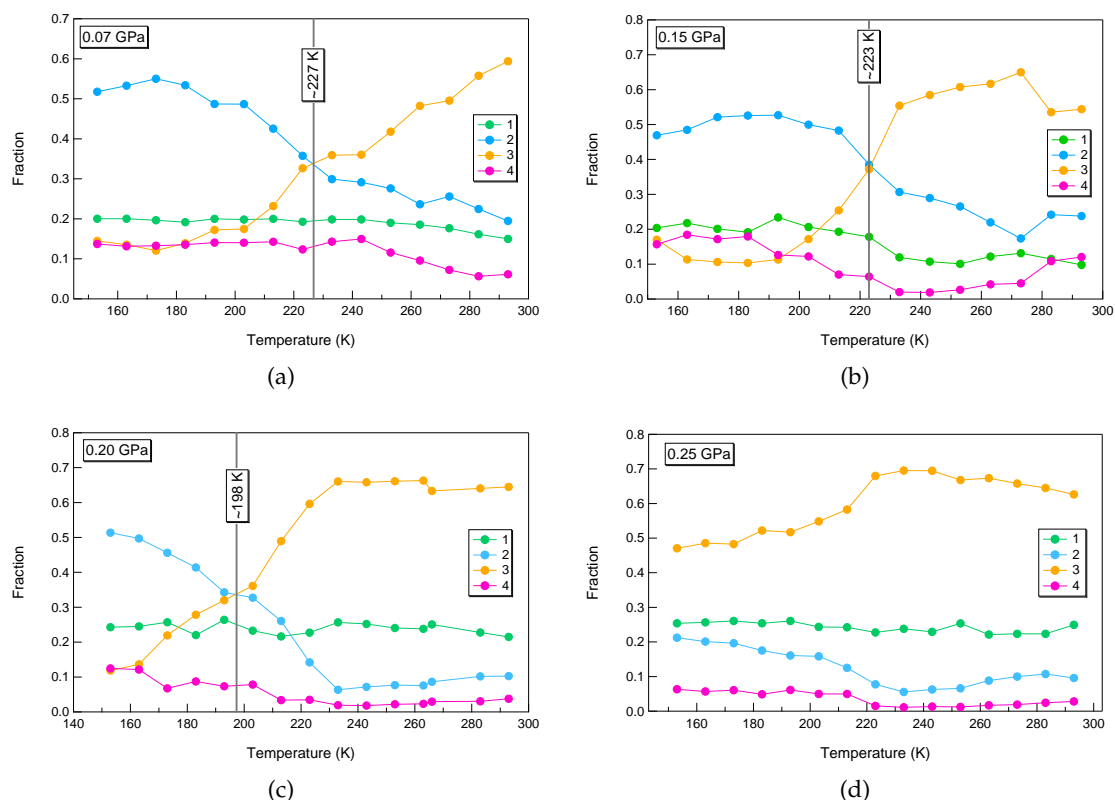


Figure 6.16: Temperature evolution of the relative integrated areas of the spectral components contributing to the OH-stretching band of confined water. Each fractional area is labelled using the same number reported in fig.6.14 onto the single sub-bands. For pressures between 0.07 and 0.20 GPa the vertical line indicates the temperature at which the two dominant components (2 and 3) cross each other.

#### 6.4.2 Far-infrared data (FIR)

Far-infrared spectroscopy applied on our sample allowed us to explore the spectral range corresponding to the so-called *connectivity band* of confined water ( $\sim 50 - 400 \text{ cm}^{-1}$ ). While the OH-stretching band probed by MIR spectroscopy corresponds to *intramolecular* modes, connectivity band covers a very low frequency range and corresponds to *intermolecular* motion. It arises from the longitudinal motion of the hydrogen atom along the hydrogen bond axis and depends more directly on the hydrogen bond network vibrations.

In principle, FIR experiments should make accessible also the librational band of water (modes relative to hindered rotations) at  $\sim 400 - 900 \text{ cm}^{-1}$ , but this was not the case. The librational band is characterized by a very low intensity and, in addition, in our spectra it was hidden by a more intense spectral component due to the silica matrix. This appears as a steep rise originating from  $\sim 350 \text{ cm}^{-1}$  upwards (fig.6.17).

Both the librational and connectivity bands are more sensitive probes of the hydrogen-bonding environment with respect to the OH-stretching [60]. Studying water confined in micelles compared to bulk water, for instance, it results that weaker hydrogen bonding in micelles causes a 25% decrease in the librational band frequency, whereas only a 3% increase is observed in the OH-stretching frequency [312]. This demonstrates that, despite OH-stretching, librational and connectivity bands all probe the OH-bond of water molecules,

they respond differently and with different sensitivity to different environments. The investigation of complex liquids like water might particularly benefit from the information embedded in the low frequency region of IR spectrum. Although the OH-stretching spectral region has been extensively studied so far, librational and connectivity bands remain under-represented in the literature due to the experimental difficulties in exploring the corresponding spectral ranges. This observation underlines the usefulness of our FIR measurements and suggests that they could be of utmost importance to describe a more complete picture of supercooled water behaviour. Moreover, as shown in the following of this chapter, FIR spectra have helped us to achieve a more reliable and solid interpretation of data presented in this thesis, concerning both the structure and the vibrational motion of confined water.

Although less evident with respect to MIR spectra, also FIR spectra were affected by big oscillations superimposed on the signal we were interested to analyse (fig.6.17). All FIR spectra were therefore pre-processed by applying the wavelet denoising technique described in section 6.3.2 (with a denoising level equal to 4). Subsequently, a liner baseline was subtracted in order to remove the contribution from the rise of the signal on the higher frequency tail of the connectivity band, corresponding to the onset of the librational band. The result is shown in fig.6.18 for all collected spectra.

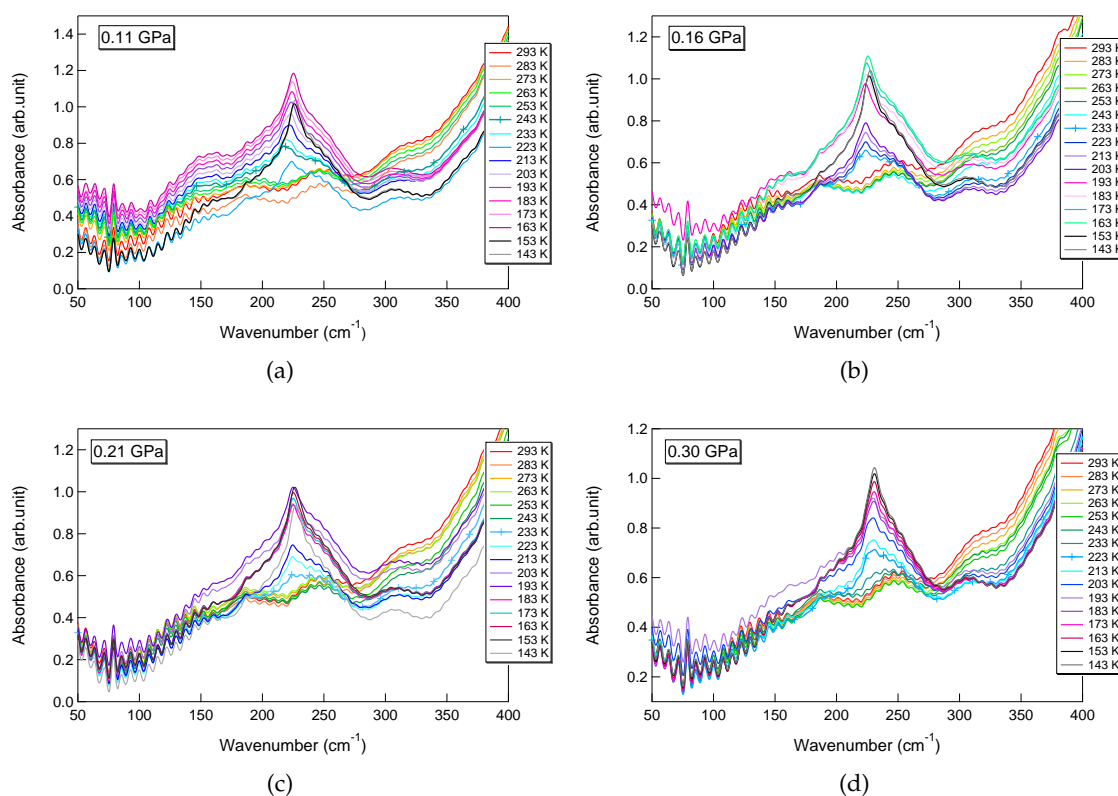


Figure 6.17: Overview of the FIR raw data (spectra as acquired, with no pre-processing) collected by varying temperature and pressure. For each pressure (0.11, 0.16, 0.21, 0.30 GPa) the temperature ranges from 143 K to 293 K. Curves marked with symbols ("+") indicate the temperature where a transition clearly occurs: the shape of the connectivity band changes from a liquid-like to a solid-like configuration.

We preferred not to perform any quantitative analysis on FIR spectra. In principle, each curve could be deconvoluted as the sum of four or five Gaussians [60], but we would not be able to assign a proper physical meaning to the different components. In our opinion, a clear correlation to the different states of connectivity of water molecules involved in the HB network is still lacking and needs further investigations. In fact such an interpretation is based on the application of the percolation model developed by Stanley and Teixeira [54], but no quantitative agreement for the connectivity band has been found so far, showing that attempting to directly link the area of the connectivity band (or of its sub-bands) with the mean number of H-bonds per molecule does not sound really reliable. At the best of our knowledge, up to now no useful hints on this regard are available in literature. However, quantitative analysis is not essential: relevant information can be extracted by relying on a qualitative approach as well.

After removing the linear background accounting for the librational band, it clearly emerges that the integrated area under the connectivity band in the limited spectral range (fig. 6.18) increases by lowering temperature, in agreement with literature [60, 306]. In particular, at room temperature the sample exhibits the FIR spectrum typical of liquid water. On cooling, as we access the temperature region where water is supercooled, the system keeps similar characteristics and looks like a liquid down to a specific temperature. When such a temperature is reached, the spectrum shows an abrupt modification and a new peak arises unambiguously proving that a solid phase is forming in water trapped inside the porous matrix. The "transition" temperature changes with pressure (243 K at 0.11 GPa, 233 K between 0.16 and 0.21 GPa, 223 K at 0.30 GPa), consistently with a negative-slope coexistence line in the  $P - T$  phase diagram.

The transition from a fully liquid system to a liquid-solid coexistence becomes less sharp as pressure increases. This distinctly emerges by taking a look at the integrated area under the connectivity band (over the spectral range included between 95 and 285  $\text{cm}^{-1}$ ) as a function of temperature for the different pressures (fig. 6.19). Two changes of slope suggest there are two dynamical transitions in the HB-bond network arrangement.

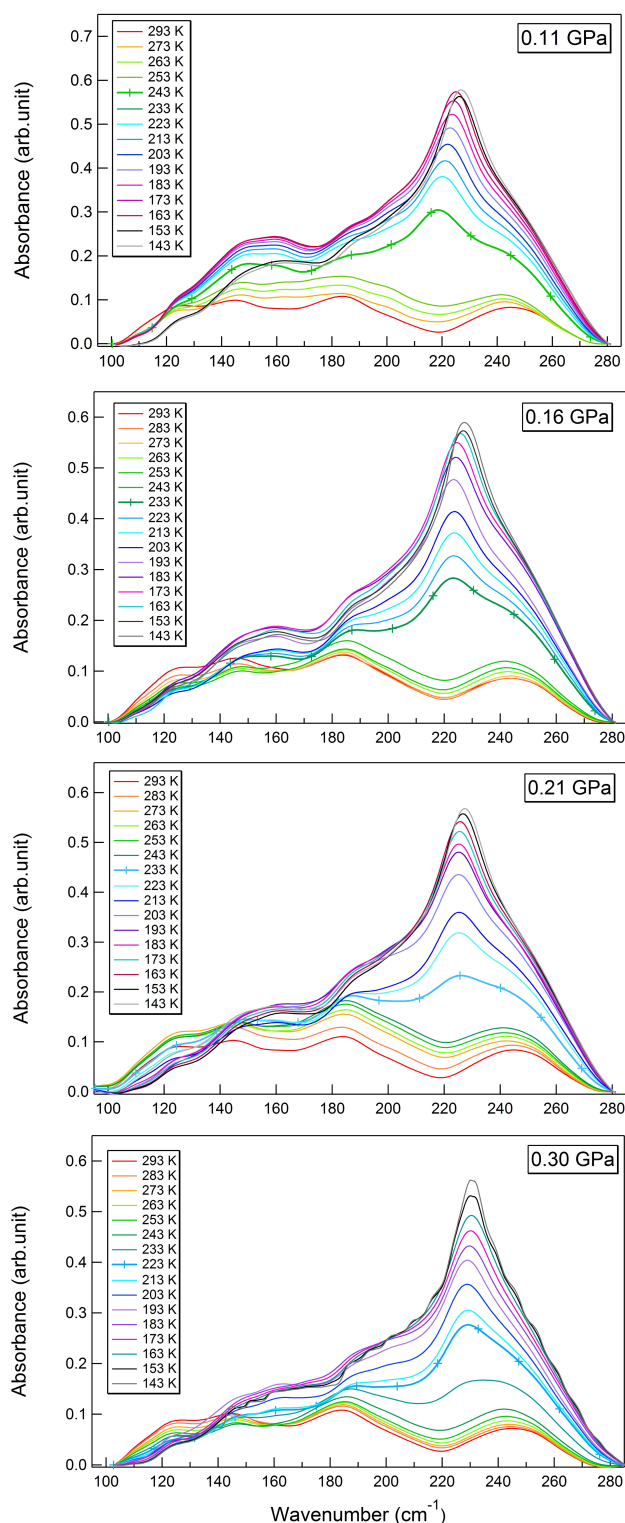


Figure 6.18: Temperature evolution of the connectivity band of H<sub>2</sub>O confined in MCM-41/C10 at different pressures (0.11, 0.16, 0.21, 0.30 GPa) after denoising and linear background subtraction. Collective motion of the OH-bond network was investigated starting from ambient temperature (293 K) down to 143 K, where water is deeply supercooled. Starting from room temperature and cooling down, the system remains completely liquid up to a certain temperature, where the corresponding curve is marked with symbols ("+" over the solid line). This temperature clearly shows the signature of the formation of a solid phase inside the pore volume, and it decreases with increasing pressure (243 K at 0.11 GPa, 233 K at 0.16 and 0.21 GPa, 223 K at 0.30 GPa).

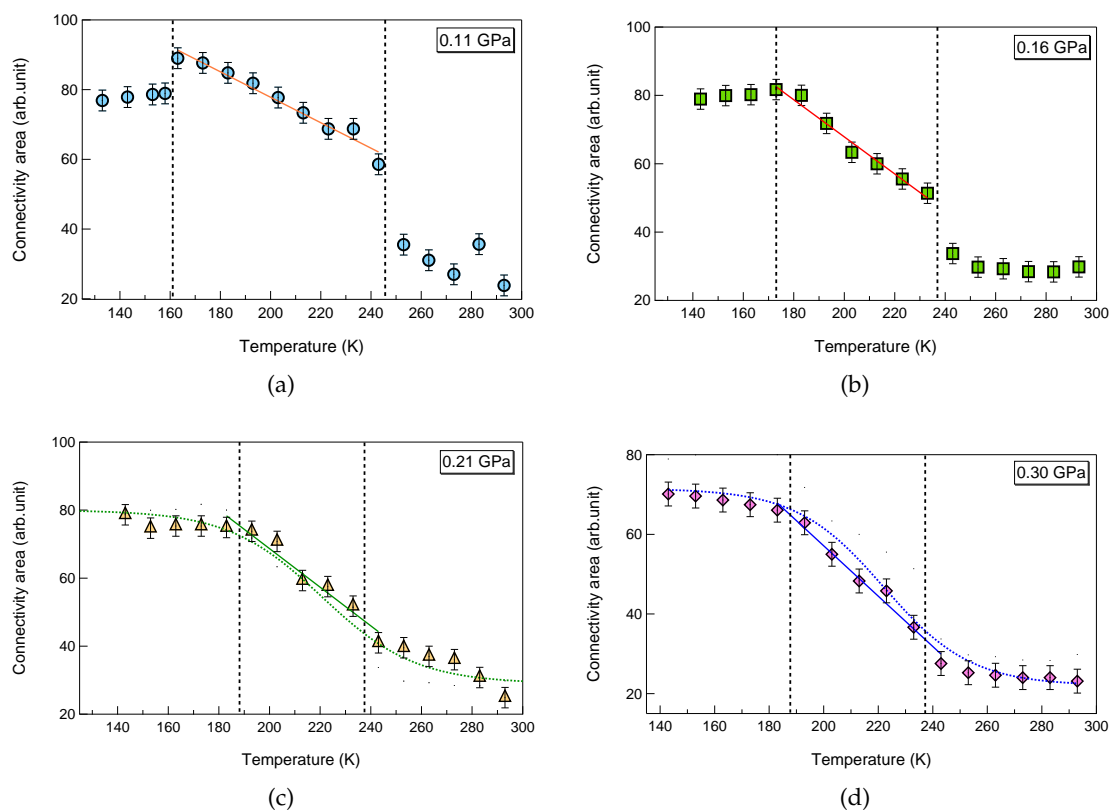


Figure 6.19: Temperature evolution of the integrated area under the connectivity band (empty symbols) for each pressure. In agreement with the literature [60, 306], the connectivity area increases upon cooling. Moreover, as the pressure increases, the transition from a liquid-like to a solid-like behaviour becomes more gradual. Solid lines are linear fits, while dotted curves are guides for the eyes. A rough calculation has allowed to estimate the error bar associated to the integrated area (it is to be intended as an upper limit estimation, thus it has been considered as a constant for all temperatures and pressures). We note that the slope ( $m$ ) of the linear fit involving the data in the region delimited by the vertical dotted lines progressively increases (in absolute value) as the pressure raises. The values obtained for  $m$  are indeed:  $(-0.365 \pm 0.027)$  at 0.11 GPa,  $(-0.542 \pm 0.038)$  at 0.16 GPa,  $(-0.568 \pm 0.059)$  at 0.21 GPa, and  $(-0.633 \pm 0.039)$  at 0.30 GPa, where the slope is expressed in arbitrary units.

## 6.5 Discussion and conclusions

IR spectroscopy, applied over a wide frequency range, has allowed us to probe both the *intra*-molecular (OH-stretching motion) and *inter*-molecular (OH $\cdots$ O stretching motion) vibrations of water molecules confined in a restricted environment. The porous substrate where water was trapped is exactly the same investigated by means of neutron scattering (chapter 5). In this manner we were able to observe the behaviour of our confined system from a different viewpoint, gathering new and relevant information about vibrational dynamics of water. This has helped us to complement the picture relative to the temperature evolution of supercooled water structure given in the previous chapter. More importantly, IR spectroscopy has strengthened our interpretation of experimental data in terms of a liquid-solid

phase transition experienced by confined water below the bulk melting temperature.

In the MIR frequency range, the OH-bond stretching vibration of H<sub>2</sub>O confined in MCM-41/C10 silica matrix gives rise to a broad absorption band extending approximately between 2800 and 3800 cm<sup>-1</sup>. The intensity of this band significantly increases on lowering temperature and its maximum shifts towards lower frequencies. A redshift of the OH-band of confined water is also observed with respect to bulk water [60, 312]. Despite some useful information can be put in evidence by a direct observation of the collected spectra, we attempted to understand the temperature evolution of the OH-stretching band of our system from a more quantitative point of view. According to literature [60, 200, 289, 311], each spectrum has been deconvoluted into four sub-bands described by Gaussian functions. Actually, there is not a general agreement in the number of sub-components and the relative interpretation. Most of the authors describes the OH-stretching band (of both bulk and confined water) in terms of three Gaussians [60, 157, 158, 308], but some descriptions also involve four [200, 289, 310], five [69, 200, 311] or six components [59]. However, although our four-Gaussian deconvolution is obviously not unique from a strictly mathematical viewpoint, this choice provides a reasonable description of the composition of the OH-stretching band and its temperature evolution.

It has been established that the vibrational modes involving the stretching of intramolecular OH-bond are sensitive to the strength of the H-bonding between water molecules [60]. Nonetheless, we do not trust the widely accepted interpretation that directly assigns to each sub-band a specific H-bond degree of coordination, i.e. the number of hydrogen bonds per water molecule ranging from 0 to 4. This interpretation relies on the following argument: the more H-bonds a water molecule establishes with its neighbours, the stronger must be its OH-oscillator strength; if the bond is stronger, then the corresponding OH-stretching frequency appears downshifted. Thus, the supporters of this interpretation presume that the substructures within the OH-stretching band can be ascribed to different populations of water molecules forming a different number of H-bonds [60, 158, 200]. In particular, the higher is the degree of coordination of water molecules, the lower is the frequency at which the corresponding sub-band is centred.

We believe, by contrast, that the OH-stretching band has a very complex structure, as it spans a broad frequencies range corresponding to manifold dynamic regimes. As shown for liquid water beyond its melting point, the broad band observed in the MIR region has to be regarded as a continuous distribution of H-bond frequencies, not necessarily due only to stretching but possibly linked to other vibrational modes [313]. From this point of view, a description of the OH-stretching band in terms of multicomponent models is far to be trustworthy and unambiguously correlated with the real structure and behaviour of the system [314]. In addition, it has been recently pinpointed that, unlike many other simpler liquids, H<sub>2</sub>O is characterized by a strong coupling between its vibrational modes and by a non-adiabatic vibrational dynamics [230]. This implies that stretching, bending and intermolecular modes can not be treated as evolving independently, but their strongly mixed character needs to be taken into account as IR spectra are analysed. That is to say, it is not possible to correctly describe the OH-stretching vibration of water simply as a local bond stretching or as the linear combination of symmetric/asymmetric modes; it is rather to be regarded as the result of a collective and complex excitation of several molecules [242].

Consequently, attempting to establish a direct link between the Gaussian sub-bands and the number of H-bonds formed by water molecules seems to be a quite oversimplified description, which might lead to a misleading interpretation of the information obtainable from

water MIR spectra. Therefore, even if we admit that OH-bonds with different vibrational frequencies experience different *local* environments, on the basis of these observations we generally interpret each substructure as representative of a water population with a distinct dynamic behaviour. More precisely, we describe each sub-band as follows (for numbers and colours, we refer to fig.6.14):

- 1<sup>st</sup> sub-band (green): interfacial water ( $\omega \approx 3000 - 3100 \text{ cm}^{-1}$ ).  
It is well known that nanoconfined water gives rise to a non-freezable layer located at the pore wall interface, as discussed in chapter 2 [175, 178]. It is reasonable to hold that interfacial water is less mobile than water inside the core pore, leading OH-bonds to oscillate with a lower frequency. Such an assignment agrees with recent findings reported in [306], where interfacial water shows the OH-stretching band position at around  $3100 \text{ cm}^{-1}$  over the temperature range of our interest.
- 2<sup>nd</sup> sub-band (blue): water population with a slower dynamics ( $\omega \approx 3150 - 3300 \text{ cm}^{-1}$ ).  
This band corresponds to the component that several authors ascribe to water molecules with the highest degree of connectivity (coordination number close to 4), resulting in a stronger H-bonding. Such a component should dominate the absorbance profile of the LDL/LDA phase [60, 289]. Some authors, like Venyaminov *et al.* [315], assign such a band to the overtone of the bending ( $2\nu_2$ ), enhanced by Fermi resonance.
- 3<sup>rd</sup> sub-band (yellow): water population with a faster dynamics ( $\omega \approx 3350 - 3500 \text{ cm}^{-1}$ ).  
This band has been assigned to the component that several authors identify as water with an average degree of connectivity, intermediate between monomers and a fully developed HB network. Such a band should result in a distorted and weaker H-bonding and may dominate the absorbance profile of the HDA/HDL phase [60, 289]. In the alternative interpretation given by [315] this band corresponds to the symmetric stretching ( $\nu_1$ ).
- 4<sup>th</sup> sub-band (magenta): water molecules not engaged in a HB network or poorly connected ( $\omega \approx 3600 - 3650 \text{ cm}^{-1}$ ). In the alternative interpretation given by [315] this band corresponds to the asymmetric stretching ( $\nu_3$ ).

It is relevant to note that components 2, 3, and 4 are well matched in MIR spectra of bulk and confined water investigated by other authors [60, 289], despite a different interpretation has been proposed. Conversely, the 1<sup>st</sup> component, which in our picture reflects the behaviour of pore interfacial water, cannot be identified in bulk water. It is also absent in the deconvolution strategy adopted by [289] for the decomposition of MIR spectra relative to confined water. Though a similar counterpart has not been found in the literature, this component was necessary to obtain a satisfactory deconvolution of our MIR spectra at all temperatures and pressures. Hence we believe that its inclusion as a deconvolution term centred in that specific frequency region (around  $3000 \text{ cm}^{-1}$ ) is required in order to achieve an adequate description of the MIR profile from both a mathematical and physical point of view, being it utterly consistent with the interpretation here proposed.

A useful overall view of the information that can be extracted from MIR spectra is given by the fractional area calculated for each component as a function of temperature at fixed pressure (fig.6.16). Although the temperature evolution of the position of the peak relative to each sub-band did not give us any useful information (fig.6.15), the integrated fractional area reveals to be a more effective and meaningful tool to understand the role played by temperature and pressure on the vibrational dynamics of our system. More specifically, at

all pressures the fraction of interfacial water molecules (green) settles on  $\sim 20\%$  and is almost independent of temperature, with a slight increase at higher pressures. This is likely due to the fact that a higher pressure applied to confined water promotes the interaction of water molecules with the pore walls, causing a moderate increase in the relative population of interfacial water. This is in accordance with what we may expect for a layer of molecules with a nearly "arrested" dynamics and that cannot experience a temperature-driven transition from a disordered phase (liquid) to a more ordered one (ice). Also the population of isolated (not-networking) water molecules is quite small (less than 20%), with a temperature behaviour closely resembling that of interfacial water. More interesting is the interplay between the two water populations in the middle of the OH-band and their evolution with temperature. In particular, while the fraction of "slower" water molecules continuously increases as the temperature decreases, the fraction of "faster" water molecules undergoes the opposite trend. By observing fig.6.16, it clearly emerges that the "slower" and "faster" water populations swap their roles at a given temperature. Indeed, starting from room temperature, water inside the core pore is mostly represented by molecules with a "faster" dynamics. This holds true also in the supercooled regime until a transition temperature is reached. Such a temperature signs an inflection point (crossover): as the temperature is lowered further, the "slower" population becomes dominant. For pressures higher than 0.20 GPa the inflection point disappears: this means that water above 0.20 GPa dynamically behaves as a more homogeneous system, whose composition does not change noticeably with temperature.

This observation leads us to focus our attention on how the vibrational behaviour of the system under investigation responds to pressure variations: up to  $\sim 0.20$  GPa the dynamic behaviour remains essentially unchanged (except for a downshift of the crossover temperature for increasing pressure), while it becomes less sensitive to the temperature at  $\sim 0.25$  GPa. Although temperature is lowered more than 100 K, the two water populations do not dramatically change: the "faster" component is dominant over the whole temperature range, probably because pressure increase hinders the formation of regular and extended cluster of hydrogen-bonded water molecules and HBs are more distorted, thus the system is overall less rigid and the "slower" population gives only a little contribution. Our conjecture is that this behaviour may be connected to the anomalous pressure dependence of the self-diffusion coefficient of supercooled bulk water at 268 K, showing a maximum between 0.150 and 0.200 GPa [316–318], at around the same pressure at which water molecules approach their first neighbours more closely [319] (the distance between two oxygen atoms,  $r_{OO}$ , reaches its minimum)<sup>5</sup>. The same result has been recently confirmed by [320] for supercooled bulk water over a wider temperature range (244 – 298 K), showing that, in the  $P-T$  plane, the locus of viscosity minima closely follows that of the self-diffusion coefficient maxima and both lie between 0.150 and 0.200 GPa. Such a maximum in the self-diffusion coefficient vs  $P$  is consistent with the dominance of the "faster" water population above 0.20 GPa pointed out in our experiments.

Although these facts have been observed in bulk water and over a narrower temperature range comparing to our experiments, it is interesting to note that the maximum of the self-diffusion coefficient of water as a function of pressure seems to coincide with the OH-stretching frequency maximum, which is reached between 0.2 and 0.4 GPa at 290 K [325, 326]. The OH-stretching frequency has also a minimum at 0.2 GPa, which has been ascribed to a possible increase in interpenetration of hydrogen bonded networks: as the pressure

<sup>5</sup>Further data and discussions about the pressure dependence of viscosity or self-diffusion coefficient in bulk and supercooled water can be found in [320–324].

starts to increase, interpenetration is likely preferred over more extreme bending or breaking of the hydrogen bonds (interpenetration increases the density without reducing the intermolecular distances).

Since a link between the local structure of water and its dynamics is expected [327–329], some authors [131] have suggested the possibility that big changes in intramolecular vibrational properties may be connected to the onset of fractional Stokes-Einstein (SE) behaviour [64, 172, 321].

The picture given in fig.6.16 would seem to confirm the presence of a coexistence line in the water phase diagram [272] (see fig.2.6), and apparently supports results provided by other studies [69, 289] (fig.6.20) on water confined in MCM-41-S using Raman and FTIR spectroscopy. However, our interpretation departs from this picture and is supported by the combination of MIR data with: *i*) the analysis of neutron scattering and diffraction experiments (chapter 5), *ii*) FIR experiments (discussed in the following).

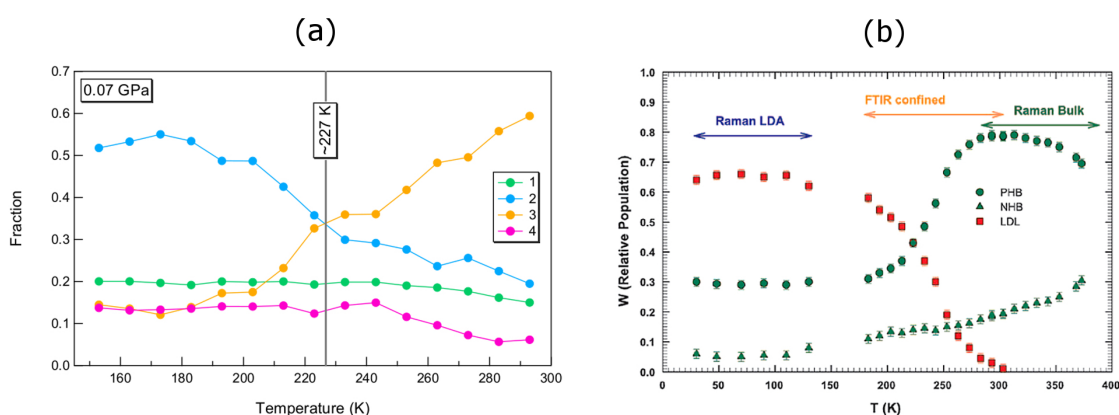


Figure 6.20: Comparison between the temperature evolution of the relative populations (fractional area) of the main spectral contributions to the OH-stretching band found by us at the lowest pressure (a) and that reported by Mallamace and his co-workers at ambient pressure (b) [69]. In the case of our experiment, the interpretation of each contribution is given in the text. As far as results shown in (b) are concerned, water is regarded to be characterized by two different local hydrogen bond structures. PHB (green circles) and NHB (green triangles) refer to partially hydrogen-bonded and free molecules, respectively. Red squares indicate molecules involved in a fully tetrahedral HB network, that, in the interpretation given in [69], characterizes the LDL phase. The different temperature regions were investigated by different experimental techniques (Raman for LDA and bulk water, FTIR for confined water in the supercooled regime).

In the FIR frequency range we focused our attention on the so-called connectivity band, which arises approximately between 100 and 280  $\text{cm}^{-1}$ . It is assigned to the *intermolecular* H-bond stretching band and is due to the collective vibrational motion of the HB network. These characteristics make it a more direct probe of the H-bond dynamics, being it much more sensitive to the environment experienced by hydrogen-bonded water molecules. Obviously, intermolecular network could be probed also by indirect way, that is to say by inferring information from intramolecular (OH-stretching) vibrational modes. As described in chapter 4, each bond can be thought as an oscillator whose elastic force is sensitive to the level of interaction of the molecules with their surroundings. Consequently, in a set of connected molecules a change in the oscillator force of a particular bond is expected to induce

correlated changes in the oscillator forces of the neighbouring bonds (whether intramolecular or intermolecular) [60, 158, 330]. Notwithstanding, a *direct* probe of the intermolecular oscillations given by the exploration of the FIR frequency domain is much more desirable, as it leads to a more reliable and complete interpretation of the experimental data.

The FIR absorbance strongly increases with decreasing temperature for all investigated pressures, as shown in fig.6.18. What is really worth noting is the remarkable change in the spectral shape occurring at a specific temperature varying with pressure.

As pointed out in section 6.4.2, such an abrupt change in the shape of the FIR spectra on cooling can be regarded as the signature of the formation of a solid phase within the pore volume. This statement can be easily confirmed by comparing our experimental FIR spectra with the signal of hexagonal ice, amorphous ice and liquid water provided by [306] over the same frequency range (fig.6.21).

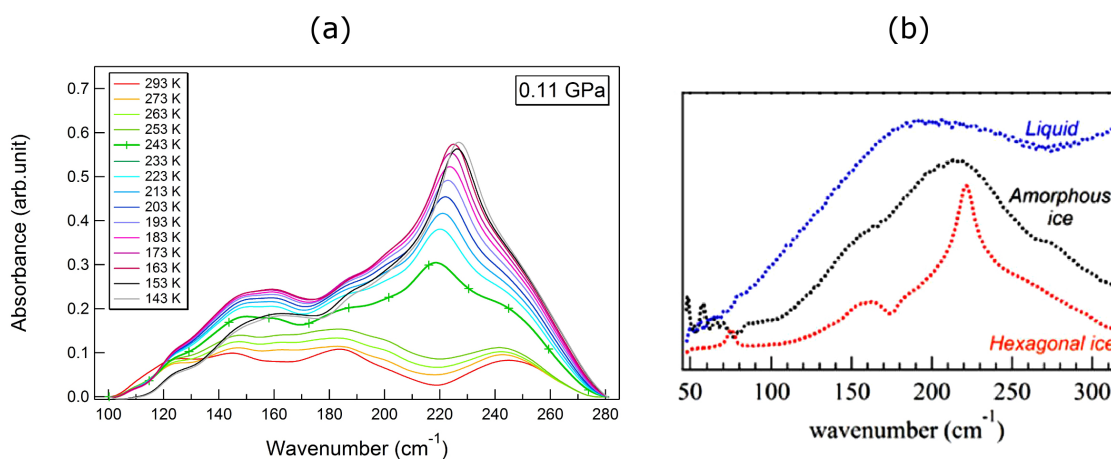


Figure 6.21: Comparison between FIR spectra of water confined in a porous silica substrate obtained from our experiment (a) and the signal of hexagonal or amorphous ice and liquid water over the same spectral region available in [306] (b). Our spectra clearly show that, on lowering temperature, the connectivity band of confined water undergoes a transition from a liquid-like to a solid-like configuration.

At ambient temperature the connectivity band is typical of liquid water and preserves the same characteristics down to  $\sim 253$  K. By cooling the system further, a well-defined peak arises at  $\sim 220$  cm<sup>-1</sup> and progressively shifts between  $\sim 220$  and  $\sim 230$  cm<sup>-1</sup>, closely resembling the peak assigned to crystalline ice [306]. This implies that a transition temperature can be identified between 253 and 243 K: starting from ambient temperature, water confined in the porous silica substrate is originally liquid, then the onset of a solid phase leads to the coexistence of ice and supercooled liquid water within the pore. As long as the temperature is lowered, the solid phase grows up and the intensity profile looks like that expected for crystalline ice (fig.6.21(b), red curve). This result confirms that the collective H-bond network of confined water starts to adopt a solid-like configuration below  $\sim 240$ – $250$  K. Consequently, on the basis of these observations, we are compelled to conclude that confined water can not be longer observed in its liquid phase below a certain temperature decreasing as pressure increases. This result confirms what was previously found with neutron diffraction data from NIMROD at ambient pressure, where we revealed the onset of a liquid-solid phase

transition at a temperature close to that identified in FIR spectra. Moreover, it is worth mentioning that the intramolecular OH-stretching band does not show any dramatic change corresponding to the transition we clearly observe in FIR spectra. This suggests that MIR spectroscopy is a much less sensitive probe of structural changes occurring in networking liquid and no conclusions should be drawn on the only basis of MIR data.

As already noticed, the transition from a fully liquid system to the coexistence of a solid and liquid phase becomes less sharp as the pressure increases (fig.6.19). This probably occurs because pressure, distorting hydrogen bonds, prevents the rearrangement of water molecules in a more ordered configuration, typical of the solid phase.

Fig.6.19 also reveals the presence of two changes of slope in the temperature evolution of the integrated area of the connectivity band. The transition occurring at higher temperature ( $\sim 230 - 250$  K) can be easily assigned to the abrupt modification in the spectral shape due to the onset of the solid phase previously discussed. The second transition may find confirmation in recent data concerning the behaviour of 2D water [306]. These authors, by studying the connectivity band of interfacial water adsorbed onto the surface of hydrophilic porous silica glass (Vycor) at very low temperatures and ambient pressure, find a transition in the integrated area of the connectivity band at a temperature not too far from that identified in our experiments (fig.6.22).

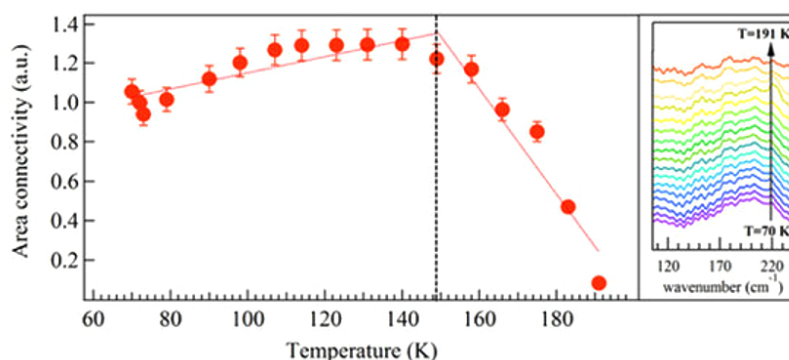


Figure 6.22: Analysis of FIR spectra of 2D water performed by [306]. Figure shows the integrated intensity of the spectra reported in the inset on the right for different temperatures, corresponding to the connectivity band of interfacial water.

Their interpretation is that the two-dimensional topology frustrates the tetrahedral geometry reached in the bulk. Hence, even at very low temperature (160 – 170 K), interfacial water does not crystallize as the thermal energy is sufficient to break a few HBs. As a consequence, water is in a low density amorphous state at low temperature, but at 160 – 170 K transient patches of hydrogen-bonded molecules appear, with a very long correlation time (slow glassy-like dynamics). By increasing the temperature, these nuclei of hydrogen-bonded water molecules become ever more likely and grow in size, giving rise to a heterogeneous system where high-density-like clusters coexist with low-density-like patches. As far as the investigation by [306] is concerned, 2D water also exhibits a second transition (observed in MIR spectra) at around 250 K: on the basis of the percolation model, the authors interpret such a phenomenon as the result of the low-density domain that percolates and finally reach a complete coverage of the surface [306]. Interestingly, although Vycor (like MCM-41) is a model system, the two transition temperatures reported by [306] may have a general interest. For example, Mazza *et al.* have studied the HB network of the hydration water of

Lysozyme (a soluble globular protein) by means of dielectric spectroscopy [143]. They observed two crossovers in protons relaxation modes at approximately 180 and 250 K. These experimental results are also consistent with coarse-grained and Monte Carlo simulations of hydration water that show two maxima in the specific heat: one is associated with a maximum of fluctuations of the cooperative local reordering of the HB water network (network relaxation), while the other is attributed to the maximum fluctuation of the formation and breaking of HBs (percolation relaxation) [143]. However, it should be noted here that the system investigated in [143] is a protein surface hydrated with only a water *monolayer*. This means that the hydration water cannot form ice at any  $T - P$  point of the phase diagram, thus the link with the results presented in [143] provides interesting hints only for dynamical aspects.

Nonetheless, we believe that in our case, even if this second transition occurred, it would be hidden by the liquid-like transition experienced by water in the core pore and put clearly in evidence by the intense peak arising in the FIR spectra around  $220 - 230 \text{ cm}^{-1}$ .

Therefore, we can assign the transition occurring in the connectivity area at higher temperature to crystallization of water inside the core pore; from this point of view, it can be interpreted as a transition towards a more ordered configuration in the confined non-interfacial hydrogen-bonded water molecules. On the other hand, the second transition spotted at lower temperatures may be interpreted as due to water molecules localized in the non-freezable layer at the pore wall interface.

Summarizing, we have provided a possible interpretation of the phenomenology concerning the structure and vibrational dynamics of confined supercooled water. Despite some similarities with the literature can be identified, our position has an original character and departs from that of most other authors. In particular, we have shown that different conclusions come out from the combined interpretation of IR spectra and neutron diffraction patterns collected with NIMROD on the same system over the same temperature range. Our idea is that, although the temperature and pressure evolution of MIR spectra proves the coexistence of two dominant water populations inside the pore volume, this is not sufficient to unambiguously confirm that two kinds of liquids differing in density exist in the supercooled region of the water phase diagram. As a matter of fact, FIR data clearly point out the formation of a solid phase in the pore core that excludes the coexistence of two liquid forms in favour of a transition to a solid-like configuration of HB network of water molecules as the temperature is lowered below  $240 - 250 \text{ K}$ .

At the pressure closest to the ambient we find a crossover between the two dominant water populations at  $\sim 227 \text{ K}$ . This is not far from results reported in [69], who find a transition temperature at  $\sim 225 \text{ K}$ . These authors identify a correlation between this temperature and the FSC temperature. Nonetheless, we think that FTIR spectroscopy is not able, by itself, to give a direct evidence of the existence of LDL phase in deeply supercooled confined water, as claimed by [69]. The finding of a crossover temperature in the relative populations close to the FSC temperature reported in the literature [128] suggests a likely different interpretation of such a phenomenon is needed: the fragile-to-strong crossover may not be the signature of the crossing of the Widom line with the continuous transformation from one liquid phase to another with lower density. It rather signs a transition between two different dynamical behaviours. This interpretation seems to find confirmation also in quasi-elastic neutron scattering (QENS) experiments that we performed at the neutron large-scale facility ILL (Grenoble, France). The first results coming out from the analysis of these data suggest that the FSC addressed in the literature is not truly a hint of liquid-liquid phase transition. It

is rather to be regarded as a symptom of the resolution limit and an inadequate fitting procedure. Anyway, these data have been currently analysing, thus the picture originating from their interpretation is not complete yet. For this reason, QENS data have not been included in this thesis.



# Chapter 7

## Conclusions

*The important thing in science is not so much to obtain new facts as to discover new ways of thinking about them.*

*Sir William Bragg*

The scientific challenge of this thesis was to shed light on the open debate about the origin of the anomalous behaviour of water that becomes strongly emphasized in the supercooled region of its phase diagram. At the molecular level, the ability of water to form hydrogen bonds inducing an open tetrahedral structure is thought to underline the counterintuitive character of water's properties. In particular, it has been found that most thermodynamic response functions, as well as transport properties, seem to diverge, according to power laws, toward a singular region of the phase diagram at  $T_S \approx 228$  K and  $P_S \approx 100$  MPa. Although this topic has sparked a vivid and prolific research activity over the years, a coherent and comprehensive explanation of this apparent singularity is still elusive. One of the most accredited theories proposed in order to give a proper explanation for water's strange behaviour is the existence of a second critical point (CP) of metastable liquid water located at the end of a liquid-liquid coexistence line [9], which divides two liquid phases differing in density (LDL and HDL). This line, if exists, should be the thermodynamic continuation of the coexisting line separating the two amorphous forms of water (LDA and HDA) experimentally discovered at lower temperature [5, 17, 331]. Nevertheless, such a CP lays between the homogeneous nucleation temperature ( $\sim 231 - 235$  K) and the crystallization temperature of glassy water ( $\sim 150$  K) at ambient pressure. This region, known as *No man's land*, has been so far unreachable to experiments because of crystallization, that hampers any investigation on bulk water in its supercooled liquid phase [17]. In other words, even if the second critical point would exist, ice crystallization proceeds at a faster rate than that required to equilibrate the two liquids below the critical point [62, 122], preventing any possible observation of such a CP. This hindrance explains why this theory still remains a hypothesis, only validated by computer simulations. Actually, plenty of water potentials have been proposed over the years [52], some confirming the existence of a liquid-liquid phase transition [9, 14, 126, 253, 332], others claiming that no CP exists in the metastable phase diagram of water [178, 286, 287]. Hence, there is much puzzlement and debate about the existence of the second CP, even in simulated water. Therefore, it clearly arises that a direct experimental

investigation of supercooled water able to confirm or rule out the liquid-liquid phase transition or another possible scenario is of paramount importance and could lead to a novel re-interpretation of the physics of water [17, 151, 306].

Nanoconfinement of water is currently used as a strategy to avoid ice nucleation [18, 149, 181, 195] and attempt to investigate water in its supercooled liquid phase between 150 and 235 K, by taking advantage of the Gibbs-Thomson effect (i.e. the depression of the freezing point). It is important to remark that, while supercooled bulk water is metastable with respect to ice, severely confined water is not in a metastable phase [265, 316]. Therefore, understanding the peculiar properties of deeply supercooled water under confinement reveals its interest by itself, and identifying their relation to the anomalies observed in bulk water has become a focal point of water research in recent years.

We have opted for confining water in the bi-dimensional environment offered by MCM-41, a micellar templated mesoporous silica matrix characterized by a highly regular structure with different pore sizes tunable in the nanometer range. Neutron scattering and experimental methods based on synchrotron radiation (in particular, X-ray scattering and IR spectroscopy) figure prominently among the many experimental techniques that have been applied throughout the years to study water upon confinement.

In particular, we employed neutron scattering over a wide  $Q$  range which has allowed us to correlate changes at the nanometer length scale to changes occurring at a scale of the order of Å. Then infrared spectroscopy over a broad frequency domain, covering both MIR and FIR frequency ranges, was used to better understand the vibrational features of water molecules, with particular attention to the HB network dynamics. All experiments we performed were primarily focused on two phenomena, one thermodynamic and one dynamic, namely, the water density minimum [70] and the fragile-to-strong crossover (FSC) (reported at  $T_L \approx 225$  K at ambient pressure [128]). Both have been observed at constant pressure with varying temperature and should be the signature of the crossing of the Widom line, i.e. the line where the correlation lengths exhibit their maxima in the  $P - T$  plane and that should emanate from the purported liquid-liquid critical point. The idea is to answer some open questions: *i*) What is the nature of the dynamic transition temperature  $T_L$  experimentally determined? *ii*) The system is in a liquid state on both sides of  $T_L$ ? *iii*) If so, what is the nature of the high-temperature and low-temperature liquids? Do they differ in density so that they can be identified as the HDL and LDL forms of supercooled water?

Most of our attention was devoted to MCM-41/C10 substrate, with a nominal pore diameter of 2.8 nm, hydrated with heavy or light water ( $D_2O$  and  $H_2O$ , respectively).

Neutron measurements were performed at the large-scale facility ISIS, on the instrument NIMROD, at ambient pressure and varying temperature. The scattering patterns over the full  $Q$  range accessible by NIMROD comprise three main regions: the high  $Q$  range, giving information about the microscopic structure of the confined liquid; the intermediate  $Q$  range, characterized by the diffraction peaks relative to the structure of the mesoporous silica matrix; and the low  $Q$  range, also known as *Porod region*, where to trace out the possible occurrence of density fluctuations.

IR measurements were carried out at the synchrotron SOLEIL, on the AILES beamline, by varying both pressure and temperature. We limited our analysis to two spectral ranges, namely  $2800 - 3800 \text{ cm}^{-1}$  (MIR) and  $100 - 280 \text{ cm}^{-1}$  (FIR). The former is characterized by the OH-stretching band, whereas the latter corresponds to the so-called connectivity band, which is ascribed to the collective motion of H-bond network.

Generally speaking, we can say that neutron measurements have given more insights into the structural modifications experienced by supercooled water upon quite severe confinement, while, on the other side, IR spectra have provided information about how vibrational modes related to H-bond motion are affected by pressure increase and temperature decrease below the freezing point. However, we want to stress that conclusions emerging from data acquired through these two experimental techniques are absolutely not independent on each other. Indeed, a full and comprehensive interpretation of structural phenomenology occurring in confined water could be achieved only by combining information embedded in neutron scattering data from a wide range of momentum transfer, corresponding to short, medium and long correlations range. At the same time, a plausible interpretation of MIR data was possible only by observing FIR spectra and by taking into consideration structural information extracted by neutron diffraction patterns. That is to say, a proper interpretation of the temperature and pressure evolution of vibrational spectra would not have been feasible without a comparison with structural information provided by neutron experiments.

The conclusions of the present work can be summarized as follows:

- In the core pore a solid heterophase grows up. This is pointed out by abrupt changes in neutron diffraction patterns and FIR spectra, compatible with ice formation. The ice form found under confinement is likely a mixture of cubic ice and hexagonal ice known as *stacking-disordered ice I* [91, 94]. The transition temperatures found with neutrons ( $T_N^*$ ) and FIR spectroscopy ( $T_{IR}^*$ ) are consistent within the experimental uncertainties<sup>1</sup>:  $T_N^* = (244.5 \pm 5.5)$  K,  $T_{IR}^* = (248.0 \pm 5.0)$  K. The conclusion is that the phenomenology we observe in our experiments on confined water is a first-order liquid-solid state transition, rather than a liquid-liquid transition. Thus any inference relative to the coexistence of two liquid states in the supercooled region of the phase diagram cannot be drawn.

We intend to emphasize that these conclusions are at odds with the results reported by other authors [70, 256, 263, 272] in their studies on supercooled water confined in MCM-41-S with a 15 Å pore diameter. In [267] the actual size of the pore substrate was questioned comparing the maximum amount of water that can be adsorbed into pores of 15 Å in diameter ( $\sim 0.01$  g D<sub>2</sub>O/g SiO<sub>2</sub>) and the full hydration level stated by [70, 263] ( $\sim 0.05$  g D<sub>2</sub>O/g SiO<sub>2</sub>). This discrepancy rises doubts on the actual pore radius of the silica matrix used in [70, 256, 263, 272], which should be significantly larger than stated by those authors. However, even if the estimate of the pore radius in [70, 256, 263, 272] was correct and thus the absence of crystallization events was due to the very small pore size of the silica substrate, the assumptions that the distribution of water density across the pore is uniform and temperature-independent are not justified on the basis of recent atomistic simulations and experimental results [151, 195, 203, 254, 279]. This inconsistency undermines the conclusions stated in [70, 256, 263, 272] and makes the finding of a water density minimum at 200 K [70] rather unreliable. In this context FIR measurements on water confined in a different MCM-41 sample, with a pore size smaller than MCM-41/C10, might be of particular relevance if we hope to elucidate such a controversial issue.

<sup>1</sup>The transition temperature has been evaluated as the arithmetic mean of the last temperature where no changes occur and the first temperature showing hints of ice formation (on cooling). Uncertainty on the transition temperature has been appraised as the semidifference between these two temperatures.

- Temperature evolution of the OH-stretching band proves that in supercooled confined water there is the coexistence of two main water molecules populations, with a different dynamic behaviour that affects their vibrational properties. Despite similarities with literature can be highlighted about MIR results [69, 289], we come to the conclusion that these populations cannot be interpreted as LDL and HDL phases expected to be found in the *No man's land* because no density fluctuations and no density minimum have been inferred from neutron data. This is a simple but effective proof about the impossibility to detect a transition between two liquid phases with different densities.
- Our results suggest that linking the structural transition occurring in supercooled water on cooling to the dynamic crossover from fragile to strong liquid claimed by several authors [128, 289] would need more cautions. In particular, we are led to conclude that the FSC may not be the signature of the crossing of the Widom line (at constant pressure and decreasing temperature) with the continuous transformation from one liquid phase (HDL) to another with a lower density (LDL). It rather appears to detect the transition between two different dynamic behaviours probed by the OH-stretching modes that reflect different local environments.
- SANS and silica Bragg peak analysis by itself are not proper methods capable of determining the density of confined water. As assessed also in previous studies [279], if the confined fluid is not homogeneously distributed within the pores, or if there is not a single phase in the core pore at all temperatures (as in our case, where we evidence the presence of ice), SANS is not adequate to measure the liquid density. Moreover, changes of the Bragg peak intensity cannot be interpreted as evidence for density changes. On the contrary, stating something about water structure and its evolution with temperature requires a full analysis of the entire scattering pattern. Any conclusion based just on a restricted  $Q$  range is to be regarded as unreliable. This conclusion is in agreement with recent observations reported in [151].
- MIR spectroscopy is not sensitive to important structural changes intervening in water under confinement, as no dramatic modifications appear in MIR spectra for the temperature interval where FIR patterns clearly show the trace of the onset of a solid phase. This leads to conclude that MIR spectroscopy alone is not suitable to give a complete and unambiguous picture of the behaviour of a networking liquid like our system. By contrast, the exploration of the whole spectral range and a more direct investigation of H-bond network dynamics is required to give a correct interpretation of IR data.
- We have not spotted any intensity fluctuation in the neutron scattering patterns at very low  $Q$ . This result rules out the presence of density fluctuations along the radial direction, i.e. across the pore. However, we have demonstrated that, even if these fluctuations exist, they would appear in the  $Q$  region where the silica Bragg peaks arise. This observation casts doubts on the validity of confinement within mesoporous silica materials with the aim to detect density fluctuations as a proof of the coexistence of two liquid phases differing in density.
- Another aspect that is worth mentioning is the possibility to extend the properties of confined water to the bulk [195]. Since no conclusive data have been available so far, we can assert that this confinement strategy cannot provide any firm conclusion about the physics of bulk water and in particular the existence of the second CP. Actually this represents a general critical issue because none of the methods exploited

for avoiding water crystallization is truly ideal. Even though some authors state that findings on confined water can be instructive for understanding bulk water at low  $T$  [172, 194], the extent to which water properties assessed upon confinement are related to those of bulk water is indeed still controversial. As many authors highlight, the real effect of the confining surface and its interaction with water molecules are difficult to estimate correctly [195, 254, 333, 334]. This implies that we cannot safely establish whether confined water can be simply regarded as bulk water for which freezing has been inhibited, or if deserve a different and more accurate description. This relevant question still remains a matter of debate [151].

Overall, this thesis contributes to reach a better comprehension of the structural and dynamical features of water under severe confinement. Moreover, it provides a detailed discussion about the strategies to extract reliable information from diffraction/scattering data and FTIR spectra, pointing out the requirement of investigating a sufficiently wide  $Q$  and frequency range as neutrons and IR radiation are employed as probes.

We want to remark that our interpretation of experimental data here presented does not firmly state that the second critical point does not exist. Therefore, we do not intend to call into question the accuracy and reliability of the huge number of simulation studies performed so far, as our results are not capable of doing so in an unambiguous manner. What we can definitely show, however, is that the experimental approach commonly followed up to now is not really appropriate to bring out the phenomenology described by computer simulations. Hence, we have not enough information to conclude that computer simulations supporting the evidence of a second critical point are wrong. But we can say to have demonstrated that the experimental methods devoted to the study of confined water are arguable and especially the interpretation of experimental results in terms of LDL and HDL is often unreliable.

To sum up, the results presented in this thesis do not provide any evidence of the existence of a liquid-liquid coexistence line ending in a second critical point located in the metastable phase diagram of water [9]. By contrast, they seem to be more consistent with the singularity-free (SF) model [10], one of the other two accredited theories proposed to explain the unusual behaviour of water (1.4). In particular, Kumar *et al.* [172, 335, 336] have recently demonstrated, via Monte Carlo simulations and mean field calculations, that a dynamic crossover at a temperature close to  $T(C_P^{\max})$  and decreasing as the pressure increases is compatible with both the liquid-liquid CP hypothesis and the singularity-free scenario. These authors have interpreted this dynamic crossover as the signature of a local breaking and reorientation of hydrogen bonds, that lead to the formation of new and more ordered (i.e. tetrahedrally oriented) bonds. Nonetheless, information extracted from our experimental data are not currently sufficient to unambiguously distinguish between the proposed CP and SF scenarios; in other words, we do not feel free to can definitely accept or reject one theory or another on the basis of the results collected so far.

Some of the points that remain unclear might be clarified in the future by taking advantage of other experimental methods that are expected to provide complimentary information to those extracted in the present work. Among the most promising techniques, we can mention: QENS under pressure (to support QENS data at ambient pressure that have been currently analysing); NMR measurements, in order to identify the fraction of molecules with very low mobility (solid-like) and those experiencing rapid reorientational dynamics (liquid-like) [306]; and dielectric spectroscopy, that may evidence the existence of two (or more) populations of H<sub>2</sub>O molecules having presumably different relaxation times.



# Bibliography

- [1] P. Ball, *Life's matrix: a biography of water*, University of California Press, **2001**.
- [2] F. R. Spellman, *The science of water: concepts and applications*, CRC press, **2014**.
- [3] R. M. Lynden-Bel, S Conway Morris, C Harper Jr, J. D. Barrow, J. L. Finney, *Water and Life: The Unique Properties of H<sub>2</sub>O*, CRC Press, **2010**.
- [4] F. Franks, *Water: a matrix of life, Vol. 21*, Royal Society of Chemistry, **2000**.
- [5] P. H. Poole, F. Sciortino, T. Grande, H. E. Stanley, C. A. Angell, *Physical Review Letters* **1994**, 73, 1632.
- [6] J. Black, *Philosophical Transactions* **1775**, 65, 124–128.
- [7] .
- [8] R. J. Speedy, *The Journal of Physical Chemistry* **1982**, 86, 982–991.
- [9] P. H. Poole, F. Sciortino, U. Essmann, H. E. Stanley, *Nature* **1992**, 360, 324–328.
- [10] S. Sastry, P. G. Debenedetti, F. Sciortino, H. E. Stanley, *Physical Review E* **1996**, 53, 6144.
- [11] L. P. N. Rebelo, P. G. Debenedetti, S. Sastry, *The Journal of Chemical Physics* **1998**, 109, 626–633.
- [12] T. M. Truskett, P. G. Debenedetti, S. Sastry, S. Torquato, *The Journal of Chemical Physics* **1999**, 111, 2647–2656.
- [13] C. Jeffery, P. Austin, *The Journal of Chemical Physics* **1999**, 110, 484–496.
- [14] G. Franzese, H. E. Stanley, *Journal of Physics: Condensed Matter* **2002**, 14, 2201.
- [15] C. A. Angell, *Annu. Rev. Phys. Chem.* **2004**, 55, 559–583.
- [16] C. A. Angell, *Science* **2008**, 319, 582–587.
- [17] P. G. Debenedetti, *Journal of Physics: Condensed Matter* **2003**, 15, R1669.
- [18] F. Caupin, *Journal of Non-Crystalline Solids* **2015**, 407, 441–448.
- [19] O. Mishima, H. E. Stanley, *Nature* **1998**, 392, 164–168.
- [20] E. Mayer, *Journal of Microscopy* **1985**, 140, 3–15.
- [21] E. Mayer, *Journal of Applied Physics* **1985**, 58, 663–667.

- [22] A. Soper, G. Neilson, J. Enderby, R. Howe, *Journal of Physics C: Solid State Physics* **1977**, *10*, 1793.
- [23] C. Angell, E. Sare, J. Donnelly, D. MacFarlane, *Journal of Physical Chemistry* **1981**, *85*, 1461–1464.
- [24] T. Koop, B. Luo, A. Tsias, T. Peter, *Nature* **2000**, *406*, 611–614.
- [25] R. Mancinelli, A. Botti, F. Bruni, M. Ricci, A. Soper, *The Journal of Physical Chemistry B* **2007**, *111*, 13570–13577.
- [26] T. Yanagisawa, T. Shimizu, K. Kuroda, C. Kato, *Bulletin of the Chemical Society of Japan* **1990**, *63*, 988–992.
- [27] C. Kresge, M. Leonowicz, W. Roth, J. Vartuli, J. Beck, et al., *Nature* **1992**, *359*, 710–712.
- [28] M. Kruk, M. Jaroniec, A. Sayari, *The Journal of Physical Chemistry B* **1997**, *101*, 583–589.
- [29] V. Alfredsson, M. Keung, A. Monnier, G. D. Stucky, K. K. Unger, F. Schüth, *Journal of the Chemical Society Chemical Communications* **1994**, 921–922.
- [30] C. Sonwane, S. Bhatia, N. Calos, *Industrial & Engineering Chemistry Research* **1998**, *37*, 2271–2283.
- [31] G. Lelong, S. Bhattacharyya, S. Kline, T. Cacciaguerra, M. A. Gonzalez, M.-L. Saboungi, *The Journal of Physical Chemistry C* **2008**, *112*, 10674–10680.
- [32] A. Gholaminejad, R. Hosseini, *Journal of Electronics Cooling and Thermal Control* **2013**, *3*, 1–6.
- [33] J. Kim, H. H. Chun, S. Park, D. Choi, S. R. Choi, S. Oh, S. M. Yoo, *Journal of Biosystems Engineering* **2014**, *39*, 330–335.
- [34] B. Cabane, R. Vuilleumier, *Comptes Rendus Geoscience* **2005**, *337*, 159–171.
- [35] A. B. Thompson, *Nature* **1992**, *358*, 295–302.
- [36] D. Pan, L. Spanu, B. Harrison, D. A. Sverjensky, G. Galli, *Proceedings of the National Academy of Sciences* **2013**, *110*, 6646–6650.
- [37] P. Jenniskens, D. Blake, *The Astrophysical Journal* **1996**, *473*, 1104.
- [38] K. E. Cyr, W. D. Sears, J. I. Lunine, *Icarus* **1998**, *135*, 537–548.
- [39] R. Cooke, I. Kuntz, *Annual Review of Biophysics and Bioengineering* **1974**, *3*, 95–126.
- [40] P. M. Wiggins, *Microbiological Reviews* **1990**, *54*, 432–449.
- [41] J. Fitter, R. Lechner, N. Dencher, Interactions of hydration water and biological membranes studied by neutron scattering, **1999**.
- [42] J. Hallett, *Low Temperature Biology of Foodstuffs: Recent Advances in Food Science* **2016**, *4*, 23.
- [43] R. Gillespie, *Coordination Chemistry Reviews* **2008**, *252*, 1315–1327.
- [44] P. W. Atkins, J. A. Beran, *General chemistry*, Scientific American Books, **1992**.
- [45] J. D. Bernal, R. H. Fowler, *Journal of Chemical Physics* **1933**, *1*, 515–548.
- [46] X.-F. Pang, *Water. Molecular structure and properties*, World Scientific, **2014**.

- [47] K. Amann-Winkel, M.-C. Bellissent-Funel, L. E. Bove, T. Loerting, A. Nilsson, A. Paciaroni, D. Schlesinger, L. Skinner, *Chemical Reviews* **2016**, *116*, 7570–7589.
- [48] D. D. Kemp, M. S. Gordon, *The Journal of Physical Chemistry A* **2008**, *112*, 4885–4894.
- [49] A. Soper, M. Phillips, *Chemical Physics* **1986**, *107*, 47–60.
- [50] K Ichikawa, Y Kameda, T Yamaguchi, H Wakita, M Misawa, *Molecular Physics* **1991**, *73*, 79–86.
- [51] A. K. Soper, M. A. Ricci, *Physical Review Letters* **2000**, *84*, 2881.
- [52] B. Guillot, *Journal of Molecular Liquids* **2002**, *101*, 219–260.
- [53] A. G. Császár, G. Czakó, T. Furtenbacher, J. Tennyson, V. Szalay, S. V. Shirin, N. F. Zobov, O. L. Polyansky, *The Journal of Chemical Physics* **2005**, *122*, 214305.
- [54] H. E. Stanley, J Teixeira, *The Journal of Chemical Physics* **1980**, *73*, 3404–3422.
- [55] I. Svishchev, P. Kusalik, *The Journal of Chemical Physics* **1993**, *99*, 3049–3058.
- [56] A. Soper, F Bruni, M. Ricci, *The Journal of Chemical Physics* **1997**, *106*, 247–254.
- [57] T. Head-Gordon, G. Hura, *Chemical Reviews* **2002**, *102*, 2651–2670.
- [58] C. Fecko, J. Eaves, J. Loparo, A Tokmakoff, P. Geissler, *Science* **2003**, *301*, 1698–1702.
- [59] C. Lawrence, J. Skinner, *Chemical Physics Letters* **2003**, *369*, 472–477.
- [60] J.-B. Brubach, A Mermet, A Filabozzi, A Gerschel, P Roy, *The Journal of Chemical Physics* **2005**, *122*, 184509.
- [61] C. Tainter, Y Ni, L. a. Shi, J. Skinner, *The Journal of Physical Chemistry Letters* **2012**, *4*, 12–17.
- [62] V. Molinero, E. B. Moore, *The Journal of Physical Chemistry B* **2009**, *113*, 4008–4016.
- [63] P. Kumar, H. E. Stanley, *The Journal of Physical Chemistry B* **2011**, *115*, 14269–14273.
- [64] S.-H. Chen, F. Mallamace, C.-Y. Mou, M. Broccio, C. Corsaro, A. Faraone, L. Liu, *Proceedings of the National Academy of Sciences* **2006**, *103*, 12974–12978.
- [65] A Giuliani, F Bruni, M. Ricci, M. Adams, *Physical Review Letters* **2011**, *106*, 255502.
- [66] R. Speedy, C. Angell, *The Journal of Chemical Physics* **1976**, *65*, 851–858.
- [67] R. A. Fine, F. J. Millero, *The Journal of Chemical Physics* **1975**, *63*, 89–95.
- [68] P. G. Debenedetti, *Metastable liquids: concepts and principles*, Princeton University Press, **1996**.
- [69] F. Mallamace, C. Branca, M. Broccio, C. Corsaro, C.-Y. Mou, S.-H. Chen, *Proceedings of the National Academy of Sciences* **2007**, *104*, 18387–18391.
- [70] D. Liu, Y. Zhang, C.-C. Chen, C.-Y. Mou, P. H. Poole, S.-H. Chen, *Proceedings of the National Academy of Sciences* **2007**, *104*, 9570–9574.
- [71] Y. Zhang, K.-H. Liu, M. Lagi, D. Liu, K. C. Littrell, C.-Y. Mou, S.-H. Chen, *The Journal Of Physical Chemistry B* **2009**, *113*, 5007–5010.
- [72] S.-H. Chen, J. Teixeira, R. Nicklow, *Physical Review A* **1982**, *26*, 3477.

- [73] J. Teixeira, M.-C. Bellissent-Funel, S.-H. Chen, A.-J. Dianoux, *Physical Review A* **1985**, 31, 1913.
- [74] L. Leuzzi, T. M. Nieuwenhuizen, *Thermodynamics of the glassy state*, CRC Press, **2007**.
- [75] C. Angell, *Chemical Reviews* **2002**, 102, 2627–2650.
- [76] G. S. Fulcher, *Journal of the American Ceramic Society* **1925**, 8, 339–355.
- [77] D. R. Reichman, P. Charbonneau, *Journal of Statistical Mechanics: Theory and Experiment* **2005**, 2005, P05013.
- [78] P. G. Debenedetti, F. H. Stillinger, *Nature* **2001**, 410, 259–267.
- [79] V. A. Popova, N. V. Surovtsev, *Physical Review E* **2014**, 90, 032308.
- [80] C. Lobban, J. Finney, W. Kuhs, *Nature* **1998**, 391, 268–270.
- [81] D. K. Lonsdale in *Proceedings of the Royal Society of London A: Mathematical, Physical and Engineering Sciences, Vol. 247*, The Royal Society, **1958**, pp. 424–434.
- [82] L. Pauling, *Journal of the American Chemical Society* **1935**, 57, 2680–2684.
- [83] B. Kamb, B. L. Davis, *Proceedings of the National Academy of Sciences* **1964**, 52, 1433–1439.
- [84] H. Fukazawa, A. Hoshikawa, Y. Ishii, B. Chakoumakos, J. Fernandez-Baca, *The Astrophysical Journal Letters* **2006**, 652, L57.
- [85] C. G. Salzmann, P. G. Radaelli, E. Mayer, J. L. Finney, *Physical Review Letters* **2009**, 103, 105701.
- [86] C. G. Salzmann, P. G. Radaelli, B. Slater, J. L. Finney, *Physical Chemistry Chemical Physics* **2011**, 13, 18468–18480.
- [87] D. Eisenberg, W. Kauzmann, *The structure and properties of water*, Oxford University Press on Demand, **2005**.
- [88] V. Fuentes-Landete, C. Mitterdorfer, P. Handle, G. Ruiz, J. Bernard, A. Bogdan, M. Seidl, K. Amann-Winkel, J. Stern, S. Fuhrmann, et al., *Water: Fundamentals as the Basis for Understanding the Environment and Promoting Technology* **2015**, 187, 173.
- [89] G. Arnold, E. Finch, S. Rabideau, R. Wenzel, *The Journal of Chemical Physics* **1968**, 49, 4365–4369.
- [90] P. Geiger, C. Dellago, M. Macher, C. Franchini, G. Kresse, J. Bernard, J. N. Stern, T. Loerting, *The Journal of Physical Chemistry C* **2014**, 118, 10989–10997.
- [91] T. L. Malkin, B. J. Murray, A. V. Brukhno, J. Anwar, C. G. Salzmann, *Proceedings of the National Academy of Sciences* **2012**, 109, 1041–1045.
- [92] B. Kärcher, *Atmospheric Chemistry and Physics* **2002**, 2, 161–170.
- [93] B. Kärcher, U. Lohmann, *Journal of Geophysical Research: Atmospheres* **2003**, 108.
- [94] W. F. Kuhs, C. Sippel, A. Falenty, T. C. Hansen, *Proceedings of the National Academy of Sciences* **2012**, 109, 21259–21264.
- [95] J. Klinger, *The Journal of Physical Chemistry* **1983**, 87, 4209–4214.

- [96] J. Russo, F. Romano, H. Tanaka, *Nature materials* **2014**, *13*, 733–739.
- [97] H Kanno, R. Speedy, C. Angell, *Science* **1975**, *189*, 880–881.
- [98] O. Mishima, *Nature* **1996**, *384*, 546.
- [99] P. Jenniskens, *Science* **1994**, *265*, 753.
- [100] T. Loerting, C. Salzmann, I. Kohl, E. Mayer, A. Hallbrucker, *Physical Chemistry Chemical Physics* **2001**, *3*, 5355–5357.
- [101] T. Loerting, K. Winkel, M. Seidl, M. Bauer, C. Mitterdorfer, P. H. Handle, C. G. Salzmann, E. Mayer, J. L. Finney, D. T. Bowron, *Physical Chemistry Chemical Physics* **2011**, *13*, 8783–8794.
- [102] N. Giovambattista, C. A. Angell, F. Sciortino, H. E. Stanley, *Physical Review Letters* **2004**, *93*, 047801.
- [103] E. Burton, W. Oliver, *Proceedings of the Royal Society of London. Series A Mathematical and Physical Sciences* **1935**, *153*, 166–172.
- [104] A. Hallbrucker, E. Mayer, G. Johari, *The Journal of Physical Chemistry* **1989**, *93*, 4986–4990.
- [105] G. Johari, A. Hallbrucker, E. Mayer, *Nature* **1987**, *330*, 552–553.
- [106] O. Mishima, Y. Suzuki, *The Journal of Chemical Physics* **2001**, *115*, 4199–4202.
- [107] O. Mishima, L. Calvert, E. Whalley, *Nature* **1984**, *310*, 393–395.
- [108] O. Mishima, L. Calvert, E. Whalley, *Nature* **1985**, *314*, 76–78.
- [109] O. Mishima, Y. Suzuki, *Nature* **2002**, *419*, 599–603.
- [110] M. Koza, H. Schober, H. Fischer, T. Hansen, F. Fujara, *Journal of Physics: Condensed Matter* **2003**, *15*, 321.
- [111] M. M. Koza, B. Geil, K. Winkel, C. Koehler, F. Czeschka, M. Scheuermann, H. Schober, T. Hansen, *Physical Review Letters* **2005**, *94*, 125506.
- [112] O. Mishima, *The Journal of Chemical Physics* **1994**, *100*, 5910–5912.
- [113] C. Tulk, C. Benmore, J. Urquidi, D. Klug, J. Neuefeind, B. Tomberli, P. Egelstaff, *Science* **2002**, *297*, 1320–1323.
- [114] P. G. Debenedetti, *Nature* **1998**, *392*, 127–128.
- [115] J. Finney, A. Hallbrucker, I. Kohl, A. Soper, D. Bowron, *Physical Review Letters* **2002**, *88*, 225503.
- [116] S. Karthika, T. Radhakrishnan, P. Kalaichelvi, *Crystal Growth & Design* **2016**, *16*, 6663–6681.
- [117] A. Haji-Akbari, P. G. Debenedetti, *Proceedings of the National Academy of Sciences* **2015**, *112*, 10582–10588.
- [118] R. A. Baragiola, *Planetary and Space Science* **2003**, *51*, 953–961.
- [119] B. Murray, D. O’Sullivan, J. Atkinson, M. Webb, *Chemical Society Reviews* **2012**, *41*, 6519–6554.

- [120] C Hoose, O Möhler, *Atmospheric Chemistry and Physics* **2012**, *12*, 9817.
- [121] L. Lupi, A. Hudait, V. Molinero, *Journal of the American Chemical Society* **2014**, *136*, 3156–3164.
- [122] E. B. Moore, V. Molinero, *Nature* **2011**, *479*, 506–508.
- [123] J. H. Lienhard, N Shamsundar, P. O. Biney, *Nuclear Engineering and Design* **1986**, *95*, 297–314.
- [124] F. H. Stillinger, A. Rahman, *The Journal of Chemical Physics* **1974**, *60*, 1545–1557.
- [125] F. Smallenburg, P. H. Poole, F. Sciortino, *Molecular Physics* **2015**, *113*, 2791–2798.
- [126] J. C. Palmer, F. Martelli, Y. Liu, R. Car, A. Z. Panagiotopoulos, P. G. Debenedetti, *Nature* **2014**, *510*, 385–388.
- [127] J. Lee, J. Kosterlitz, *Physical Review Letters* **1990**, *65*, 137.
- [128] L. Liu, S.-H. Chen, A. Faraone, C.-W. Yen, C.-Y. Mou, *Physical Review Letters* **2005**, *95*, 117802.
- [129] K. Amann-Winkel, C. Gainaru, P. H. Handle, M. Seidl, H. Nelson, R. Böhmer, T. Loring, *Proceedings of the National Academy of Sciences* **2013**, *110*, 17720–17725.
- [130] K. Ito, C. T. Moynihan, C. A. Angell, *Nature* **1999**, *398*, 492–495.
- [131] L. Xu, F. Mallamace, Z. Yan, F. W. Starr, S. V. Buldyrev, H. E. Stanley, *Nature Physics* **2009**, *5*, 565–569.
- [132] L. Xu, P. Kumar, S. V. Buldyrev, S.-H. Chen, P. H. Poole, F. Sciortino, H. E. Stanley, *Proceedings of the National Academy of Sciences of the United States of America* **2005**, *102*, 16558–16562.
- [133] C. Vega, J. L. Abascal, M. Conde, J. Aragones, *Faraday Discussions* **2009**, *141*, 251–276.
- [134] C. Angell, J Shuppert, J. Tucker, *The Journal of Physical Chemistry* **1973**, *77*, 3092–3099.
- [135] W. Kauzmann, *Chemical Reviews* **1948**, *43*, 219–256.
- [136] J. W. Biddle, V. Holten, M. A. Anisimov, *The Journal of Chemical Physics* **2014**, *141*, 074504.
- [137] L Bove, C Dreyfus, A Polian, B. Bonello, I Malfanti, A Taschin, R Torre, R. Pick, *The Journal of Chemical Physics* **2011**, *134*, 034514.
- [138] B Prével, J. Jal, J Dupuy-Philon, A. Soper, *The Journal of Chemical Physics* **1995**, *103*, 1886–1896.
- [139] M. A. Ricci, F. Bruni, A. Giuliani, *Faraday Discussions* **2009**, *141*, 347–358.
- [140] M.-C. Bellissent-Funel, J Teixeira, L Bosio, J. Dore, *Journal of Physics: Condensed Matter* **1989**, *1*, 7123.
- [141] R Mancinelli, F Bruni, M. Ricci, S Imberti, *The Journal of Chemical Physics* **2013**, *138*, 204503.
- [142] Y. Aray, M. Marquez, J. Rodríguez, S. Coll, Y. Simon-Manso, C. Gonzalez, D. A. Weitz, *The Journal of Physical Chemistry B* **2003**, *107*, 8946–8952.

- [143] M. G. Mazza, K. Stokely, S. E. Pagnotta, F. Bruni, H. E. Stanley, G. Franzese, *Proceedings of the National Academy of Sciences* **2011**, *108*, 19873–19878.
- [144] T. Takamuku, M. Yamagami, H. Wakita, Y. Masuda, T. Yamaguchi, *The Journal of Physical Chemistry B* **1997**, *101*, 5730–5739.
- [145] F. Bruni, M. A. Ricci, A. K. Soper, *The Journal of Chemical Physics* **1998**, *109*, 1478–1485.
- [146] C. Hartnig, W. Witschel, E. Spohr, P. Gallo, M. A. Ricci, M. Rovere, *Journal of Molecular Liquids* **2000**, *85*, 127–137.
- [147] S. H. Lee, P. J. Rossky, *The Journal of Chemical Physics* **1994**, *100*, 3334–3345.
- [148] V Nigro, F Bruni, M. Ricci, *Water: Fundamentals as the Basis for Understanding the Environment and Promoting Technology* **2015**, *187*, 209.
- [149] H. Thompson, A. K. Soper, M. A. Ricci, F. Bruni, N. T. Skipper, *The Journal of Physical Chemistry B* **2007**, *111*, 5610–5620.
- [150] C. G. Sonwane, C. W. Jones, P. J. Ludovice, *The Journal of Physical Chemistry B* **2005**, *109*, 23395–23404.
- [151] A. K. Soper, *Chemical Physics Letters* **2013**, *590*, 1–15.
- [152] Y. Suzuki, M. Steinhart, R. Graf, H.-J. Butt, G. Floudas, *The Journal of Physical Chemistry B* **2015**, *119*, 14814–14820.
- [153] G. McKenna, *The European Physical Journal-Special Topics* **2010**, *189*, 285–302.
- [154] M.-C. Bellissent-Funel, J Lal, L Bosio, *The Journal of Chemical Physics* **1993**, *98*, 4246–4252.
- [155] P Gallo, M. Ricci, M Rovere, *The Journal of chemical physics* **2002**, *116*, 342–346.
- [156] M. Ricci, V Tudisca, F Bruni, R Mancinelli, E Scoppola, R Angelini, B Ruzicka, A. Soper, *Journal of Non-Crystalline Solids* **2015**, *407*, 418–422.
- [157] C Boissiere, J. Brubach, A Mermet, G De Marzi, C Bourgaux, E Prouzet, P Roy, *The Journal of Physical Chemistry B* **2002**, *106*, 1032–1035.
- [158] J.-B. Brubach, A Mermet, A. Filabozzi, A Gerschel, D Lairez, M. Krafft, P Roy, *The Journal of Physical Chemistry B* **2001**, *105*, 430–435.
- [159] J. Catafesta, F. Alabarse, C. Levelut, A. Isambert, P. Hébert, S. Kohara, D. Maurin, J.-L. Bantignies, O. Cambon, G. Creff, et al., *Physical Chemistry Chemical Physics* **2014**, *16*, 12202–12208.
- [160] S. Dalla Bernardina, E. Paineau, J.-B. Brubach, P. Judeinstein, S. Rouzière, P. Launois, P. Roy, *Journal of the American Chemical Society* **2016**, *138*, 10437–10443.
- [161] S. Takahara, M. Nakano, S. Kittaka, Y. Kuroda, T. Mori, H. Hamano, T. Yamaguchi, *The Journal of Physical Chemistry B* **1999**, *103*, 5814–5819.
- [162] P. Smirnov, T. Yamaguchi, S. Kittaka, S. Takahara, Y. Kuroda, *The Journal of Physical Chemistry B* **2000**, *104*, 5498–5504.

- [163] H.-J. Butt, K. Graf, M. Kappl, *Physics and Chemistry of Interfaces*, John Wiley & Sons, **2006**.
- [164] E. P. Barrett, L. G. Joyner, P. P. Halenda, *Journal of the American Chemical Society* **1951**, *73*, 373–380.
- [165] N. Seaton, J. Walton, et al., *Carbon* **1989**, *27*, 853–861.
- [166] P. Ravikovitch, S. Ó. Domhnaill, A. Neimark, F. Schüth, K. Unger, *Langmuir* **1995**, *11*, 4765–4772.
- [167] A. V. Neimark, P. I. Ravikovitch, M. Grün, F. Schüth, K. K. Unger, *Journal of Colloid and Interface Science* **1998**, *207*, 159–169.
- [168] K. Sing, *Colloids and Surfaces A: Physicochemical and Engineering Aspects* **2001**, *187*, 3–9.
- [169] H. Yildirim, *Surface chemistry of solid and liquid interfaces*, **2006**.
- [170] K. S. Sing, *Pure and Applied Chemistry* **1985**, *57*, 603–619.
- [171] S. Brunauer, P. H. Emmett, E. Teller, *Journal of the American Chemical Society* **1938**, *60*, 309–319.
- [172] H. Stanley, S. Buldyrev, G. Franzese, P. Kumar, F. Mallamace, M. G. Mazza, K. Stokely, L. Xu, *Journal of Physics: Condensed Matter* **2010**, *22*, 284101.
- [173] C. Alba-Simionesco, B. Coasne, G. Dosseh, G. Dudziak, K. Gubbins, R. Radhakrishnan, M. Sliwinska-Bartkowiak, *Journal of Physics: Condensed Matter* **2006**, *18*, R15.
- [174] G. H. Findenegg, S. Jähnert, D. Akcakayiran, A. Schreiber, *ChemPhysChem* **2008**, *9*, 2651–2659.
- [175] K. Morishige, K. Kawano, *The Journal of Chemical Physics* **1999**, *110*, 4867–4872.
- [176] K. Yoshida, T. Yamaguchi, S. Kittaka, M.-C. Bellissent-Funel, P. Fouquet, *The Journal of Chemical Physics* **2008**, *129*, 054702.
- [177] S. Jähnert, F. V. Chávez, G. Schaumann, A. Schreiber, M. Schönhoff, G. Findenegg, *Physical Chemistry Chemical Physics* **2008**, *10*, 6039–6051.
- [178] D. T. Limmer, D. Chandler, *The Journal of Chemical Physics* **2012**, *137*, 044509.
- [179] M. D. Fayer, N. E. Levinger, *Annual Review of Analytical Chemistry* **2010**, *3*, 89–107.
- [180] B. Webber, J. Dore, *Journal of Physics: Condensed Matter* **2004**, *16*, S5449.
- [181] A. Schreiber, I. Ketelsen, G. H. Findenegg, *Physical Chemistry Chemical Physics* **2001**, *3*, 1185–1195.
- [182] Y. Suzuki, H. Duran, M. Steinhart, M. Kappl, H.-J. Butt, G. Floudas, *Nano letters* **2015**, *15*, 1987–1992.
- [183] J. C. Rasaiah, S. Garde, G. Hummer, *Annu. Rev. Phys. Chem.* **2008**, *59*, 713–740.
- [184] P. Kumar, S. V. Buldyrev, F. W. Starr, N. Giovambattista, H. E. Stanley, *Physical Review E* **2005**, *72*, 051503.
- [185] M. Ø. Jensen, O. G. Mouritsen, G. H. Peters, *The Journal of Chemical Physics* **2004**, *120*, 9729–9744.

- [186] H. K. Christenson, *Journal of Physics: Condensed Matter* **2001**, *13*, R95.
- [187] J. Baker, J. C. Dore, P. Behrens, *The Journal of Physical Chemistry B* **1997**, *101*, 6226–6229.
- [188] N. Floquet, J. P. Coulomb, N. Dufau, G. Andre, R. Kahn, *Adsorption* **2005**, *11*, 139–144.
- [189] K. Morishige, H. Yasunaga, H. Uematsu, *The Journal of Physical Chemistry C* **2009**, *113*, 3056–3061.
- [190] T. Hansen, M. Koza, W. Kuhs, *Journal of Physics: Condensed Matter* **2008**, *20*, 285104.
- [191] T. Hansen, M. Koza, P Lindner, W. Kuhs, *Journal of Physics: Condensed Matter* **2008**, *20*, 285105.
- [192] R. Srivastava, H. Docherty, J. K. Singh, P. T. Cummings, *The Journal of Physical Chemistry C* **2011**, *115*, 12448–12457.
- [193] F. Leoni, G. Franzese, *The Journal of Chemical Physics* **2014**, *141*, 174501.
- [194] F. Leoni, G. Franzese, *Physical Review E* **2016**, *94*, 062604.
- [195] R Mancinelli, *Journal of Physics: Condensed Matter* **2010**, *22*, 404213.
- [196] P. Kumar, F. W. Starr, S. V. Buldyrev, H. E. Stanley, *Physical Review E* **2007**, *75*, 011202.
- [197] M Cammarata, M. Levantino, A Cupane, A Longo, A Martorana, F Bruni, *The European Physical Journal E: Soft Matter and Biological Physics* **2003**, *12*, 63–66.
- [198] R Bergman, J Swenson, *Nature* **2000**, *403*, 283–286.
- [199] V Crupi, D Majolino, P Migliardo, V Venuti, M. Bellissent-Funel, *Molecular Physics* **2003**, *101*, 3323–3333.
- [200] M Erko, G. Findenegg, N Cade, A. Michette, O Paris, *Physical Review B* **2011**, *84*, 104205.
- [201] A. Lerbret, G. Lelong, P. E. Mason, M.-L. Saboungi, J. W. Brady, *Food Biophysics* **2011**, *6*, 233–240.
- [202] R. Mancinelli, S. Imberti, A. Soper, K. Liu, C. Mou, F. Bruni, M. A. Ricci, *The Journal of Physical Chemistry B* **2009**, *113*, 16169–16177.
- [203] R Mancinelli, F Bruni, M. Ricci, *Journal of Molecular Liquids* **2011**, *159*, 42–46.
- [204] T. G. Lombardo, N. Giovambattista, P. G. Debenedetti, *Faraday Discussions* **2009**, *141*, 359–376.
- [205] I. M. Briman, D. Rebiscoul, O. Diat, J.-M. Zanutti, P. Jollivet, P. Barboux, S. Gin, *The Journal of Physical Chemistry C* **2012**, *116*, 7021–7028.
- [206] N. C. Osti, A Coté, E Mamontov, A Ramirez-Cuesta, D. Wesolowski, S. Diallo, *Chemical Physics* **2016**, *465*, 1–8.
- [207] L Liu, A Faraone, C. Mou, C. Yen, S. Chen, *Journal of Physics: Condensed Matter* **2004**, *16*, S5403.
- [208] S. Takahara, N. Sumiyama, S. Kittaka, T. Yamaguchi, M.-C. Bellissent-Funel, *The Journal of Physical Chemistry B* **2005**, *109*, 11231–11239.

- [209] J.-M. Zanotti, M.-C. Bellissent-Funel, S.-H. Chen, *Physical Review E* **1999**, 59, 3084.
- [210] L. Liu, S.-H. Chen, A. Faraone, C.-W. Yen, C.-Y. Mou, A. I. Kolesnikov, E. Mamontov, J. Leao, *Journal of Physics: Condensed Matter* **2006**, 18, S2261.
- [211] S Bhattacharyya, G Lelong, M.-L. Saboungi, *Journal of Experimental Nanoscience* **2006**, 1, 375–395.
- [212] C. D. Williams, K. P. Travis, N. A. Burton, J. H. Harding, *Microporous and Mesoporous Materials* **2016**, 228, 215–223.
- [213] D. Bowron, A. Soper, K Jones, S Ansell, S Birch, J Norris, L Perrott, D Riedel, N. Rhodes, S. Wakefield, et al., *Review of Scientific Instruments* **2010**, 81, 033905.
- [214] G. L. Squires, *Introduction to the theory of thermal neutron scattering*, Cambridge university press, **2012**.
- [215] D. Sivia, *Elementary Scattering Theory for X-ray and Neutron Users*, (Ed.: O. U. Press), **2010**.
- [216] B. H. Bransden, C. J. Joachain, *Quantum mechanics*, Pearson Education, **2000**.
- [217] A. Soper, *Chemical Physics* **1996**, 202, 295–306.
- [218] A. Soper, *Journal of Molecular Liquids* **1998**, 78, 179–200.
- [219] A. K. Soper, *Empirical Potential Structure Refinement: EPSRshell: a User's Guide: Version 24: January 2015*, STFC, **2011**.
- [220] J. Finney, A. Soper, *Chemical Society Reviews* **1994**, 23, 1–10.
- [221] L. Feigin, D. I. Svergun, G. W. Taylor, *Structure analysis by small-angle X-ray and neutron scattering*, Springer, **1987**.
- [222] A. J. Jackson, *NIST Center for Neutron Research Gaithersburg* **2008**, 12.
- [223] B. Hammouda, *Probing Nanoscale Structures—the SANS Toolbox*. National Institute of Standards and Technology. Center for Neutron Research, Gaithersburg, MD, **2010**.
- [224] A. Soper, *Nuclear Instruments and Methods In Physics Research* **1983**, 212, 337–347.
- [225] A. K. Soper, *Molecular Physics* **2009**, 107, 1667–1684.
- [226] G Placzek, *Physical Review* **1952**, 86, 377.
- [227] A Voute, M Deutsch, A Kalinko, F Alabarse, J.-B. Brubach, F Capitani, M Chapuis, V. T. Phuoc, R Sopracase, P Roy, *Vibrational Spectroscopy* **2016**, 86, 17–23.
- [228] B. H. Stuart, *Infrared spectroscopy: fundamentals and applications*, John Wiley & Sons, Chichester, UK, **2004**.
- [229] N. Colthup, *Introduction to Infrared and Raman spectroscopy*, Elsevier, **2012**.
- [230] K. Ramasesha, L. De Marco, A. Mandal, A. Tokmakoff, *Nature Chemistry* **2013**, 5, 935–940.
- [231] F. Perakis, L. D. Marco, A. Shalit, F. Tang, Z. R. Kann, T. D. Kühne, R. Torre, M. Bonn, Y. Nagata, *Chemical Reviews* **2016**, 116, 7590–7607.

- [232] A. Pietzsch, F. Hennies, P. S. Miedema, B. Kennedy, J. Schlappa, T. Schmitt, V. N. Strocov, A. Föhlisch, *Physical Review Letters* **2015**, *114*, 088302.
- [233] A. Pakoulev, Z. Wang, D. D. Dlott, *Chemical Physics Letters* **2003**, *371*, 594–600.
- [234] M. Cowan, B. D. Bruner, N Huse, J. Dwyer, B Chugh, E. Nibbering, T Elsaesser, R. Miller, *Nature* **2005**, *434*, 199–202.
- [235] .
- [236] M. Sovago, R. K. Campen, G. W. Wurpel, M. Müller, H. J. Bakker, M. Bonn, *Physical Review Letters* **2008**, *100*, 173901.
- [237] Y. Ni, J. Skinner, *The Journal of Chemical Physics* **2015**, *143*, 014502.
- [238] K. B. Møller, R. Rey, J. T. Hynes, *The Journal of Physical Chemistry A* **2004**, *108*, 1275–1289.
- [239] R. Rey, J. T. Hynes, *Physical Chemistry Chemical Physics* **2012**, *14*, 6332–6342.
- [240] T. Yagasaki, S. Saito, *The Journal of Chemical Physics* **2011**, *134*, 184503.
- [241] B. Auer, J. Skinner, *The Journal of Chemical Physics* **2008**, *128*, 224511.
- [242] .
- [243] M. Praprotnik, D. Janežič, J. Mavri, *The Journal of Physical Chemistry A* **2004**, *108*, 11056–11062.
- [244] S. Dalla Bernardina, Ph.D. Thesis, Université Paris-Saclay – Synchrotron Soleil.
- [245] M. P. Blakeley, S. S. Hasnain, S. V. Antonyuk, *IUCrJ* **2015**, *2*, 464–474.
- [246] D Seo, F Tomizato, H Toda, K Uesugi, A Takeuchi, Y Suzuki, M Kobayashi, *Applied Physics Letters* **2012**, *101*, 261901.
- [247] M. Faye, M. Bordessoule, B. Kanouté, J.-B. Brubach, P. Roy, L. Manceron, *Review of Scientific Instruments* **2016**, *87*, 063119.
- [248] T. Takeda, Y. Itai, K. Hayashi, Y. Nagata, H. Yamaji, K. Hyodo, *Journal of Computer Assisted Tomography* **1994**, *18*, 98–101.
- [249] S Dalla Bernardina, F Alabarse, A Kalinko, P Roy, M Chapuis, N Vita, R Hienerwadel, C Berthomieu, P Judeinstein, J.-M. Zanotti, J. L. Bantignies, H Haines, J Catafesta, G Creff, L Manceron, J.-B. Brubach, *Vibrational Spectroscopy* **2014**, *75*, 154–161.
- [250] P. L. Geissler, *Annual Review of Physical Chemistry* **2013**, *64*, 317–337.
- [251] G. Carr, M Hanfland, G. Williams, *Review of Scientific Instruments* **1995**, *66*, 1643–1645.
- [252] G. Franzese, H. E. Stanley, *Journal of Physics: Condensed Matter* **2007**, *19*, 205126.
- [253] J. L. Abascal, C. Vega, *The Journal of Chemical Physics* **2010**, *133*, 234502.
- [254] M Erko, D Wallacher, A Hoell, T Hauss, I Zizak, O Paris, *Physical Chemistry Chemical Physics* **2012**, *14*, 3852–3858.
- [255] A. K. Soper, *Journal of Physics: Condensed Matter* **2012**, *24*, 064107.
- [256] D. Liu, Y. Zhang, Y. Liu, J. Wu, C.-C. Chen, C.-Y. Mou, S.-H. Chen, *The Journal Of Physical Chemistry B* **2008**, *112*, 4309–4312.

- [257] K.-H. Liu, Y. Zhang, J.-J. Lee, C.-C. Chen, Y.-Q. Yeh, S.-H. Chen, C.-Y. Mou, *The Journal of Chemical Physics* **2013**, *139*, 064502.
- [258] F Mallamace, M Broccio, C Corsaro, A Faraone, U Wanderlingh, L Liu, C.-Y. Mou, C. S. H, *The Journal of Chemical Physics* **2006**, *124*, 161102.
- [259] S.-H. Chen, F Mallamace, L Liu, D. Liu, X. Chu, Y Zhang, C Kim, A Faraone, C.-Y. Mou, E Fratini, et al. in AIP Conference Proceedings, Vol. 982, AIP, **2008**, pp. 39–52.
- [260] P. H. Poole, I. Saika-Voivod, F. Sciortino, *Journal of Physics: Condensed Matter* **2005**, *17*, L431.
- [261] H. L. Pi, J. L. Aragonés, C. Vega, E. G. Noya, J. L. Abascal, M. A. Gonzalez, C. McBride, *Molecular Physics* **2009**, *107*, 365–374.
- [262] C. Angell, R. Bressel, M Hemmati, E. Sare, J. Tucker, *Physical Chemistry Chemical Physics* **2000**, *2*, 1559–1566.
- [263] Y. Zhang, A. Faraone, W. A. Kamitakahara, K.-H. Liu, C.-Y. Mou, J. B. Leão, S. Chang, S.-H. Chen, *Proceedings of the National Academy of Sciences* **2011**, *108*, 12206–12211.
- [264] W. A. Kamitakahara, A. Faraone, K.-H. Liu, C.-Y. Mou, *Journal of Physics: Condensed Matter* **2012**, *24*, 064106.
- [265] C. E. Bertrand, Y. Zhang, S.-H. Chen, *Physical Chemistry Chemical Physics* **2013**, *15*, 721–745.
- [266] J. Swenson, H. Jansson, R. Bergman, *Physical Review Letters* **2006**, *96*, 247802.
- [267] A. K. Soper, *Proceedings of the National Academy of Sciences* **2011**, *108*, E1192–E1192.
- [268] C. Clarkson, R. Bustin, *Fuel* **1999**, *78*, 1333–1344.
- [269] A. K. Soper, GudrunN and GudrunX. Programs for correcting raw neutron and X-ray total scattering data to differential cross section, **2012**.
- [270] V. F. Sears, *Advances in Physics* **1975**, *24*, 1–45.
- [271] H. Paalman, C. Pings, *Journal of Applied Physics* **1962**, *33*, 2635–2639.
- [272] S.-H. Chen, Z. Wang, A. I. Kolesnikov, Y. Zhang, K.-H. Liu, M. Tokuyama, I. Oppenheim in AIP Conference Proceedings, Vol. 1518, AIP, **2013**, pp. 77–85.
- [273] Z. Wang, K. Ito, J. B. Leão, L. Harriger, Y. Liu, S.-H. Chen, *The journal of physical chemistry letters* **2015**, *6*, 2009–2014.
- [274] P Gallo, M Rovere, S.-H. Chen, *The Journal of Physical Chemistry Letters* **2010**, *1*, 729–733.
- [275] E Tombari, G Salvetti, C Ferrari, G. Johari, *The Journal of Chemical Physics* **2005**, *122*, 104712.
- [276] K. Morishige, K Nobuoka, *The Journal of Chemical Physics* **1997**, *107*, 6965–6969.
- [277] E. B. Moore, E. De La Llave, K. Welke, D. A. Scherlis, V. Molinero, *Physical Chemistry Chemical Physics* **2010**, *12*, 4124–4134.

- [278] I. V. Golosovsky, I. Mirebeau, V. P. Sakhnenko, D. A. Kurdyukov, Y. A. Kumzerov, *Phys. Rev. B* **2005**, 72, 144409.
- [279] R Mancinelli, F Bruni, M. Ricci, *The Journal of Physical Chemistry Letters* **2010**, 1, 1277–1282.
- [280] K.-H. Liu, Y. Zhang, U.-S. Jeng, C.-Y. Mou, *The Journal of Chemical Physics* **2015**, 143, 094704.
- [281] Z. Wang, K.-H. Liu, L. Harriger, J. B. Leão, S.-H. Chen, *The Journal of chemical physics* **2014**, 141, 014501.
- [282] G. Franzese, G. Malescio, A. Skibinsky, S. V. Buldyrev, H. E. Stanley, *arXiv preprint cond-mat/0102029* **2001**.
- [283] S. Cervený, J. Colmenero, A. Alegría, *Physical Review Letters* **2006**, 97, 189802.
- [284] J. Hedström, J. Swenson, R. Bergman, H. Jansson, S. Kittaka, *The European Physical Journal-Special Topics* **2007**, 141, 53–56.
- [285] W. Doster, S. Busch, A. M. Gaspar, M.-S. Appavou, J. Wuttke, H. Scheer, *Physical Review Letters* **2010**, 104, 098101.
- [286] D. T. Limmer, D. Chandler, *The Journal of Chemical Physics* **2011**, 135, 134503.
- [287] D. T. Limmer, D. Chandler, *The Journal of Chemical Physics* **2013**, 138, 214504.
- [288] S. Kittaka, S. Takahara, H. Matsumoto, Y. Wada, T. J. Satoh, T. Yamaguchi, *The Journal of Chemical Physics* **2013**, 138, 204714.
- [289] F. Mallamace, M. Broccio, C. Corsaro, A. Faraone, D. Majolino, V. Venuti, L. Liu, C.-Y. Mou, S.-H. Chen, *Proceedings of the National Academy of Sciences* **2007**, 104, 424–428.
- [290] P. Larkin, *Infrared and Raman spectroscopy: principles and spectral interpretation*, Elsevier, **2011**.
- [291] M. Farge, *Annual Review of Fluid Mechanics* **1992**, 24, 395–458.
- [292] I. Daubechies, *Ten lectures on wavelets*, SIAM, **1992**.
- [293] M. Mancinelli, T. Pagliaroli, A. Di Marco, R. Camussi, T. Castelain, *Journal of Fluid Mechanics* **2017**, 813, 716–749.
- [294] P. Kumar, E. Foufoula-Georgiou, *Reviews of Geophysics* **1997**, 35, 385–412.
- [295] E. Foufoula-Georgiou, P. Kumar, *Wavelets in geophysics, Vol. 4*, Academic Press, **2014**.
- [296] S. G. Mallat, *IEEE Transactions on Pattern Analysis and Machine Intelligence* **1989**, 11, 674–693.
- [297] C. Torrence, G. P. Compo, *Bulletin of the American Meteorological Society* **1998**, 79, 61–78.
- [298] S. D. Meyers, B. G. Kelly, J. J. O'Brien, *Monthly Weather Review* **1993**, 121, 2858–2866.
- [299] D. F. Walnut, *An introduction to wavelet analysis*, Springer Science & Business Media, **2013**.
- [300] G. Kaiser, *A friendly guide to wavelets*, Springer Science & Business Media, **2010**.

- [301] C. Meneveau, *Journal of Fluid Mechanics* **1991**, 232, 469–520.
- [302] D. L. Donoho, I. M. Johnstone, *Biometrika* **1994**, 425–455.
- [303] R. Madan, S. SKr, N Jain, *International Journal of Recent Trends in Engineering* **2009**, 2, 96–98.
- [304] J. Zanotti, M. Bellissent-Funel, S. Chen, A. Kolesnikov, *Journal of Physics: Condensed Matter* **2006**, 18, S2299.
- [305] D. Klug, E Whalley, *The Journal of Chemical Physics* **1984**, 81, 1220–1228.
- [306] J.-M. Zanotti, P. Judeinstein, S. Dalla-Bernardina, G. Creff, J.-B. Brubach, P. Roy, M. Bonetti, J. Ollivier, D. Sakellariou, M.-C. Bellissent-Funel, *Scientific Reports* **2016**, 6.
- [307] G. Walrafen, *The Journal of Chemical Physics* **1967**, 47, 114–126.
- [308] H MacDonal, B Bedwell, E. Gulari, *Langmuir* **1986**, 2, 704–708.
- [309] G. Onori, A. Santucci, *The Journal of Physical Chemistry* **1993**, 97, 5430–5434.
- [310] Z. Wang, A. Pakoulev, Y. Pang, D. D. Dlott, *The Journal of Physical Chemistry A* **2004**, 108, 9054–9063.
- [311] Q. Sun, *Vibrational Spectroscopy* **2009**, 51, 213–217.
- [312] D. S. Venables, K. Huang, C. A. Schmuttenmaer, *The Journal of Physical Chemistry B* **2001**, 105, 9132–9138.
- [313] Y. Maréchal, *Journal of Molecular Structure* **2011**, 1004, 146–155.
- [314] J. D. Smith, C. D. Cappa, K. R. Wilson, R. C. Cohen, P. L. Geissler, R. J. Saykally, *Proceedings of the National Academy of Sciences of the United States of America* **2005**, 102, 14171–14174.
- [315] S. Y. Venyaminov, F. G. Prendergast, *Analytical Biochemistry* **1997**, 248, 234–245.
- [316] S.-H. Chen, P. Tartaglia, *Scattering methods in complex fluids*, Cambridge University Press, **2015**.
- [317] F Bruni, A Giuliani, J Mayers, M. Ricci, *The journal of Physical Chemistry Letters* **2012**, 3, 2594–2597.
- [318] K. R. Harris, P. J. Newitt, *Journal of Chemical & Engineering Data* **1997**, 42, 346–348.
- [319] A. Okhulkov, Y. N. Demianets, Y. E. Gorbaty, *The Journal of Chemical Physics* **1994**, 100, 1578–1588.
- [320] L. P. Singh, B. Issenmann, F. Caupin, *Proceedings of the National Academy of Sciences* **2017**, 201619501.
- [321] A. Dehaoui, B. Issenmann, F. Caupin, *Proceedings of the National Academy of Sciences* **2015**, 112, 12020–12025.
- [322] W. S. Price, H. Ide, Y. Arata, *The Journal of Physical Chemistry A* **1999**, 103, 448–450.
- [323] F. Prielmeier, E. Lang, R. Speedy, H.-D. Lüdemann, *Berichte der Bunsengesellschaft für physikalische Chemie* **1988**, 92, 1111–1117.

- [324] A Pietropaolo, R Senesi, C Andreani, A Botti, M. Ricci, F Bruni, *Physical Review Letters* **2008**, *100*, 127802.
- [325] Q. Sun, H. Zheng, J.-a. Xu, E Hines, *Chemical Physics Letters* **2003**, *379*, 427–431.
- [326] T. Okada, K. Komatsu, T. Kawamoto, T. Yamanaka, H. Kagi, *Spectrochimica Acta Part A: Molecular and Biomolecular Spectroscopy* **2005**, *61*, 2423–2427.
- [327] M. G. Mazza, N. Giovambattista, F. W. Starr, H. E. Stanley, *Physical Review Letters* **2006**, *96*, 057803.
- [328] N. Giovambattista, F. W. Starr, F. Sciortino, S. V. Buldyrev, H. E. Stanley, *Physical Review E* **2002**, *65*, 041502.
- [329] F. Sciortino, P. H. Poole, H. E. Stanley, S. Havlin, *Physical Review Letters* **1990**, *64*, 1686.
- [330] M. Bey Temsamani, M. Maeck, I. El Hassani, H. D. Hurwitz, *The Journal of Physical Chemistry B* **1998**, *102*, 3335–3340.
- [331] P. H. Poole, U. Essmann, F. Sciortino, H. E. Stanley, *Phys. Rev. E* **1993**, *48*, 4605–4610.
- [332] I. Brovchenko, A. Geiger, A. Oleinikova, *The Journal of Chemical Physics* **2005**, *123*, 044515.
- [333] J. A. Sellberg, C Huang, T. A. McQueen, N. Loh, H Laksmono, D. Schlesinger, R. Sierra, D Nordlund, C. Hampton, D. Starodub, et al., *Nature* **2014**, *510*, 381–384.
- [334] N. E. Levinger, *Science* **2002**, *298*, 1722–1723.
- [335] P. Kumar, G. Franzese, H. E. Stanley, *Physical Review Letters* **2008**, *100*, 105701.
- [336] P. Kumar, G. Franzese, H. E. Stanley, *Journal of Physics: Condensed Matter* **2008**, *20*, 244114.



## *Acknowledgements*

This manuscript is the result of my experience as a Ph.D. student in the Department of Science of the University of Roma Tre. After more than three years, I wish to express my heartfelt thanks to whom, in one way or another, contributed to the accomplishment of this important goal making me feel at home. First of all, my deep and sincere gratitude goes to my supervisor Prof. Fabio Bruni for the continuous support, for his patience, motivation, enthusiasm, and encouragement. He has often believed in me and in this thesis much more than I did. A special thank needs to be conveyed to my co-supervisor Prof. Livia Bove for her invaluable collaboration in this project: she gave me the possibility to be involved in several experiments at international facilities and many of the results presented in this thesis would not have been achieved without her motivation, support and helpful discussions during my visits at UPMC in Paris.

In addition, I am also deeply thankful to the "big boss" of the group, Prof. Maria Antonietta Ricci: her wide experience in the neutron science and her extended knowledge about the physics of water have notably enriched my educational path in the Liquids Group. Her suggestions, insightful comments and clear explanations have been of fundamental importance for me and my scientific growth.

These three "reference points" have never left me alone and have guided me despite several difficulties and also when the goal seemed too far to reach. The completion of this doctoral dissertation was possible only with their backing, effort, and precious guide; for this reason, I would like to express my sincere gratitude to all of them.

My special appreciation is also for Dr. Frederico Alabarse, who shared his time with me at Synchrotron Soleil and at ILL, teaching me the "secrets" of measuring under pressure, generously helping me all the time and taking care of my experiments with participation, sincere enthusiasm and tolerance. I have learnt so much during the time spent with him and his broad experience and scientific know-how have been of utmost importance for my Ph.D. project's progress.

But the list of my acknowledgements would not be complete without mentioning all the members of Liquids Group and Neqo Group in Roma Tre, who have made the years of my Ph.D. study more enjoyable, exciting and colourful. Some are still working in Roma Tre, while someone else has found his way in another job, but I feel lucky to have met all of them as their presence has brightened my days spent in the lab. It is especially due to them that I will have a beautiful memory of this experience in Roma Tre and I will look back nostalgically at my time spent there. I could not have imagined a better group for sharing my time during my Ph.D. "adventure".

Firstly, I would like to express my gratitude to Armida, for her sympathy and her solar soul. Then I obviously cannot forget Alfonso, one of the most resourceful people I have met in Roma Tre. I have particularly appreciated his elegance and kindness; he has always been sweet and thoughtful, available to everybody all the time, and was able to lighten the stress and the difficulties over these years. Thanks, Alf!

A special thank goes to my three colleagues, who brightened my Ph.D. experience from the beginning: Laura, Annalaura and Valentina. Thanks for your presence and your patience. Laura was a perfect partner for scientific and light conversations, although all the problems she had to face during her Ph.D. project. Jokes and time spent together in the gym are unforgettable.

Annalaura and Valentina started being simply labmates, but now they have become trusted friends...and this is quite surprising! Annalaura and I were firstly sitting beside, saying nearly no words. But from day to day I have learned to know her and to appreciate her company. I must thank her for all the time spent together, because with her I never felt alone. She also deserves my gratitude for let me get involved in her interesting activities, for teaching me to drink beer, for her valuable and funny English lessons, for the yoghurt-box (the most appropriate gift ever received in my life), for her excellent sweets and, above all, for patiently standing my chatter, my complaints and my pranks. Valentina sat next to me for two years and she knows how I missed her presence when she went away. Although she did not speak a lot, time spent with her was always enjoyable and I know she still is a person I can count on, both as a colleague and a true friend.

A sincere and deep thank goes to Marco S.: even if I never have sweet words for him, he knows to deserve more than the acknowledgements I can write here. I must be grateful to him for making me smiling again and giving me some of the funniest moments lived during my stay in the Liquids Lab. I said nothing when I should have done, but it is never too late to write "I'm glad I met you".

I would like to thank the "new entry" in the Liquids Group, Ludovica, because she has decided to grant me some confidence even if I am "strange". I am sorry we cannot share a longer way and we will not have the possibility to work together, but I trust in her and in her brilliant scientific future. Good luck for your Ph.D. project, Ludo, and never give up! The way is long, sometimes difficult and often rising, but you'll be stronger than everything and everyone, I am sure.

I am also keenly grateful to all the members of Neqo Group: Luca, Emanuele, Ilaria and the boss, Prof. Marco Barbieri, whose knowledge is boundless and can tell something about everything. His useful advices, history lessons and curiosities from all over the world have been sincerely appreciated.

Last but not the least, I wish to warmly thank my family: my parents, my extraordinary brother and Tiziano. They have never stopped to support me before and throughout the accomplishment of this goal, and I know they will be always present in the rest of my life. All my achievements belong also to them.

*Eleonora*